CIVIL ENGINEERING JOURNAL

číslo 1/2022

Obsah:

CIVIL ENGINEERING JOURNAL

Article no. 1

THE CIVIL ENGINEERING JOURNAL 1-2022

A SUSTAINABLE APPROACH TO IMPROVEMENT OF CORROSION PROTECTION COATINGS FOR STEEL STRUCTURES

Parviz Soroushian[1], Anagi Balachandra[2] , Rankothge Weerasiri[2], Nalin Darsanasiri[2] and Nastran Abdol[2]

1. *Metna Co., 3927 Dobie Road, Okemos, MI 48864, USA; metnaco@gmail.com*
2. *Metna Co., 1926 Turner Street, Lansing, MI 48906, USA; abmetnaco@gmail.com, wrmetnaco@gmail.com, ndmetnaco@gmail.com, nametnaco@gmail.com*

ABSTRACT

Corrosion is a primary factor compromising the safety and service life of steel structures. Corrosion protection coatings are generally employed for protection of the steel structures that are exposed to different aggressive environments. This research evaluated the use of biobased ion exchangers as a sustainable means of improving corrosion protection coatings.

Two base polymer coatings (vinyl and coal-tar epoxy) were considered. The following types and dosages of biobased ion exchangers were evaluated in these coatings: (i) strong-base ion exchange cellulose in OH, PO_4, SiO_3, BO_3, NO_2, SO_4 and NO_3 forms at 1% by weight of resin; (ii) weak-acid starch citrate ion exchanger in H form at 1 wt.%; and (iii) strong-base ion exchange cellulose in OH form at 2 wt.%. In addition, a strong-base ion exchange resin in OH form was considered at 1 and 2 wt.% as control. Different coating formulations were evaluated based on the outcomes of salt-fog corrosion, moisture resistance, pull-off strength, and abrasion resistance tests. The introduction of certain biobased ion exchangers in protective coatings was found to be an effective means of achieving improved levels of corrosion resistance, adhesion capacity, moisture stability and abrasion resistance.

KEYWORDS

Biobased ion exchanger, Protective coatings, Corrosion resistance, Sustainability, Moisture stability, Adhesion capacity, Abrasion resistance

INTRODUCTION

Preface

The cost burden associated with corrosion of metals is ~3.4% of the global GDP.[1] Use of protective coatings is a common approach to mitigating corrosion of steel structures. The global markets for protective coatings are approaching $50 billion.[2] There are, however, limits on the extent of protection against corrosion provided by coatings. Their effectiveness can diminish over time due to a host of factors, including deterioration of coatings under environmental, erosive and other

[1] http://impact.nace.org/economic-impact.aspx

[2] https://www.grandviewresearch.com/press-release/global-protective-coatings-market

damaging effects. The work presented here seeks to develop an economical and sustainable approach to improvement of corrosion protection coatings. This approach employs biobased ion exchangers derived from different sources, emphasizing agricultural residues which are abundantly available (320 million tons/yr in the United States) and are generally of limited monetary value. Applications in protective coatings can consume close to 300,000 tons/yr of biobased ion exchangers [1-3]. The corrosion inhibitors currently used in protective coatings could pose environmental hazards; they are costly (few thousand dollars per ton) and are made using exhaustible raw materials.

Many byproducts of agricultural crop processing have native ion-exchange attributes provided by their constituent polymers (especially cellulose). Cost-effective strategies involving chemical modification and crosslinking have been developed to enhance the ion-exchange capacity and physical stability of ion exchangers derived from crop residues [1]. These biobased ion exchangers provide a desired balance of performance, cost and sustainability attributes. They could be used in polymer-based protective coatings to remove aggressive ions from corrosive solutions as they diffuse through coatings towards metallic surfaces.

Corrosion, as an electrochemical reaction, requires the presence of an electrolyte. Pure water, unlike solutions (which incorporate ions), is a poor electrolyte. Certain ions (e.g., Cl^- and SO_4^{2-}) not only form electrolytes but also stimulate corrosion reactions [4]. This investigation used biobased ion exchangers in protective coatings with the objective of removing such aggressive ions as well as their counter-ions from the solutions diffusing through the coating towards steel surfaces, thereby abating both the electrolyte and the corrosion stimulants.

Ion exchangers are insoluble solid materials which carry exchangeable cations or anions [5,6]. These ions can be exchanged for a stoichiometrically equivalent amount of other ions of the same sign when the ion exchanger is in contact with an electrolyte solution. Ion exchangers comprise a framework with electric surplus charge together with mobile counter-ions. Carriers of exchangeable cations and anions are called cation exchangers and anion exchangers, respectively. A typical anion exchange is:

$$\underline{XOH} + NaCl\ (aq) \rightarrow \underline{XCl} + NaOH\ (aq) \quad (1)$$

The resulting *NaOH* can be removed from the solution through a typical cation exchange:

$$\underline{XH} + NaOH\ (aq) \rightarrow \underline{XNa} + H_2O \quad (2)$$

where, X is a structural unit of the anion and cation exchangers (XOH and XH, respectively), (*aq*) indicates that the electrolyte is in aqueous solution, and solid phases are underlined.

Insoluble cation and anion exchangers of particular forms are used commonly to substantially deionize salt solutions. Ion exchangers of petrochemical, mineral and plant origins are used in water purification.

Basic Principles

Fine anion and cation exchangers (XOH and XH) were incorporated into protective coatings in order to remove soluble corrosive salts (anions and cations) from the diffusing solutions (Fig. 1). The ion-exchange process was used in this approach to diminish the electrolyte, and to render the corrosive solutions innocuous as they diffuse into the coating towards the metal surfaces. The example of Fig. 1 depicts the ion-exchange effects which essentially remove NaCl from the salt solution as it diffuses through the coating (by converting NaCl to H_2O). Removal of Na^+ and Cl^- ions from the solution diminishes the electrolyte, and mitigates the corrosive effects of chloride ions.

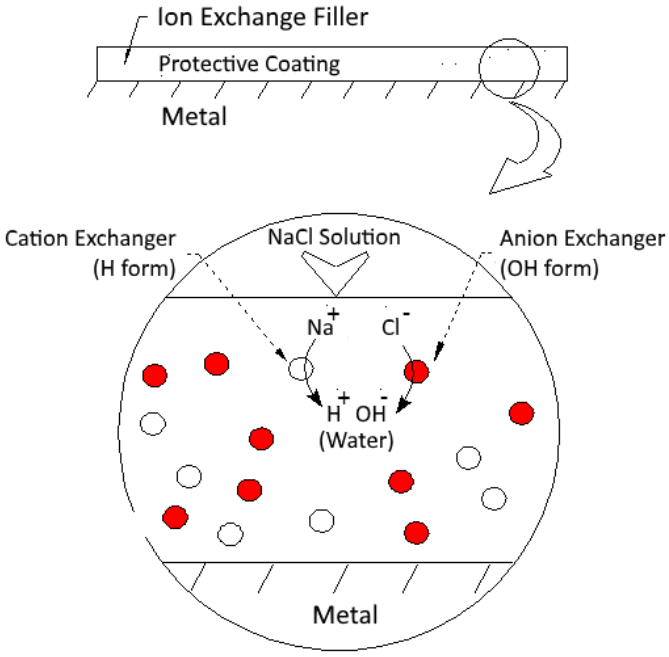

Fig. 1 - Schematic depiction of the approach.

Ion exchange occurs because the ion exchanger prefers one species to the other. The preference for one species may have several reasons. The most important are [5-8]: (i) electrostatic interactions between the charged framework and counter-ions depend on the size and, in particular, the valence of the counter-ion; and (ii) large counter-ions may be sterically excluded from the narrow pores of ion exchanger. These and other factors lead to preferential uptake of certain species by the ion exchanger. The ability of ion exchanger to distinguish between various counter-ion species is called *selectivity*. In the case of a cation exchanger, for example, the selectivity sequence $K^+ > NH_4^+ > Na^+ > H^+$ implies that the cation exchanger in hydrogen (H^+) form can exchange the K^+, NH_4^+ and Na^+ cations.

Different Types of Ion Exchangers

Ion exchangers are available in resin, plant (cellulose, starch, etc.) and mineral forms. The general structural principle (i.e., a framework with electric surplus charge and mobile counter-ions) is common to all ion exchangers. Nevertheless, various types of ion exchanger show marked differences in behavior.

Ion exchange *resins* in the form of crosslinked polyelectrolytes are in common use [5-9]. The matrix of these polymers is hydrophobic; hydrophilic components are introduced by the incorporation of ionic groups such as $–SO_3^-H^+$. Ion-exchange resins are made insoluble by introduction of crosslinks which interconnect the various hydrocarbon chains; an ion-exchange resin particle is practically one single macromolecule. The ion-exchange behavior as well as the chemical, thermal and mechanical stability of different ion-exchange resins depend mainly on the structure and the degree of crosslinking of matrix, and also on the nature and number of fixed ionic groups. The most common polymer matrix used today is based on crosslinked polystyrene. Sulfonated copolymers of styrene and divinylbenzene are some commonly used ion exchangers. Cation-exchange resins are subdivided into strong-acid and weak-acid groups; similarly, anion-exchange resins are divided into strong-base and weak-base materials. Different ion-exchange resins generally provide 1-10 meq/g capacity for ion exchange.

Biobased ion exchangers are produced by attaching substitute groups with basic or acidic properties to plant-based (cellulose, starch, etc.) molecules [10]. Their ion-exchange properties are similar to those of ion-exchange resins. Biobased ion exchangers, however, are generally finer with greater specific surface area. Their porous structure provides for a higher rate of exchange, and allows for entrance and attachment of large molecules that are not readily adsorbed in ion-exchange resins [7-9]. The cellulose used for production of biobased ion exchangers is commonly derived from wood and cotton. Biobased ion exchangers can also be produced via chemical modification and crosslinking of agricultural residues such as corn stalk, sugar beet pulp, soybean hull and wheat straw [11,12].

The following considerations provide the rationale for use of biobased ion exchangers in lieu of ion-exchange resin in corrosion protection coatings: (i) many biobased ion exchangers, when compared with ion-exchange resins, offer higher rates of exchange and greater accessibility for diverse categories of ions; (ii) the commonly higher fineness of biobased ion exchangers favors their use as filler in polymer coatings; (iii) application in protective coatings does not involve regeneration; the favorable regeneration qualities of ion-exchange resins are thus irrelevant in this application; (iv) the cost of biobased ion exchangers is an order of magnitude less than that of ion-exchange resins; and (v) agricultural residues, which are available in tremendous quantities and are generally of limited monetary value, can be used as raw materials for production of biobased ion exchangers.

Ion-Exchange Celluloses

The biobased ion exchangers used in this investigation were: (i) a strong-base anion exchange cellulose (Whatman® from Millipore Sigma) in OH^-, PO_4^-, SiO_3^-, BO_3^-, NO_2^-, SO_4^-, NO_3^- forms; (ii) a weak-acid cation exchange starch (starch citrate in H^+ form); and (iii) a strong-base anion exchange cellulose (Whatman® from Millipore Sigma). In addition, a strong-base anion exchange resin in OH^- form (Dowex Marathon MSA from DOW Chemical) was used as control.

The biobased anion exchangers were received in Cl^- form, and were converted into other ionic forms to provide them with the capability to render corrosion protection effect by exchanging the diffusing Cl^- ions with innocuous anions. All biobased ion exchangers were dried in an oven at 55^{o}C for 18 hours, and then subjected to size reduction via ball-milling. For this purpose, a ceramic jar was used together with ceramic balls, and the biobased ion exchangers were milled to 6-9 μm particle size.

Fig. 2 shows an example biobased ion exchanger used in protective coatings.

Fig. 2 - An example biobased ion exchanger (anion-exchange cellulse in SO_3^- form) after ball milling.

Formulation of Protective Coatings

Two different coating formulations based on vinyl and coal-tar epoxy were used in this investigation. Strong-base and weak-acid biobased ion exchangers of different ionic forms were incorporated into these polymer matrices as corrosion inhibitors.

Vinyl resins are used to formulate high-efficiency anti-corrosion coatings due to their good physicochemical characteristics (chemical resistance, and desired barrier qualities against water and oxygen). Vinyl resins modified with maleic acid can be applied directly on steel surfaces because acid groups improve adhesion. Tricresyl phosphate was employed as a plasticizer at a resin: plasticizer weight ratio of 4:1. The long-chain copolymer of vinyl consolidates into a film which is resistant to water, weathering, immersion, acids, alkalis, and many other chemicals. The vinyl-based resin used in this investigation (Trade Name: UCAR-Solution Vinyl Resin supplied by Union Carbide) can be applied without a primer. Tricresyl Phosphate (Trade Name: Tritolyl Phosphate, Tec 90% mixture of isomers - Sigma Aldrich) was used as plasticizer at 25% by weight of resin to make the vinyl resin flexible.

Coal-tar epoxies, with coal tar used as filler, rely upon barrier qualities against moisture movement for protection of steel against corrosion. They provide desired adhesion capacity, and can be applied directly on roughened (e.g., sandblasted) steel surfaces. The coal tar filler provides for improved moisture resistance without undermining the toughness, adhesion capacity, UV resistance and thermal stability of epoxy. The desired alkali resistance of epoxies benefits their performance under seawater exposure. Cathodic protection is another favorable attribute of epoxy resin; the high dielectric strength of these coatings contributes insulating qualities which prevent the electrochemical flow that drives the corrosion process.

The biobased ion exchangers and the control ion-exchange resin introduced earlier were used as corrosion inhibitors. Ferric (Iron III) oxide (<5 micron particle size, 99+% supplied by Sigma Aldrich) and barium sulfate (98% supplied by Sigma Aldrich) were also used in the coating composition. Isobutylketone (4-methyl-2-pentanone, 99+%), xylene (xylene isomers plus ethylbenzene), and butyl acetate (99.5+% A.C.S. reagent), supplied by Sigma Aldrich, were used as solvent at 10:20:70 weight ratios.

The composition of the vinyl-based corrosion protection coatings considered in this investigation are presented in Tab. 1. The compositions of the coal-tar epoxy Parts A and B are presented in

Tab. 2. The protective coating formulations with (or without) ion exchangers considered in the experimental program are introduced in Tab. 3.

Tab. 1 - Compositions of vinyl-based corrosion protection coatings.

Constituent	Weight%
Ferric Oxide	19
Barium Sulfate	19
Vinyl Resin	50
Tricresyl phosphate	12

Tab. 2 - Composition of the corrosion protection coating based on coal-tar epoxy.

(a) Part A

Material	Trade Name	Manufacturer/Supplier	Weight%
Coal-tar	Coal-tar.	Alpha Aesar	35.5
Versamid	VERSAMID 100PMX60	Palmer Holland,	24.4
Nytal 300	Nytal 300 Industrial Talc	R.T. Vandorbilt Company, Inc,	24.8
CAB-O Lite M-5	CAB-O SIL M-5	Cabot Corporation	5.90
Aluminum Stearate	Aluminum Stearate, Technical Grade	Alpha Aesar	0.80
Xylol	o-xylene, HPLC Grade, 96%	Alpha Aesar	8.60

(b) Part B

Material	Trade Name	Manufacturer/Supplier	Weight%
Epoxy Araldite 471x75	Araldite GZ 471X-75, Xylene Solution	Vantico, Inc	46.3
Butanol	1-Butanol, A.C.S., 99.4+%	Alpha Aesar	11.5
Cellosolve Acetate	2-Ethoxyethyl acetate, 98%	Sigma Aldrich	7.70
Xylol	o-xylene, HPLC Grade, 96%	Alpha Aesar	34.5

Tab. 3 - The protective coating formulations considered in the experimental program.

Polymer	Ion Exchanger	Specimen #	Ion Exchanger Weight% (Form)
Vinyl	None	VR-0	0
	Starch citrate cation exchanger (H^+ form)	VRCAH-1	1 (H^+)
	Strong-base anion exchange cellulose	VRCBOH-1	1 (OH^-)
		VRCBOH-2	2 (OH^-)
		VRCBSIO3-1	1 (SiO_3^-)
		VRCBPO4-1	1 (PO_4^-)
		VRCBBO3-1	1 (BO_3^-)
		VRCBSO4-1	1 (SO_4^-)
		VRCBNO2-1	1 (in NO_2^-)
		VRCBNO3-1	1 (in NO_3^-)
	Strong-base anion exchange resin	VRRBOH-1	1 (OH^-)
		VRRBOH-2	2 (OH^-)
Coal-tar Epoxy	None	CT-0	0
	Starch citrate cation exchanger (H^+ form)	CTCAH-1	1 (H^+)
	Strong-base anion exchange cellulose	CTCBOH-1	1 (OH^-)
		CTCBOH-2	2 (OH^-)
		CTCBSIO3-1	1 (SiO_3^-)
		CTCBPO4-1	1 (PO_4^-)

		CTCBBO3-1	1 (in BO_3^-)
		CTCBSO4-1	1 (SO_4^-)
		CTCBNO2-1	1 (in NO_2^-)
		CTCBNO3-1	1 (in NO_3^-)
	Strong-base anion exchange resin	CTRBOH-1	1 (OH^-)
		CTRBOH-2	2 (OH^-)

Preparation of Protective Coatings

The viny-based coating was prepared in a laboratory-scale porcelain jar ball mill with 3 liters volume, operated at 60 revolutions per minute with a ceramic ball-to-material weight ratio of 10: 1. These conditions were selected to produce a homogenous end product. The vinyl resin (150 g) was added to the ball mill, and milled for 2 hours. The remaining constituents of the formulation, except for tricresyl phosphate, were then added to the ball mill, and milled for 24 hours. The product was transferred to a laboratory-scale planetary mixer, the tricresyl phosphate constituent was added, and mixed for 10 minutes. Solvents were then added as needed (150 ml initially, and more added if required) to produce the required viscosity, and mixed for 20 minutes. The end product was left for 24 hours to ensure homogeneity, and then applied.

Coatings based on coal-tar epoxy were mixed for 20 minutes in a planetary mixer with polyamide and the remaining constituents of Part A of the formulation. Part B of the formulation was then added, and mixing was continued for 20 more minutes.

Selection, Preparation and Coating of Steel Substrates

ASTM A 1008–CS Type B steel (Cold Rolled) was obtained from Heidtman Steel Products, Inc. This is a low-carbon matte finish steel that is suitable for application of paints and enamels. Its yield and tensile strengths are 38,000, and 52,000 psi, respectively. The steel was cut into 76.2mm x 127mm (3in x 5 in) pieces. Edges were rounded, and corners were made smooth. The steel surfaces were vigorously rubbed using clean lint-less cloth wet with mineral spirits until all soluble and loosely adhering particles removed. The surfaces were then flushed with clean solvent, and dried at 52 to 93°C (125 to 200°F) before use or storage (ASTM D 609 Procedure D). Fig. 3**a** shows examples of the resulting substrate that are ready for application of protective coatings.

Protective coatings were applied following ASTM C823 Procedure B, using a dip coater that withdraws test specimens from a container of the coating material at a constant rate. The coating thickness after withdrawal was measured per ASTM D1005 (Fig. 3b). The withdrawal rate was adjusted to yield the targeted coating thickness (measured at three different locations).

(a) A substrate prepare for coating (b) Withdrawal of substrate from the coating mix

Fig. 3 - Example substrate and the coating process.

Test Methods

The pull-off strength of protective coatings was measured following the ASTM D4541 and ASTM B117procedures using the test setup shown in Fig. 4a. Abrasion resistance was evaluated using the ASTM D968 procedures (Fig. 4b). Salt fog corrosion tests (Fig. 4c) were performed on scribed (Fig. 4c) or non-scribed tests per ASTM D1654 (Fig. 4d). The exposure period was 1944 hours. Loss of adhesion at the scribe mark for scribed specimens, and blistering associated with corrosion for non-scribed specimens (as well as other failure conditions) were evaluated per ASTM D1654 and ASTM D714, respectively. In the case of the scribed specimens, corrosion rating was based on the extension of paint loss from the scribe mark, with ratings of 10 and 0 assigned to cases with 0 mm (0 in) and 13 mm (5/8 in) scribe extension, respectively. The non-scribed specimens were dried with paper towel, and their surfaces were evaluated for detection of corrosion spots, blisters and any other types of failure. When the character of failure permitted, photographic blister standards (ASTM D714) were used to describe the results with respect to the size of blisters or corroded areas. Moisture resistance tests were performed for evaluating the stability of protective coatings when immersed in water (Fig. 4e). Specimens were immersed in water at 27°C, and were evaluated for any indication of degradation, including color change, blistering and loss of adhesion.

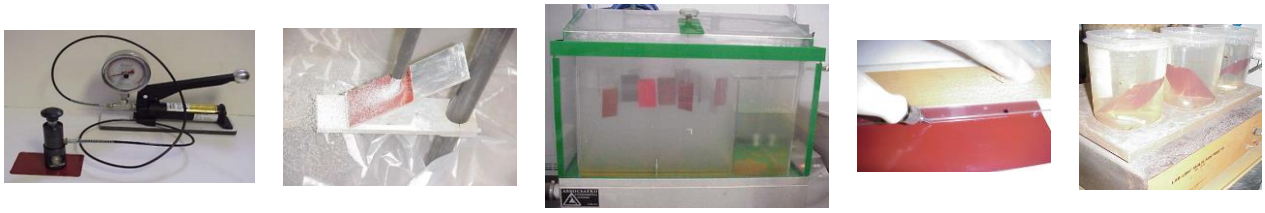

(a) Pull-off *(b) Abrasion* *(c) Salt fog spray* *(d) Scribing* *(e) Immersion*

Fig. 4 - Test setups.

RESULTS

Pull-Off Strength

Failure in pull-off tests generally occurred at the coating-substrate interface for vinyl coatings (Fig. 5a), and through the coating thickness for coal-tar epoxy coatings (Fig. 5b). Four replicated pull-off tests were performed with each coating formulation. The pull-off strength test results are presented in Fig. 6. The pull-off strengths of coatings based on coal-tar epoxy are observed to be smaller than those based on vinyl. Given the differences in failure modes of these two coating systems (Fig. 5), however, the lower pull-off strength of coatings based on coal-tar epoxy does not necessarily points at their lower adhesion capacity. The pull-off strength test results for vinyl coatings indicate that different biobased ion exchangers can either decrease or increase the pull-off strength; the effects are moderate to small. The highest pull-off strength of vinyl-based coatings was obtained with the addition of 1 wt.% strong-base anion exchange cellulose in OH^- form. The addition of strong-base anion exchange resin at 2 wt.%, on the other hand, produced the lowest pull-off strength for vinyl-based coatings. The effects of biobased ion exchangers on the pull-off strength of the coal-tar epoxy coating were moderate to small. Addition of strong-base anion exchange cellulose in NO_3^- form at 1 wt.% produced a slight rise in the pull-off strength of coal-tar epoxy. The lowest pull-off strength for coatings based on coal-tar epoxy was obtained with the addition of strong-base anion exchange resin in OH^- form at 1 wt.%. This drop was the only statistically significant change (at 5% level of significance) in pull-off strength of the coal-tar epoxy coatings resulting from the addition of ion exchangers.

(a) Vinyl (b) Coal-tar epoxy

Fig. 5 - Typical failure modes in pull-off tests.

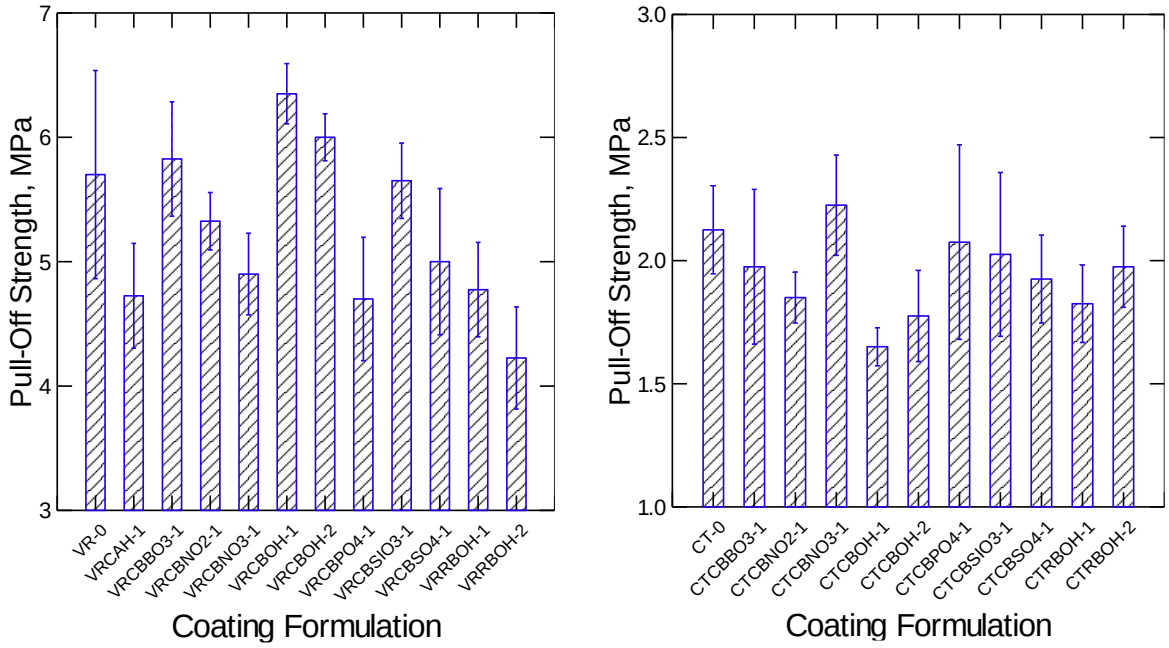

(a) Vinyl (b) Coal-tar epoxy

Fig. 6 - Pull-off strength test results (means & standard errors).

Abrasion Resistance

Four replicated abrasion tests performed for each coating; the test results are presented in Fig. 7. Vinyl-based coatings are observed to provide relatively high levels of abrasion resistance when compared with the coatings based on coal-tar epoxy. There was a statistically significant improvement (at 5% level of significance) of the abrasion resistance of vinyl-based coatings with the addition of 1 wt.% strong-base ion-exchange cellulose in NO_3^- form. The effects of most biobased ion exchangers on the abrasion resistance of the vinyl-based coating were not statistically significant. Only the anion exchange resin (at 1 and 2 wt.%) and the cation exchange starch citrate (at 1 wt.%) had statistically significant adverse effects (at 5% level of significance) on the abrasion resistance of the vinyl-based coating. In the case of coatings based on coal-tar epoxy, addition of 1 wt.% strong-base ion-exchange cellulose in NO_3^- form or 1 wt.% anion exchange resin in OH^- form produced statistically significant (at 5% level of significance) improvements in abrasion resistance.

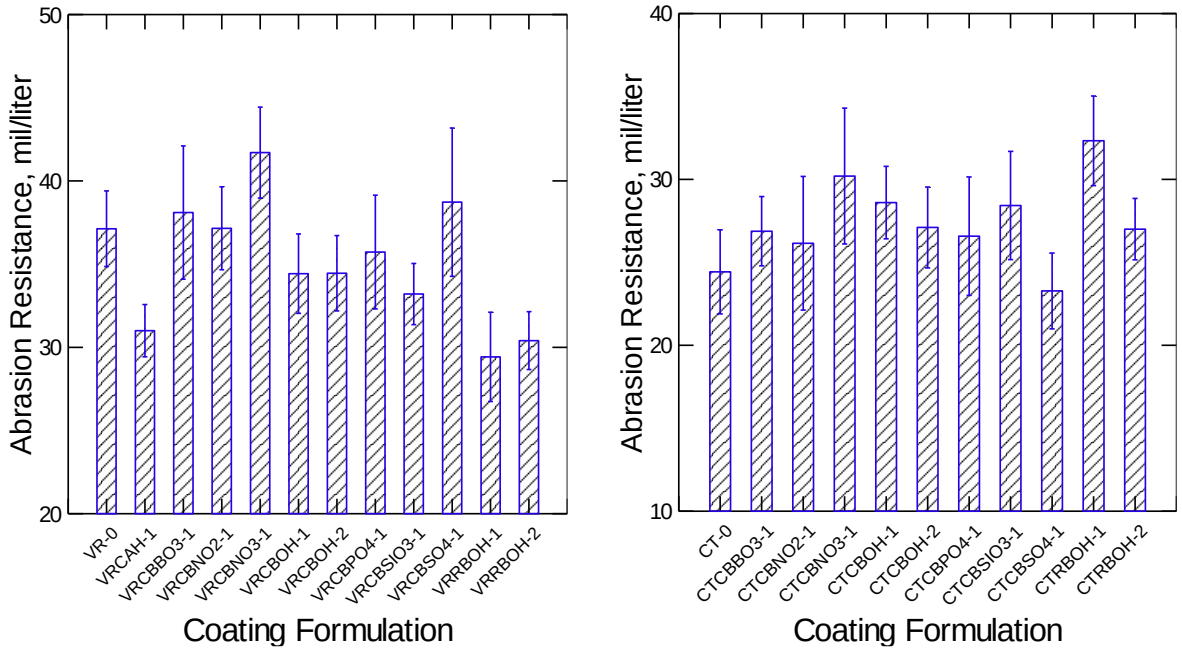

(a) Vinyl *(b) Coal-tar epoxy*

Fig. 7 - Abrasion resistance test results (means & standard errors)

Salt Fog Corrosion Resistance

Scribed Specimens

Examples of scribed specimens with modified coatings based on vinyl and coal tar epoxy after exposure to salt fog are presented in Fig. 8. Results of three replicated salt fog corrosion tests performed on scribed specimens with each coating formulation are presented in Fig. 9. In the case of formulations based on vinyl, most ion-exchange celluloses at the dosages considered (1 or 2 wt.%) did not produce notable (statistically significant at 5% level of significance) changes in the salt fog corrosion resistance rating. Introduction of the ion-exchange resin considered here (in OH^- form at 1 and 2 wt.%) as well as Starch citrate cation exchanger in H^+ form at 1 wt.%, on the other hand, compromised the salt fog corrosion resistance rating of the vinyl-based coating. In the case of coating formulations based on coal-tar epoxy, introduction of anion-exchange cellulose in NO_3^- form at 1 wt.% and anion-exchange resin in OH^- form at 2 wt.% produced notable (statistically significant at 5% level of significance) improvements in the salt fog corrosion resistance rating.

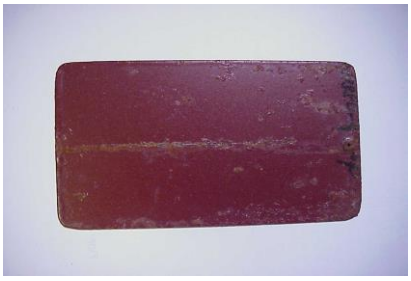

(a) Vinyl coating with 1 wt.% anion exchange cellulose in PO_4^- form

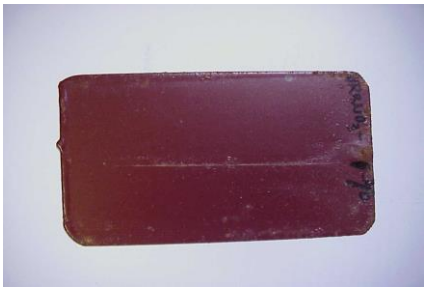

(b) Vinyl coating with 1 wt.% anion exchange cellulose in NO_3^- form

(c) Coal tar epoxy coating with 1 wt.% anion exchange cellulose in SO_4^- form

(d) Coal tar epoxy coating with 1 wt.% anion exchange cellulose in NO_3^- form

Fig. 8 - Examples of scribed specimens after salt fog exposure.

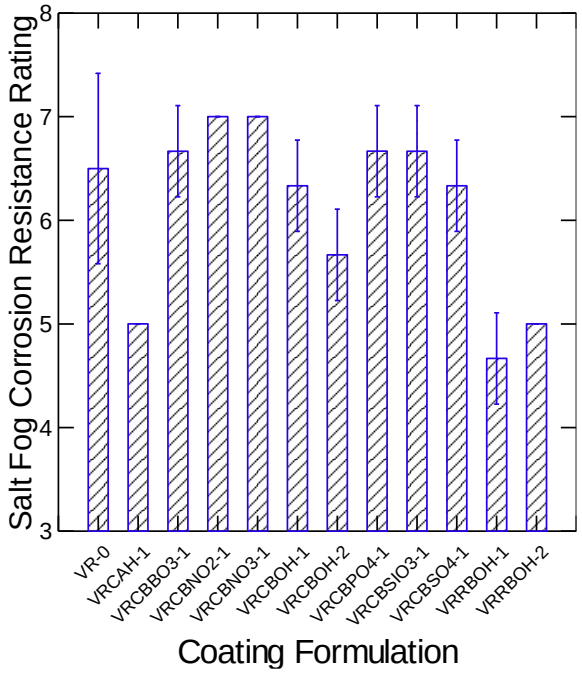

(a) Vinyl

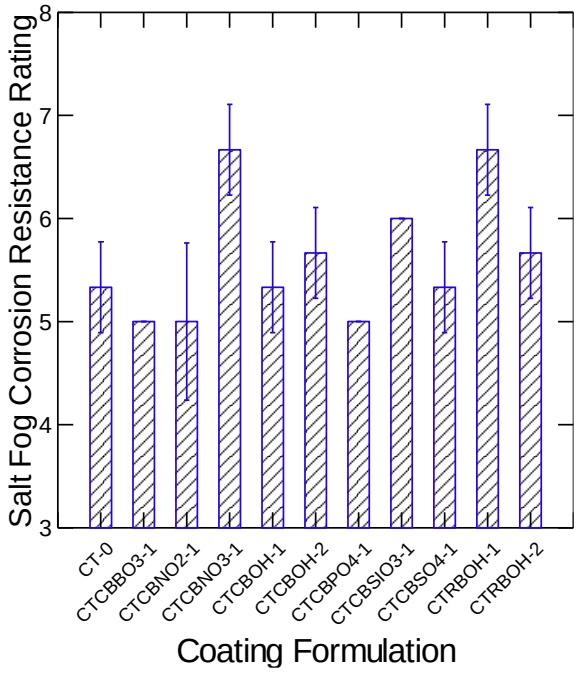

(b) Coal-tar epoxy

Fig. 9 - Salt fog corrosion test results for scribed specimens (means and standard errors).

Non-Scribed Specimens

Examples of non-scribed specimens after completion of the salt fog corrosion exposure period are presented in Fig. 10. In an effort to quantify the test data, the following ratings were assigned to the density of blistering: Few = 1; Medium = 2; Medium Dense = 3; Dense = 4. The blistering level was then defined as the multiplication of the degree and the density of blistering. Fig. 11 presents the blistering level of non-scribed test specimens after completion of the salt fog corrosion period for non-scribed specimens with different coating formulations. As far as the vinyl coatings applied to non-scribed specimens are concerned, the addition of 1 wt.% anion exchange cellulose in SiO_3^- form and 2% anion exchange cellulose in OH^- form produced notable and statistically significant reductions in blistering level. The effects of other ion exchange celluloses and resin on the blistering level of non-scribed specimens with vinyl coating were not statistically

significant. In the case of coal tar epoxy-based coatings, addition of 1 wt.% anion exchange cellulose in PO_4^- form produced notable and statistically significant (at 5% level of significance) reduction in blistering level. The effects of other ion exchange celluloses and ion exchange resin on the blistering level of non-scribed specimens with coal tar epoxy coating were not statistically significant.

(a) Vinyl coating with 1 wt.% anion exchange cellulose in PO_4^- form

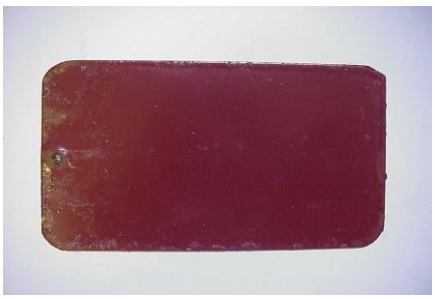

(b) Vinyl coating with 1 wt.% anion exchange cellulose in NO_3^- form

(c) Coal tar epoxy coating without ion exchanger

(d) Coal tar epoxy coating with anion exchange cellulose in NO_3^- form

Fig. 10 - Examples of non-scribed specimens after conclusion of the salt fog corrosion exposure period.

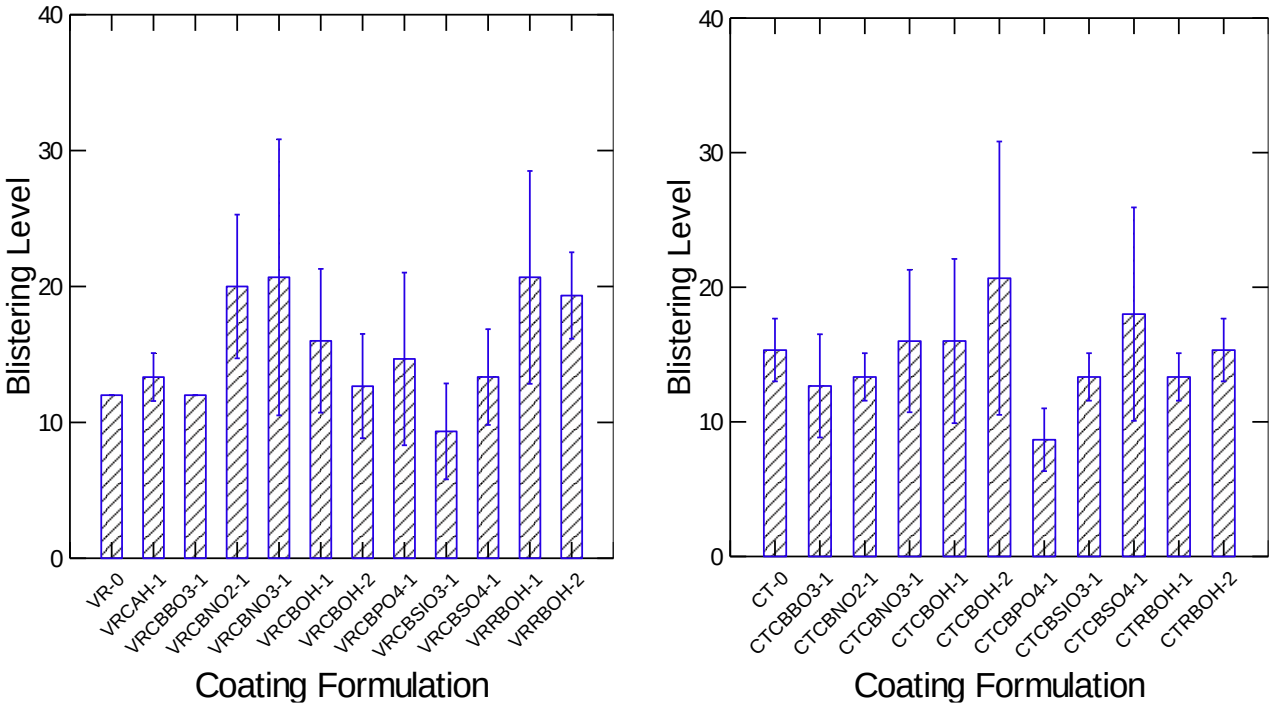

(a) Vinyl *(b) Coal-tar epoxy*

Fig. 11 - Blistering levels (means and standard errors) of non-scribed specimens with different coating formulations after completion of the salt fog corrosion exposure period.

Moisture Resistance

The extent of damage reflecting on moisture resistance is expressed as the change in color, degree of blistering, or loss of adhesion of the coating. Figure 12 shows examples of vinyl-based coating with different ion exchange celluloses after immersion in water for 81 days. The moisture resistance test results are summarized in

Tab. 4. The moisture resistance of coatings based on vinyl and coal tar epoxy generally benefited from the introduction of biobased ion exchangers. For example, 1 wt.% anion exchange celluloses in NO_3^- and SiO_3^- forms improved the moisture resistance of vinyl and coal-tar epoxy coatings, respectively.

(a) 1% ion-exchange cellulose in SiO_3 form *(b) 1% ion-exchange cellulose in NO_3 form*

Figure 12. Examples of specimens with vinyl-based coatings incorporating different ion-exchange celluloses after 81 days of immersion.

Tab. 4 - Moisture resistance test results.

Coating Formulation	Color Change	Loss of adhesion	Degree of Blistering
VR-0	No	~25% of surface area lost adhesion	8-Medium Dense
VRCBOH-1	Yes	No	6-Medium Dense
VRCBOH-2	Yes	No	8-Medium
VRCBSIO3-1	Yes	~10% of surface area lost adhesion	8-Medium
VRCBNO3-1	Yes	No	8-Few
VRCBNO2-1	Yes	No	6-Medium
VRRBOH-2	Yes	No	6-Medium Dense
CT-0	Yes	No	4-Dense
CTCBOH-1	Yes	No	6-Medium Dense
CTCBSIO3-1	Yes	No	4-Medium Dense
CTCBNO2-1	Yes	No	8-Few
CTCBNO3-1	Yes	No	6- Medium
CTRBOH-2	Yes	No	4-Dense

The effects of ion exchange celluloses on various aspects of the protective coating performance strongly depends on their type. Statistically significant gains in the abrasion, salt fog corrosion and moisture resistance were realized by the addition of ion exchange cellulose in NO_3^- form at 1 wt.%. The pull-off strength of the coating was retained in the presence of this ion exchange cellulose. These findings suggest that selective use of ion exchange cellulose in coatings can be a sustainable means of enhancing their protective attributes.

CONCLUSION

Biobased ion exchangers, including those synthesized using agricultural residues, offer promise as sustainable, environmentally friendly and cost-effective alternatives to the corrosion inhibitors currently used in protective coatings. Biobased ion exchangers, when incorporated into polymer-based protective coatings at 1 to 2 weight%, can remove corrosive ions from the solution diffusing through the coating towards metallic surfaces, thus rendering the originally aggressive solutions innocuous. In addition, biobased ion exchanges either retain or improve the key engineering properties of protective costings, including their abrasion resistance, pull-off bond strength and moisture resistance. These findings were based on the test data generated using various types of biobased ion exchangers of different ionic forms, which were used in different polymer-based protective coatings. Major distinctions were identified between the effects of different biobased ion exchangers on the performance attributes of specific polymer-based protective coatings. Further investigations are needed in order to explain the differences in the benefits realized by introducing various types of biobased ion exchangers in different protective coatings.

ACKNOWLEDGEMENTS

This research was funded by the United States Department of Agriculture Contract No. 2003-35504-12845.

REFERENCES

[1] Mosa, A.A., El-Ghamry, A., Truby, P., 2011. Chemically Modified Crop Residues as a Low-Cost Technique for the Removal of Heavy Metal Ions fro m Wastewater. Water, Air and Soil Pollution, vol. 217 (1-4): 637-647.

[2] Kamel, S., 2005. Preparation of cation-exchange resin from lignin. International Journal of Polymeric Materials and Polymeric Biomaterials, vol. 55 (4): 283-291.

[3] Dhodapkar, R., Rao, N., Pande, S., Kaul, S., 2006. Removal of basic dyes from aqueous medium using a novel polymer. Bioresource Technology, vol. 97: 877-885.

[4] Roberge, P.R., 2008. Corrosion Engineering (McGraw-Hill, New York).

[5] Neumann, S., Fatula, P., 2009. Principles of Ion Exchange in Wastewater Treatment. Asian Water , March: 14-19.

[6] Liu, Z., Lompe, K.M., Mohseni, M., Berube, P.R., Sauve, S., Barbeau, B., 2020. Biological ion exchange as an alternative biological activated carbon for drinking water treatment. Water Research, vol. 168: 1-9.

[7] Luqman, M., 2012. Ion Exchange Technology I: Theory and Materials (pringer Science & Business Media).

[8] Luqman, M., 2012, Ion exchange technology II: Applications (Springer Science & Business Media).

[9] Koshel, N.D., Smimova, E.V., 2021. Nonsteady electrochemical processes in ion exchangers. Surface Engineering and Applied Electrochemistry, vol. 57 (4): 439-447.

[10] Bolisetty, S., Peydayesh, M., Mezzenga, R., 2019. Sustainable Technologies for Water Purification from Heavy Metals: Review and Analysis. Chemical Society Reviews **2019**, 48 (2) 463-487.

[11] Wing, .R. , 1996. Corn Fiber Citrate: Preparation and Ion-Exchange Properties. Industrial Crops and Products, vol. 5 (4): 301-305.

[12] Sud, D., Mahajan, G., Kaur, M.P., 2008. Agricultural Waste Material as Potential Adsorbent for Sequestering Heavy Metal Ions from Aqueous Solutions – A Review. Bioresource Technology, vol. 99 (14): 6017-6027.

CIVIL ENGINEERING JOURNAL

Article no. 2

THE CIVIL ENGINEERING JOURNAL 1-2022

STUDY ON MECHANICAL BEHAVIOR OF CABLE-STAYED BRIDGE SUPPORT SYSTEM IN MULTI-FULCRUM UNBALANCED SWIVEL

Gu Zifeng, Sun Quansheng，Liu Meng， Kong Dandan，Guo Yang*

Department of Civil Engineering, Northeast Forestry University, Harbin， 150040, China; sunquansheng@nefu.edu.cn

ABSTRACT

With the maturity and wide application of the bridge swivel construction technology, the single-fulcrum balance swivel cannot meet the need of crossing over the high-speed railway catenary and other obstacles, so the unbalanced swivel construction is often needed. In order to ensure the stability and safety of the unbalanced swivel process, a multi-fulcrum swivel method is proposed. In this paper, the railway cable-stayed bridge over Harbin West Avenue is taken as the research object, and the multi-fulcrum swivel construction method over the metal contact network is adopted. The abaqus finite element model is established to study the influence of different swivel angular velocity, friction coefficient of slideway and position of support foot on the force of support system in the course of swivel. The results show that, compared with the traditional single-fulcrum swivel, the support foot of the multi-fulcrum swivel becomes the main force component, and the force on the spherical hinge decreases. The swivel angular velocity is positively correlated with Mises stress of the support foot and the spherical hinge. When the friction coefficient of the slideway changes in order of 0.02, 0.04, 0.06, 0.08 and 0.1, the friction stress of the outer edge of the support foot increases linearly. Considering the force of the spherical hinge and the support foot, the best position of support foot is 7.3 m from the center of the spherical hinge. The research in this paper can be used for reference multi-fulcrum unbalanced swivel construction in the future.

KEYWORDS

Unbalanced swivel construction, High-speed railway catenary, Multi-fulcrum swivel method, Finite element model, Support system

INTRODUCTION

Current status of research

The swivel construction refers to a kind of construction method that the bridge structure is first poured and formed outside the completed bridge position, and can reduce the influence of construction on the traffic line to a large extent through turning into position. The commonly used methods of swivel are vertical swivel, horizontal swivel, horizontal swivel and vertical swivel combined method[1]~[4]. the length of the two sides of the main swivel bridge of Wuhan Changqing Road was doubled, and the difference between the bottom of the beam and the railway catenary was 2.5 m, as shown in Figure 1. At this point, the traditional balanced swivel is no longer satisfied with the complex construction conditions, and it is necessary to seek more advanced swivel methods.

DOI 10.14311/CEJ.2022.01.0002

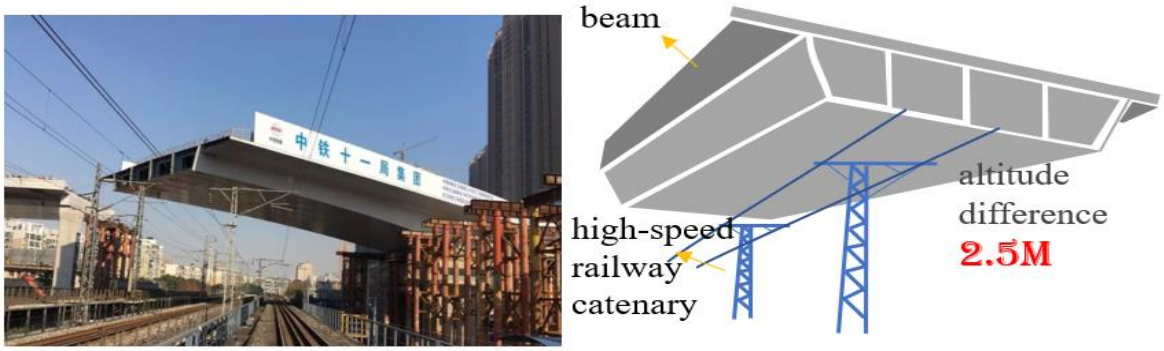

Fig. 1 – Wuhan Changqing Road main line swivel bridge

The traditional swivel is single-fulcrum support, that is, the bridge is supported by the spherical hinge to complete the swivel. Although traditional horizontal swivel construction has many advantages, the overall stability of the swivel structure is the worst at this time because the structure is in a transient equilibrium state during the swivel process[6]~[7]. As for the swivel bridges, the stress of the consolidation of the tower and beam, the maximum cantilever end, the turntable, the shaft and the spherical hinge are complex in the swivel process, which is the focus of domestic and foreign scholars. Sun[8] used finite element software to analyze and study the stress of the beam , the turntable and the shaft during the swivel process of the Suifenhe cable-stayed bridge during the acceleration and uniform processes. Liu[9] analyzed the stress of spherical hinge with different velocities and acceleration by dynamic time history, and obtained the limit value of acceleration. Furthermore, Che [10] conducted in-depth research on key mechanical problems in the process of bridge horizontal swivel by means of theoretical analysis, numerical simulation and experimental measurement.

There are more researches on traditional swivel construction monitoring, force analysis or calculation theory, but less research on swivel bridges with extremely asymmetrical ends or extremely unbalanced swivel across obstacles. At present, the methods adopted by Lv[10]~[11], and others[11]~[15] are the additional front outrigger auxiliary support technology and the auxiliary support walking power system technology. But Wuhan changing road swivel bridge construction method and the method of Lv[11]~[15] have greatly increased the construction volume, construction difficulty and swivel difficulty.

Because the overall stability of the traditional swivel is poor, and it cannot meet the needs of extremely unbalanced swivels, the multi- fulcrum swivel with additional front outrigger support is more complicated. Therefore, in order to provide a reasonable and simple swivel method for the multi- fulcrum swivel in the future, this paper takes the Haxi Street cross-rail cable-stayed bridge (hereinafter referred to as the Haxi cable-stayed bridge) as the research object, and puts forward the method of multi- fulcrum unbalanced swivel of support foot auxiliary spherical hinge. In fact, the support foot of the swivel system, as an auxiliary support component to prevent the roll, can be completely combined with the spherical hinge to form a multi-fulcrum swivel support system. Based on the analysis of the influencing factors of the force of the support foot and the spherical hinge in the process of swivel, the unbalanced swivel construction of the bridge was successfully completed by using the fine finite element analysis, inclined counterweight and unbalanced weighing[16]~[18], which can provide reference for the unbalanced multi-fulcrum swivel construction in the future.

Engineering situation

Harbin West Avenue Cable-stayed Bridge is located in Harbin West Marshalling Station, across more than 20 railway lines, whose span arrangement is (118+198+118) m, and the intersection angle with the railway line is 80.4°. The total length of the bridge is 434 m. The layout and swivel of the bridge are shown in Figures 2 and 3. The swivel span of the Tower 9 is (97+101) m, and the span of the Tower 10 is (90+107) m. The swivel weight of the two towers both are about 28000 t.

Due to the limitation of the railway line, the bridge side span is larger than that of the conventional cable-stayed bridge (generally 0.45-0.5:1). Since the side span of tower 10 of the bridge crosses the metal catenary of high-speed railway during swivel, the distance between the bottom of the beam and the metal catenary is only 151 mm. Considering the safety of the swivel process, the swivel method of multi-fulcrum unbalanced swivel is adopted to avoid the collision between the bottom of bottom and the catenary during the swivel process. The multi-fulcrum swivel needs to be counterweighted in the middle span to make the mid-span side support foot landing and the side span lifting, so as to increase the spacing between the bottom of the beam and the catenary, which constitutes a multi-fulcrum swivel system with the joint force of the support foot and the spherical hinge, and ensures the smooth and safe swivel process.

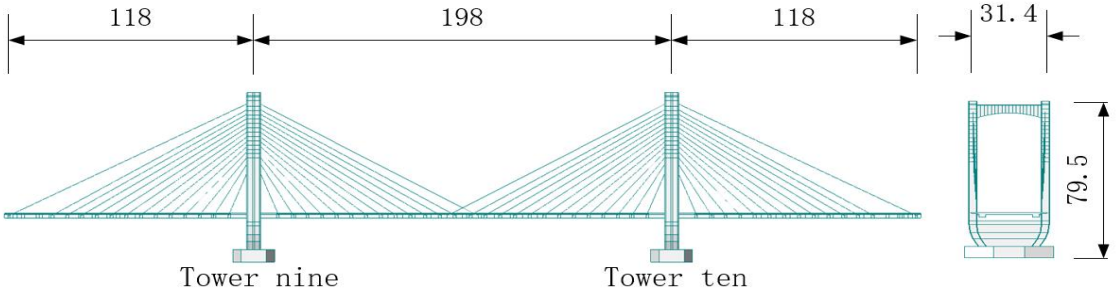

Fig.2 - Bridge type layout(Unit：m)

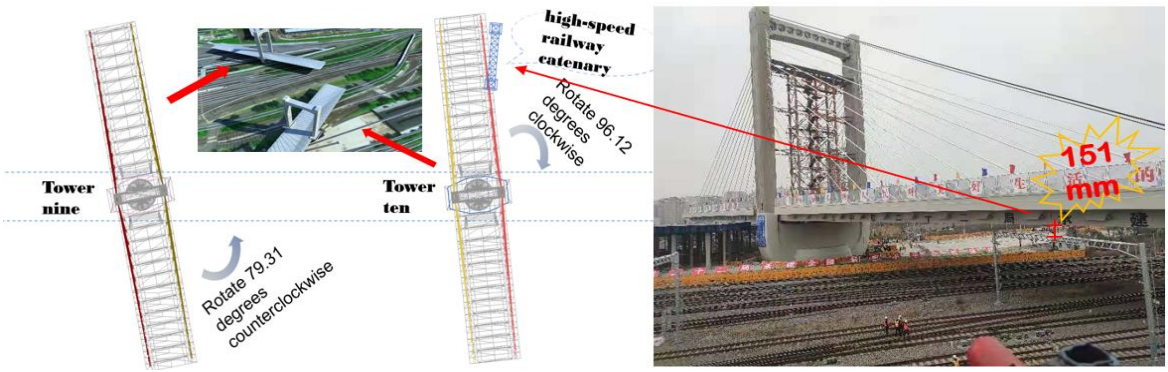

Fig.3 - Swivel orientation diagram

The difference between multi-fulcrum swivel and traditional swivel system is mainly the support system. The support structure of traditional swivel system is mainly the spherical hinge, while the support system of multi-fulcrum swivel system is composed of the spherical hinge and the support foot. The diameter of the spherical hinge is 4500mm and the total height is 890mm. It is one of the stress components of the support system. The upper turntable is equipped with six support feet symmetrically distributed on both sides of the longitudinal axis of the beam. The structure diagram of the swivel system is shown in Figure 4, and the detailed structure of the support system is shown in Figure 5.

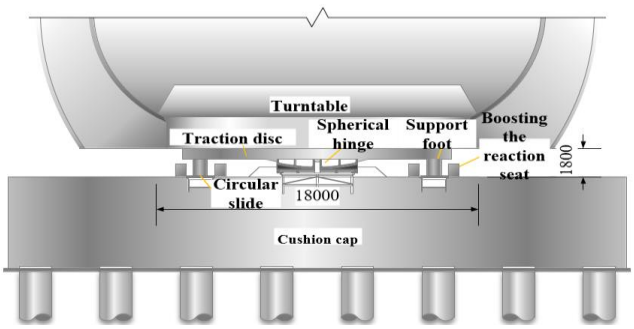

Fig.4 - The structure diagram of the swivel system(Unit：mm)

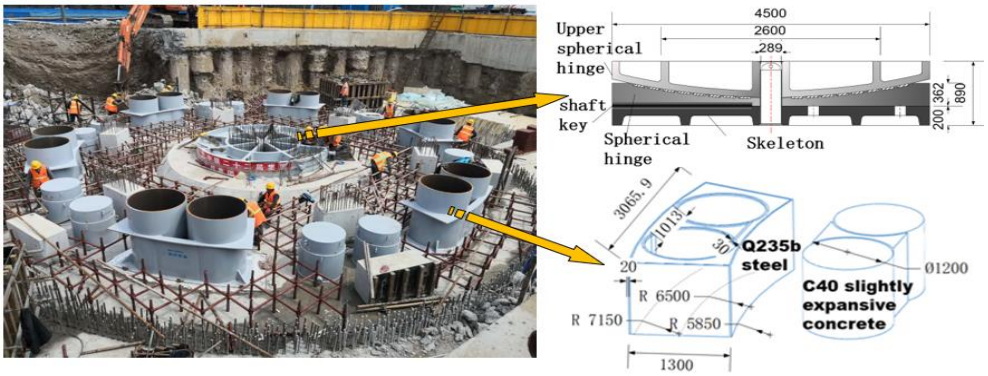

Fig.5 - Detail structure of support system(Unit：mm)

METHODS

Test determination of parameters

Determination of friction coefficient of the spherical hinge

Unbalanced weighing is needed before multi-fulcrum unbalanced swivel. Different from the traditional balanced rotation, the unbalanced torque of the multi-support unbalanced rotation must be greater than the friction torque, which is caused by the tilt counterweight. Figure 6 shows the unbalanced weighing test process.

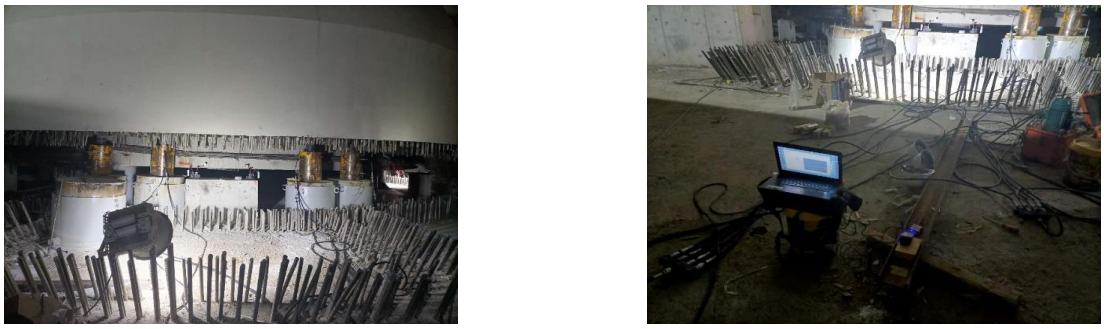

(a) Jack arrangement *(b) The data collection*

Fig.6 - Unbalanced weighing test process

According to the measured results of the unbalanced weighing test, the following calculations are obtained: unbalance torque Mg=14200kN·m, friction torque Mz=13000kN·m, friction coefficient μ_0=0.0054, eccentricity e=0.051m.

Determination of swivel angular velocity

The angular velocity sensor is installed on the swivel structure and connected with the acquisition module. The angular velocity collected during the swivel is transmitted to the online monitoring platform through the wireless transmission module and recorded. The angular velocity acquisition process is shown in Figure 7, and the measured angular velocity in the process of multi-fulcrum unbalanced swivel is shown in Figure 8.

Fig.7 - Angular velocity acquisition process

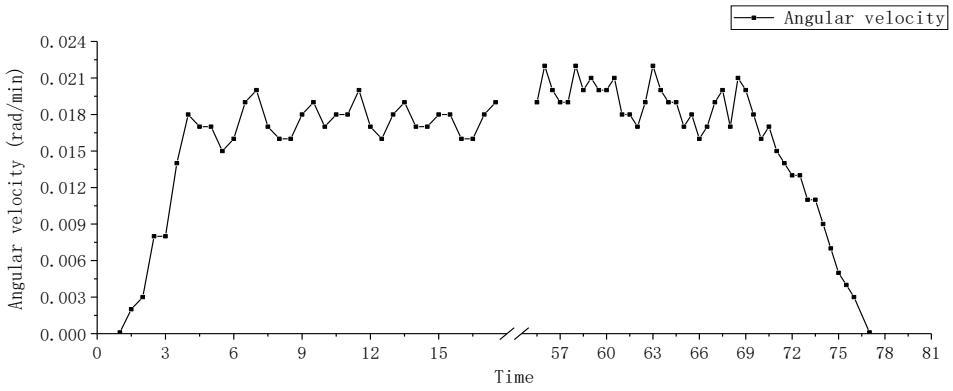

Fig.8 - Measured angular velocity during swivel

It can be seen from Figure 8 that the angular velocity is stable in the range of 0.016rad/min ~ 0.024rad/min in the process of uniform swivel.

Establishment of finite element model

The multi-fulcrum swivel system is different from the traditional single-fulcrum swivel. The coordinated force of the entire swivel structure during the swivel is crucial. Therefore, Abaqus is used to establish an accurate and simplified finite element model of the swivel structure. Compare the multi-fulcrum swivel with the single-fulcrum swivel, and conduct in-depth research on the influence of the swivel angular velocity, the friction coefficient of the slideway and the position of the support foot on the force of the support system. The materials and parameters used in the main components of the swivel structure are shown in Table 1.

Tab.1 - Material of the main components of the swivel structure

Structural part	Detailed structure	material	density (kg/m^3)	Poisson ratio	Young's modulus (MP_a)	Unit
Upper turntable	/	C40 concrete	2.5×10^3	0.3	3.25×10^4	C3D8R
Turntable	/	C40 concrete	2.5×10^3	0.3	3.25×10^4	C3D8R
Spherical hinge	Upper spherical hinge	Q345 steel	7.85×10^3	0.28	2.06×10^5	C3D8R
	Spherical hinge	Q345 steel	7.85×10^3	0.28	2.06×10^5	C3D8R
Support foot	Support foot steel pipe	Q235b steel	7.85×10^3	0.274	2.06×10^5	C3D8R
	Concrete in steel pipe	C40 micro-expansion concrete	2.5×10^3	0.3	3.25×10^4	C3D8R

The element types and material parameters selected for each component of the Abaqus partial model are shown in Table 1. Build the solid parts according to the size of the construction drawings, and then assemble them through the combine in the assembly. For example, the support feet are composed of steel plates, concrete cylinders and steel pipes, and the upper part of the swivel structure is composed of a turntable, six support feet and an upper spherical hinge. The partial model of the swivel structure is shown in Figures 8 and 9.

By calculating the unbalanced load, the uniform force and bending moment on the top surface of the upper cap are obtained. The uniform force is applied to the top surface of the upper cap of the Abaqus partial model, and a feature point is coupled on the top surface of the upper cap. The bending moment and swivel speed are applied to the feature point, so that the mid-span side support foot contacts with the top surface of the lower cap and swivels. The influence of various factors on the force of the support system in the swivel process is studied.

The contact between the lower surface of the ground support foot and the upper surface of the cushion cap, and the contact between the upper and lower spherical hinges is surface-surface contact. The tangential behavior of the contact is a nonlinear algorithm of the penalty function algorithm[19], and the normal behavior uses "hard" contact, and allows separation after contact. The friction coefficient of the upper and lower spherical hinges is 0.0054 measured by weighing test.

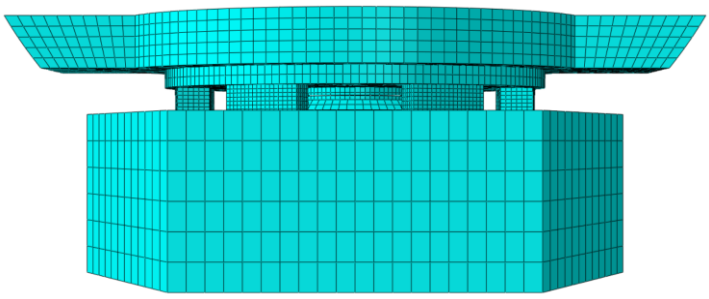

Fig.9 - Overall model of swivel system

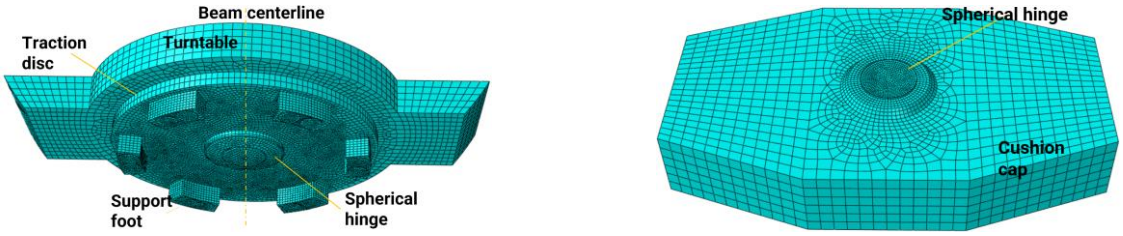

Fig.10 - Finite element model of up-and-down turntable

The layout of the support foot nodes is shown in Figure 11, and the layout of the spherical hinge nodes is shown in Figure 12. Strain gauges are arranged on the side of the foot, and when the counterweight is tilted, the strain data when the foot hits the ground will be collected, and the entire rotation process will be monitored through monitoring. The arrangement of the strain gauges is consistent with the side node of support foot layout, as shown in Figure 13.

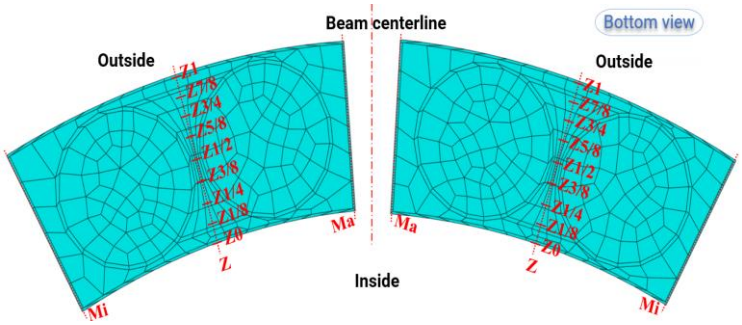

Fig.11 - Support foot node layout

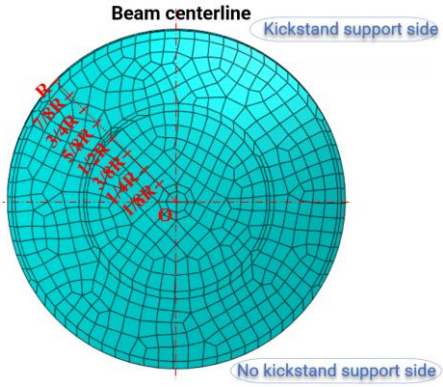

Fig.12 - Spherical joint node layout

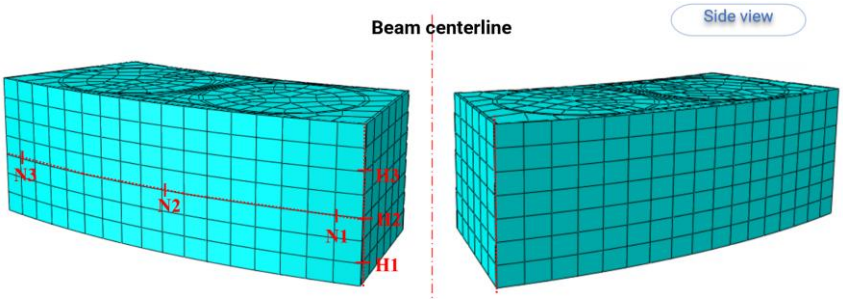

Fig.13 - Side node of support foot layout

RESULTS

Comparative Analysis of Multi-Fulcrum Swivel and Traditional Single-Fulcrum Swivel

The traditional swivel method is single fulcrum balanced swivel, and its support system only has spherical hinge single support. The multi-fulcrum swivel is that the support foot and the spherical hinge participate in the force together, forming a multi-fulcrum support system. By comparing the force of the support system of multi-fulcrum swivel and traditional swivel in the process of swivel by finite element method, the force changes of the support foot and spherical hinge of multi-fulcrum swivel and traditional swivel are analyzed. The Mises stress nephograms of the traditional single-fulcrum swivel and multi-fulcrum swivel support systems are shown in Figure 14 and 15, respectively.

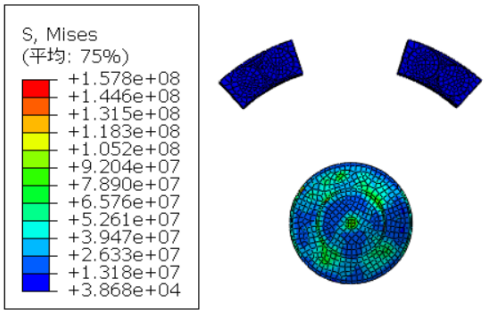

Fig.14 - Mises stress nephogram of single-fulcrum balanced swivel support system(Unit: P_a)

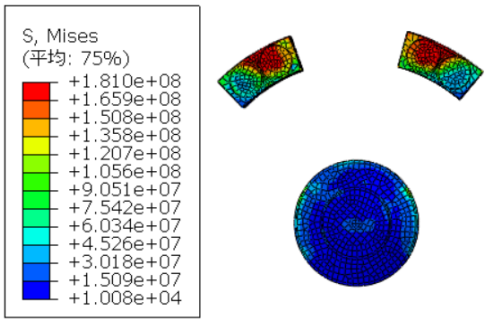

Fig.15 - Mises stress nephogram of multi-fulcrum swivel support system(Unit: P_a)

As shown in Figure 14 and 15, the spherical hinge in the traditional single-fulcrum swivel is the main force component, and the Mises stress at the maximum force is 157.8MP$_a$. Besides the Mises stress at the maximum stress of the support foot is 1.4MP$_a$, which is mainly caused by centrifugal force. Since the inclined counterweight of the bridge increases the unbalanced moment, the inclination of the bridge body makes the counterweight side support foot land, and the support foot of the multi-fulcrum swivel becomes the main force-bearing member. The Mises stress value at the maximum force of the support foot is 181.0MP$_a$, and the Mises stress value at the maximum force of the spherical joint is 106.9MP$_a$. Compared with single-fulcrum swivel, the force of the spherical hinge is reduced by 32.3%, and the maximum Mises stress is far less than its yield strength of 345MP$_a$. Besides the force of the support foot increases by 128 times, and the maximum Mises stress had a strength reserve of 0.77 compared with its yield strength of 235MP$_a$.

Study on the force influence of support system swivel process

The influence of the angular velocity of swivel on the force of the support system

The whole swivel process of cable-stayed bridge is divided into four stages: accelerated swivel, uniform swivel, deceleration braking and inching adjustment posture. The acceleration and deceleration process is relatively short, and the uniform swivel process will last for several tens of minutes, which is the longest period[20]. In the process of swivel, due to the existence of centrifugal force, it will inevitably produce a "centrifugal" tendency to the swivel structure, that is, tensile stress will be generated. At the same time, the size of the centrifugal force is closely related to the swivel speed, and the centrifugal force is proportional to the square of the swivel angular velocity. As the swivel speed increases, the centrifugal force also increases significantly[21]. Therefore, the angular velocity of swivel is an important factor in the swivel of the swivel bridge. This paper studies and analyzes the angular velocity of the angular velocity on the force of the support system in the process of multi-fulcrum swivel.

By collecting the angular velocity in the process of multi-fulcrum swivel, the angular velocity in the process of uniform swivel is obtained to be 0.016rad/min~0.024rad/min. Therefore, the angular velocity of 0.016rad/min is used as the benchmark to study the force of the multi-fulcrum swivel support system at the angular velocities of 0.016rad/min, 0.032rad/min, 0.048rad/min, 0.064rad/min, and 0.080rad/min. The Mises stress nephograms of the support system are shown in Figure 16 and Figure 17.

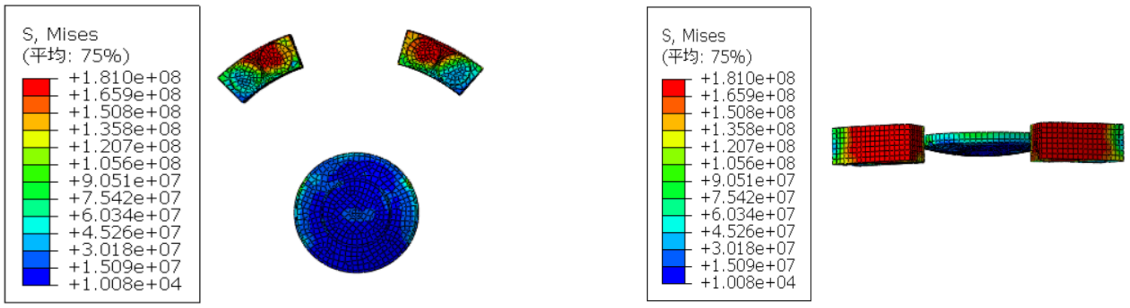

（a）Bottom view　　（b）Side view

Fig.16 - Mises stress nephograms of the support foot and the spherical hinge at speed 0.016rad/min（Unit：P_a）

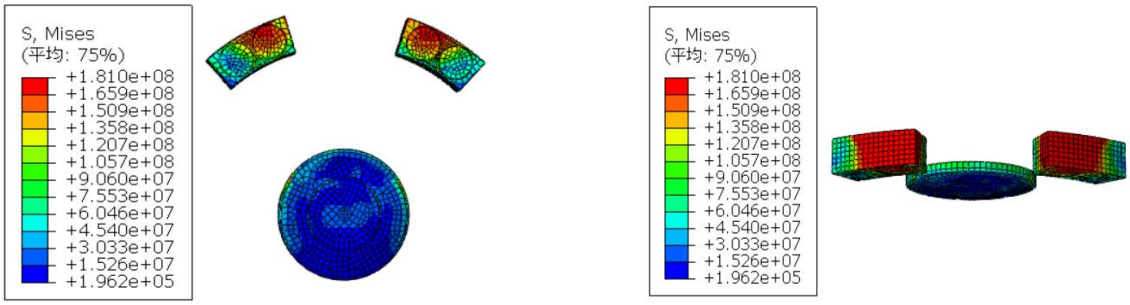

（a）Bottom view　　（b）Side view

Fig.17 - Mises stress nephograms of the support foot and the spherical hinge at speed 0.032rad/min（Unit：P_a）

As shown in Figures 16 and 17, in the multi-fulcrum system, the stress on the side of the spherical hinge near the ground support foot is larger, and the Mises stress at the edge R is the maximum, and the stress at the center O of the spherical hinge is about 12.3 % of the stress at the edge R.

The Mises stress curves at support foot Z1 and the spherical joint R of five swivel angular velocities are shown in Figure 18.

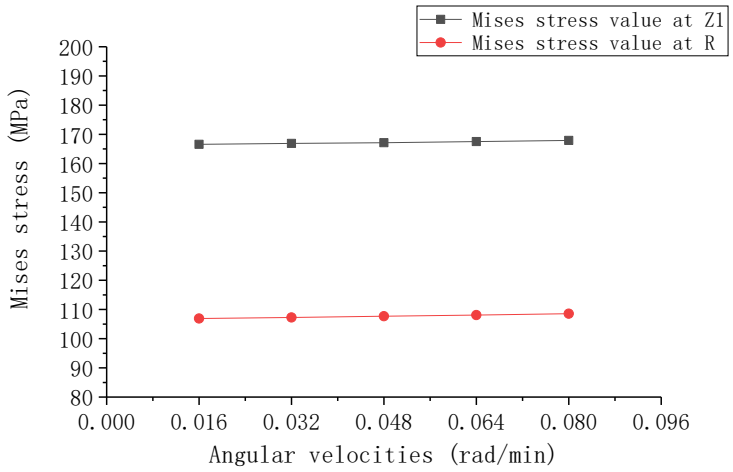

Fig.18 - Mises stress of five angular velocities at the support foot Z1 and the spherical hinge R

As shown in Figure 18, the Mises stress at the bottom of the support foot Z1 and the spherical hinge R is positively correlated with the angular velocity, which is the result of the centrifugal force generated by the swivel angular velocity. With every increase of the angular velocity of 0.016rad/min,

the Mises stress at the support foot Z1 only increases by 0.18%, and the Mises stress at the spherical hinge R only increases by 0.33%.

The model data using the actual rotational angular velocity is compared with the measured data, that is, the force comparison of the support foot, which is divided into the vertical H-axis and the horizontal N-axis. The data comparison diagram is shown in Figure 19.

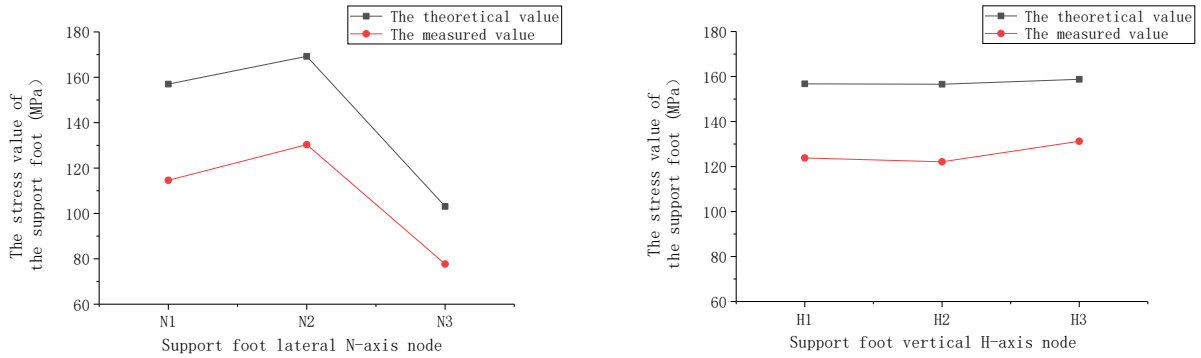

（a）N-axis nodal stress comparison *（b）H-axis nodal stress comparison*

Fig.19 - Comparison between the measured stress on the side of the support foot and the stress calculated by the model

It can be seen from Figure 19 that the measured values of the lateral and vertical node stresses on the side of the support foot are roughly the same as the theoretical values calculated by the model. The measured value is up to 82.67% of the calculated value of the model, and the smallest is 73.09%. By comparing with the measured values, it can be seen that the model simulation is more accurate.

The influence of friction coefficient on the force of support system

The traditional swivel support system only produces friction between the upper and lower spherical hinges. However, the friction between the support feet and the slideway and the upper and lower spherical hinges is both produced in the multi-fulcrum swivel system. Through the field unbalanced weighing test, the friction coefficient of the spherical hinge in the multi-fulcrum support system is 0.054. Here, only the influence of the friction coefficient between the support foot and the slideway on the force of the support system is studied. In order to reduce the friction between the support foot and the slideway to minish the tonnage of the tension traction equipment, the method of brushing lubricating materials on the slide is selected. The friction coefficient of butter method is 0.06, and the friction coefficient of butter adding poly tetra fluoroethylene(PTFE) powder is 0.03~0.06[22]~[24]. In order to simulate the different friction coefficients of the slideway, at a constant angular velocity of 0.016 rad/min, it is assumed that the friction coefficients between the support foot and the slideway are 0.001, 0.02, 0.04, 0.06, 0.08 and 0.1. In the absence of friction, the friction coefficient is selected to be 0.001.

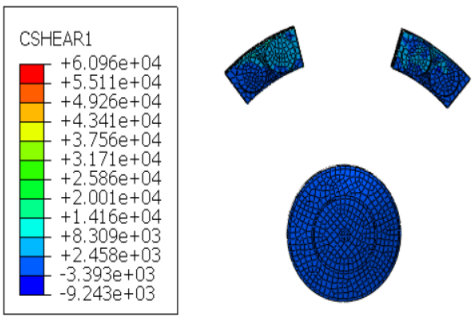

Fig.20 - Friction stress nephogram of the support foot and the spherical hinge when the friction coefficient is 0.001（Unit：P_a）

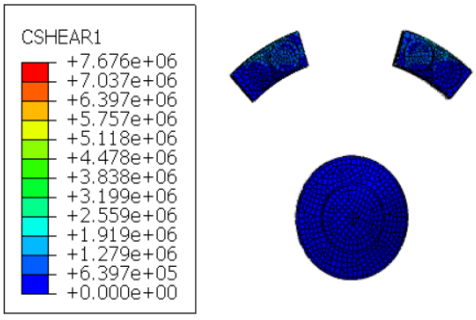

Fig.21 - Friction stress nephogram of the support foot and the spherical hinge when the friction coefficient is 0.02（Unit：P_a）

The friction stress nephograms of the support foot and the bottom surface of the spherical hinge are shown in Figures 20 and 21. The friction stress values of each node on the Z-axis of the support foot bottom surface with the friction coefficients of 0.001, 0.02, 0.04, 0.06, 0.08 and 0.1 are extracted, sorted and drawn as shown in Figure 22.

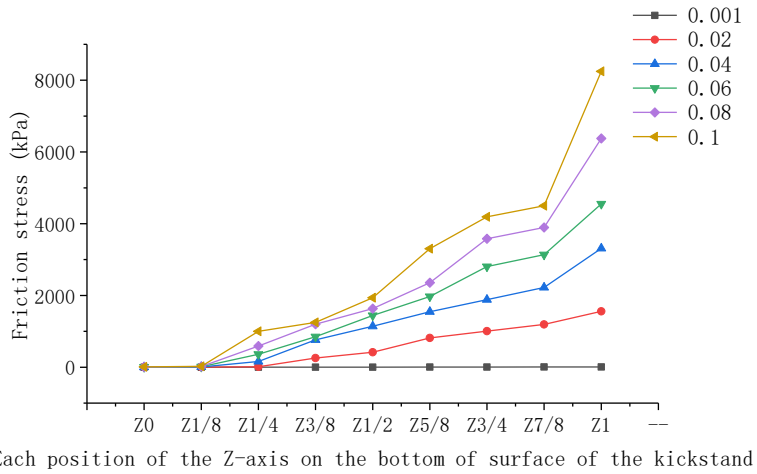

Fig.22 - Friction stress at various positions on the Z-axis of the bottom surface of the support foot with different friction coefficients

It can be seen from Figures 20~22 that: at a constant angular velocity of 0.016 rad/min, the friction stress at each point on the Z-axis of the foot bottom surface is proportional to the friction coefficient. As the friction coefficient increases by 0.02, the friction stress at the support foot Z1 increases by 112.7%, 186.0%, 309.5% and 430.0%. The increase in stress value is linearly related to the friction coefficient, which conforms to the Coulomb friction law. The friction stress on the outside of the support foot is larger than that on the inside, that is, the greater the distance from the center of the spherical hinge, the greater the friction stress. With a friction coefficient of 0.06, the friction stress at Z1 is 4552.34KP$_a$, and the friction stress at Z0 is 4.56KP$_a$. Consequently, the friction stress at Z1 on the outside is 998 times that at Z0 on the inside.

The influence of the position of the support foot on the force of the support system

The support foot is the "fulcrum" in the "lever" of the support system, and the distance between the support foot and the center of the spherical hinge is an important factor affecting the force of the support system. For the sake of study the influence of support foot position on the force of support system, it is proposed to choose 0.016rad/min angular velocity and 0.06 friction coefficient. Under the premise of not increasing the superstructure, the distance between the support foot position and the center radius of the spherical hinge is changed to: 7.1m, 7.3m and 7.5m.

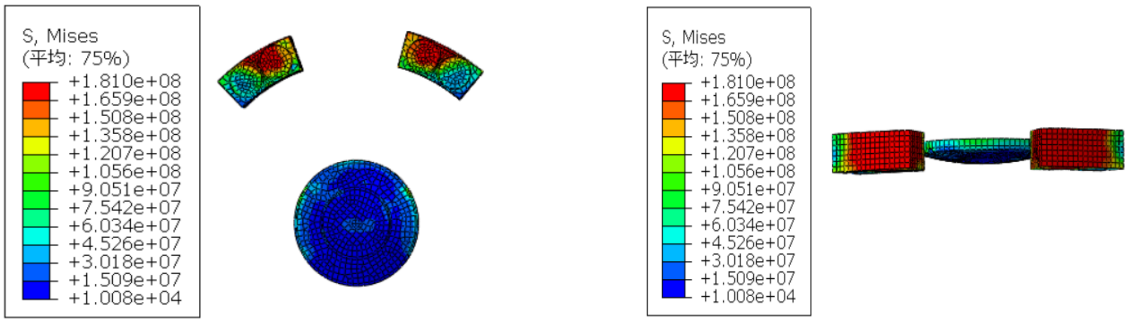

（a）Bottom view　　（b）Side view

Fig.23- Mises stress nephograms of the support foot and the spherical hinge and when the radius from the spherical joint is 7.1m（Unit：P_a）

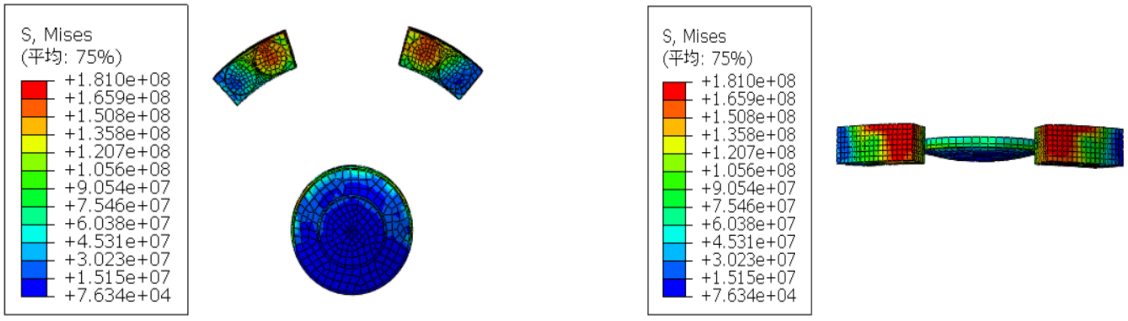

（a）Bottom view　　（b）Side view

Fig.24 - Mises stress nephograms of the support foot and the spherical hinge when the radius from the spherical joint is 7.5m（Unit： P_a）

The Mises stress nephograms of the support foot and the spherical joint are shown in Figures 23 and 24. When the radius of the spherical hinge is 7.1m, 7.3m and 7.5m, the Mises stress of each node of the Z-axis at the bottom of the foot is plotted as Figure 25, and the Mises stress of each node of the R-axis at the bottom of the spherical hinge is plotted as Figure 26.

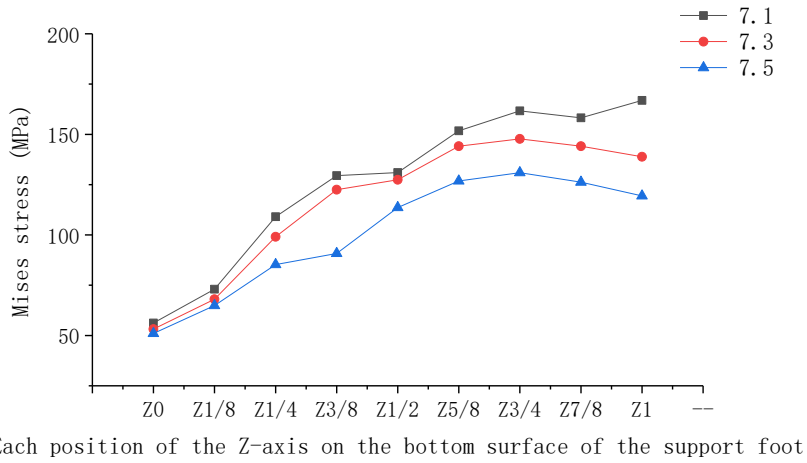

Fig.25 - Mises stress at each position of the Z-axis on the bottom surface of the support foot at different positions

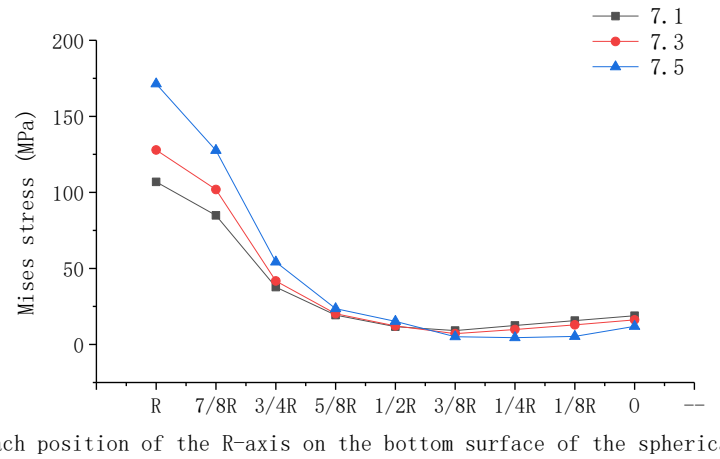

Fig.26 - Mises stress at each position of the R-axis on the bottom surface of the spherical joint at different positions

It can be seen from Figures 23 -26 that: moving the support foot outward means increasing the radius from the center of the spherical joint, which can effectively reduce the force on the support foot. The position of the support foot moved from 7.1m away from the center of the spherical hinge to 7.3m and 7.5m. The Mises stress at Z1 decreased by 28.1MP$_a$ and 19.4MP$_a$, respectively, accounting for 16.8% and 13.9%. At the same time, as the position of the support foot moves outward, the center of force of the spherical hinge moves outward, the force of the spherical hinge center O decreases, and the force of the edge R near the support foot increases. The position of the support foot is moved from 7.1m away from the spherical hinge center to 7.3m and 7.5m. The Mises stress values at O decreases by 2.69MP$_a$ and 4.2MP$_a$ respectively, and the Mises stress values at R increases by 21.0MP$_a$ and 43.5MP$_a$ respectively, accounting for 19.6% and 34.0%. Therefore, the position of the support foot needs to be considered together according to the force of the support foot and the spherical hinge. According to the above conclusions, the force of the support foot is reduced by 16.8% and the force of the outer edge of the spherical hinge increases by 19.6% when the position of the support foot is moved to 7.3m from the center of the spherical hinge. When the support foot position moves to 7.5m away from the center of the spherical hinge, the force of the support foot decreases by 13.9%, and the decrease amplitude decreases to 82.7%. The force of the outer edge of the spherical hinge increases by 34.0%, and the increase amplitude doubles to 204.8%. In summary, the position of the support foot at a distance of 7.3m from the center of the spherical hinge, which is 325% of the radius of the spherical hinge, is more suitable for Haxi Cable-stayed Bridge.

SUCCESSFUL SWIVEL

Through the research on the mechanical behavior of the support system in the swivel process to select each parameter, such as a swivel angular velocity of 0.016rad/min, a method of reducing friction between the slide feet with butter and PTFE powder, and the position of the support feet 7.3m away from the spherical joint, at 12:02 on November 12, 2020, Haxi cable-stayed bridge crossed the high-speed rail catenary and successfully swiveled. This swivel refreshes the world 's swivel bridge with the largest total weight in cold region, cross-railway operation railway tracks most, the most ' unbalanced ' bridge swivel weight and the most accurate (centimeter level) swivel precision control.

Fig.27 - Successful swivel

CONCLUSION

In order to study the support system of multi-fulcrum swivel, the unbalanced swivel is simulated by abaqus finite element simulation. The traditional swivel and multi-fulcrum swivel are compared and analyzed. In view of the influence of swivel angular velocity, friction coefficient and support foot position on the force of the support system in the swivel process, the following conclusions are drawn :

(1) Swivel bridges usually need to be swivelled across lines, but many obstacles such as high-speed rail metal contact network prevent the swivel of the beam body and cannot be removed in the process of swivel. In view of the swivel bridge in such cases, this paper puts forward a multi-fulcrum swivel method under the joint force of the support foot and the spherical hinge. Through the comparative analysis with the traditional single-fulcrum swivel, it can be seen that the force of the spherical hinge of the multi-fulcrum swivel is reduced by 32.3%. The force of the support foot increases by 128 times and becomes the main force component. Therefore, for multi-fulcrum swivel bridges, steels with lower strength, such as Q235 steel, can be selected for the spherical hinge, and steels with higher strength, such as Q355 steel, should be selected for the support foot to provide higher strength reserves.

(2) This paper studies the force of the support system at angular velocities of 0.016rad/min, 0.032rad/min, 0.048rad/min, 0.064rad/min, and 0.080rad/min. For every 0.016 rad/min increase in angular velocity, the Mises stress values at Z1 and R of the spherical hinge only increase by 0.18% and 0.33%, which indicates that the angular velocity has a small effect on the support system.

(3) The swivel bridge usually discusses the influence of the friction coefficient at the spherical hinge. In this paper, the friction coefficient between the support foot and the slideway is analyzed. As the coefficient of friction increases, the frictional stress on the spacer foot increases，which conforms to the Coulomb friction law. It can be seen from the stress clouds that the friction stress on the outside of the support foot is larger than that on the inside, that is, the greater the distance from the center of the spherical hinge, the greater the friction stress. It follows that a material with a lower coefficient of friction can be used on the outer edge of the slideway.

(4) Although the position of the support foot can be moved out to effectively reduce the force of the support foot, as the force of the support foot decreases, the force on the outer edge of the spherical hinge increases. From the above analysis, the position of the support foot at a distance of 7.3m from the center of the spherical hinge, which is 325% of the radius of the spherical hinge, is more suitable for Haxi Cable-stayed Bridge.

In this paper, the construction method of multi-fulcrum swivel is proposed for unbalanced swivel unbalanced swivel bridges with excessive obstacles. The abaqus finite element model is established. Meanwhile the multi-fulcrum swivel and the traditional swivel are compared and

analyzed. Based on the traditional swivel, the force characteristics of multi-fulcrum swivel are obtained. The influence of swivel angular velocity, friction coefficient and support foot position on the force of support system is studied. The following work can change the contact form between the support foot and the slideway according to the above research data, such as adding pulleys under the support foot to optimize the multi-fulcrum swivel system, and provide reliable reference for the future projects using multi-fulcrum swivel.

ACKNOWLEDGEMENTS

The research in this paper was supported by the Research on the mechanical characteristics of steel box girders in cold regions (Department of Transportation of Heilongjiang Province, China, Grant No. 2020HLJ018) and the study on the application of corrugated steel arch bridges for small and medium spans on highways and preparation of technical standards for design and construction (Department of Transportation of Heilongjiang Province, China, Grant No. 2020HLJ059).

REFERENCES

[1] Li Lapu, 2009. Construction Technology of Plane Swivel of Continuous Box Girder Bridge. Railway Standard Design, vol. 2009(08):55-57.,doi.10.13238/j.issn.1004-2954.2009.08.019.
[2] Ren Hui, Bai Baohong, Jiao Pengcheng, 2008. Construction Control for Gushan Bridge of Shitai Passenger Line, vol.2008,21(04):5256., doi.10.13319/j.cnki.sjztddxxbzrb.2008.04.013
[3] Zhang Jiefang, 2006. Construction Technology of Level Swing Method of a T-Rigid Frame Bridge, vol.2006(04):114-117, doi.10.13319/j.cnki.sjztddxxbzrb.2006.04.028
[4] Zhang Wenxue, Huang Jian, Wang Xiuping, 2012. Analysis of Factors Influencing Stability of Continuous Girder Bridge during Horizontal Swivel Construction. JOURNAL OF SHIJIAZHUANG TIEDAO UNIVERSITY (NATURAL SCIENCE), vol. 2012,25(04):30-33.,doi.10.13319/j.cnki.sjztddxxbzrb.2012.04.014
[5] Xu Tianbing, Lin Chengli, 2018. The First Extremely Unbalanced Swivel Bridge in China Successfully Swivel to Three Worlds First. Construction and Architecture,vol. 2018(05):81
[6] Ministry of Transport of China,2011. Technical specification for highway bridge and culvert construction (JTG/T F5O—2011). China Communications Publishing.
[7] Ministry of Transport of China, 2004. Code for design of highway reinforced concrete and prestressed concrete bridges and culverts (JTJ D62—2004). China Communications Publishing.
[8] Sun Yongcun, 2007. Research on Mechanical Prope rties of Suifenhe Cable-stayed Bridge under Level Swivel. NORTHEAST FORESTRY UNIVERSITY.
[9] Liu Jian, 2019. Force analysis and unbalanced torque pred of spherical hinge in parallel swivel bridge construction. Shangdong University.
[10] Che Xiaojun, 2015. Refined Analysis of Swivel Spherical Hinge and Balance Control of Parallel Swivel Construction Bridge. Wuhan University of Technology.
[11] Lv Yu, 2019. Key Technology of Multi-point Bridge Swivel System and Applied Researches. HUAZHONG UNIVERSITYOF SCIENCE AND TECHNOLOGY.
[12] Zhao Kaibing, 2018. Research on the Swivel Construction of Steel Box Girder Bridge Under Unbalanced Conditions. RAILWAY CONSTRUCTION TECHNOLOGY, vol. 2018(08):60-63.
[13] Guo Zhaoying, 2020. Construction Technology of Asymmetric Beam Swivel Driven by Multi-fulcrum Gear. Road Machinery & Construction Mechanization, vol. 2020,37(10):40-44.
[14] Guo Zhaoying, 2019. Feasibility Study on Construction Technology for Swivel Bridge with Two fulcrums. RAILWAY CONSTRUCTION TECHNOLOGY, vol. 2019(02):64-68. Doi. 10.3969/j. issn.1009-4539.2019.02.015.
[15] Xu Haoran, 2020.Research on Key Techniques for Construction of Multi-fulcrum Turning Bridge Based on Auxiliary Track Bridge Based on Auxiliary Track. RAILWAY CONSTRUCTION TECHNOLOGY, vol. 2020(07):64-66+93.
[16] Wei Feng, Chen Qiang, Ma Lin, 2005. Analysis on Unbalanced Weight Weighing Test of Swivel Body of Beijing Wuhuan Road Cable - stayed Bridge. Railway Enigneering, vol. 2005(04):4-6.
[17] Ma Yingying, You Zhongyi, Gao Chengming, Gu Jianjun, 2021. Research on construction weighing and unbalanced weight distribution of Dade Bridge in Kunchu Expressway. Highway, vol. 2021,66(04):102-106.
[18] Guo Ying, 2017. Construction Technology of Weighing and Counterweight with Unbalanced Moment Method for Plane Swivel Structure. RAILWAY CONSTRUCTION TECHNOLOGY, vol. 2017(08):53-57.

[19] Hu Yulong, 2019. Study on Mechanical Characteristics of Swivel Structure of Zoucheng Overpass Railway Bridge. Hubei University of Technology.
[20] J. Zhang,T. E. El-Diraby. 2006, Constructability Analysis of the Bridge Superstructure Swivel Construction Method in China. Journal of Construction Engineering and Management, Vol.2006,132(4).
[21] Guo Xiaoguang., 2012, Research on Mechanical Behavior of Cable-stayed Bridge Swivel Construction under Multi-factor Coupling Action. Northeast Forestry University
[22] Tongmin W., 2008, A brief in troduction to the self balancing system of single spherical hinge cable - stayed bridge, Technology of Highway and Transport,Vol .3 No. 24, pp.84-86.
[23] Watanabe E.， Maruy ama T.， Tanak a H. ,and Takeda S., 2000, Design and construction of a floating swing bridge in Osaka, Marine Structures,Vol.13 Nos 4-5,pp. 437-445
[24] Wang Jiawei.,Sun Quansheng., 2019.Dynamic analysis of swivel construction method under multi-variable coupling effects. International Journal of Structural Integrity, vol. 2019,10(4).

CIVIL ENGINEERING JOURNAL

Article no. 3

THE CIVIL ENGINEERING JOURNAL 1-2022

BLAST FURNACE SLAG PROPERTIES AT DIFFERENT GRINDING TIMES AND ITS EFFECT ON FOAM CONCRETE COMPRESSIVE AND FLEXURAL STRENGTH

Kim Dien Vu[1], Sofya Ildarovna Bazhenova[1], Trong Chuc Nguyen[2], Van Lam Tang[3], Minh Chien Do[4], Van Loi Le[4], Van Duong Nguyen[4], Cong Ly Nguyen[4] and Minh Thuan Hoang[4]

1. *Department of technology of binders and concretes, National Research Moscow State University of Civil Engineering, d. 26, Yaroslavskoe Shosse, Moscow, 129337, Russian Federation; e-mail. kimdienxdtb@gmail.com, sofia.bazhenova@gmail.com*
2. *Institute of Special Construction Engineering, Le Quy Don Technical University, Hanoi, Vietnam; e-mail. trongchuc198@gmail.com*
3. *Hanoi University of Mining and Geology, 18 Pho Vien, Duc Thang, Bac Tu Liem, Ha Noi, Vietnam; e-mail. lamvantang@gmail.com*
4. *College of industrial and constructional, Phuong Dong, Uong Bi, Quang Ninh, Viet Nam; e-mail. dominhchien@cic.edu.vn, levanloi@cic.edu.vn, nguyenvanduong@cic.edu.vn, nguyencongly@cic.edu.vn, hoangminhthuan@cic.edu.vn*

ABSTRACT

The paper presents the blast furnace slag properties at different grinding times by the dry grinding method. The process of fine grinding blast furnace slag is prepared at different times (10 minutes, 20 minutes, 30 minutes, 40 minutes). The results indicated that the main component in BFS is the amorphous structure defined in about 25÷35 degrees (with the appearance of Akermanite at 31.1, Calcite at 29.2 and Aragonite at 26.4). The results also showed that the compressive strength and activity index of blast furnace slag increased significantly after extending the grinding time from 0-40 minutes (corresponding to compressive strength from 51.2 ÷ 72.1 MPa at 28 days of age and activity index of blast furnace slag from 91.92% -129.44%). The fine grinding process shows that the particle size of blast furnace slag is significantly reduced.

In addition, the paper also presents the effect of finely ground blast furnace slag in 40 minutes on foam concrete properties. Research results show that the use of finely crushed blast furnace slag by the mechanical grinding method to replace sand in foam concrete not only improves the mechanical properties such as compressive strength, flexural strength, the elastic modulus of foam concrete but also protects the environment, reduces product costs.

KEYWORDS

Blast furnace slag, Mechanical properties, Mixtures, Concrete, Mechanical grinding

INTRODUCTION

Blast furnace slag (BFS) is a by-product formed during the production of pig iron. In the process of smelting cast iron, when silicon and aluminium oxides react from barren rock of iron-bearing ore with calcium oxide and magnesium oxide of the flux, a fiery liquid alloy is formed.

Due to the peculiarities of steel and pig iron smelting, since the 19th century, blast furnaces have a by-product in the amount of up to 1 ton of slag per 1 ton of pig iron products, which contributed to the accumulation of a large number of slag dumps, causing the need for their disposal. To date, slags are also mainly taken to landfills, where they accumulate, which leads to a deterioration of the ecological situation. At present, thanks to the development of iron ore beneficiation technology, the yield of BFS is 200–500 kg per 1 ton of cast iron [1].

Currently, worldwide production of BFS is about 0.5 billion tons, while effective utilization rates are still relatively low [2]. Therefore, the reuse of BFS is an urgent issue. The main application area for waste, such as slag is the construction industry. The use of BFS brings excellent benefits such as increasing the durability of concrete, reduce the heat of hydration and saving natural resources [3-5].

The chemical composition of BFS depends on the type and properties of iron ores, coke quality, and the type of cast iron. Blast furnace slags contain CaO, SiO_2, Al_2O_3, MgO, FeO and some other oxides. The chemical composition of blast furnace slags, %, varies within wide limits: CaO 30-49; Al_2O_3 4.5-20; Fe_2O_3 0.3-0.8; SiO_2 33-44; MgO 1.5-15; MnO 0.3-3.0. In recent decades, BFS used as a partial substitute for Cement has increased [6,7]. In there, mechanical grinding improves the blast furnace slag's chemical activation and is interested in many researchers [8,9]. There are two mechanical grinding methods: dry grinding method and a wet grinding method. The wet grinding method has been studied by many scientists [10,11].

Meanwhile, the dry grinding method has been used for traditional Cement. Many experimental studies have been made about BFS performance with a different particle size as a raw material for cement supplements. Norrarat et al. [12] studied the effect of BFS with varying sizes of a particle on the hydration kinetics of Cement. They found that the Cement's water loss rate increased as the BFS size decreased due to its reaction. Wang et al. [13] also studied the effect of the fineness and particle size distribution of BFS on the performance of Cement. They found that the BFS with a higher fineness react with more incredible speed and BFS fraction smaller than 5 microns has an important role in hydration [9,14,15].

As you know, foam concrete is a lightweight concrete with a porous structure obtained by hardening solutions, including binders, fine aggregates, water, additives and a foaming agent. Foam concrete with a density of 400 kg/m^3 to 1700 kg/m^3 is used to manufacture structures (walls, floors), heat and sound insulation of buildings and structures [16,17].

Research on foam concrete using BFS has been interested in many researchers [18-20]. However, there has not been any research on the properties of BFS at different grinding times. Then, using finely ground BFS obtained to produce foam concrete.

Based on the above analysis, the authors have studied the fine grinding blast furnace slag's properties at different times (10, 20, 30, 40 minutes) and its effect on foam concrete properties.

MATERIALS AND METHODS

Materials

The main binder material used in this work was blast furnace slag (BFS). Ordinary Portland Cement (OPC), which meets the requirements of GOST 31108-2016, was used as a binder. The cement compressive strength at the age of 3 days is 27.2 MPa and at the period of 28 days is 46.1 MPa. The experiments are performed according to the standard GOST 310.4-81.

Quartz sand (QS) with a size modulus MK = 3.0 and = 2.64 g/cm^3, the sand properties are given in Table 1.

Tab. 1 - The sand properties

Sieve (hole size), mm	5	2.5	1.25	0.63	0.315	0.14
Residues on test sieves, %	0	0	0.83	14.23	73.2	6.28
Full balance, %	0	0	0.83	15.06	88.26	94.54

In this study, superplasticizers (SR5000) were used to improve the performance of concrete mixtures with ρ= 1.1 g/m^3 at a temperature of 25 ± 5°C. Besides, Silica Fume SF-90 (SF90) "Vina Pacific" was used as a binder. Table 2 presents the chemical and physical properties of Portland cement, SF90 and BFS.

This section should describe in detail the study material, procedures and methods used.

Tab. 2 - Properties of OPC, BFS and SF90

Property		SF90	BFS	OPC
Chemical	SiO_2	90.78	36.01	21.98
	Al_2O_3	2.23	13.77	5.31
	Fe_2O_3	2.51	-	3.46
	CaO	0.52	41.05	62.33
	MgO	-	7.36	2.01
	SO_3	-	0.14	-
	Na_2O	0.57	-	0.14
	K_2O	-	0.28	0.62
	Loss on ignition	3.39	1.39	4.15
Physical	Specific gravity (g/m^3)	2.15	2.29	3.12
	Fineness (cm^2/g)	10160	4540	3650

EABASSOC Foaming Agent (United Kingdom) is a highly concentrated, highly efficient liquid used in Foamed Concrete production. Dosage Rate: (0.3 - 0.6) l/m³ with ρ = 1.02 g/cm^3. Mixing water (W) to obtain a concrete mixture, pH = 7.5.

Methods

The activity index of BFS in mortar mixtures was determined by the requirements of the TCVN 11586: 2016 standard;

Compressive and flexural strength of concrete was determined following the requirements of GOST 10180-2012 and TCVN 10303: 2014;

The crystal phases of BFS and blast furnace cement-slag mortar sample were determined by X-ray diffraction (MiniFlex x-ray diffractometer);

Particle shape is determined by device (QUANTA FEG 450);

The Matersizer 3000 laser particle analyzer determined particle size distribution;

The elasticity modulus of samples was determined using cylindrical samples of 150×300 mm. Samples were tested at the age of 28 days following GOST 24452-80 [21]. According to the formula, the elasticity modulus (Es) of each sample is calculated in daN/cm^2.

$$E_s = \frac{\Delta_s}{\Delta_e} = \frac{\sigma_a - \sigma_b}{\varepsilon_a - \varepsilon_b} \quad (1)$$

Where: ε_a - the strain under σ_a; ε_b - the strain under σ_b; σ_a= f'c/3 - the upper loading stress (MPa); σ_b - the basic stress (i.e. 0.5 MPa).

BFS used in work is received from the factory. A production process chart is shown in Figure 1. The BFS is dried in a laboratory oven at T = 100 ± 10°C for 2 hours, then crushed the obtained product in a mill (Model SM500x500, China) in 10, 20, 30 and 40 minutes to obtain BFS in fine powder form (Figure 1).

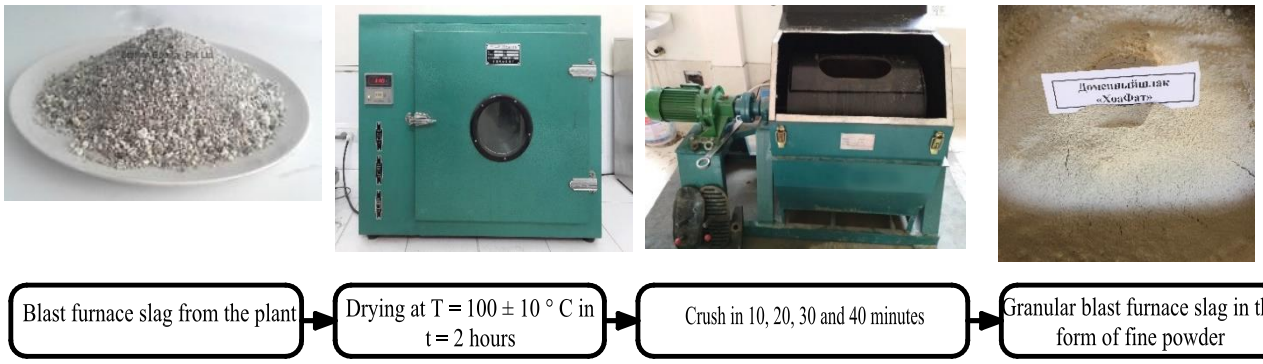

Fig. 1 – Process finely ground BFS

RESULTS AND DISCUSSION

Finely ground blast furnace slag properties

Sieving analysis BFS

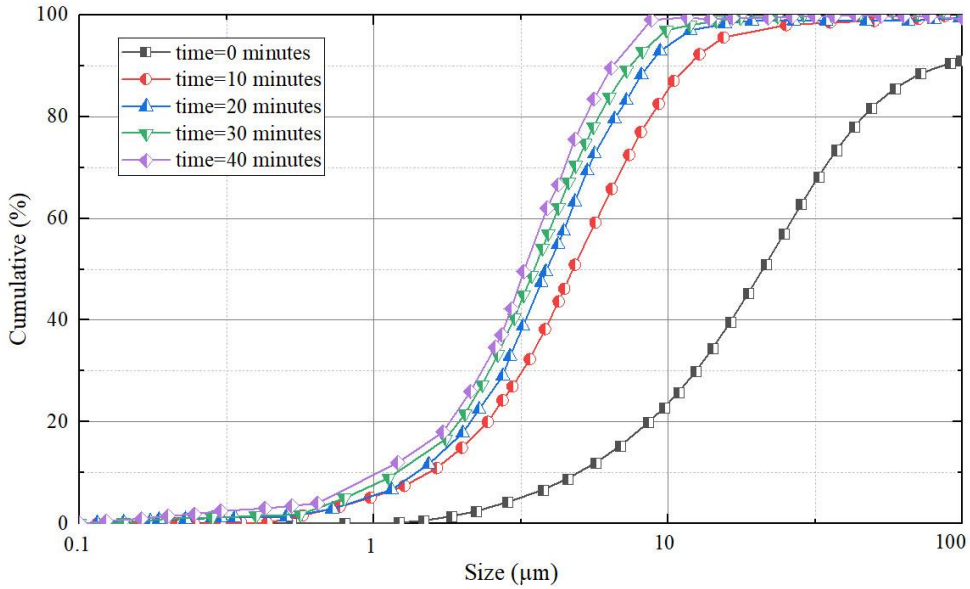

Fig. 2 – Particle size distribution of BFS

The average particle size of BFS, as well as particle size distribution without mechanical activation and after mechanical activation for 10 to 40 minutes by grinding it in a vibrating mill. Which determined using a laser particle analyzer "Coulter LS Particle Size Analyzer" are shown in Figure 2. Figure 2 shows that the obtained BFS is mainly distributed in the range of 1÷100μm. In which the particles with size > 10 μm are about 80%. In addition, fine grinding of BFS at different times (10, 20, 30, 40 minutes) showed a significant improvement in the particle size distribution. Figure 2 also shows that the particle size decreased significantly after grinding for 10 minutes. This was also reported in the study of M. Oner [23]. After 40 min grinding, the particle size did not change much, which can be explained by their aggregation.

XRD of BFS

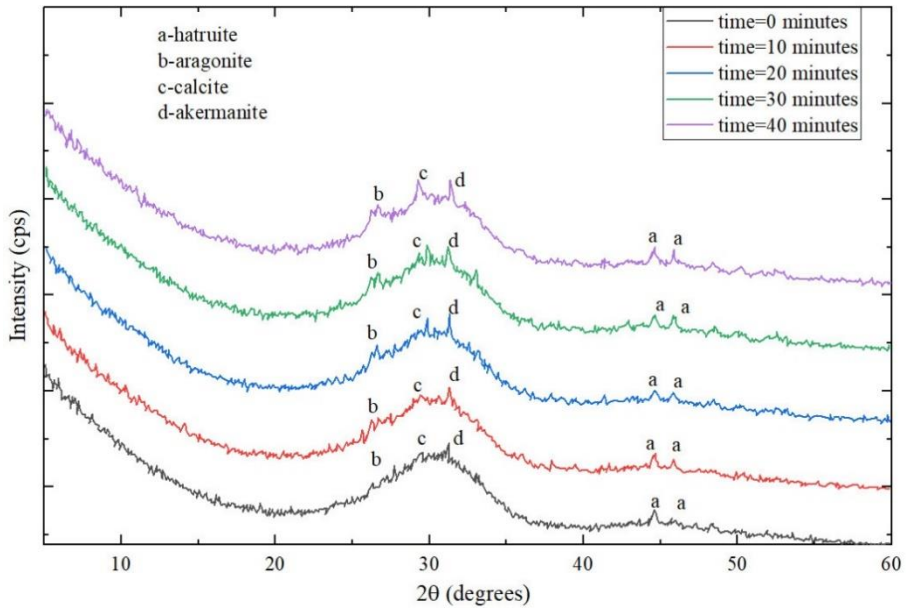

Fig. 3 – XRD samples of BFS at different grinding times

Comparing the finely ground BFS at 10, 20, 30, 40 minutes and BFS is shown in Figure 3. It can be seen that the main component in BFS is the amorphous structure defined in about 25-35 degrees (with the appearance of Akermanite at 31.1, Calcite at 29.2 and Aragonite at 26.4). According to Lei Gan, etc [24], Calcite Aragonite is the structural feature of BFS. In addition, [9] it was reported that the XRD samples of BFS were also present in the presence of Hatruite.

SEM of BFS

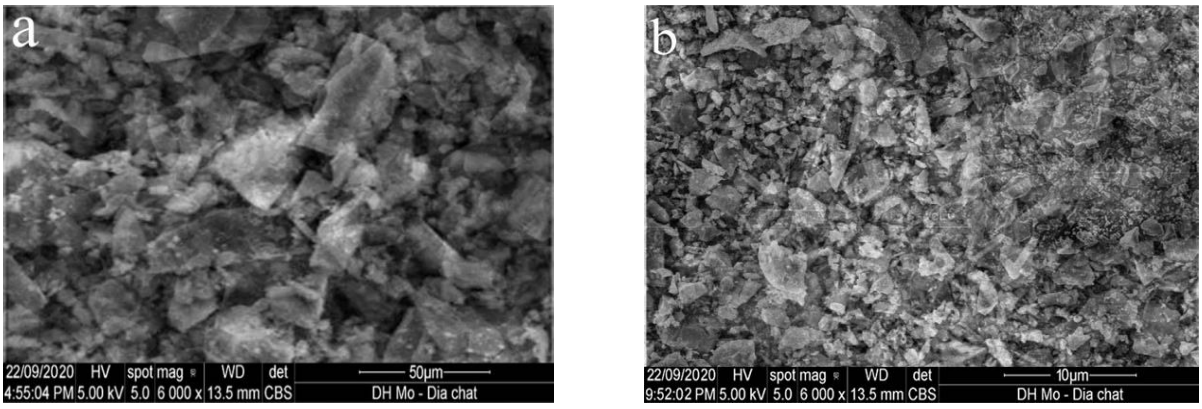

Fig. 4 – SEM of BFS samples at different grinding times: a-0 minutes, b-10 minutes, c-20 minutes, d-30 minutes, e-40 minutes

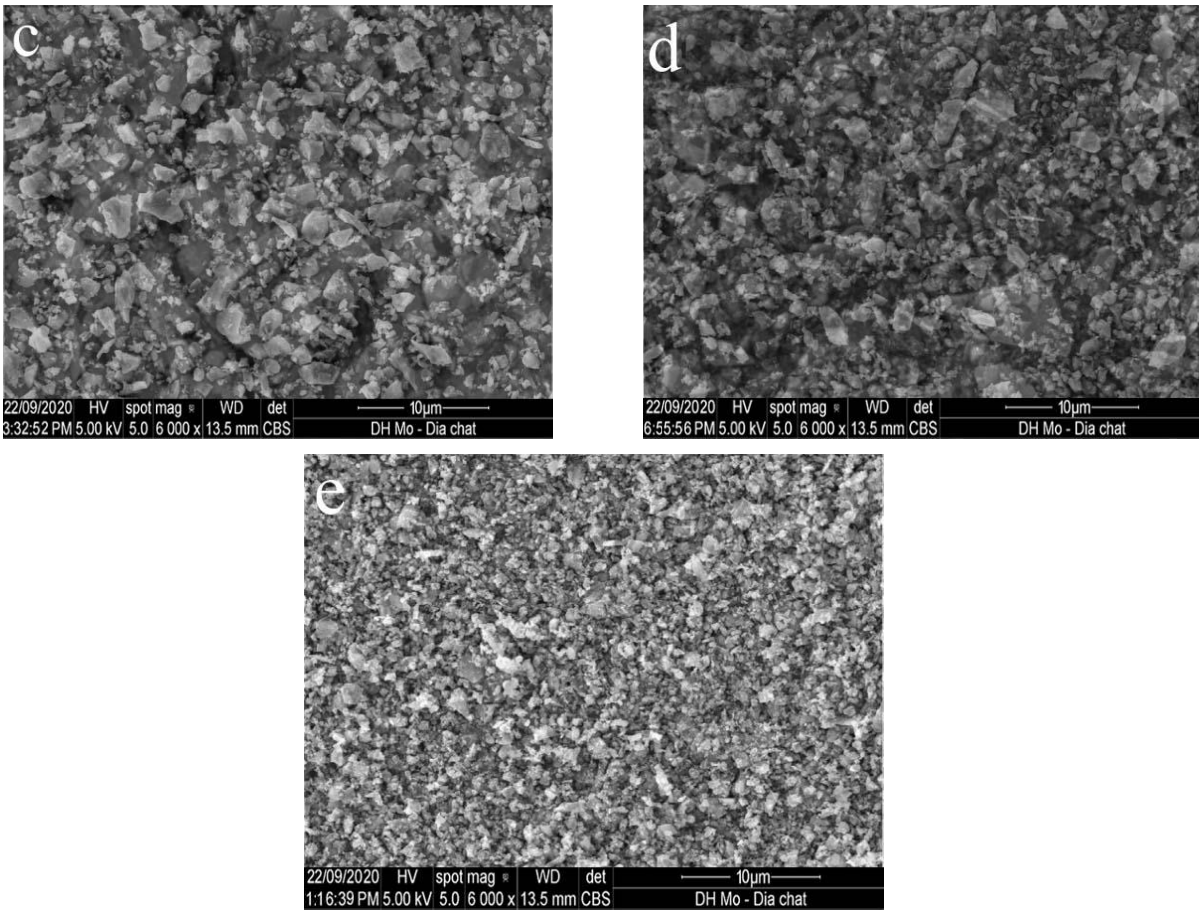

Fig. 4 – SEM of BFS samples at different grinding times: a-0 minutes, b-10 minutes, c-20 minutes, d-30 minutes, e-40 minutes

The change of BFS particle size at different grinding times is shown in Figure 4. It can be seen that the resulting BFS has a dense structure and an uneven shape. The fine grinding process shows that the particle size of BFS is significantly reduced. The impact of the grinding process results leads to BFS particles to break and become smooth.

Mixture proportions

In the present study, the proportions and composition of the mixture are presented in Table 3. Water/binder = 0.5 (binder = Cement + BFS). Mixtures 2, 3, 4 use 50% of finely crushed BFS to replace Cement [22].

Tab. 3 - Mix proportion of BFS -cement mortar

Mix number	BFS grinding time	Cement	Sand	BFS	Water
No-0	100% Cement	513	1539	-	256
No-1	0 minutes (50% Cement – 50%BFS)	256.5	1539	256.5	256
No-2	10 minutes (50% Cement – 50%BFS)	256.5	1539	256.5	256
No-3	20 minutes (50% Cement – 50%BFS)	256.5	1539	256.5	256
No-4	30 minutes (50% Cement – 50%BFS)	256.5	1539	256.5	256
No-5	40 minutes (50% Cement – 50%BFS)	256.5	1539	256.5	256

XRD of blast furnace cement-slag mortar sample

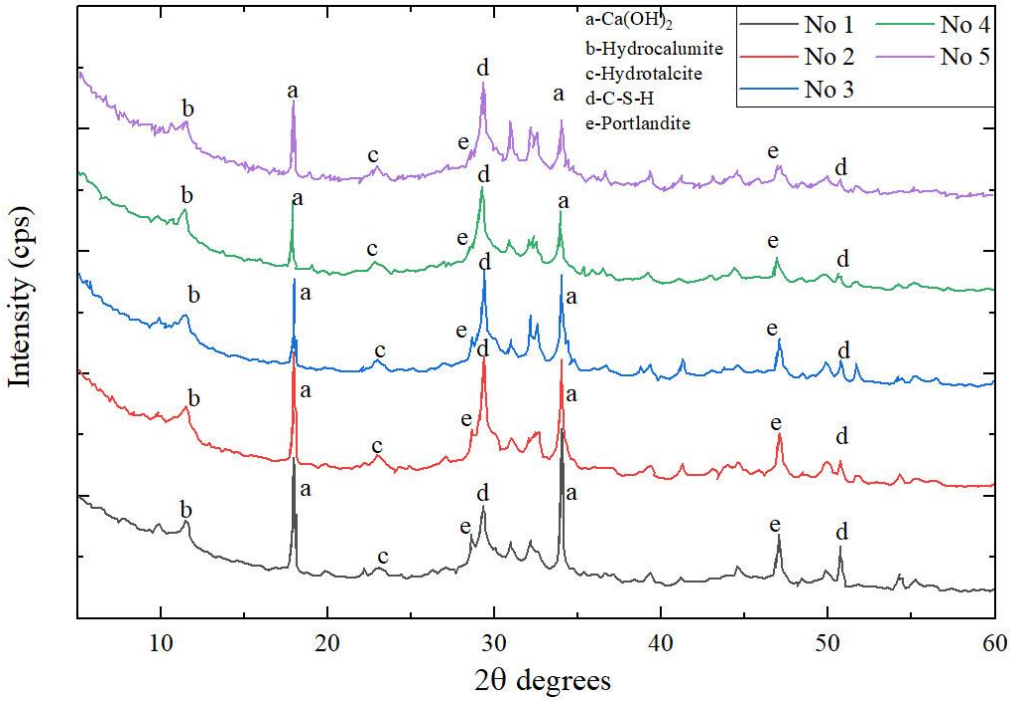

Fig. 5 – XRD of the samples uses BFS for different grinding times

Figure 5 presents XRD results of experimental samples after 28 days of age. This result is to evaluate the effect of finely ground BFS on the reaction processes. Hydration products include C-S-H gel and portlandite derived from Cement due to the carbonation of $Ca(OH)_2$, Hydrotalcite and hydrocalumite due to the reaction of BFS. Therefore, it can be seen that the hydration products are the same for all samples. This study's material composition is the same, only different at BFS grinding time. The $Ca(OH)_2$ content can reflect the blast furnace slag's reactive properties, as shown in Figure 5. In addition, the intensity of $Ca(OH)_2$ decreases significantly as the BFS grinding time increases. This suggests that the BFS grinding process can substantially promote the reactivity of BFS.

Compressive strength

Tab. 4 - Compressive strength of experimental samples

Mix number	Compressive strength (MPa)		
	3 d	7 d	28 d
No-0	24.1	39.2	55.7
No-1	17.9	30.3	51.2
No-2	23.5	39.8	57.3
No-3	34.4	46.1	65.8
No-4	35.4	53.2	68.6
No-5	39.4	61.7	72.1

Table 4 shows that the compressive strength of the concrete sample (No-1) is 17.9, 30.3, 51.2 MPa after 3, 7, 28 days of age. It is lower than the compressive strength of concrete sample (No-0), respectively 24.1, 39.2 and 55.7 MPa. Untreated BFS was shown to have a negative effect on the compressive strength of the concrete at all testing ages. Meanwhile, the effect of increasing concrete strength when extending BFS grinding time occurred in samples (No-2, No-3, No-4, No-5) corresponding to grinding time of 10, 20, 30 and 40 minutes. The compressive strength of the

experimental concrete samples has proven that the use of finely ground BFS significantly improves the concrete's strength. This is also confirmed in the study of Dien Vu Kim and etc [17].

Activity index of BFS

The activity index of BFS (I_R,%) is the ratio of a sample's compressive strength made of a cement-sand mortar, where part of the binder - Cement is replaced by BFS (R_2). The compressive strength of the sample control, no-additive cement-sand mortar (R_1). The BFS activity index was calculated using formula (2) given in the TCVN 11586: 2016 standard.

$$I_R = \frac{R_2}{R_1}.100\% \quad (2)$$

where: I_R - activity index of BFS, %; R_1 - compressive strength of control samples made on no additive cement-sand composition at the age of 28 days, MPa; R_2 - compressive strength of samples from cement-sand-BFS mortars at the age of 28 days, MPa.

Figure 6 shows the activity index of the BFS. It can be seen that untreated BFS has a low activity index (91.92%) whereas finely ground BFS has a high activity index (102.87%, 118.13%, 123.16% and 129.44%). This is explained that, due to the finely ground BFS with microparticles, it fills the void and has an excellent pozzolanic effect. This helps to form more hydration products and more compact structure.

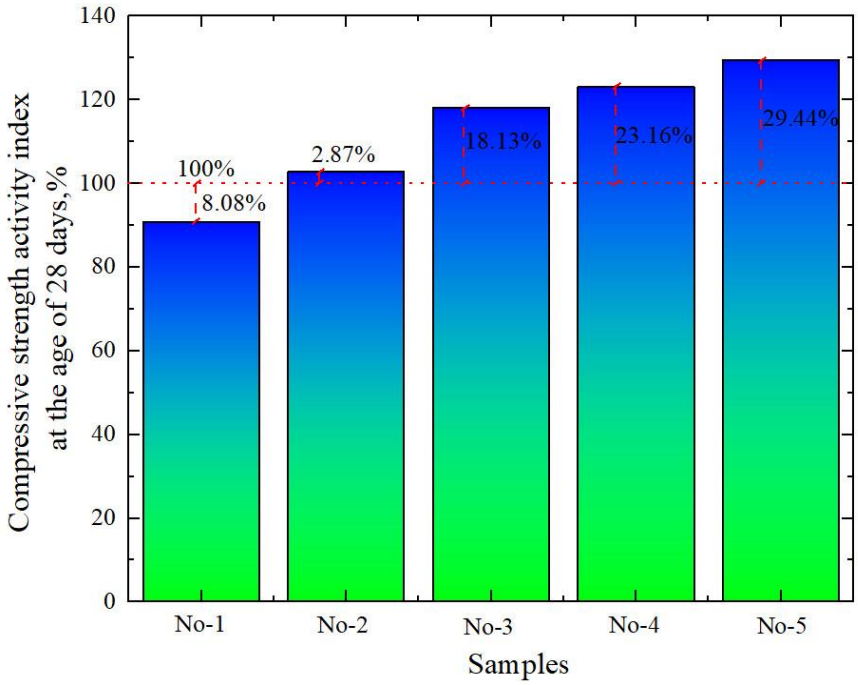

Fig. 6 – Diagram of comparing activity index of BFS

Effect of BFS on foam concrete properties

Foam concrete mix compositions

The purpose of this section is to study two types of foam concrete, produced from QS and BFS finely ground in 40 minutes. Type I with a wet density of 1700 kg/m^3. Type II with a wet density of 900 kg/m^3. The composition of the foam concrete mixture is given in Table 2. According to [25] the amount of fixed cement with the mixture = 1700 kg/m^3 and cement = 350 kg/m^3 with mixes 900 kg/m^3. For Series I-2, II-2 used QS to replacement of 100% BFS [16]. Besides, SF90 and SR5000 have been used to increase strength and reduce water with ratio SF90/OPC = 0.1,

SR5000/OPC = 0.015, [26]. The composition of the foam concrete mixture is shown in Table 5.

Tab. 5 - Component foam concrete mixture

Series	Mix number	Component foam concrete mixture, kg/m^3						
		OPC	BFS	QS	SR5000	SF90	W	Foam (l)
Series I	1	450	926	-	4,5	69	271.9	206.92
	2	450	-	926	4,5	69	181.5	206.92
Series II	1	350	356	-	3,5	39	139.5	567.54
	2	350	-	356	3,5	39	104.8	567.54

Mechanical properties of foam concrete

The experimental results of the mechanical properties of foam concrete are presented in Table 6.

Tab. 6 - Results of flexural strength, compressive strength and elastic modulus of foam concrete

Series	Mix number	Compressive strength at different curing times (MPa)					Flexural strength at 28 days (MPa)	Elastic modulus 10^3 (MPa)
		3 - day	7 - day	14 - day	21-day	28 - day		
Series I	1	32.1	39.56	44.11	44.9	45.6	6.74	26.78
	2	22.78	26.96	32.57	33.01	33.34	5.36	21.95
Series II	1	6.76	7.76	8.21	8.55	8.63	1.067	7.71
	2	4.73	5.51	5.69	5.77	5.91	0.824	5.76

Compressive strength of foam concrete

As shown in Figure 7 the use of additives (Silica fume, Superplasticizer) and BFS significantly improves the development of compressive strength in all test periods. This is due to the decrease in water content due to the use of the Superplasticizer and pozzolanic characteristics of SF90 and BFS. In addition, this leads to an improvement in the bonding of aggregates with the less porous interphase formation and better adhesion between the mortar and aggregate mixture.

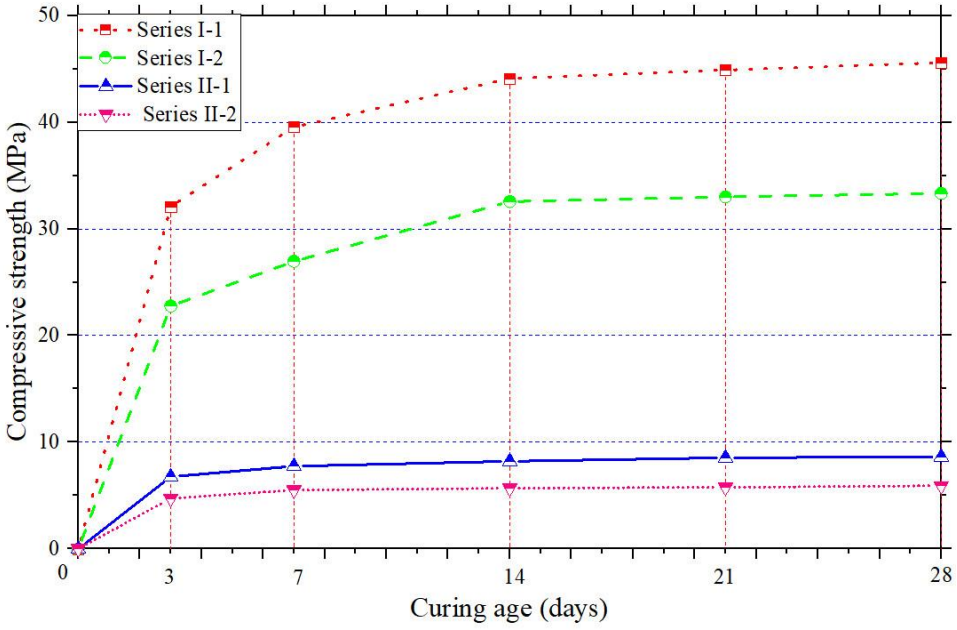

Fig. 7 – Dependences of the strength of foam concrete on the age of the samples

It can be seen from Figure 7 that the compressive strength of Series I-1 and Series II -1 is higher than the strength of Series I -2 and Series II -2. This is because using fine grinding BFS can

help achieve a more even distribution of air voids, providing a uniform coating on each bubble, thereby preventing the coalescence of bubbles, leading to an increase in strength. In addition, replacing QS with BFS increases both compressive strength and flexural strength. This is because BFS has high pozzolanic activity due to the average content of amorphous SIO_2 in them is 36.01%.

Basically, foam concrete with BFS as a filler material has a higher compressive strength than foam concrete with QS as a filler material. This is also confirmed in the study of Dien Vu Kim, etc. [16].

Flexural strength of foam concrete

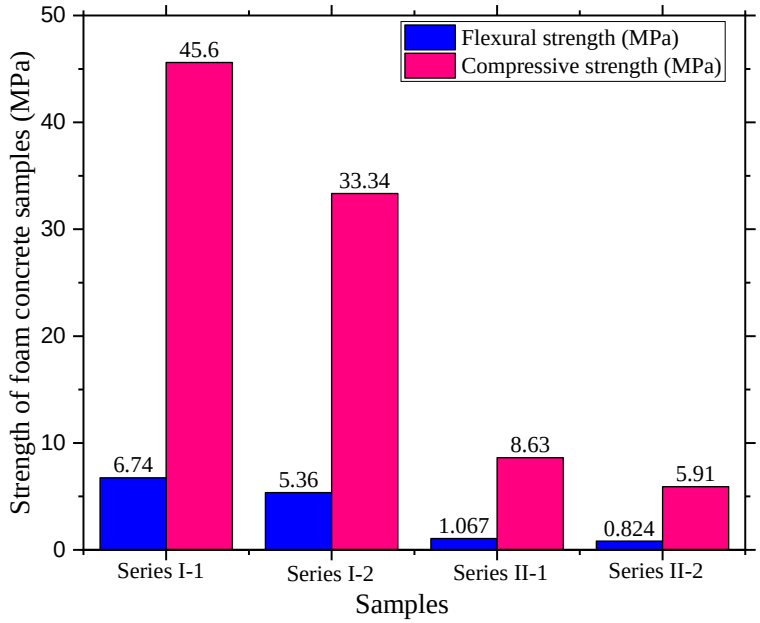

Fig. 8 – Dependences of the strength of foam concrete on the age of the samples

Figure 8 shows the increase in compressive and flexural strength, respectively, depending on the proportions of fine grinding BFS in the foam concrete mixture's compositions. In addition, from Figure 8, it can be seen that with an increase in compressive strength, the flexural strength also increases. This is entirely consistent with the law of the strength development of concrete.

Elastic modulus of foam concrete

The static modulus of elasticity (Es) of the mixtures (Series I-1, Series I-2, Series II-1, Series II-2) was determined using cylindrical samples 150 × 300 mm in size; two samples were tested for each mixture at the age of 28 days following GOST 24452-80 [21][27]. Each sample was equipped with four potentiometers in different quadrants to measure axial deformation, see Figure 9.

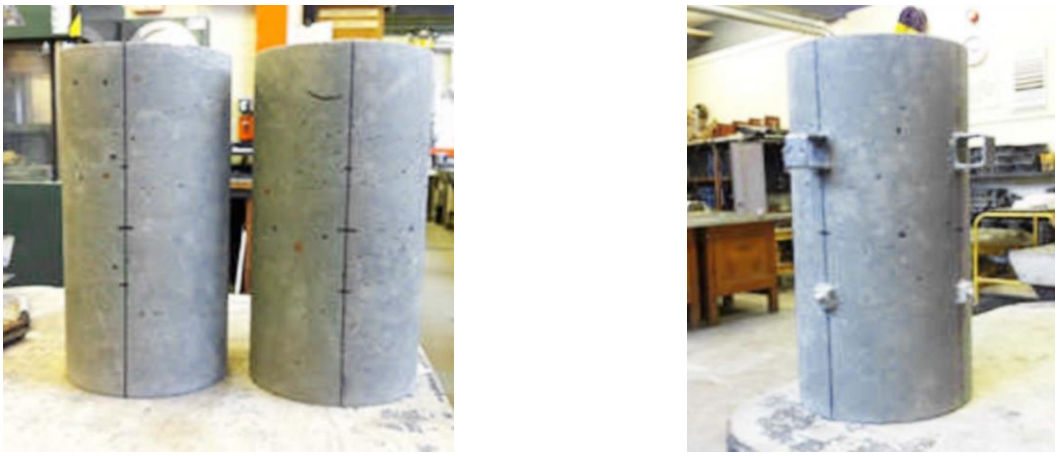

Fig. 9 – Samples for testing elasticity modulus

Figure 10 shows that the modulus of elasticity of the Series I-1and Series II-1 is higher than the Series I-2 and Series II-2. This is directly proportional to the compressive and flexural strength of the foam concrete. Therefore, it can be concluded that when the compressive strength, the flexural strength increases to lead the elastic modulus increases. Compared to the [28] study results, this research result is completely consistent.

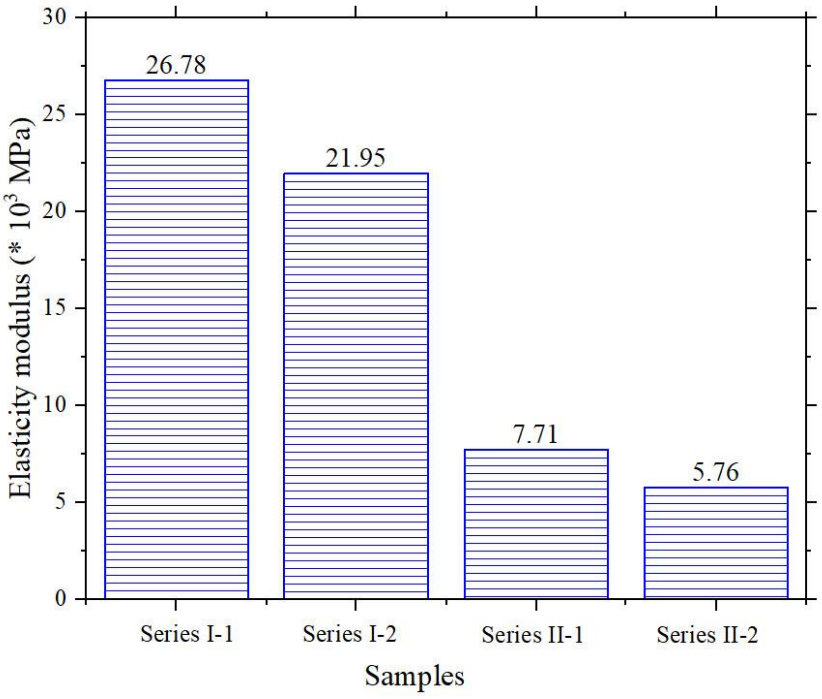

Fig. 10 – Elasticity modulus of foam concrete

CONCLUSIONS

Based on the test results, the following conclusions are drawn:

- Finely ground BFS by mechanical grinding method obtained a minimum average particle size of 5 μm after 40 minutes of treatment. This proves that this method is an effective method for obtaining finely ground BFS. In addition, the fine grinding of BFS after 40 minutes did not affect the particle size much.

- Finely ground BFS by mechanical grinding in 40 minutes with an activity index = 129% can replace activated mineral additives to produce construction mortar and concrete, reducing costs and improving friendly environmental situation.
- The mechanical grinding method can improve the reaction of BFS. The compressive strength increases when the BFS grinding time is extended. Specifically, compressive strength at 28 days increased from 55.7 MPa to 72.1 MPa, corresponding to grinding time from 0-40 minutes.
- The mechanical grinding method results showed that the particle size of BFS decreased significantly. The main constituents of BFS are amorphous structures (Akermanite, Calcite, Aragonite).
- Research results show that the use of finely crushed BFS by the mechanical grinding method to replace QS in foam concrete not only improves the mechanical properties such as compressive strength, flexural strength and elastic modulus of foam concrete. Besides, it can protect the environment, reduce product costs.

REFERENCES

[1] Vu, K.D., Bazhenova, S.I., 2020. Blast furnace slag application in mortars and concrete. In the collection: Sustainable development of the region: architecture, construction, transport. Materials of the 7th International Scientific and Practical Conference. Pp. 5.

[2] Tsakiridis, P.E., Papadimitriou, G.D., Tsivilis, S., Koroneos, C., 2008. Utilization of steel slag for Portland cement clinker production. Journal of Hazardous Materials. 152(2). Pp. 805–811. DOI:10.1016/j.jhazmat.2007.07.093.

[3] Van Deventer, J.S.J., Provis, J.L., Duxson, P., Brice, D.G., 2010. Chemical research and climate change as drivers in the commercial adoption of alkali activated materials. Waste and Biomass Valorization. 1(1). Pp. 145–155. DOI:10.1007/s12649-010-9015-9.

[4] Nochaiya, T., Wongkeo, W., Pimraksa, K., Chaipanich, A., 2010. Microstructural, physical, and thermal analyses of Portland cement-fly ash-calcium hydroxide blended pastes. Journal of Thermal Analysis and Calorimetry. 100(1). Pp. 101–108. DOI:10.1007/s10973-009-0491-8.

[5] Cheah, C.B., Chung, K.Y., Ramli, M., Lim, G.K., 2016. The engineering properties and microstructure development of cement mortar containing high volume of inter-grinded GGBS and PFA cured at ambient temperature. Construction and Building Materials. 122. Pp. 683–693. DOI:10.1016/j.conbuildmat.2016.06.105. URL: http://dx.doi.org/10.1016/j.conbuildmat.2016.06.105.

[6] Sajedi, F., 2012. Effect of curing regime and temperature on the compressive strength of cement-slag mortars. Construction and Building Materials. 36. Pp. 549–556. DOI:10.1016/j.conbuildmat.2012.06.036. URL: http://dx.doi.org/10.1016/j.conbuildmat.2012.06.036.

[7] Bilim, C., Karahan, O., Atiş, C.D., Ilkentapar, S., 2013. Influence of admixtures on the properties of alkali-activated slag mortars subjected to different curing conditions. Materials and Design. 44. Pp. 540–547. DOI:10.1016/j.matdes.2012.08.049.

[8] Aljoumaily, Z.S., Noordin, N., Awang, H., Almulali, M.Z., 2012. The Effect of Blast Furnace Slag on Foam concrete in terms of Compressive strength. Advanced Materials Research. 587. Pp. 81–87. DOI:10.4028/www.scientific.net/AMR.587.81.

[9] Oren, O.H., Gholampour, A., Gencel, O., Ozbakkaloglu, T., 2020. Physical and mechanical properties of foam concretes containing granulated blast furnace slag as fine aggregate. Construction and Building Materials. 238. Pp. 117774. DOI:10.1016/j.conbuildmat.2019.117774.

[10] Ngamnikom, P., Songsermpong, S., 2011. The effects of freeze , dry , and wet grinding processes on rice flour properties and their energy consumption. Journal of Food Engineering. 104(4). Pp. 632–638. DOI:10.1016/j.jfoodeng.2011.02.001. URL: http://dx.doi.org/10.1016/j.jfoodeng.2011.02.001.

[11] Sajedi, F., Razak, H.A., 2011. Comparison of different methods for activation of ordinary Portland cement-slag mortars. Construction and Building Materials. 25(1). Pp. 30–38. DOI:10.1016/j.conbuildmat.2010.06.060. URL: http://dx.doi.org/10.1016/j.conbuildmat.2010.06.060.

[12] Norrarat, P., Tangchirapat, W., Jaturapitakkul, C., 2017. Evaluation of Heat Evolution of Pastes Containing High Volume of Ground River Sand and Ground Granulated Blast Furnace Slag. 23(1).

[13] Wang, P.Z., Trettin, R., Rudert, V., 2005. Effect of fineness and particle size distribution of granulated blast-furnace slag on the hydraulic reactivity in cement systems. (4). Pp. 161–166.
[14] Wainwright, P.J., Rey, N. Cement & Concrete Composites The influence of ground granulated blastfurnace slag (GGBS) additions and time delay on the bleeding of concrete. Cement & Concrete Composites. 2000. 22. Pp. 253–257.
[15] Siddique, R., Kaur, D., 2012. Properties of concrete containing ground granulated blast furnace slag (GGBFS) at elevated temperatures. Journal of Advanced Research. 3(1). Pp. 45–51. DOI:10.1016/j.jare.2011.03.004. URL: http://dx.doi.org/10.1016/j.jare.2011.03.004.
[16] Kim, D.V., Cong, L.N., Van, L.T., Bazhenova, S.I., 2020. Foamed concrete containing various amounts of organic-mineral additives. Journal of Physics: Conference Series. 1425. Pp. 12. DOI:10.1088/1742-6596/1425/1/012199.
[17] Kim, D.V., Bazhenova, S., Van, L.T., Cong, L.N., 2020. Sustainable use of industrial-waste as fine-aggregate of Foam Concrete. IOP Conference Series: Materials Science and Engineering. 869. Pp. 10. DOI:10.1088/1757-899X/869/3/032022.
[18] Zhao, X., Lim, S., Tan, C., Li, B., Ling, T., Huang, R., Wang, Q., 2015. Properties of Foamed Mortar Prepared with Granulated Blast-Furnace Slag. Materials. Pp. 462–473. DOI:10.3390/ma8020462.
[19] Gökçe, H.S., Hatungimana, D., Ramyar, K., 2019. Effect of fly ash and silica fume on hardened properties of foam concrete. Construction and Building Materials. 194. DOI:10.1016/j.conbuildmat.2018.11.036.
[20] Othuman, M.A., Wang, Y.C., 2011. Elevated-temperature thermal properties of lightweight foamed concrete. Construction and Building Materials. 25(2). Pp. 705–716. DOI:10.1016/j.conbuildmat.2010.07.016. URL: http://dx.doi.org/10.1016/j.conbuildmat.2010.07.016.
[21] GOST 24452-80., 1982. Concretes. Methods of prismatic, compressive strength, modulus of elasticity and Poisson's ratio determination 8p.
[22] TCVN 11586-2016,. 2016. Ground granulated blast-furnace slag for concrete and mortar. 12p.
[23] Öner, M., 2000. Study of intergrinding and separate grinding of blast furnace slag cement. Cement and Concrete Research. 30(3). Pp. 473–480. DOI:10.1016/S0008-8846(00)00197-6.
[24] Gan, L., Zhang, C., Zhou, J., Shangguan, F., 2012. Continuous cooling crystallization kinetics of a molten blast furnace slag. Journal of Non-Crystalline Solids. 358(1). Pp. 20–24. DOI:10.1016/j.jnoncrysol.2011.08.008. URL: http://dx.doi.org/10.1016/j.jnoncrysol.2011.08.008.
[25] Zhou, X.S. and V., 2016. Lightweight concrete. 304p
[26] Vu, K.D., Bazhenova, S.I., Tang, V.L., 2020. Influence-of-mineral-additives-fly-ash-blast-furnace-slag-on-mechanical-properties-of foam concrete. Building materials and technologies. 88(2). Pp. 25–34. DOI:10.33979/2073-7416-2020-88-2-25-34.
[27] Neville, A.M., 2011. Properties of concrete. 53(9).
[28] Eltayeb, E., Ma, X., Zhuge, Y., Youssf, O., Mills, J.E., 2020. Influence of rubber particles on the properties of foam concrete. Journal of Building Engineering. 30(December 2019). Pp. 101217. DOI:10.1016/j.jobe.2020.101217. URL: https://doi.org/10.1016/j.jobe.2020.101217.

CIVIL ENGINEERING JOURNAL

Article no. 4

THE CIVIL ENGINEERING JOURNAL 1-2022

MECHANICAL BEHAVIOR OF COMPOSITIONS OF GLASS-FIBER REINFORCED PLASTIC MORTAR PIPES BASED ON THEIR FUNCTIONING

*Huawang Shi, Chongchong Xue, Feng Qiao and Yancang Li**

Hebei University of Engineering, School of Civil Engineering, Handan, Hebei 056038, China

ABSTRACT

The experimental investigation on the mechanical parameters compositions of glass-fiber reinforced plastic mortar (GRPM) pipe is the basis of simulating and analyzing the mechanical characteristics of the complete structure of GRPM pipe. Due to the anisotropic material properties of GRPM pipe, the compressive property test is carried out, and the results show that the circumferential compressive strength(CCS) is 49.93 MPa, the axial compressive strength(ACS) is 40.79 MPa, the circumferential elastic modulus(CEM) is 4.84 GPa, and the axial elastic modulus(AEM) is 4.04 GPa. The difference between the CCS and ACS and EM is about 20%, as well as the CCS and EM are greater than the ACS and modulus of elasticity. Conclusions drawn from the tests provide an important basis for checking whether the materials meet the design requirements.

KEYWORDS

GRPM pipe culvert, Mechanical behavior, Elastic modulus, Compressive strength

INTRODUCTION

Glass-fiber reinforced plastic mortar (GRPM) pipe has been developed and applied in many industries, and its excellent properties such as high strength and stiffness, high corrosion resistance and smooth internal surface et al. are widely considered as the most suitable pipe material in culvert engineering [1]. As a buried GRPM pipe in highway engineering, in addition to good drainage performance, it also needs to bear the impact of external load and surrounding earth pressure on the pipe itself. Therefore, before studying the stress characteristics of the whole structure of GRPM pipe, it is necessary to test and study the basic mechanical parameters of GRPM pipe. In 2015, Rafiee et al. [2] and others investigated the failure mechanism of glass fiber reinforced pipes, and established a failure assessment model including stress analysis, failure assessment and material function degradation. The effects on the failure pressure for four different fiber volume fractions: 52.5%, 55%, 57.5% and 60%, and three different winding angles: 52.5%, 57.5% and 60.19% were studied. The results show that the failure pressure of function and the first ply decrease with the increase of fiber volume fraction, while an increase in winding angle (measured from the axial axis) increases the failure pressure. Melo et al. [3] presented experimental and numerical result of filament-wound E-glass/polyester pipes with nominal inside diameter of 300 mm and wall thickness of 5.7 mm, which were produced with the incorporation of quartz sand as filler and tested to failure under internal pressure. According to the results presented, both failure criteria predicted values which are within one standard deviation of the measured mean response. The average experimental leakage pressure (4.55 MPa) was about 2% below the ficco-ply-failure numerical prediction, using the failure criterion of Hoffman (4.66 MPa) and 4% below the prediction adopting the failure theory of Tsai–Hill (4.75 MPa). Schrock [4]

studied the design method of GRPM pipe and pointed out that according to the structural characteristics and bearing requirements of GRPM pipe, it is necessary to calculate the maximum load, bending strength, shear strength and bearing capacity of each layer of the pipe in detail.

In this paper, the production technology, compressive strength and elastic modulus of GRPM pipes are studied. The mechanical performance of such structural components, which are normally subjected to external parallel load, depends on the manufacturing process and includes aspects such as microstructure and volume fractions of the constituents, as well as distribution, sizes and shapes of the reinforcing phases, voids and cracks [5]. These aspects as well as the mechanical behavior of the pipes, are discussed in this study. The experimental analysis and calculation results provide basic data for the evaluation of the mechanical properties and numerical simulation of the GRPM pipe.

DESCRIPTION OF GRPM PIPE

The production process of GRPM pipe mainly includes filament winding and centrifugal casting [6]. The GRPM pipe selected in this paper is GRPM pipe of filament winding type, and as the highway buried pipe culvert, the performance of the winding pipe culvert is more suitable [7].

The wall structure of GRPM pipe can be generally divided into five layers, from the inside to the outside are interior liner, inner structure layer, core, outer structure layer and exterior surface. Figure 1 shows a GRPM pipe wall construction demonstrating laminated structure.

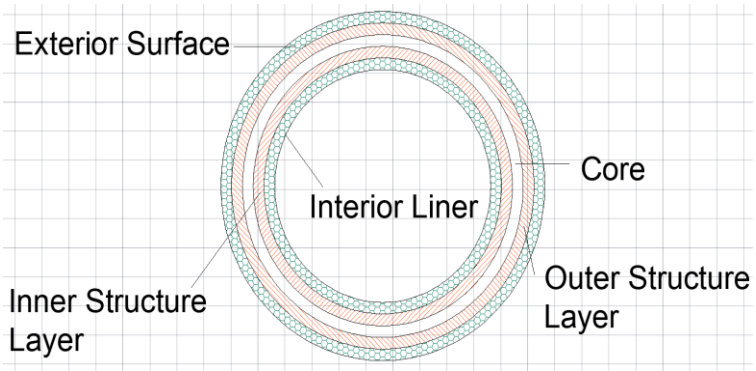

Fig.1 - GRPM pipe wall construction

Interior liner

The inner liner directly contacts with the fluid conveyed in the pipeline, which should meet the requirements of the conveyed fluid in the pipe, and has the functions of anti-seepage, wear-resistant, corrosion-resistant, etc. The interior liner should be particularly smooth, without defects, cracks or stratification. In order to obtain a smooth and dense inner surface, the process of first gluing and then wrapping felt is adopted, and the secondary inner layer is directly formed by spray method. It is usually produced on a cylindrical metallic mold composed of stitched glass fiber mat (450 g/m^2), surface mat (30 g/m^2) shown in Figure 2 and unsaturated polyester resin with the approximate thickness of 1.5 mm..

Inner structural layer

The inner structural layer, also known as the inner reinforcement layer, is mainly composed of the tensile and compressive stresses caused by the internal pressure load and the axial bending load on the circumferential and spiral fibers. The fiber consumption, resin composition, winding thickness and wire arrangement of the layer are determined by the design and calculation of the internal and external pressure load requirements of the pipeline.

Core layer

The core layer, also known as resin mortar layer, is composed of structural resin and quartz sand. Its thickness is determined according to the buried depth of the pipeline and the rigidity design required by the ground load. The main function is to enhance the rigidity of the pipeline.

Outer structural layer

The outer structural layer, also known as the outer reinforcement layer, has the same circular layer and spiral layer as the inner winding layer, which is the outer skin with sand layer structure. Its thickness and layout design depend on internal pressure, external pressure and bending load. In this way, the pipe wall of sandwich structure is composed of inner and outer structural layers and core layers.

Exterior surface

The exterior surface, also known as anti-aging layer, is composed of anti-corrosion resin, weather resistant resin and other auxiliary materials. Unsaturated polyester resin is one of the most commonly used thermosetting resins. It is a linear polymer formed by condensation of saturated dicarboxylic acid, unsaturated dicarboxylic acid and diol. It is a resin solution with certain viscosity diluted by cross linking monomer or active solvent, which is called up for short. It can resist the erosion of natural environment factors such as atmospheric aging, sunlight and water immersion. In addition, its hardness is generally high, which can improve the anti-collision ability of pipeline.

(a)Glass fiber roving *(b)Surface mat* *(c)Chopped mat*

Fig.2 - Glass fiber

According to the analysis of the cross section structure of GRPM pipe wall as shown in Figure 1, it is not difficult to discover that GRPM pipe is a reasonable pipe wall structure with clear structure level and clear function division.

In the discontinuous winding process, first, the lining is made on the lining machine, and then the winding and sanding operation is carried out on the basis of the completion of the anti-seepage lining layer according to the structural design requirements of the pipe wall. The continuous fiber is used in turn to move back and forth along the axis of the rotating core mold through the dip groove. The placement of the fiber relative to the mandrel axis and the winding angle are controlled by the ratio of the moving speed of the glue bath and the rotation speed of the mandrel. The inner winding layer, the sand layer, the outer winding layer and the outer protective layer are completed respectively. The whole process is controlled by the computer. The wrapped pipe is placed on the curing machine and rotated, heated by far-infrared electric heating plate, heated and solidified while rotating until the curing process is completed. After curing, it shall be lifted to the correction machine for bearing and socket turning, and then it shall be lifted to the demoulding machine for oil pressure demoulding. The production procedure is shown in Figure 3.

(a) Lining fabrication *(b) Filament winding* *(c) Sand winding*

(d) Solidification *(e) Demoulding*

Fig.3 - Fabrication process of the filament-wound pipe

EXPERIMENTAL PROCEDURE

Materials and test specimens

The specimens for test of compressive strength and modulus of elasticity of the GRPM pipe composite was fabricated according to the Standard ANSI/AWWA C950-01[8]. The length of pipe is 6 m with 1.5 m diameter and 0.05 m wall thickness.The thickness of test specimen wall is taken as the section with length a=50 mm, width b=47 mm, and the height of the specimen is taken as h =150 mm. The fabrication and size of specimens are shown in Figure 4.

The compressive strength and elastic modulus of GRPM pipe can be tested in two directions: circumferential direction and axial direction. A vernier callipers with an accuracy of 0.02 mm was used to measure the specific dimensions of each specimen. The length, width and height of each specimen are respectively three different positions of the specimens. The detailed dimension data of specimens are shown in Table1.

Where HY1-5 are representative of No.1-5 specimens in hoop direction, and ZY1-5 stand for No.1-5 specimen in axial direction. The following three requirements should be met for sample preparation:

(1) The samples should be prepared by machining method, and the positions without bubble and crack defects should be selected for sampling, and the number of test pieces should not be less than 5 effective test pieces;

(2) The upper and lower, left and right, front and rear of the sample should be parallel to each other;

(3) The error of length, width and height of the sample is within 5mm.

Tab.1 - Size of specimens

	Hoop specimen	Unit: mm			Axial specimen	Unit: mm	
No.	Length a	Width b	Height h	No.	Length a	Width b	Height h
HY1	50.60	46.78	150.20	ZY1	51.62	47.02	151.80
	50.66	47.06	149.92		51.58	47.26	151.74
	50.78	47.08	149.80		51.72	47.06	151.60
M-value	50.68	46.97	149.97	M-value	51.64	47.11	151.71
HY2	51.10	47.18	145.66	ZY2	51.48	47.58	151.80
	50.72	47.10	145.30		51.22	47.42	151.40
	50.72	46.92	145.20		50.60	47.08	151.38
M-value	50.84	47.06	145.38	M-value	51.10	47.36	151.52
HY3	51.38	47.10	148.92	ZY3	51.60	47.10	151.40
	51.18	46.78	148.78		51.98	47.28	151.38
	51.36	47.30	149.10		52.20	47.48	151.36
M-value	51.30	47.06	148.93	M-value	51.92	47.28	151.38
HY4	51.20	47.10	147.46	ZY4	52.10	47.10	150.98
	51.48	47.08	147.80		51.60	47.12	151.10
	51.12	47.14	147.10		51.36	47.20	151.18
M-value	51.26	47.11	147.45	M-value	51.68	47.14	151.08
HY5	50.78	47.10	148.44	ZY5	52.02	47.26	151.42
	50.98	47.38	148.34		51.60	47.22	151.16
	50.80	47.76	148.04		51.50	47.24	151.30
M-value	50.85	47.21	148.27	M-value	51.37	47.24	151.29

In this test, the samples are taken from the hoop and axial direction of GRPM pipe. Each type includes two mechanical indexes of compressive strength and elastic modulus with 5 specimens respectively.

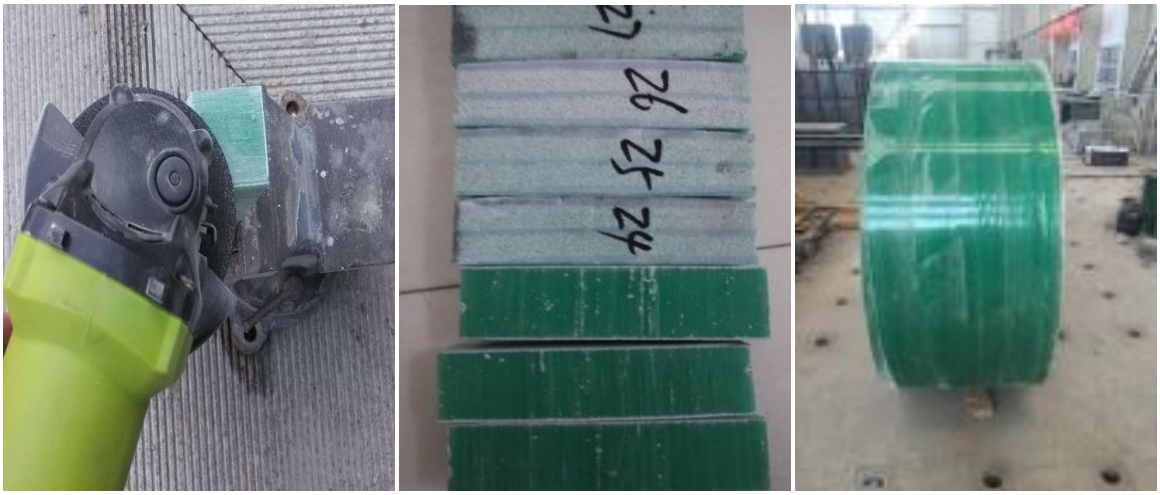

Fig.4 - Pipe specimens

Test equipment

In this test, the dual space system of WAW-1000 universal testing machine controlled by computer, which can be seen in Figure 5, is adopted. The test system is composed of main engine, hydraulic power unit, dscc-5000 multi-channel electro-hydraulic servo closed-loop control system and computer data processing system. It adopts the electro-hydraulic servo control technology, which can meet the three closed-loop control requirements of load, deformation and displacement. It has three control modes of load, deformation and displacement, and can realize smooth switching according to the set control mode, and achieve constant speed Rate load control, constant rate deformation control, constant rate displacement control and other programs to meet the requirements of various material tests. The equipment can be used for tensile test and compression test of bar, plate and other samples. Bending and shearing tests can be carried out with bending and shearing clamps.

Fig. 5 - WAW-1000 universal testing machine

Experimental procedures

The test was conducted at (23 ± 2) ℃ and relative humidity with (50 ± 10)%. Before the test, the sample shall be placed under the standard environmental conditions of the laboratory for at least 24 hours. The basic procedures were carried out according to the Standard [8].

(1) Prepare the sample according to the requirements of the test standard, then number the sample and measure the size of any three places and fill in the table;

(2) The loading head of the testing machine should be smooth and free of sundries. The parallelism of the upper and lower pressboards should be adjusted before testing;

(3) Adjust the position of the lower crossbeam of the testing machine, install and place the test piece, make the center line of the test piece align with the center of the upper and lower pressing plates of the testing machine, and put it in the state of load to be applied;

(4) Load according to the set test loading speed. When the compressive strength is tested, the loading speed is 3 mm/min, and the uniform and continuous load is applied to the specimen until the specimen is damaged. The tester automatically records the maximum load and fills the value in the corresponding table;

(5) The loading speed is 2 mm/min for the elastic modulus testing. The dial indicator is placed, the initial load is applied, and the test piece and the dial indicator are checked and adjusted, so that the whole system is in normal working state and the compression deformation of both sides of the test piece is consistent. Then the load is applied at a certain loading speed, divided into six levels of loading, the applied load should not exceed 50% of the maximum load, and the repeated loading is three. The deformation size of each test piece is recorded and the average value is taken. The test load application procedure is shown in Figure 6.

Fig.6 - Specimen loading

The compressive strength σ_c of GRPM pipe is calculated by the following equation.

$$\sigma_c = \frac{P}{a \times b} \tag{1}$$

where σ_c is compressive strength, kN/cm^2;

P is the load at failure, kN;

$a \times b$ is the loading section area, cm^2;

The applied load of testing the elastic modulus of GRPM pipe should not exceed half of the failure load, and then calculate the elastic modulus according to Equation 2.

$$E_c = \frac{L \cdot \Delta P}{a \cdot b \cdot \Delta L} \tag{2}$$

where, E_c is elastic modulus;

ΔP is the increment of applied load, kN,

ΔL is the increment of deformation corresponding to ΔP, mm;

RESULTS AND DISCUSSION

The typical curve of the compressive strength test results of DN1500 spiral wound GRPM pipe material is shown in Figure 7. Figure 7 shows the failure mode of the samples. In Figure 6, the vertical axis is the test load (kN), and the horizontal axis is the deformation (mm). According to the test results, one can determine the compressive strength of the material and its corresponding failure displacement, determine the maximum load according to the first peak of the test result curve, take the maximum load as the ultimate compressive load to calculate the compressive strength, and determine the final result according to the average strength of the five samples.

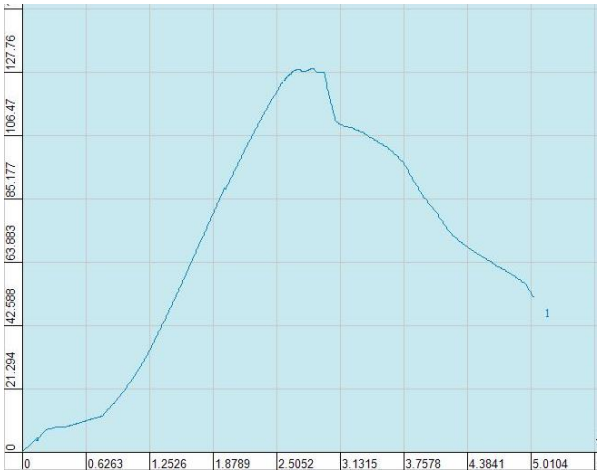

Fig.7 - Compressive strength curve

Fig.8 - Failure modes of specimens

As shown in Fig.8, under the continuous loading, there will be small cracks between the sand layer and the numerical layer. As the load increases continuously, the cracks increase, and develop in longitudinal direction. Finally, the cracks connect with each other, and the sample fails. Under the continuous loading of the circumferential sample, at first, there will be inclined small cracks with an angle of about 45° with the horizontal in the sand layer. With the continuous increase of the load, the inclined cracks will increase. Finally, the cracks will penetrate into each other and form the main cracks with an angle of about 45° with the horizontal. The sample fails.

Based on the classical laminated plate theory, the stress-strain relationship of the middle layer in the principal direction coordinate is expressed as follows by the stiffness component:

$$\begin{Bmatrix}\sigma_1\\ \sigma_2\\ \tau_{12}\end{Bmatrix}_0 = \begin{bmatrix}Q_{11} & Q_{12} & 0\\ Q_{12} & Q_{22} & 0\\ 0 & 0 & Q_{66}\end{bmatrix}_0 \begin{bmatrix}\varepsilon_1\\ \varepsilon_2\\ \gamma_{12}\end{bmatrix} \tag{3}$$

Where $Q_{11}=\frac{E_1}{1-v_{12}v_{21}}, Q_{22}=\frac{E_2}{1-v_{12}v_{21}}, Q_{66}=G_{12}, Q_{12}=v_{12}Q_{22}=v_{21}Q_{11}$

According to the coordinate transformation relationship, the stress-strain relationship of filament winding layer in off-axis coordinate system is:

$$\begin{Bmatrix}\sigma_x^{(k)}\\ \sigma_y^{(k)}\\ \tau_{xy}^{(k)}\end{Bmatrix}_k = \begin{bmatrix}\overline{Q_{11}} & \overline{Q_{12}} & \overline{Q_{16}}\\ & \overline{Q_{22}} & \overline{Q_{26}}\\ sym. & & \overline{Q_{66}}\end{bmatrix}_k \left\{\begin{bmatrix}\varepsilon_x^0\\ \varepsilon_y^0\\ \gamma_{xy}^0\end{bmatrix} + z_k\begin{bmatrix}k_x\\ k_y\\ k_{xy}\end{bmatrix}\right\} \tag{4}$$

Where, Q_{ij} is the stiffness modulus component in the off-axis coordinate system. Similarly, for the core inclusion layer, first assume that its stress-strain formula in the off-axis coordinate system is

$$\begin{Bmatrix}\sigma_x\\ \sigma_y\\ \tau_{xy}\end{Bmatrix} = \begin{bmatrix}Q_{11,m} & Q_{12,m} & Q_{16,m}\\ Q_{12,m} & Q_{22,m} & Q_{26,m}\\ Q_{16,m} & Q_{26,m} & Q_{66,m}\end{bmatrix}_k \left\{\begin{bmatrix}\varepsilon_x^0\\ \varepsilon_y^0\\ \gamma_{xy}^0\end{bmatrix} + z\begin{bmatrix}k_x\\ k_y\\ k_{xy}\end{bmatrix}\right\} \tag{5}$$

Where, $Q_{ij,m}$ is the stiffness coefficient of sand inclusion layer.

The core layer of GRPM pipe can be regarded as isotropic material, and its stress-strain can be expressed as

$$\begin{Bmatrix}\sigma_x\\ \sigma_y\\ \tau_{xy}\end{Bmatrix} = \begin{bmatrix}1 & & sym.\\ v & 1 & 0\\ 0 & 0 & \frac{1-v}{2}\end{bmatrix}_0 \begin{bmatrix}\varepsilon_x\\ \varepsilon_y\\ \gamma_{xy}\end{bmatrix} \tag{6}$$

The stiffness coefficient of sand layer of FRP sand pipe is

$$Q_{11,m}=Q_{22,m}=\frac{E}{1-v^2}, Q_{12,m}=E\frac{v}{1-v^2}, Q_{66,m}=\frac{E}{2(1+v)}, Q_{16,m}=Q_{26,m}=0$$

Then, the stress of filament winding layer and sand inclusion layer is integrated in the direction of pipe wall thickness

$$\begin{pmatrix}N\\ M\end{pmatrix} = \begin{bmatrix}A & B\\ B & D\end{bmatrix}\begin{pmatrix}\varepsilon_0\\ k\end{pmatrix} \tag{7}$$

Where

$$\begin{cases} A_{ij} = \sum_{k=1}^{n_f} (\overline{Q_{ij,f}})_k (h_k - h_{k-1}) + \sum_{l=1}^{n_m} (Q_{ij,m})_l (h_l - h_{l-1}), i, j = 1,2,6 \\ B_{ij} = \frac{1}{2}\left[\sum_{k=1}^{n_f} (\overline{Q_{ij,f}})_k (h_k^2 - h_{k-1}^2) + \sum_{l=1}^{n_m} (Q_{ij,m})_l (h_l^2 - h_{l-1}^2) \right], i, j = 1,2,6 \\ D_{ij} = \frac{1}{2}\left[\sum_{k=1}^{n_f} (\overline{Q_{ij,f}})_k (h_k^3 - h_{k-1}^3) + \sum_{l=1}^{n_m} (Q_{ij,m})_l (h_l^3 - h_{l-1}^3) \right], i, j = 1,2,6 \end{cases} \quad (8)$$

According to the test results, sort out the test data of the annular and axial specimens of the GRPM pipe, and get the average value of the compressive strength, as shown in Table 2 and 3.

Tab. 2 - Hoop compressive strength

Specimen	Length a （mm）	Width b （mm）	Height h （mm）	Ultimate load (kN)	Compressive strength Σ(MPa)	Failure displacement (mm)
HY1	50.68	46.97	149.97	120.98	50.82	3.06
HY2	50.84	47.06	145.38	121.94	50.97	2.96
HY3	51.30	47.06	148.93	118.65	49.14	3.08
HY4	51.26	47.11	147.45	119.18	49.35	3.00
HY5	50.85	47.21	148.27	118.54	49.38	3.04
Average value	50.99	47.08	148.00	119.86	49.93	3.13
Dispersion coefficient	0.54	0.19	1.17	1.47	1.77	3.96

Tab. 3 - Axial compressive strength

Specimen	Length a （mm）	Width b （mm）	Height h （mm）	Ultimate load (kN)	Compressive strength σ(MPa）	Failure displacement （mm）
ZY1	51.64	47.11	151.71	100.71	41.10	3.01
ZY2	51.10	47.36	151.52	98.23	40.59	3.00
ZY3	51.92	47.28	151.38	98.37	40.07	3.09
ZY4	51.68	47.14	151.08	99.02	40.64	2.92
ZY5	51.37	47.24	151.29	100.15	41.27	3.08
Average value	51.54	47.23	151.40	99.30	40.79	3.02
Dispersion coefficient	0.61	0.21	0.16	1.10	1.33	2.28

As shown in Table 3, the average hoop compressive strength and the average axial compressive strength of GRPM pipe are 49.93 MPa and 40.79 MPa respectively. The circumferential compressive strength is slightly higher than the axial compressive strength.

The ultimate compressive load of GRPM pipe material determined above, then the elastic modulus test should be carried out. The maximum loading amount of the elastic modulus test is 50% of the ultimate compressive load. For the same sample, one need repeat loading for three cycles, record the corresponding deformation and load, determine the elastic modulus according to the load, deformation and sample size, and take the average value of three loading and unloading cycle tests as the elastic modulus of each sample modulus.

The elastic modulus in the direction of hoop and axial are shown in Table 4 and 5.

Table 4 - Hoop modulus of elasticity

Specimen	Experimental data								Modulus of elasticity E (GPa)
HY1	Load (kN)	5	10	15	20	25	30	35	4.39
	Deformation (mm)	0.095	0.171	0.244	0.314	0.385	0.450	0.532	
HY2	Load (kN)	5	10	15	20	25	30	35	5.96
	Deformation (mm)	0.112	0.162	0.245	0.306	0.369	0.436	0.491	
HY3	Load (kN)	5	10	15	20	25	30	35	4.64
	Deformation (mm)	0.110	0.172	0.244	0.309	0.380	0.444	0.504	
HY4	Load (kN)	5	10	15	20	25	30	35	4.50
	Deformation (mm)	0.120	0.196	0.271	0.340	0.400	0.468	0.529	
HY5	Load (kN)	5	10	15	20	25	30	35	4.70
	Deformation (mm)	0.083	0.151	0.217	0.279	0.350	0.415	0.476	
	Average (GPa)		4.84		Dispersion coefficient		13.20		

As shown in Table 4, the average hoop modulus of elasticity measure from five specimens was 4.84 GPa, with dispersion coefficient of 13.20. It can also be seen in Table 4, the stiffness modulus at different degree of loads are much different in values, the comparative analysis can't be made directly using the stiffness modulus. In order to further explain the change rule between load and displacement, linear regression analysis is carried out for the data in the table, and the results are shown in the Figure 9.

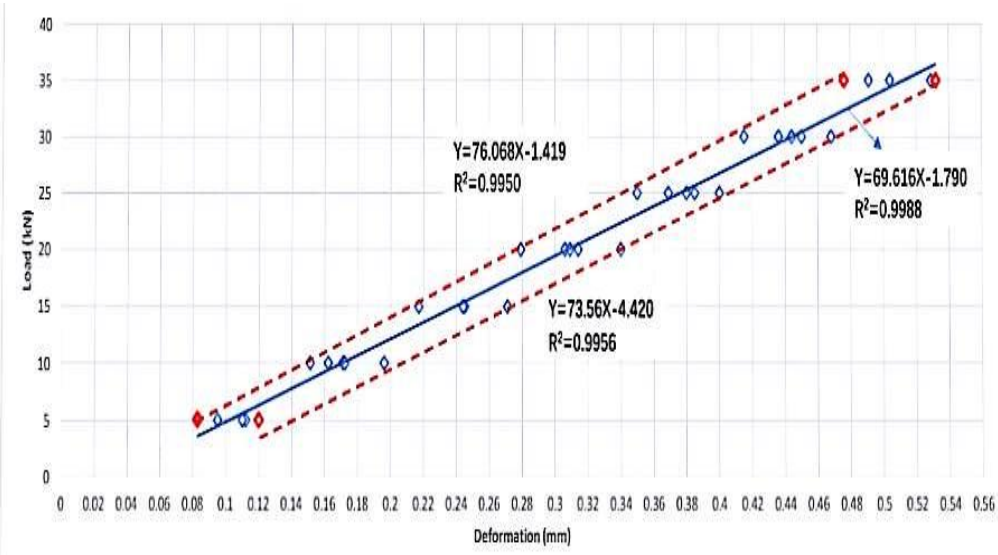

Fig.9 - Hoop elastic modulus

Tab. 5 - Axial modulus of elasticity

Specimen	Experimental data								Modulus of elasticity E (GPa)
ZY1	Load (kN)	5	10	15	20	25	30	35	3.74
	Deformation（mm）	0.130	0.251	0.356	0.468	0.570	0.697	0.823	
ZY2	Load (kN)	5	10	15	20	25	30	35	4.14
	Deformation（mm）	0.157	0.279	0.381	0.472	0.571	0.670	0.763	
ZY3	Load (kN)	5	10	15	20	25	30	35	4.04
	Deformation（mm）	0.117	0.220	0.320	0.415	0.510	0.626	0.730	
ZY4	Load (kN)	5	10	15	20	25	30	35	4.05
	Deformation（mm）	0.123	0.211	0.306	0.406	0.511	0.622	0.728	
ZY5	Load (kN)	5	10	15	20	25	30	35	4.24
	Deformation (mm)	0.106	0.194	0.279	0.375	0.473	0.571	0.684	
	Average (GPa)		4.04		Dispersion coefficient			6.16	

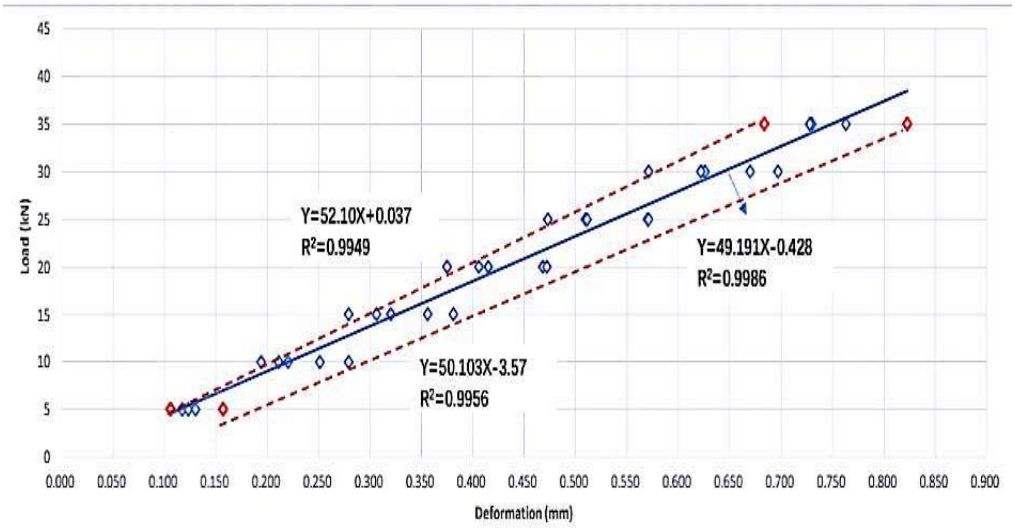

Fig.10 - Axial elastic modulus

As shown in Figure 9 and Figure 10, the optimal relation curve after fitting is drawn as a solid line. The hoop and axial deformation of specimen is changed linearly with loading, this trend agrees with the results obtained by R. Rafiee et al. [9].The hoop deformation-load curve slope of GRPM pipe is greater than of axial ,as the hoop elastic modulus are bigger than axial elastic modulus.

According to the above experimental results and analysis, it can be obtained that the hoop compressive strength of GRPM pipe is 42.66 MPa, the failure deformation is 3.59 mm, and the elastic modulus is 3.21 GPa; the axial compressive strength of GRPM pipe is 43.51 MPa, the failure deformation is 4.01mm, and the elastic modulus is 3.83 GPa; the hoop compressive strength of GRP fiber is 149.84 MPa, the failure deformation is 3.91mm, and the elastic modulus is 10.76 GPa; the glass fiber The compressive strength of glass fiber is 72.67 MPa, the failure deformation is 3.76 mm, and the elastic modulus is 4.82 GPa; the compressive strength of sand layer is 38.13 MPa, the failure deformation is 5.74 mm, and the elastic modulus is 1.79 GPa.

For the spiral wound GRPM pipe, the difference between the hoop and axial compressive strength and elastic modulus is not significant; the hoop compressive strength and elastic modulus of fiberglass are much larger than that of the axial; and the compressive strength and elastic modulus of the sand layer are relatively small.

CONCLUSION

GRPM pipe is a new composite material, the pipe wall is composed of layers in the thickness direction. According to this characteristic, the influence of each layer of GRPM pipe on the overall properties of the composite pipe is studied, and the compression tests of single material layer and composite material layer are carried out respectively. The conclusions are as follows:

For the spiral wound GRPM pipe, the values of circumferential and axial compressive strength are similar, but the circumferential elastic modulus is slightly larger than the axial elastic modulus. Due to the manual operation in the winding process, the uniformity of the material itself is poor, so the dispersion coefficient of the compressive strength results is slightly larger. Because the extensometer and displacement sensor of the test equipment cannot be used, the dial indicator used in the elastic modulus test is installed manually to level the sample for testing. Each sample is greatly affected by the human environment factors, and the instrument error leads to a large discrete coefficient of elastic modulus measurement but increasing the number of tests to take the average value can reduce the error of the test results.

From the failure state of the sample, it can be seen that the circumferential failure of the sample of the wound GRPM pipe is basically along the interface between layers, that is, the weak surface of the material of the wound GRPM pipe is generally the interface between layers, while the axial failure of the sample is more similar to the failure of the concrete sample, that is, along a certain sliding crack surface.

ACKNOWLEDGEMENTS

This work is supported by Natural Science Foundation of Hebei (E2019402395).

REFERENCES

[1] ASTM D 3517-96. Standard specification for ‘‘GRP’’ (glass-fiber-reinforced thermosetting-resin) pressure pipe. Philadelphia: American Society for Testing and Materials, 1996.

[2] Rafiee R, Reshadi F, Eidi S. Stochastic analysis of functional failure pressures in glass fiber reinforced polyester pipes[J]. Materials & Design, 2015, 67:422-427.

[3] JD. D. Melo et al. Mechanical behavior of GRP pressure pipes with addition of quartz sand filler. Journal of Composite Materials, vol. 45, 6: pp. 717-726.

[4] B. Jay Schrock, P.E., F.ASCE. Annulus Grouting of Slipliner Rehabilitation. Pipeline Division Specialty Conference 2001.

[5] Daniel IM and Ishai O. Engineering mechanics of composite materials. Oxford: Oxford University Press, 2006.

[6] ASTM D 3754-96. Standard specification for ‘‘GRP’’ (glass-fiber-reinforced thermosetting-resin) sewer and industrial pressure pipe. Philadelphia: American Society for Testing and Materials, 1996.

[7] ASTM D 3262-96. Standard specification for ‘‘GRP’’ (glass-fiber-reinforced thermosetting-resin) sewer pipe. Philadelphia: American Society for Testing and Materials, 1996.

[8] ANSI/AWWA C950. Standard for GRP pressure pipe. Denver: American Water Works Association, 2001.

[9] ASTM D 2412-02. Standard test method for determination of external loading characteristics of plastic pipe by parallel-plate loading. Philadelphia: American Society for Testing and Materials, 2002.

[10] Shi Huawang, Wei Lianyu. Laboratory Evaluation on Performance of Glass Fiber Reinforced Plastic Mortar Pipe Culverts. Civil Engineering Journal,2018,27(1):60-71.

[11] Roham Rafiee , Ali Amini. Modeling and experimental evaluation of functional failure pressures in glass fiber reinforced polyester pipe[J].Computational Materials Science, 2015 ,23(96):579-588.

CIVIL ENGINEERING JOURNAL

Article no. 5

THE CIVIL ENGINEERING JOURNAL 1-2022

HIGH AIR-VOID VOLUME IMPLICATIONS FOR ASPHALT CONCRETE SERVICE-LIFE AND PRICE PENALTY

Reus Salini[1] and Carl Anders Lenngren[2]

1. *Neogennium, Brasília, Brazil; salini@neogennium.com*
2. *AFRY, Stockholm, Sweden; Lenngrensbox@telia.com*

ABSTRACT

In road industry, the construction of asphalt concrete layers is a dynamic process that, if not properly done, will lead to problems compromising the pavement performance. One of the most common problems is poor compaction leading to air-void volume above the maximum acceptable. This study discusses the impact of compaction/density deficiencies and presents an innovative model to calculate the asphalt pavement service-life loss in a simple and objective way, and in line with the road construction managers needs to calculate price penalty for contractors. The model was optimized for dense graded asphalt concrete, that typically has a maximum acceptable air-void volume between 4% and 7%.

KEYWORDS

Asphalt Concrete, Density, Air-Void Volume, Service-Life, Modelling, Contract, Penalty

INTRODUCTION

Asphalt pavements constitute a critical factor for road transportation infrastructure worldwide. Its long-term cost is continuously rising with the increasing of prices of its components, especially bitumen, gravel and labor.

The density is one of the most important parameters in construction of asphalt concrete (AC) layers and its proportion of air-voids is probably the single most important factor that affects performance and service-life for asphalt pavements; thus the compaction is an important factor that affects pavement performance in terms of durability, fatigue life, resistance to deformation (rutting), strength and moisture damage [1] [2].

The failure in obtaining the required density for AC layers is a rather common problem and requires a scheme for evaluating the loss in service-life and an appropriate price reduction penalty for contractors. There are surprisingly few studies or consolidated technical procedures to evaluate the impact in the pavement performance or how to calculate a suitable price penalty for those cases. Hence, in lieu of guiding documents unnecessary and painful negotiations between transportation agencies and contractors are frequent.

The present study is a practical and objective approach to calculate the service-life loss for dense graded asphalt concrete caused by deficiency in too low density, that is, air-void volume higher than the maximum specified in the applicable standards or as contracted. The reduced life can then be used as a parameter to specify contract penalties.

DOI 10.14311/CEJ.2022.01.0005

LITERATURE REVIEW

A review of available studies conducted in 2016 at the National Center for Asphalt Technology (NCAT), on the densification/compaction of AC and its implications for durability and service-life, found 5 studies citing fatigue service-life implications and 7 studies citing rutting. In general terms, this literature review found that an 1% decrease in air-voids was estimated to improve the fatigue performance of asphalt pavements between 8.2% and 43.8%, to improve the rutting resistance by 7.3 to 66.3%, and to extend the service-life by conservatively 10%. Based on these results, NCAT conducted a life-cycle cost analysis (LCCA) for AC with two alternatives of density, 92% and 93%. The LCCA results show that the user agency would see a net-present-value cost savings of $88,000 on a $1,000,000 paving project (or 8.8%) by increasing the minimum required density by 1%. Higher AC density also has impacts on road operation, maintenance and road users' cost [3].

In Australia, the Pavement Work Tips No.17 published the results of an interesting study where an asphalt concrete mixture with different air-void volumes was tested. It shows the increasing of air-voids from 5% to 8% leads to fatigue life reduction of about 50% (Fig. 1), a reduction of AC modulus by 20% (Fig. 2) and an increase of about 75% in rutting depth (Fig. 3) [4].

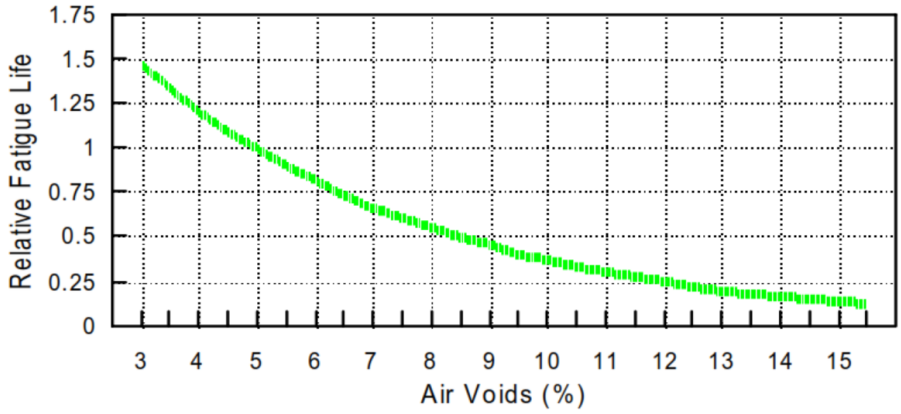

Fig. 1 – Fatigue life versus air-voids for asphalt concrete [4]

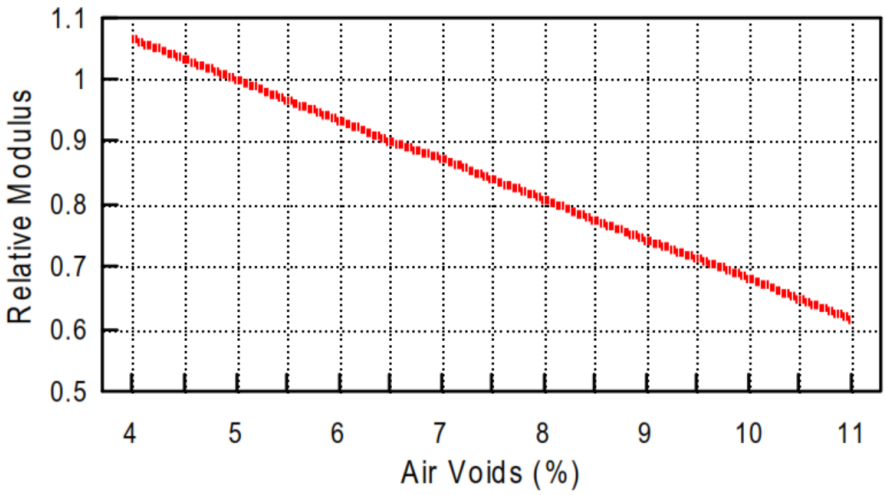

Fig. 2 – Relative modulus versus air-voids for asphalt concrete [4]

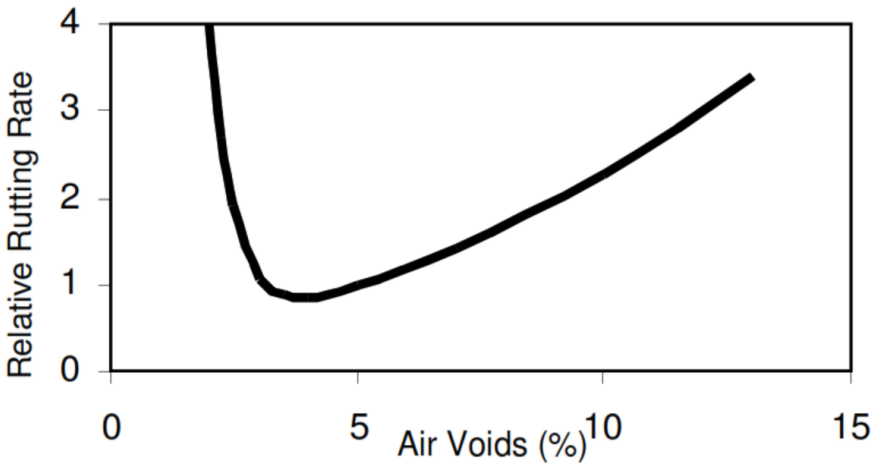

Fig. 3 – Relative rutting versus air-voids for asphalt concrete [4]

In United States, the Kentucky Transportation Center (KTC) conducted a research to identify factors affecting the asphalt concrete density and its influence on long term pavement performance. It was found that reducing the air-voids from 11% to 7% leads to an increase of 50% in fatigue life [5].

A summary of studies showing the impact of 1% increase in air-voids for was presented by Aschenbrener at the FHWA Asphalt Mixture - Expert Task Group meeting in 2016 [6]. It shows a reduction in AC fatigue life between 8.2% and 43.8% (Tab. 1) and an increasing in rutting depth between 7.3% and 66.3% (Tab. 2).

Tab. 1 - Fatigue life versus air-void volume [6]

Study	Lab/field	Mix type	Air-voids evaluated	Reduction in fatigue life for 1% air-voids increase
UC Berkeley (1969)	Lab	British Std	4 - 14%	20.6%
		CA Fine	5 - 8%	43.8%
		CA Coarse	2.5 – 7%	33.8%
UCB (1996)	Lab	CA Dense Graded	1 - 3%	15.1%
			4 - 6%	
			7 - 9%	
WesTrack (2002)	Lab	Fine	4, 8, 12%	13.5%
		Fine-Plus		13.3%
		Coarse		9.0%
	Field	Fine/Fine-Plus		21.3%
		Coarse		8.2%
AI (2010)	Lab	9.5 mm Dense	4 – 11.5%	9.2%

Tab. 2 - Fatigue life versus air-void volume [6]

Study	Lab/field	Mix type	Air-voids evaluated	Final field ruth depth (mm)	Increase in ruth depth for 1% air-voids increase
WesTrack (2002)	Field	Fine/Fine-Plus	4, 8, 12%	9 - 35	11.5%
		Original Coarse		13 - 36	9.6%
		Replacement Coarse		12 - 26	66.3%
		Fine/Fine-Plus/Coarse		9 - 36	7.3%
		Replacement Coarse		12 - 26	10.9%
AI (2010)	Lab	9.5 mm Dense-Graded	4 – 11.5%	N/A	22.7%

In 2015 Wang and others developed a procedure based on life-cycle cost analysis (LCCA), for price reduction for in-place air-void of asphalt pavements, using data of projects constructed in New Jersey from 1995 to 2005 and pavement condition index (PCI) extracted from the pavement management system. Empirical pavement performance models were developed with sigmoidal functions and Monte Carlo simulations were used to capture the uncertainty of overlay service-life. This is a quite complex approach where the price reduction may be affected by the considered maintenance strategy and other variables [7].

In 1989 Linden and others [8] published the "*Effect of Compaction on Asphalt Concrete Performance*" with the results of an extensive research to evaluate the loss of service-life of dense graded asphalt concrete due to air-voids. The study comprised three data-sets, (1) from a literature review, (2) a robust research at the American State Highway Agencies (SHA) and (3) data from the Washington State Pavement Management System (WSPMS). According to the authors "*the rule-of-thumb that emerges is that each 1 percent increase in air-voids (over a base air-void level of 7 percent) results in about a 10 percent loss in pavement life*". The conclusions of this research are suitable only for the cases where the maximum acceptable air-void volume base-line is 7%; for all other cases such a rule can be subject of discussions and disputes [8].

AIR-VOID VOLUME MEASUREMENT AND CALCULATION

The required air-void volume usually is specified in contracts or standards as an envelope, with minimum and maximum acceptable characteristic values. For example: minimum characteristic air-voids = 2%, and maximum characteristic air-voids = 6%.

The way the characteristic air-void volume is calculated is another important aspect to be considered. The voids are usually measured in extracted cores or with nuclear densometer, that is an evaluation by sampling. Given such sampling nature the results must be evaluated from a statistical perspective, for every constructed pavement lot. At Fiji Roads Authority, for example, the way the characteristic values are calculated is specified at the standard FRA 5100:2020 considering the available number of measurements/cores, the standard deviation and the producer risk [9]. Other agencies usually adopt similar procedures.

MODEL DEVELOPMENT

In an ideal world all AC layers will be constructed with the air-voids inside the required envelope, but this frequently does not happen, forcing project managers and contractors to negotiate a price reduction. Despite to be an important problem, surprisingly there are almost no studies

proposing technical parameters for price reduction that are easy to implement and also reflect the true cost for the loss of the predicted life.

In the present study an innovative model to calculate the AC service-life loss for any air-void requirement in the typical range of dense graded AC (4% to 7%) is presented. This model can also be used as a parameter for price reduction. The model was constructed by performing a reanalysis of two data-sets synthesis, literature review and SHA survey (Tab. 3), originally published by Linden and others [8], that are considered the ground truth. This generalized model allows to by-pass the limitation of the original authors' conclusion, that have a fixed base-line of 7% for air-voids.

The base data (Tab. 3) was plotted and a power trendline equation was calculated (Fig. 4). The trendline equation was then used as basis for engineering an adaptative mathematical formula by doing intensive computer-based simulations. The final developed and optimized model is presented in Eq. 1. It has three components and considers the life loss at the constructed air-void volume (Eq. 2.a), the theoretical life loss at the maximum acceptable air-void volume (Eq. 2.b) and an adjusting component (Eq. 2.c) that was optimized to improve the model's accuracy. The adjusting component (Eq. 2.c) was constructed in a way that keeps the model's mathematical consistency, showing service-life loss equal to zero (L = 0) when the contracted and constructed air-voids are equal (A = B). To evaluate the model's performance, its predictions compared the base data are shown in Fig. 5.

The situations where the model is needed and can successfully be used are shown in Tab. 4. It is important to mention the model is not suitable to evaluate the pavement service-life loss resulting of constructed characteristic air-void volume smaller than the minimum acceptable; for those cases other procedures must be used.

Tab. 3 – Base data for model's development [8]

Source	Air-void volume (%)	Pavement life reduction (%)
Literature review [8]	8	10
	9	20
	10	30
	11	40
	12	50
SHA Survey [8]	7	7
	8	13
	9	21
	10	27
	11	38
	12	46

$$\boldsymbol{L = \left(0.00663 \cdot B^{3.61035}\right) - \left(0.00663 \cdot A^{3.61035}\right) + \left[\left(\frac{B}{A}\right)^{2.15} - 1\right]}$$

Where:

A: Maximum acceptable air-void volume according to the applicable standard or contract (%)

B: Air-void volume of the constructed asphalt concrete (%)

L: Asphalt concrete service-life loss (%)

Eq. 1 – Model to calculate the service-life loss for dense graded asphalt concrete

Tab. 4 – Scenarios where the model is valid and/or needed

Scenario	Interpretation
B > A	the model is suitable to calculate service-life loss and price penalty
B = A	the model will report service-life loss equal to zero
L ≥ 100	the AC pavement will have a marginal service-life only
B ≤ A	there is no service-life loss because of air-void volume (model's calculation is not needed)
B is smaller than the minimum acceptable characteristic air-void volume	this model is unsuitable

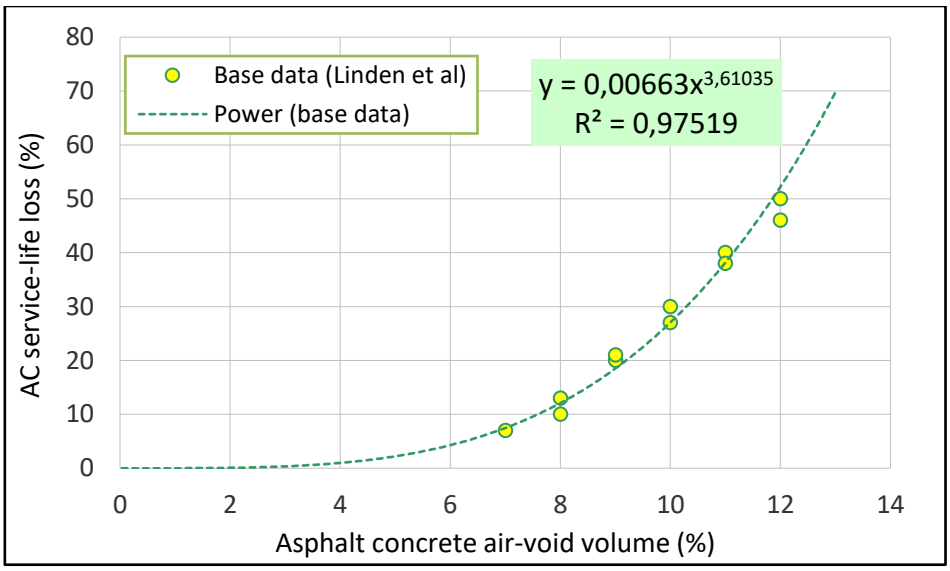

Fig. 4 – Asphalt concrete service-life loss according to the air-void volume

$$L = \underbrace{(0.00663 \cdot B^{3.61035})}_{\text{a}} - \underbrace{(0.00663 \cdot A^{3.61035})}_{\text{b}} + \underbrace{\left[\left(\frac{B}{A}\right)^{2.15} - 1\right]}_{\text{c}}$$

Eq. 2 – Components of the engineered model

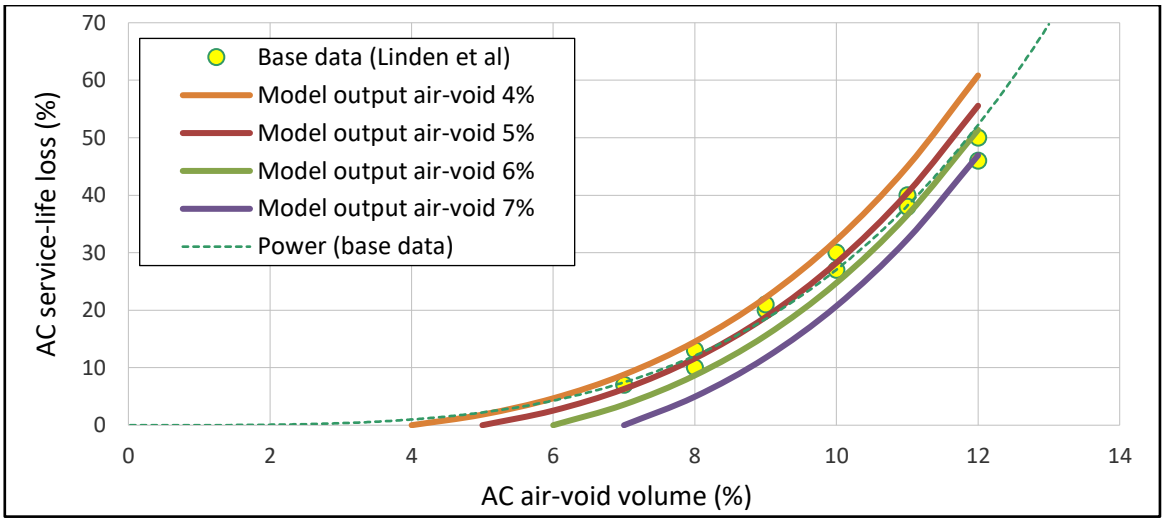

Fig. 5 – Base data versus model output (Eq. 1) for maximum allowed air-void volume of 4% to 7%

EXAMPLE OF SERVICE-LIFE LOSS CALCULATION AND PRICE PENALTY

In this example is considered a contract rate of \$100.00/m^2 for the AC meeting the contract requirement of a maximum characteristic of air-void volume of 6%, but the constructed pavement was found with a characteristic air-void volume of 8%, for the analyzed construction lot. (This example does not consider other problems that eventually are present, such as bitumen content outside the required range, aggregate grading outside the envelope, AC thickness smaller than contracted, and others.)

A = 6

B = 8

Eq. 1:

$$L = \left(0.00663 \cdot 8^{3.61035}\right) - \left(0.00663 \cdot 6^{3.61035}\right) + \left[\left(\frac{8}{6}\right)^{2.15} - 1\right]$$

$$L = 8.66$$

Conclusion: the asphalt concrete lost 8.66% of its expected service-life. Remaining service-life is 91.34%.

Price penalty

Rate for AC with maximum characteristic air-void volume of 6%:	\$ 100.00/m^2
Penalty because of constructed air-void volume is 8%:	8.66%
Rate to be paid for AC after penalty:	\$ 91.34/m^2

CONCLUSION

A consensus exists among researchers and departments of transportation regarding the negative impact of high air-void volumes on the asphalt concrete service-life and, for road construction projects, the need to apply a price penalty for contractors. The existing studies on the subject are few and usually don't provide an objective and practical way to evaluate the impact of excessive air-voids on the pavement performance nor calculate a price penalty.

The developed model can be used with success to calculate the service-life loss of dense graded asphalt concrete resulting of air-void volume above the maximum allowed by contracts or standards, and to calculate contract price penalties for such cases.

The mode is not suitable for cases where the constructed AC has air-void volume lower than the minimum acceptable, and does not consider other problems that may be present in the same pavement, such as bitumen content outside the required range, aggregate grading outside the envelope, AC thickness smaller than contracted, and others that also affect the service-life and may lead to price penalties.

REFERENCE

[1] Brown, E.R. (1990) Density of Asphalt Concrete - How Much is Needed? in: 69th Annu. Meet. Transp. Res. Board, Washington, D.C., USA.

[2] Hughes, C.S. (1989) Synthesis of Highway Practice 152 - Compaction of Asphalt Pavement. Washington, D.C., USA.

[3] Tran, N., Turner, P., and Shambley, J. (2016) NCAT REPORT 16-02 - Enhanced Compaction to Improve Durability and Extend Pavement Service life: A Literature Review. Auburn, Alabama, USA.

[4] Austroads & AAPA (n.d.) Pavement Work Tips No. 17. 2.

[5] Fisher, J., Graves, C., Blankenship, P., Hakimzadeh-Khoee, S., and Anderson, R.M. (2010) Factors Affecting Asphalt Pavement Density and the Effect on Long Term Pavement Performance - Research Report KTC-10-05/RSF14-05-1F. USA.

[6] Aschenbrener, T. (2016) Enhanced Durability Through Increased In-Place Pavement Density. in: FHWA Asph. Mix. Expert Task Gr. Meet., USA.

[7] Wang, H., Wang, Z., Blight, R.J., and Sheehy, E.C. (2015) Derivation of pay adjustment for in-place air void of asphalt pavement from life-cycle cost analysis. *Road Materials and Pavement Design*. 16 (3), 505–517.

[8] Linden, R.N., Mahoney, J.P., and Jackson, N.C. (1989) Effect of Compaction on Asphalt Concrete Performance. *Transportation Research Record 1217*. 20–18.

[9] Fiji Roads Authority (2020) FRA 5100:2020 CALCULATION OF CHARACTERISTIC VALUES BASED ON STATISTICAL ANALYSIS. 4.

CIVIL ENGINEERING JOURNAL

Article no. 6

THE CIVIL ENGINEERING JOURNAL 1-2022

ANALYSIS ON INFLUENCING FACTOR OF COST CONTROL OF EPC PROJECT BASED ON THE DEMATEL-ISM

Li Lin

Chengde Petroleum College, Department of Construction Engineering, Shuangqiao District, Chengde City, China; lihonglin19880501@163.com

ABSTRACT

The paper selects the influencing factors of EPC project's cost control，analyzes and builds the model of EPC project's cost control from the point of view of system engineering，and utilizes the integrating DEMATEL—ISM method to study the relationships between the influencing factors and their impacts on cost control. It gets the multilevel structure model of the influencing factors of EPC project's cost control. The results show that project construction management level, procurement system, procurement process and standards project content acceptance and project settlement basis are the direct impacting factors of EPC project's cost control. The study provides a reference of EPC project's enterprises to improve project management level, effectively control project cost and achieve project management objectives.

KEYWORDS

EPC Project, Cost Control, Influencing Factors, DEMATEL Method, ISM Method

INTRODUCTION

With the rapid development of Chinese national economy, EPC (Engineering Procurement Construction) projects are widely used in various fields and become a new construction mode of construction project. EPC mode integrates design, construction and procurement. The coordination between various disciplines is strengthened, and the disadvantages of disconnection between design and budget, design and construction are overcome, which is conducive to the realization of the overall goal of the project [1]. But it also brings huge risks to the general contractor, especially in cost control.

At present, many scholars at home and abroad have studied the cost control of EPC project, Zeng Xiang pointed out that project managers need to strengthen cost management in the links of design, construction, acceptance and completion, so as to effectively control the capital investment of the project and ensure the smooth completion of the project [2]. Yuan Yamin elaborated the risks existing in the cost of EPC project. Combined with the current situation of EPC project, she proposed to take effective measures to prevent the cost risk from four aspects [3]. Based on practical cases, Ye Zhaoping and his colleagues put forward the importance of material and equipment procurement cost control, and strictly controlled it from the procurement link, so as to improve the project efficiency [4]. By comparing the EPC project mode with the traditional

contracting mode, Shu Jianping put forward the advantages and disadvantages of the EPC project mode, he also put forward the effective management of EPC project cost from multiple angles, so as to improve the economic benefits of enterprises [5]. On the basis of practical engineering cases, Wu Zhuxu put forward the key points [6] of project cost control under the EPC mode of construction projects, and expounded the specific application in cost control.

With the development of EPC projects in foreign countries increasingly mature, foreign scholars on EPC project research is more and more in-depth. The PCA's Report 1/2016 raised several issues [7]. The most impressing problems mentioned in the 2016 Report were:

（1）Contract changes were being reported in public works contracts in just under 50% of the awarded contracts;

（2）In the total projects analyzed, there was, on average, an increase in contract costs of around 6.75%[8];

（3）Design alterations and modifications were a recurring pattern, especially in building retrofitting projects;

（4）Modifications occurred especially in architectural designs and water supply and sewage project designs;

（5）Deficiencies in the project design were present in 57% of all projects analyzed;

Jan Pícha, Aleš Tomek, Harry Löwitt put forward that necessary and good contract management [9] plays a good role in promoting the development of EPC; otherwise, it would have a negative impact on all relevant parties--customers, contractors, lenders, governments, etc. Once the management of the contract was not in place, it would have a negative impact on the whole project, which may include delayed schedule, cost overruns, quality, safety and so on. Mary Bajomo, Akinola Ogbeyemi, Wenjun Zhang believed that material procurement management and material transportation logistics [10] played an important role in EPC project construction, and EPC projects often encountered problems such as cost overrun, schedule overrun, material supply delay and production efficiency decline in the management process. To overcome these problems and realize the sustainable development of EPC system, it was necessary to conduct in-depth research on the procurement of building materials. Johnny Kwok Wai Wong, Jackson Kit San Chan, Mesthrige Jayantha Wadu put forward his own views on promoting the better development of architecture. Through questionnaires and interviews with experts, he explored the important role of procurement [11] in the construction industry and put forward some factors affecting procurement. Through the analysis of the potential influencing factors, it was pointed out that how to effectively promote the healthy development of the construction industry by using the procurement link.

Procurement is a key process in construction project management. Paying more attention to procurement is crucial to the sustainable development of construction projects. Rajeev Ruparathna, Kasun Hewage believed that adopting sustainable procurement measures [12] was very necessary in construction projects and played an important role in promoting the development of construction projects. Research showed that government regulations was the main driver for sustainable procurement.

By analyzing real cases and from the perspective of engineering design, Manman Xia, Lemeng Zhao, and Li Zhao found that construction and design could bring potential risks to EPC projects, and strengthening the management of these two links laid a foundation for the realization of project

objectives [13]. For EPC projects in the oil and gas industry, how to help general contractors to effectively manage the cost and schedule of EPC projects, Myung-hun Kim, Eul-bum Lee, and han-suk Choi believed that it was necessary to start at the design stage. Identify the factors that influenced project management during the design phase to help the general contractor reduce risk and achieve the stated objectives [14]. Pan Gong, Ningshuang Zeng, Kunhui Ye and Markus Konig proposed to use 4D BIM technology to solve the problems in the construction and completion acceptance stages of EPC projects. Reduce the impact of various influencing factors on cost and schedule management [15].

Through the analysis, induction and summary of the above research results, it is found that most of the above research contents focus on a certain link, only propose improvement measures for a certain link, do not comprehensively consider the factors affecting EPC project cost control, and lack a set of models and methods that can evaluate and analyze the influencing factors of EPC project cost control. In view of this, the cost control of EPC project will be discussed from the perspective of system engineering, and the influencing factors of cost control will be analyzed by using integrated laboratory decision analysis method (DEMATEL) and interpretative structure model (ISM). It is expected to provide a theoretical basis for EPC project enterprises to reduce engineering costs and improve economic benefits.

The remaining sections of this paper are organized as follows. Section 2 collects the factors that significantly influence the EPC project's cost control. Section 3 applies the DEMATEL-ISM method to the classification and importance analysis of the influencing factors, then obtains the multi-level hierarchical structure model and finally analyses the different levels according to the influencing factors, demonstrating the interrelationships among the influential factors. Based on the result of Section 3, in-depth analysis and effective suggestion on the interrelationships and prioritization of the involved influential factors are provided in Section 4. Finally, in Section 5, the conclusion, limitation and future researches of the study is presented.

SELECT THE INFLUENCING FACTORS OF EPC PROJECT COST CONTROL

Aiming at the problems that the cost amount of EPC project far exceeds the expected cost target and leads to the decline of project economic benefits. Summarize the influencing factors of cost control involved in the existing research [16]. The above influencing factors are tested by questionnaire survey, and experts and scholars with rich experience in the field of EPC project are invited to score. The contents of the questionnaire were evaluated by Likert scale's 5-point system. A total of 145 questionnaires were issued and 122 were recovered. Among them, 110 valid questionnaires were tested by SPSS 24.0 software（IBM SPSS Statistics24.0 is launched in August 2016 by IBM Corporation, which is located in the City of Chicago, the United States）Cronbach's α is equal to 0.854, greater than 0.7, with good reliability, indicating that the data has high reliability. Because the implementation of EPC project is based on the contract signed by both parties. In the process of project implementation, according to the development progress of the project can be divided into design, procurement, construction, completion and other stages, and the cost control of the project mainly involves the above stages, but also need to consider the impact of external environmental factors. Finally, according to the development of the EPC project, it is determined to

identify the influencing factors of EPC project cost control from six dimensions: contract factors, design factors, construction factors, procurement factors, completion acceptance factors and external environmental factors. The sub-factors of each influencing factor are ranked according to the scores of experts and scholars in the questionnaire survey, and the score represents the importance of the factor, as shown in Table 1.

Tab.1 - Influencing Factors and Literature Sources of EPC project's Cost Control

Partition dimension	Influencing Factors(*M*)
Contract Factors	Formulation of Contract Terms (M_1)
	Contract Bidding Management (M_2)
	Division of Contract Responsibility (M_3)
Design Factors	Selection of Design Unit (M_4)
	Rationality of Design Scheme (M_5)
	Cost Control Consciousness of Design Unit (M_6)
Construction Factors	Selection of Construction Scheme (M_7)
	Project Construction Management Level (M_8)
	Engineering Change and Claim (M_9)
Procurement Factors	Procurement Method (M_{10})
	Procurement System (M_{11})
	Procurement Process and Standards (M_{12})
Completion Acceptance Factors	Acceptance of Changed Data (M_{13})
	Acceptance of Project Contents (M_{14})
	Price Settlement Basis (M_{15})
External Environmental Factors	National Policies and Regulations (M_{16})
	Market Price of Manual Work, Material and Machine (M_{17})
	Development Level of Science and Technology (M_{18})

Construction projects were complex with regard to variety of works, budget, duration, and the number of parties involved[17].The use of time, cost, and quality as critical success factors of construction projects for the purpose of construction project performance evaluation have widely been studied by several researchers [18], however, there was great need to understand these critical success factors with regard to EPC phases of the construction projects and to identify and prioritize the factors that could affect critical success factors of the project in the different stages of EPC and affect project performance[19].

Contract Factors

（1）Formulation of contract terms

The formulation of contract terms includes the ownership of the project, the delivery time of the project, quality assurance, inspection methods, conformity standards, the treatment of force majeure factors, as well as the procurement method of materials, including the quality, quantity, specifications and price of materials, etc.

（2）Contract bidding management

Bidding is a part of the contract content, but also a very important part of project construction quality and cost control. The specific contents of contract bidding management include separate bidding plans for projects, construction equipment and construction materials. Combined with the actual situation of the project construction to choose public bidding or bid negotiation and other ways to determine the bidding and bidding time, process, in addition to the bidding enterprise construction qualification and enterprise reputation evaluation.

（3）Division of contract responsibility

In EPC mode, the division of contract responsibility should be reflected in the signed contract documents. For example, in the process of project implementation, due to the limitation of construction technology, the design must be changed, and the impact on the project cost should be made clear in the contract, so as to avoid possible conflicts of interest between the contractor and the owner.

Design Factors

（1）Selection of design unit

Selection of design units is an important step in the design stage, which mainly determines the selection method, bidding process and evaluation standards of design units. Meanwhile, it also needs to inspect the qualification of design units, their familiarity with EPC project fields and their concept of design projects. Design units are selected based on the above factors.

（2）Rationality of design scheme

The rationality of the design scheme should be combined with the actual situation of the project, comprehensively considering the scale, construction intention, function, use and other factors of the project, and should also consider the total investment of the project, under the premise of safety, rationality and economy, to ensure that the design scheme meets the requirements of the project.

（3）Cost control consciousness of design unit

The consciousness of unit cost control is mainly reflected in the quota design of the project. Quota design includes the following aspects: first, the rationality of professional allocation, construction drawing design and budget synchronous, technology and economy combined to meet the requirements of the project; Second, the implementation of reward and punishment measures to strengthen the cost control consciousness of designers.

Construction Factors

（1）Selection of construction scheme

According to the structural characteristics of the project, the project scale and other factors, the construction content can be decomposed into the main civil engineering, decoration engineering,

power supply and distribution engineering. Construction scheme is for a specific construction content of the construction planning to achieve the construction goal, the selection of construction scheme needs to consider the construction process, construction section division, construction sequence arrangement, construction process and other factors, so as to determine the best construction scheme.

（2）Project construction management level

The construction management level of EPC projects is mainly reflected in the following aspects: First, control the extent of the project progress and rational allocation and use of funds. Second, to establish the project manager responsibility system as the core of the management system, organization and launch enterprise management, project management, project operation layer and other levels actively participate in the construction project management activities, to achieve the whole process of all-round management. Third, according to the development of the general construction scheme, construction method for construction, reasonable arrangement of construction strength, machinery and deployment. The use and maintenance of all kinds of equipment and maintenance responsibility gradually clear, implement to people, reduce the wear and tear of equipment improper operation.

（3）Engineering change and claim

Engineering change and claim is a common phenomenon in the construction stage. Engineering change is mainly reflected in two aspects, one is design change, the design is unreasonable or there is conflict with the construction process need to be changed, the other is the owner temporarily change the intention of the project, change the current project design. The claim is due to the external environment, drawing changes and other factors, the contractor requires the Owner to compensate in terms of economy and time limit.

Procurement Factors

（1）Procurement method

Scientific and reasonable procurement methods can effectively reduce the cost input of EPC project materials procurement. Currently, there are mainly the following procurement methods. The first is bidding procurement, which is generally used in some EPC projects that need to purchase a large number of construction materials and equipment. The second is to adopt the way of inquiring price procurement. Inquiring price procurement refers to inquiring about the price of materials and equipment required by the project from the supplier, comparing these quotations with several suppliers, and finally selecting a supplier with the most reasonable price and relatively good quality to sign the contract. The third is direct procurement, which is usually used only in the case of designated suppliers or special materials and equipment. The specific procurement method needs to be combined with the actual situation of the project.

（2）Procurement system

The procurement system includes formulating standardized procurement procedures and

standards and assigning procurement responsibilities for equipment and materials to departments and individuals. Procurement system requires every link, every post to do a good job of coordination, clear division of labor, and materials and equipment in and out of storage management.

（3）Procurement process and standards

Procurement process and standards include the following aspects, the first is the formulation of the procurement plan, according to the construction process and characteristics of the procurement plan to determine the content, the correct grasp of the quantity and quality of material procurement; The second is to compare the price of materials given by different suppliers, including the quality of materials, the price of materials, purchase concessions and transportation costs.

Completion Acceptance Factors

（1）Acceptance of changed data

The acceptance of changed data mainly includes the following aspects: first, the acceptance of the contents of the modification documents and the signature of each participant; the second is the acceptance of the drawings of the changed parts, and the third is the inspection of the field record of the number of manual work, material and machine consumed when the change occurs; the fourth is related to the demolition of completed projects, acceptance of recyclable equipment and materials record form.

（2）Acceptance of project contents

The acceptance of the project content is mainly to examine and accept the location, elevation and axis of the building to meet the design requirements. Check the data of foundation engineering, structural engineering and other engineering, and also need to check the equipment installation engineering, process equipment installation engineering, check whether the specification, model and quantity of equipment meet the design requirements.

（3）Price settlement basis

Price settlement basis shall be based on contract terms, national pricing specifications, construction contracts, as-built drawings and materials, quantities confirmed by both parties, additional (less) project price confirmed by both parties, claims confirmed by both parties, on-site visa matters and price, bidding documents and other evidence.

External Environmental Factors

（1）National policies and regulations

National policies and regulations play an important role in promoting the healthy and orderly development of EPC projects. National policies and regulations include a series of policies issued to promote the implementation of EPC projects, such as preferential policies for EPC general contractors, qualification requirements of general contractors, responsibilities of general contractors, and responsibilities and obligations of participating units

（2）Market price of manual work, material and machine

The market price of manual work, material and machine is easily affected by the external environment, which directly affects the project cost. The market price of manual work, material and machine includes the market price of manual work, the market price of materials and the market price of machine. The market price of manual work refers to the cost of construction workers and auxiliary production workers. The market price of manual work, material includes cement, steel, sand and other building materials. The market price of machine mainly refers to the use fee of machinery and the rental fee paid by the leased machinery.

（3）Development level of science and technology

The development level of science and technology includes the use of new building materials, new construction technology and the use of information technology, such as BIM technology and procurement management system. The application of BIM technology in the construction stage can effectively manage the construction process and reduce the impact of various influencing factors on cost and schedule management. Procurement management system to the procurement stage of the whole process of supervision and management, reduce procurement links caused by the increase in project costs.

BUILDING THE INFLUENCING FACTOR MODEL OF EPC PROJECT COST CONTROL BASED ON DEMATEL-ISM

Based on the above selected influencing factors of EPC project cost control, this paper uses DEMATEL method to analyze the importance of the above EPC project cost control factors. On this basis, the hierarchical structure model of the influencing factors of EPC project cost control is constructed by using ISM model, the hierarchical relationship between various influencing factors is analyzed. The process of model analysis and construction is as follows:

Establish the Direct Influence Matrix

Record the influencing factors of EPC project cost control as M={M_1，M_2，…，M_{18}}, The relationship between M_i（i =1，2，…，18）and M_j（j=1，2，…，18）is expressed as b_{ij}, Use 0, 1, 2 and 3 to represent the influence intensity of factor M_i on M_j . It means:

$$b_{ij}=\begin{cases}0 & no\ \ impact\\ 1 & weak\ \ impact\\ 2 & medium\ \ impact\\ 3 & strong\ \ impact\end{cases} \tag{1}$$

The direct influence matrix A of influencing factors of EPC project cost control can be obtained:

$$A=\begin{bmatrix} b_{11} & b_{12} & \cdots & b_{1j} \\ b_{21} & b_{22} & \cdots & b_{2j} \\ \vdots & \vdots & \vdots & \vdots \\ b_{i1} & b_{i2} & \vdots & b_{ij} \end{bmatrix} \quad (2)$$

An expert discussion group is established according to the 18 influencing factors in Table 1. The members of the group include 12 from the building unit, 10 from the general contractor, 12 from the design unit, 10 from the construction unit, 10 from the procurement department and 11 teachers studying EPC projects in colleges and universities. From the perspective of achieving EPC project management objectives, the relationship between the influencing factors of EPC project cost control is discussed and finally an agreement is reached, so as to establish a direct matrix A of the influencing factors of EPC project cost control. $A=\left(b_{ij}\right)_{18\times18}$ is shown as below:

$$A=\begin{bmatrix}
0&1&3&0&0&0&0&0&0&0&0&0&0&0&0&0&0&0\\
0&0&0&0&0&0&0&0&2&0&0&0&0&0&2&0&0&0\\
0&0&0&0&0&0&0&0&3&0&0&0&0&0&0&0&0&0\\
0&0&0&0&3&2&0&0&1&0&0&0&0&0&1&0&0&0\\
0&0&0&0&0&0&3&2&3&0&0&0&0&0&0&0&0&0\\
0&0&0&0&3&0&0&0&0&0&0&0&0&0&0&0&0&0\\
0&0&0&0&0&0&0&3&0&0&0&0&0&0&0&0&0&0\\
0&0&0&0&0&0&0&0&0&0&0&0&0&0&0&0&0&0\\
0&0&0&0&0&0&0&3&0&0&0&0&0&2&1&0&0&0\\
0&0&0&0&0&0&0&0&0&0&0&2&0&0&0&0&0&0\\
0&0&0&0&0&0&0&0&1&0&0&1&0&0&0&0&0&0\\
0&0&0&0&0&0&0&1&0&0&0&0&0&0&0&0&0&0\\
0&0&0&0&0&0&0&0&0&0&0&0&0&0&3&0&0&0\\
0&0&0&0&0&0&0&0&0&0&0&0&0&0&1&0&0&0\\
0&0&0&0&0&0&0&0&0&0&0&0&1&1&0&0&0&0\\
3&0&0&0&0&0&0&0&0&0&0&0&0&0&0&0&3&0\\
0&0&0&0&0&0&3&0&0&0&0&0&0&0&0&1&0&0\\
0&0&0&0&0&0&0&2&0&0&0&0&1&0&1&0&0&0
\end{bmatrix} \quad (3)$$

Establish the Comprehensive Influence Matrix

The planning impact matrix is obtained by normalizing the above direct impact matrix, the calculation formula is as follows:

$$N=\left(\frac{b_{ij}}{Max\,\mathrm{var}}\right)_{18\times18} \quad (4)$$

Among them, $Max\,\mathrm{var}=\max\left(\sum_{j=1}^{18}b_{ij}\right)$

Based on the standard influence matrix, the comprehensive influence matrix of the influencing

factors of EPC project cost control is obtained by using the following calculation formula *T*, $T=\left(t_{ij}\right)_{18\times18}$, the matrix is shown below:

$$T=N\left(I-N\right)^{-1} \tag{5}$$

Among them matrix *I* is identity matrix.

$$T=\begin{bmatrix}
0 & 0.13 & 0.38 & 0 & 0 & 0 & 0 & 0.06 & 0.17 & 0 & 0 & 0 & 0.01 & 0.05 & 0.08 & 0 & 0 & 0\\
0 & 0 & 0 & 0 & 0 & 0 & 0 & 0.09 & 0.25 & 0 & 0 & 0 & 0.06 & 0.12 & 0.45 & 0 & 0 & 0\\
0 & 0 & 0 & 0 & 0 & 0 & 0 & 0.14 & 0.38 & 0 & 0 & 0 & 0.01 & 0.1 & 0.06 & 0 & 0 & 0\\
0 & 0 & 0 & 0 & 0.47 & 0.25 & 0.18 & 0.3 & 0.3 & 0 & 0 & 0 & 0.02 & 0.1 & 0.18 & 0 & 0 & 0\\
0 & 0 & 0 & 0 & 0 & 0 & 0.38 & 0.53 & 0.38 & 0 & 0 & 0 & 0.01 & 0.1 & 0.06 & 0 & 0 & 0\\
0 & 0 & 0 & 0 & 0.38 & 0 & 0.14 & 0.2 & 0.14 & 0 & 0 & 0 & 0 & 0.04 & 0.02 & 0 & 0 & 0\\
0 & 0 & 0 & 0 & 0 & 0 & 0 & 0.38 & 0 & 0 & 0 & 0 & 0 & 0 & 0 & 0 & 0 & 0\\
0 & 0 & 0 & 0 & 0 & 0 & 0 & 0 & 0 & 0 & 0 & 0 & 0 & 0 & 0 & 0 & 0 & 0\\
0 & 0 & 0 & 0 & 0 & 0 & 0 & 0.38 & 0 & 0 & 0 & 0 & 0.02 & 0.27 & 0.17 & 0 & 0 & 0\\
0 & 0 & 0 & 0 & 0 & 0 & 0 & 0.03 & 0 & 0 & 0 & 0.25 & 0 & 0 & 0 & 0 & 0 & 0\\
0 & 0 & 0 & 0 & 0 & 0 & 0 & 0.06 & 0.13 & 0 & 0 & 0.13 & 0 & 0.03 & 0.02 & 0 & 0 & 0\\
0 & 0 & 0 & 0 & 0 & 0 & 0 & 0.13 & 0 & 0 & 0 & 0 & 0 & 0 & 0 & 0 & 0 & 0\\
0 & 0 & 0 & 0 & 0 & 0 & 0 & 0 & 0 & 0 & 0 & 0 & 0.05 & 0.05 & 0.4 & 0 & 0 & 0\\
0 & 0 & 0 & 0 & 0 & 0 & 0 & 0 & 0 & 0 & 0 & 0 & 0.02 & 0.02 & 0.13 & 0 & 0 & 0\\
0 & 0 & 0 & 0 & 0 & 0 & 0 & 0 & 0 & 0 & 0 & 0 & 0.13 & 0.13 & 0.07 & 0 & 0 & 0\\
0.39 & 0.05 & 0.15 & 0 & 0 & 0 & 0.15 & 0.08 & 0.07 & 0 & 0 & 0 & 0 & 0.02 & 0.03 & 0.05 & 0.39 & 0\\
0.05 & 0.01 & 0.02 & 0 & 0 & 0 & 0.39 & 0.15 & 0.01 & 0 & 0 & 0 & 0 & 0 & 0 & 0.13 & 0.05 & 0\\
0 & 0 & 0 & 0 & 0 & 0 & 0 & 0.25 & 0 & 0 & 0 & 0 & 0.15 & 0.02 & 0.18 & 0 & 0 & 0
\end{bmatrix} \tag{6}$$

Calculate the influence degree, affected degree, center degree and cause degree

Add the values of the influencing factors in each row of the above comprehensive influence matrix *T* to obtain the comprehensive influence value, as is influence degree D_i. The affected degree C_i is obtained by adding the values of the influencing factors in each column of the comprehensive influence matrix *T.* The sum of the influence degree and the affected degree of the influencing factor *i* is the center degree F_i of the influencing factor, and the difference between the them, is the cause degree R_i. The specific formula is as follows:

$$D_i=\sum_{j=1}^{18}t_{ij}\left(i=1,2,3,\cdots,18\right) \tag{7}$$

$$C_i=\sum_{j=1}^{18}t_{ji}\left(i=1,2,3,\cdots,18\right) \tag{8}$$

$$F_i=D_i+C_i\left(i=1,2,3,\cdots,18\right) \tag{9}$$

$$R_i=D_i-C_i\left(i=1,2,3,\cdots,18\right) \tag{10}$$

The above formula is used to calculate the influence degree, affected degree, center degree and cause degree of each influencing factor of EPC project cost control. The results are shown in Table 2.

Tab.2 - Influence Degree，Affected Degree，Center Degree，Cause Degree of Influencing Factors of EPC Project's Cost Control

influence factor	influence degree D_i	affected degree C_i	Center degree F_i	Cause degree R_i
M_1	0.88	0.44	1.32	0.44
M_2	0.97	0.18	1.15	0.79
M_3	0.69	0.54	1.23	0.15
M_4	1.80	0	1.80	1.80
M_5	1.46	0.84	2.30	0.62
M_6	0.92	0.25	1.17	0.67
M_7	0.38	1.23	1.61	-0.86
M_8	0	2.78	2.78	-2.78
M_9	0.83	1. 82	2.65	-0.99
M_{10}	0.28	0	0.28	0.28
M_{11}	0.37	0	0.37	0.37
M_{12}	0.13	0.38	0.51	-0.26
M_{13}	0.50	0.48	0.98	0.02
M_{14}	0.17	1.06	1.23	-0.89
M_{15}	0.33	1.87	2.20	-1.54
M_{16}	1.38	0.18	1.56	1.20
M_{17}	0.81	0.44	1.25	0.37
M_{18}	0.60	0	0.60	0.60

Center degree indicates the importance of each influencing factor. The greater the value of center degree, the greater the role of this factor in the index system. According to the center degree value in the above table, draw the importance curve of influencing factors of EPC project cost control, as shown in Figure 1 below.

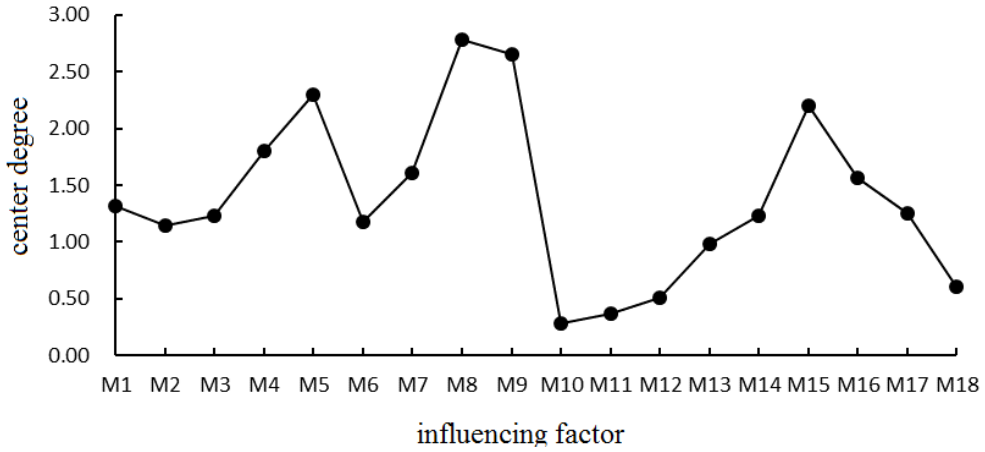

Fig.1-Curve of center degree of influencing factors of EPC project's cost control

It can be seen from Figure 1 that the factor that has a great impact on the cost control of EPC project is the project construction management level M_8, engineering change and claim M_9, rationality of design scheme M_5, price settlement basis M_{15}; secondly, the selection of design unit M_4, the selection of construction scheme M_7, national policies and regulations M_{16}, the formulation of contract terms M_1, the market price of human resources, materials and machines M_{17}, the division of contract responsibility M_3, the acceptance of project content M_{14}, the cost control awareness of design unit M_6, and the contract bidding management M_2; finally, the acceptance M_{13} of the changed data, the level of scientific and Technological Development M_{18}, the procurement process and standard M_{12}, the procurement system M_{11}, and the procurement method M_{10}.

The cause degree of the influencing factor is greater than 0. The greater the value, the greater the impact of the factor on other factors. It is the cause index in the system, if the cause degree is less than 0, the more obvious the value is, the smaller the impact of this factor on other factors is. It is the result index in the system. According to the cause degree value in Table 2, it draws the cause and effect diagram of the influencing factors of EPC project cost control, as shown in Figure 2 below.

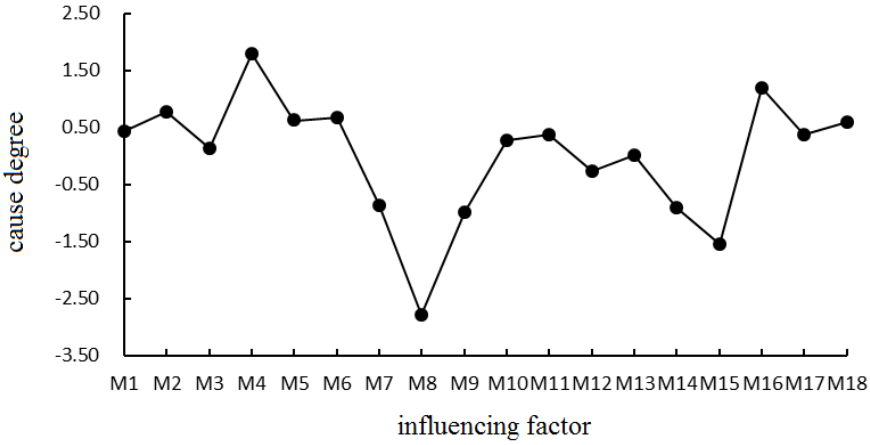

Fig.2-Curve of cause degree of influencing factors of EPC project's cost control

As can be seen from Figure 2, the designer selection M_4, national policies and regulations M_{16}, contract bidding management M_2, the designer's cost control awareness M_6, the rationality of the

design scheme M_5, the project construction management level M_8, the formulation of contract terms M_1, the procurement system M_{11}, the market price of human resources M_{17}, the procurement method M_{10}, the division of contract responsibilities M_3, Acceptance M_{13} of changed data is the cause index in the influencing factor system of EPC project cost control; Project construction management level M_8, price settlement basis M_{15}, engineering change and claim M_9, project content acceptance M_{14}, construction scheme selection M_7, procurement process and standard M_{12} , those influencing factors are the result indicators in the EPC project cost control influencing factor system.

Establish Reachability Matrix

In the comprehensive influence matrix, due to the lack of consideration of the influence of influencing factors on itself, the following formula needs to be used to obtain the overall influence matrix *P* of the system, the formula is as follows:

$$P = I + T \tag{11}$$

Among them matrix *I* is identity matrix.

Set the threshold value λ according to the system impact matrix, by setting the threshold λ, The system can be simplified by eliminating the factors that have little impact on the system[20]. The value of threshold λ will have a great impact on the relationship between influencing factors. If the value is too large, the system structure is relatively simple, it is difficult to measure the relationship between factors, and if the value is too small, the system structure is relatively complex, and the relationship between factors will become complex. In order to obtain the optimal system structure, The values of the threshold λ used in this paper are set to 0.05, 0.1, 0.15 and 0.2 respectively, which are compared and analyzed for many times, and the node degree of each influencing factor under different thresholds is calculated, as is shown in Figure 3. According to the principles[21] of moderate node degree and nodes with large node degree fall in the key node domain determined by DEMATEL method. It is more appropriate when the value of λ is 0.15. The reachability matrix *S* of influencing factors of EPC project cost control can be obtained according to the following formula.

$$a_{ij} = \begin{cases} 0, & a_{ij} < \lambda \\ 1, & a_{ij} \geq \lambda \end{cases} \left(i = 1,2,3,\cdots,18;\ j = 1,2,3,\cdots,18\right) \tag{12}$$

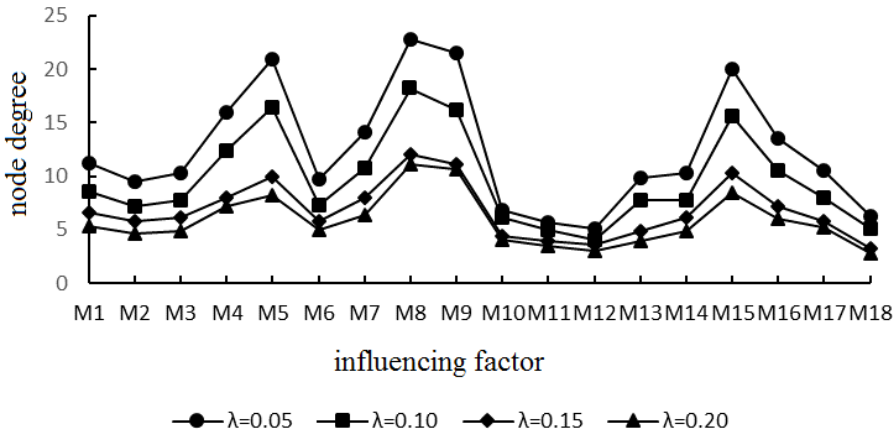

Fig.3 - node degree diagram of influencing factors under different thresholds

$$S = \begin{bmatrix} 1 & 0 & 1 & 0 & 0 & 0 & 0 & 0 & 0 & 0 & 0 & 0 & 0 & 0 & 0 & 0 & 0 \\ 0 & 1 & 0 & 0 & 0 & 0 & 0 & 0 & 1 & 0 & 0 & 0 & 0 & 0 & 1 & 0 & 0 & 0 \\ 0 & 0 & 1 & 0 & 0 & 0 & 0 & 0 & 1 & 0 & 0 & 0 & 0 & 0 & 0 & 0 & 0 & 0 \\ 0 & 0 & 0 & 1 & 1 & 0 & 0 & 0 & 1 & 0 & 0 & 0 & 0 & 0 & 1 & 0 & 0 & 0 \\ 0 & 0 & 0 & 0 & 1 & 0 & 1 & 1 & 1 & 0 & 0 & 0 & 0 & 0 & 0 & 0 & 0 & 0 \\ 0 & 0 & 0 & 0 & 1 & 1 & 0 & 0 & 0 & 0 & 0 & 0 & 0 & 0 & 0 & 0 & 0 & 0 \\ 0 & 0 & 0 & 0 & 0 & 0 & 1 & 1 & 0 & 0 & 0 & 0 & 0 & 0 & 0 & 0 & 0 & 0 \\ 0 & 0 & 0 & 0 & 0 & 0 & 0 & 1 & 0 & 0 & 0 & 0 & 0 & 0 & 0 & 0 & 0 & 0 \\ 0 & 0 & 0 & 0 & 0 & 0 & 0 & 1 & 1 & 0 & 0 & 0 & 0 & 1 & 0 & 0 & 0 & 0 \\ 0 & 0 & 0 & 0 & 0 & 0 & 0 & 0 & 0 & 1 & 0 & 1 & 0 & 0 & 0 & 0 & 0 & 0 \\ 0 & 0 & 0 & 0 & 0 & 0 & 0 & 0 & 0 & 0 & 1 & 0 & 0 & 0 & 0 & 0 & 0 & 0 \\ 0 & 0 & 0 & 0 & 0 & 0 & 0 & 0 & 0 & 0 & 0 & 1 & 0 & 0 & 0 & 0 & 0 & 0 \\ 0 & 0 & 0 & 0 & 0 & 0 & 0 & 0 & 0 & 0 & 0 & 0 & 1 & 0 & 1 & 0 & 0 & 0 \\ 0 & 0 & 0 & 0 & 0 & 0 & 0 & 0 & 0 & 0 & 0 & 0 & 0 & 1 & 0 & 0 & 0 & 0 \\ 0 & 0 & 0 & 0 & 0 & 0 & 0 & 0 & 0 & 0 & 0 & 0 & 0 & 0 & 1 & 0 & 0 & 0 \\ 1 & 0 & 0 & 0 & 0 & 0 & 0 & 0 & 0 & 0 & 0 & 0 & 0 & 0 & 0 & 1 & 1 & 0 \\ 0 & 0 & 0 & 0 & 0 & 0 & 1 & 0 & 0 & 0 & 0 & 0 & 0 & 0 & 0 & 0 & 1 & 0 \\ 0 & 0 & 0 & 0 & 0 & 0 & 0 & 1 & 0 & 0 & 0 & 0 & 0 & 0 & 0 & 0 & 0 & 1 \end{bmatrix} \quad (13)$$

Establish Multi-layer Hierarchical Structure Model of Influencing Factors

The reachable set $H(M_i)$, antecedent set $K(M_i)$ and common set $N(M_i)$ of influencing factors of EPC project cost control is determined by reachability matrix *S*, as is shown in Table 3 below. Among them, reachable set $H(M_i)$ is a set of all the influencing factors that can be reached by the influencing factors in the reachability matrix, antecedent set $K(M_i)$ represents the set of all influencing factors that can be reached in the reachability matrix, the common set $N(M_i)$ is the intersection of reachable set and antecedent set.

Tab.3: Reachable set, antecedent set and common set of influencing factors of EPC project cost control

M_i	$H(M_i)$	$K(M_i)$	$N(M_i)$
1	1、3	1、16	1
2	2、9、15	2	2
3	3、9、	1、3	3
4	4、5	4	4
5	5、7、8、9	4、5、6	5
6	5、6	4、6	6
7	7、8	5、7、17	7
8	8	5、7、8、9、18	8
9	8、9、14	2、3、5、9	9
10	10、12	10	10
11	11	11	11
12	12	10、12	12
13	13、15	13	13
14	14	9、14	14
15	15	2、13、15	15
16	1、16、17	16	16
17	7、17	16、17	17
18	8、18	18	18

The method of level division is to extract levels according to the condition of $H(M_i)=N(M_i)$, as is shown in Table 3, when *i* =8、11、12、14、15, $H(M_i)=N(M_i)$, this is expressed as the top level of the system and the highest element set of influencing factors of EPC project cost control, it is $L_1=\{M_8、M_{11}、M_{12}、M_{14}、M_{15}\}$. At this time, $M_8、M_{11}、M_{12}、M_{14}、M_{15}$ will be deleted from the reachability matrix, on this basis, the highest-level feature set in the reachability matrix will be found again. And so on, finally it gets $L_3=\{M_2、M_3、M_5、M_{17}\}$, $L_4=\{M_1、M_4、M_6\}$, $L_5=\{M_{16}\}$. Therefore, the levels of factors affecting EPC project cost control are divided into five levels, as it means L_1, L_2, L_3, L_4, L_5. It establishes a hierarchical structure model of influencing factors of EPC project cost control, as shown in Figure 4.

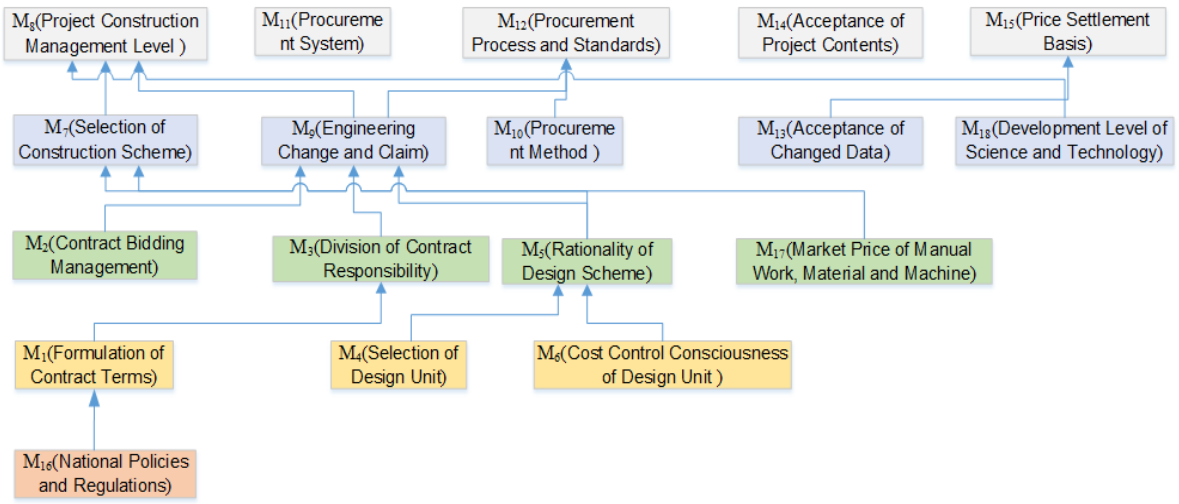

Fig.4-Hierarchical structure model of influencing factors of EPC project cost control

ANALYSIS AND SUGGECTIONS ON HIERARCHICAL STRUCTURE MODEL OF INFLUENCING FACTORS OF EPC PROJECT COST CONTROL

Direct influencing factors of EPC project cost control

According to the above hierarchical structure model diagram, the direct factors affecting the cost control of EPC project are project construction management level M_8, procurement system M_{11}, procurement process and standard M_{12}, project content acceptance M_{14} and price settlement basis M_{15}. Good project construction management can reasonably arrange the use of labor, materials and machinery, ensure the smooth implementation of EPC project and avoid engineering changes caused by improper construction. On the basis of paying attention to the project construction management level, it can avoid increasing the procurement cost by establishing a sound procurement system and improving the procurement process and standards. In the completion acceptance stage of EPC project, the acceptance of project content needs to check whether the project meets the needs of Party A and is consistent with the design drawings to ensure the smooth progress of acceptance. By checking the engineering change, design change, material change and other problems in the process of project construction, all parties involved in the construction of EPC project need to determine the basis of price settlement according to the specific situation, so as to ensure the interests of all parties involved.

Indirect Influencing Factors of EPC Project Cost Control

(1) The second level influencing factors are the selection of construction scheme M7, engineering change and claim M9, procurement method M10, acceptance of changed data M13, and scientific and technological development level M18. Through the in-depth study of the design drawings, selecting a reasonable construction scheme can ensure the smooth progress of each link in the construction. At the same time, we also need to pay attention to engineering changes and claims. On the one hand, we should effectively record the contents of changes and claims and

retain effective documents. On the other hand, we should do a good job in the management of changes and claims to reduce the impact of engineering changes and claims on project implementation. Scientific and reasonable procurement methods can effectively reduce the procurement costs of EPC project equipment and materials, select the most suitable way for the project benefit objectives, and improve the cost performance of purchased equipment and materials. By checking the validity and authenticity of visa, change and claim documents, the probability of disputes in completion acceptance can be effectively controlled. The advanced scientific and technological level can effectively promote the in-depth development of EPC project, especially the promotion and application of BIM technology, which provides strong scientific and technological support for the future development of EPC project.

(2) The third level influencing factors are contract bidding management M2, contract responsibility division M3, rationality of design scheme M5 and market price of manual works, materials and machines M17. Through the review of the bidding documents, the key information involved, such as construction standards, project scale, technical requirements, etc., shall be deeply studied, so as to ensure the accuracy of the bidding documents. If the responsibilities or obligations of Party A and the general contractor cannot be clearly specified during the formulation of the contract, it will lead to a conflict of interest. Therefore, clarifying the division of contract responsibilities can protect the interests of both parties of the EPC project. The rationality of the design scheme directly affects whether the subsequent construction links can be carried out smoothly. The design unit and the construction party shall participate in the strict review and optimization of the design drawings to improve the rationality, integrity and scientific of the design scheme. Combined with the development status of market and regional economy, master the market price fluctuation of talents and machines, and evaluate the expected economic benefits of the project to avoid unnecessary waste in the process of cost control.

(3) The fourth level influencing factors are the formulation of contract terms M1, the selection of design units M4 and the awareness of cost control M6. In terms formulation, the general contractor of the project needs to carefully review the contract terms, reasonably foresee the potential risks, and establish a perfect contract review process. The selection of EPC project design unit shall be based on the principle of paying equal attention to technology and economy, so as to avoid the consequences of high project cost caused by only paying attention to technology and not paying attention to economy. At the same time, it is also necessary to constantly strengthen the cost control awareness of the design unit, so as to make the project design economical and meet the needs of the project.

Fundamental Influencing Factors of EPC Project Cost Control

Based on the above analysis, national policies and regulations M16 is the fundamental factor affecting the cost control of EPC project. Therefore, in order to effectively reduce the cost of EPC projects, the state needs to introduce a series of policies and measures to ensure the continuous improvement and promotion of EPC projects. On the one hand, the government can give preferential treatment to EPC projects in terms of finance and taxation and create more relaxed financing conditions and environment. On the other hand, the government can focus on supporting representative enterprises to drive the rapid development of EPC mode, In addition, more EPC

professionals will be trained through industry training to make the development of EPC project more standardized, standardized and sustainable, so as to realize the benign development of EPC project.

CONCLUSION

Combined with the relevant literature on EPC project cost control, this paper summarizes and analyzes the influencing factors, and puts forward 18 factors affecting EPC project cost control from six dimensions: contract factors, design factors, construction factors, procurement factors, completion acceptance factors and external environmental factors. The decision laboratory analysis method (DEMATEL) is used to calculate the centrality and cause degree of each influencing factor, and classify them. On this basis, the interpretative structure model (ISM) is used to study the relationship between each influencing factor, and a multi-layer hierarchical structure model of the influencing factors of EPC project cost control is established, so as to improve the economic benefits and provide theoretical basis for reducing project construction cost.

The research in this paper also has some limitations. As EPC projects are widely used in various fields, there will be more and more factors affecting the cost control of EPC projects. The number of influencing factors of EPC project cost control identified in this paper is still present, and the implicit influencing factors, such as the reputation and communication ability of both parties, are not taken into account. Although the analytical method in the paper is scientific, it relies to some extent on people's experience, and the accuracy of the analytical conclusions is mainly determined by the factors selected and the number and quality of the experts consulted. The subsequent study can complete the analysis of the cost control of EPC projects by comparing quantitative data with qualitative results to make the analysis conclusions more convincing.

ACKNOWLEDGEMENTS

Special thanks to National Social Science Foundation of the Ministry of Education of China, I would like to thank Northeast Petroleum University and Chengde Petroleum College for their support.

REFERENCES

[1] Xu Lili. Key points of EPC project design control based on cost control [J]. Engineering economy, 2020, 30(11): 25-28.

[2] Zeng Xiang. Cost management measures for EPC project [J]. China's collective economy, 2020(36): 33-35.

[3] Yuan Yamin. Analysis on risk prevention strategy of construction project cost under EPC mode[J]. Chinese architectural metal structure, 2020(12):62-63.

[4] Ye Zhao Ping, Pan Chang Qian, Ye Shui Ying. Research on material and equipment procurement cost control of small town upgrading and reconstruction project under EPC mode [J]. China Construction, 2020(10): 50-51.

[5] Shu Jian Ping. Research on cost management mode of EPC project [J]. Engineering construction

and design, 2018(23): 292-293+296.

[6] Wu Zhu Xiang. Construction cost control measures under EPC mode of construction projects [J]. China Construction, 2020(11):38-39.

[7] Tribunal de Contas (2016), “Evolução global dos trabalhos adicionais no âmbito dos contratos de empreitada”, Relatório n.º 1/2016 –AUDIT. 1.ª S., Lisboa: Tribunal de Contas.

[8] Rui A. F. de Oliveira, Jorge Lopes, Maria I. Abreu. Insights from a project procurement strategy through an action research. International Conference on ENTERprise Information Systems / ProjMAN -International Conference on Project MANagement / HCist - International Conference on Health and Social Care Information Systems and Technologies 2020.

[9] Jan Pícha a*, Aleš Tomek b, Harry Löwit c. Application of EPC contracts in international power projects. Procidea Engineering, volume123,2015, pages 397-404.

[10] Mary Bajomo, Akinola Ogbeyemi, Wenjun Zhang. A systems dynamics approach to the management of material procurement for Engineering, Procurement and Construction industry. International Journal of Production Economics 244 (2022) 108390.

[11] Johnny Kwok Wai Wong, Jackson Kit San Chan, Mesthrige Jayantha Wadu. Facilitating effective green procurement in construction projects: An empirical study of the enablers. Journal of Cleaner Production 135 (2016) 859-871.

[12] Rajeev Ruparathna 1, Kasun Hewage .Sustainable procurement in the Canadian construction industry: current practices, drivers and opportunities. Journal of Cleaner Production 109 (2015) 305-314.

[13] Manman Xia, Lemeng Zhao, and Li Zhao.A Comprehensive Risk-Assessment Method for Prefabricated Buildings Using EPC: A Case Study from China. Sustainability 2022, 14, 1910. https://doi.org/10.3390/su14031910.

[14] Myung-Hun Kim, Eul-Bum Lee, and Han-Suk Choi .Detail Engineering Completion Rating Index System (DECRIS) for Optimal Initiation of Construction Works to Improve Contractors’ Schedule-Cost Performance for Offshore Oil and Gas EPC Projects. Sustainability 2018, 10, 2469; doi:10.3390/su10072469.

[15] Pan Gong, Ningshuang Zeng, Kunhui Ye and Markus König. An Empirical Study on the Acceptance of 4D BIM in EPC Projects in China. Sustainability2019,11,1316; doi:10.3390/su11051316.

[16] Duan Yong Hui, Zhang Yue, Guo Yi Bin, Wang Xiang. Risk assessment and strategy suggestion of EPC project based on structural equation [J]. Friends of accounting, 2021(02):104-110.

[17] Zavadskas, E.K.; Vilutien˙e, T.; Turskis, Z.; Šaparauskas, J. Multi-criteria analysis of projects’ performance in construction. Arch. Civ. Mech. Eng. 2014, 14, 114–121.

[18] Ngacho, C.; Das, D. A performance evaluation framework of development projects: An empirical study of constituency development fund (cdf) construction projects in Kenya. Int. J. Proj. Manag. 2014, 32, 492–507.

[19] The impact of Engineering, Procurement and Construction (EPC) Phases on Project Performance: A Case of Large-scale Residential Construction Project. Buildings 2019, 9, 15; doi:10.3390/buildings9010015.

[20] Liu Ming Fei, Chen Wei. Research on Influencing Factors of logistics service quality risk in front warehouse of fresh and cold chain based on integrated DEMATEL-ISM [J]. Safety and environmental engineering, 2020, 27(01):118-125.

[21] Wang Wen He, Zhu Zheng Xiang, Mi Hong Fu, etc. Study on Influencing Factors of fire accident in urban underground comprehensive pipe gallery based on DEMATEL-ISM [J]. Safety and environmental engineering, 2020, 20(03):793-800.

CIVIL ENGINEERING JOURNAL

Article no. 7

THE CIVIL ENGINEERING JOURNAL 1-2022

THE HYDROCHLORIC ACID EFFECTS ON MODIFIED CEMENT WITH NEW COMBINATIONS BASED ON CALCINED DAM'S MUD AND NATURAL POZZOLAN

Abdelkadir Belghit[1], Nasr Eddine Bouhamou[1], Miloud Hamadache[2,3] and Belkacem Ziregue[1].

1. *Abd el Hamid Ibn Badis University (UMAB), Faculty of Science and Technology, Laboratory of Materials and Construction Process (LMPC), belhacel street 27000, Mostaganem, Algeria, abdelkadir.belghit.etu@univ-mosta.dz; nbouhamou@yahoo.fr; ziregue.kacem@gmail.com.*
2. *National Polytechnic School, Laboratory of Materials (LABMAT), El M'Naouer, Oran, Algeria, hamadache.miloud@yahoo.fr*
3. *Relizane University Center, Department of Civil Engineering, Relizane, Algeria*

ABSTRACT

Reducing the amount of clinker in the cement industry using Supplementary Cementitious Materials (SCMs) is one of the solutions developed by researchers in our field to respect environmental requirements. In the same context, the present work aims to test the feasibility of new combinations using two Algerian SCMs and evaluate their behavior while exposed to hydrochloric acid. To concretize this objective, we fabricated a control mortar (based on cement CEMI) and nine other mortars containing modified cement by a binary and ternary mixtures of Portland Cement CEMI, Calcined Mud of Chorfa Dam, and Natural Pozzolans. All these mixtures were tested at fresh state for consistency and setting time of pastes and at hardened state for apparent density measure, water absorption, and compressive strength of mortars. After that, the ten of them were immersed in hydrochloric acid (HCl) 5% during fifteen weeks (105 days). Then they were examined for mass loss, volume loss, density decrease (apparent density), and visual appearance. The results obtained in most tests showed that the mixtures containing SCMs, especially the ternary mixtures, are realizable, economical, and more advantageous compared to the control mortar with higher water demand and a better behavior after compression and HCl attacks. In the end, we propose the mortars containing ternary mixtures with rates of 10% and 20% to develop new formulations with high performance.

KEYWORDS

Cement, Mortar, Natural Pozzolan, Calcined dam's mud, Hydrochloric acid

INTRODUCTION

To stop the global warming, we should respect the international strategy to reduce CO2 emission in atmosphere, evaluated to 33 Gt in 2021 [1], Alone the cement industry is responsible for 2.2 Gt of world CO2 emission [2] 50 to 60% of this amount is caused by limestone decomposition, and 30 to 40% is due to fuel combustion in kiln factories [3], reducing the quantity of clinker in the cement industry by using supplementary cementitious materials (SCMs) is one of the solutions adopted by researchers to respect environmental requirements [4-5], several sorts of SCMs were discovered by time as natural pozzolan, fly ash, silica fume, granulated blast furnace, limestone, and metakaolin [6], which have diversified the types of cement produced [7-8] and improved their behavior towards the aggressive environment [6,8], this situation gave builders

more freedom to choose the quality of cement to use in their structures to withstand different types of exposure [6,8], Algerian regulations authorize the production of 27 cement products [9-10] but in reality, only four products are available in the market [11], natural pozzolan is a material of unaltered or partially altered volcanic origin located in volcanic regions, existing in several deposits in Algeria [6,12] which is currently used as an SCMs in local cement industry, the Beni Saf deposit in Ain Temouchent city has a reserve exceeding 18 million cubic meters [13], on the other hand, several materials have proven their place in this field, among them the calcined mud of some dams in western Algeria (Bouhnifia, Fergoug, and Chorfa), which exist in nature as hydraulic wastes in millions of cubic meters (estimated at 32 million cubic meters per year in 2010) [14], However, it has never been used in the cement industry before. The dredging of these dams periodically - by the National Agency of Dams and Transfer- to recover their storage capacity is very expensive [14]; this operation results in a considerable quantity of wastes stored next to the dams. After being heated at 750°C for 5 hours [15], the calcined mud of Chorfa dam replaces cement by 30%, according to Semcha. A, 2006 [15]; At fresh state is characterized by a decrease in manoeuvrability which increases the water -or admixtures- consumption [15-18], and better compressive strength than natural pozzolan at an early age and long term [17], chemically its high reactive silica content (Sio2) offers the capacity to react with hydrated phases like calcium hydroxide (CH) that produces a second degree of calcium silicate hydrate (CSH) in a pozzolanic reaction, which was reflected in the increase in long-term of the compressive strength after the age of 120 days [16], Both mortar and concrete based on calcined mud have given a higher compressive strength than Portland cement CEMI for rates of 10% and 20% and a similar behavior with CEMI for 30% replacement rate, these results were considered as better than wastes of the other dams (Bouhnifia and Fergoug) [16-18], physically and because of its high finesse at the nano and micro scale, these particles filled concrete microstructure which is favorable for durability [18], the use of the calcined mud from Chorfa dam decreases the heat of the cement hydration and especially for the 20% replacement rate of CEMI cement by CM compared to other replacement rates that are also beneficial for mortars and concrete's durability [19], the tests done to evaluate the resistance of these sediments against acid attacks were carried out by Safer. O [16] who tested the resistance of ordinary concrete based on cement containing levels of 10%, 20%, and 30% of CM immersed in sulfuric acid and found a similar behavior to CEMI cement, especially for 10% and 20%, the exposure of CM to hydrochloric acid has not been well evaluated, because -in formulations of self-compacting concrete – only Belaribi. O [17] followed the resistance of his formulation containing one replacement rate (20%) by calcined mud of Chorfa dam. It proved a better resistance than the self-compacting concrete control (based on a CEMI cement). On the other hand, natural pozzolan has also shown resistance to acid attacks; explained by the consumption of calcium hydroxide resulting from hydration during the pozzolanic reaction and the filler behavior due to the high finesse of pozzolanic materials [20-21], all cement containing lime is sensible to acid attacks, especially when the pH is less than 3.5 [6], also Mohit. M [22] explained that the resistance of pozzolanic materials is better than ordinary cement exposed to acid solutions by the CH consumption that reacts with HCl and products soluble chloride of calcium CaCl2, which is harmful to the cement matrix and facilitates the decomposition of CSH and calcium aluminate hydrate (CAH).

In the present experimental work, we will test the feasibility of a new combination using two sorts of Algerian SCMs (natural pozzolan "NP" and calcined mud of Chorfa dam "CM") and evaluate their behavior while exposed to hydrochloric acid.

MATERIALS AND METHODS

Cement

The cement used in the present work is the Portland Cement CEMI 42.5 produced by GICA-Algeria, conform to the Algerian standard NA-442, 2013 [9] that is similar to the European standard NF EN197-1 [7], the physical characteristics are shown in Table1, the chemical composition in

Table 4 and the mineralogical composition of clinker calculated with Bogue formula [6] presented in Table 2.

Natural pozzolan

The natural pozzolan used in this work is from the Beni-Saf deposit in Ain Temouchent city in western Algeria (Figure 1-a), recovered from the GICA Oran cement plant, then crushed by a ball mill (Figure 1-b), sieved in 63 µm mesh (Figure1-c) the physical and chemical characteristics are shown in Tables1 and 4.

(a) (b) (c) (d)

Fig. 1 - (a) natural pozzolan, (b) ball mill, (d) sieving of natural pozzolan in 63 µm mesh, (d) natural pozzolan powder ready to use.

Calcined Mud of Chorfa Dam

The mud was extracted from the drain valve of Chorfa Dam (Figure2-a), transported to the laboratory, dried outdoors for a few days (Figure2-b), calibrated in crusher in medium dimensions 15/25 mm (Figure2-c), dried by temperature between (40°-50 C) until water elimination (Figure2-e), crushed by a ball mill (Figure2-f), sieved in 63 µm mesh, then thermally treated in calciner at 750°C during 5 hours, increasing the heating by 5°C/Min- [15] (Figure2-e), the Tables 1 and 4 present physical and chemical characteristics of calcined mud of Chorfa dam.

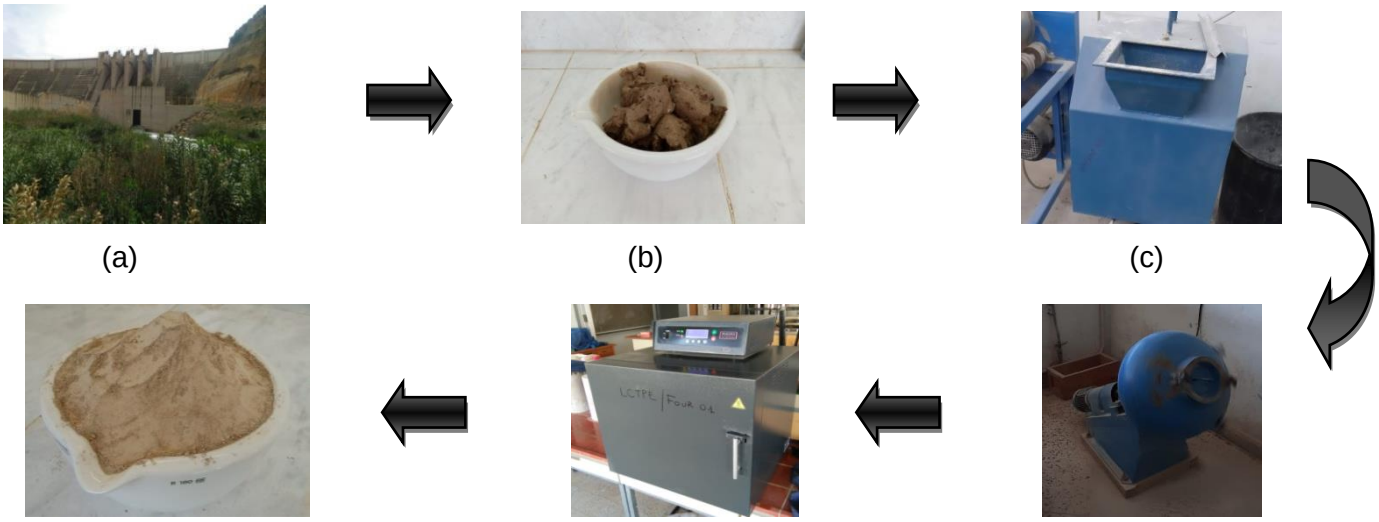

(a) (b) (c) (d) (e) (f)

Fig. 2 - Steps of the mud of Chorfa dam calcination (a) Extraction, (b) The mud of Chorfa dam (c) Calibration to 25mm,(d) Grinding, (e) Thermal treatment 750°C,(f) Calcined mud ready to use.

Tab. 1- Technical characteristics of cementitious materials.

properties	Bulk density	Finesse by Blaine method (Cm^2/g)	Pozzolanic activity index« i %»	pH
Cement CEM I	3.14	3285	/	/
Natural pozzolan	2.50	4323	86	8.92
Calcined mud	2.58	7190	92	10.51

Tab. 2 - Mineralogical composition of clinker calculated with Bogue Formula.

Components	C3S (%)	C3A (%)	C2S (%)	C4AF (%)
Cement CEMI	62.22	3.66	12.26	15.15

Aggregates

The present work used two sorts of sand as fine aggregates, natural siliceous sand from Oued El Kheir (Figure 3-a) and crushed limestone sand from Terga (Figure 3-b). Initially, the two sorts were washed in a 63 µm sieve until fine particles were eliminated, with the conservation of fines of crushed sand apart, after the two sorts of sands were dried at a temperature of 105°C during 48 hours until the elimination of water, the results of technical characterization and chemical composition of are shown in Tables 3 and 4, and the particles' size distribution is shown in Figure 4.

(a) *(b)*

Fig. 3 - (a) Natural sand of Oued El Kheir, (b) Crushed sand of Terga.

As seen in Tables 3, 4, and Figure 4, the crushed sand has a good technical requirement except for the high finesse modulus that equals 3.7. To obtain sand that respects the technical requirements of standardization NF P 18-545 [23], we elaborated a mixture (40% of natural sand and 60% of crushed sand) that modifies the finesse modulus and obtains values of corrected sand equal to 2.8; Figure 4 presents the particles size distribution of the corrected sand, which fits into the acceptance zone described by NF P 545-18.

Tab. 3 - Technical characteristics of Aggregates.

Properties	Bulk density	Finesse modulus	Sand equivalent	prohibited impurities	Absorption Coefficient	Organic matter	pH
Natural sand	2.70	1.48	84.26	None	1.53	0.59	9.53
Crushed sand	2.73	3.70	89.79	None	4.12	0.69	9.95

Tab. 4 - Chemical composition of cementitious materials.

Constituents	SiO_2(%)	Al_2O_3(%)	Fe_2O_3(%)	CaO(%)	Na_2O(%)	K_2O(%)	MgO(%)	So_3(%)	Cl (%)
Cement CEM I	20.72	04.56	4.98	63.24	0.21	0.79	1.82	2.54	0.05
Natural pozzolan	44.33	12.77	11.26	16.48	0.10	0.18	3.62	0.20	0.01
Calcined mud	49.22	12.11	07.23	23.99	0.44	3.22	2.45	0.13	0.00
Natural sand	86.90	0.00	0.39	11.68	0.00	0.00	0.00	0.00	0.0213
Crushed sand	10.89	0.33	0.78	74.77	0.00	0.00	0.00	0.00	0.0284

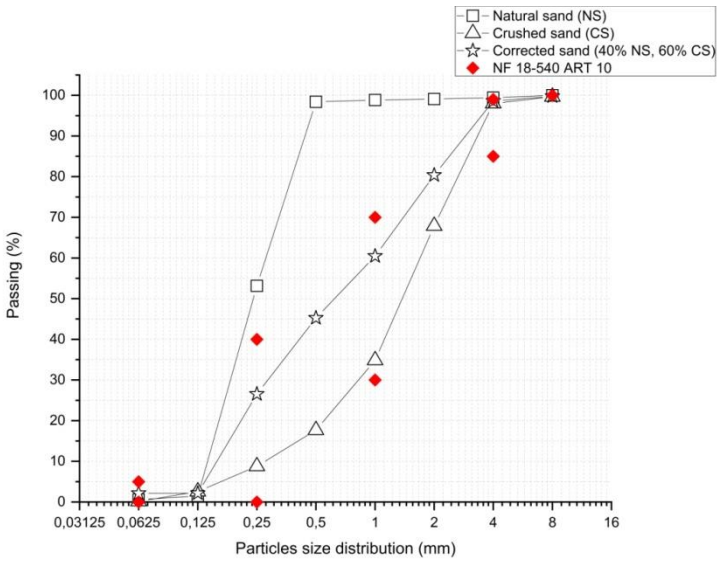

Fig. 4 - Particle size distribution of sands used.

To evaluate the modified cements of our experimental program, ten mortars mixtures were developed according to NF EN 196-1 [25], with three components Sand: Cement : Water by mass proportion 3:1:1/2 respectively for control mortar [24], and for mortars mixtures that contain modified cements, the same mass proportions used previously except the quantity of water that was adjusted using type B workability meter, by similar flow time for all ten mortars in accordance with NF P 18-452 and NF P15-437 [26-27], to insure the exact quantity of water needed for hydration -since we increased the volume by replacing the cement with SCMs grains characterized by a higher surface area-; The mixtures shown in Table 5 were made with normalized mixer "CONTROLAB" with method described in NF 196-1 [24], after the mixtures were casted in prismatic molds 40x40x160 mm and cubic molds 50 mm, compacted in vibrant Table during 30 second for maximum elimination of voids and air bubbles, after the upper surface was smoothed with a trowel, the molds were protected from evaporation by plastic film in the first 24 hours, the samples were demolded and cured in lime saturated water at 20°C temperature, until the day of the test to elaborate.

Tab. 5 - Mortar mixtures.

composition / Types	Sand (g)	CEMI (g)	CM (g)	NP (g)	Water (g)	E/(C+SCMs)
MC	1350	450	0	0	225	0,5
MM10	1350	405	45	0	229,5	0,51
MM20	1350	360	90	0	240,75	0,535
MM30	1350	315	135	0	247,5	0,55
MP10	1350	405	0	45	227,25	0,505
MP20	1350	360	0	90	236,25	0,525
MP30	1350	315	0	135	243	0,54
MM5P5	1350	405	22,5	22,5	229,5	0,51
MM10P10	1350	360	45	45	238,5	0,53
MM15P15	1350	315	67,5	67,5	245,25	0,545

The prismatic samples 40x40x160 mm were made for compressive strength test [24] and water absorption [32-34], while the cubic samples of 50 mm were fabricated to test the mass loss, volume loss, density decrease [31-32], and visual appearance of the ten mortars exposed to hydrochloric acid HCl 5% [27].

TEST PROCEDURES

The standardized consistency and the setting time tests of pastes were determined by Vicat's needles according to NF EN 196-3 [28], with the initial E/C ratio equal 0.25.

The prismatic specimens of 40x40x160 mm have been cut into two parts of 40x40x80 mm to elaborate the compressive strength test [24]; the mortars were tested by a compressive strength machine "CONTROLAB" that applies a uniaxial force by parallel squares with a surface pressure of 40x40 mm applied on the lateral facets [24].

The apparent density (D) of mortars was calculated by Formula 1 [29-30] with the determination of M and V by a method described below, and (g/cm3); the apparent density measurement schedule is at 3, 7, 14, 28, 56, 90 180 days, the values of M were recorded in gram, V in a cubic centimeter and $\rho water$ in g/cm^3 .

$$D = \frac{M}{V} \times \frac{1}{\rho\ water} \quad (1)$$

The liquid transfer properties of our mortars were tested by the water absorption after immersion, determined on prismatic mortars of 40x40x160 mm at the age of 28 and 180 days, measuring the mass (M) of the samples defined below, then they were subjected to oven 105°C observing the variation in mass every 24 hours until an error of 0.2% between two successive weightings (Md), the values of Md were recorded in gram;

Also, the water absorption (W.A) values after immersion were calculated by Formula 2 [31-32].

$$W.A = \frac{M - Md}{Md} \quad (2)$$

Two cubic specimens of 50 mm of each mortar group were produced and cured in saturated lime water during a maturation period of 90 days, removed from the curing tanks 24 hours before the exposure to acid, and left in open air [16-17]. The cubes were immersed in hydrochloric acid solution HCl 5% (Figure 5), examined for mass loss, volume loss, density decrease, and visual appearance, and were carried out each week; After each weekly examination, the solutions of the acid were renewed [16-17, 21,27].

Fig. 5 - Cubic specimens 50 mm immersed in HCl 5% solution.

On the day of Mass measurement, they were removed from the liquid, wiped by a piece of cloth to remove the excess water, weighed in the open air to obtain the mass of the sample in the saturated state (M). The volume was determined by measuring their masses underwater (Mw) with a mass measurement caliper underwater (Mst) [according to the standardization NF EN 12390-7-[29-30], with the determination of the volume by the following formula (3), with the values of Mst and Mw were recorded in gram and ρ water in g/cm^3;

$$V = \frac{M - [(Mst - Mw) - Mst]}{\rho\ water} \quad (3)$$

The mass and volume loss (X%) of the tested samples were calculated with the (Formula 4);

$$X = \frac{X1 - X2}{X1} \times 100 \quad (4)$$

RESULTS AND DISCUSIONS

Standardized consistency

Figure 6 presents the results of standardized consistency tests of the pastes evaluated. We can see that SCMs used in the present work increase the water demand compared to the control cement, proportionally with the rate of replacement (10%, 20%, and 30%) to reach the standardized consistency, the calcined mud of Chorfa dam consumes more water compared to the natural pozzolan and a similar quantity of water consumption between the NP and the combination CM-NP. This combination of CM-NP decreases the water demand slightly compared to the CM alone.

These results are related to the irregularity form of grains and the finesse of SCMs used compared to cement grains [6,18]. The works carried out by A. Semcha, O. Belarii, O. Safer, K. Belguessmia, and F. Taieb also note that the calcined mud and the natural pozzolan in the replacement of cement reduce the maneuverability of mortars [16-19]. The slight decrease in water consumption by the combination CM-NP is beneficial to develop new economic formulations based on these materials by using admixture to avoid the problem of water demand.

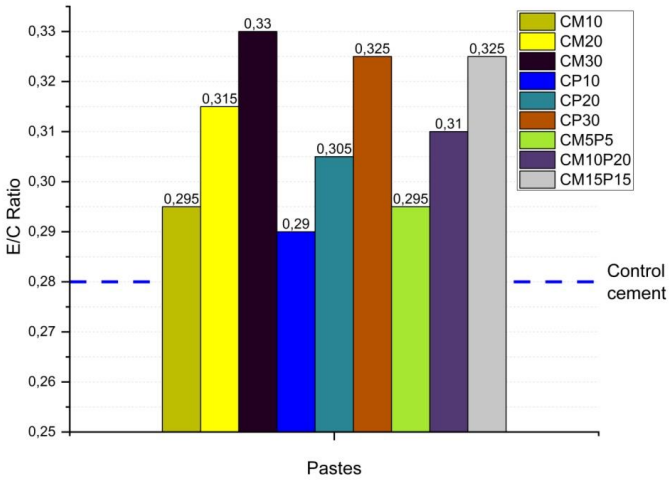

Fig. 6 - E/C Ratio relative to the standardized consistency by the Vicat apparatus.

Setting time tests

The results of the setting time of the ten pastes studied in the present work are shown in Figure 7. The setting times of pastes decrease proportionally with the rate of replacement of cement by SCMs, especially for the calcined mud that records important values. Slightly lower values were saved for the NP's pastes, with the similar behavior between NP and the combinations CM-NP. In general, the use of our SCMs decreases the setting time of pastes slightly, and the results of setting time tests of CM and NP presented in Figure 7 are similar to those cited in literature elaborated by O.Belaribi and O.Safer [16-17]. Also, the new combinations recorded the same behavior (reducing the setting time slightly), which is advantageous for their use in formwork striking times and works in cold weather as natural admixtures.

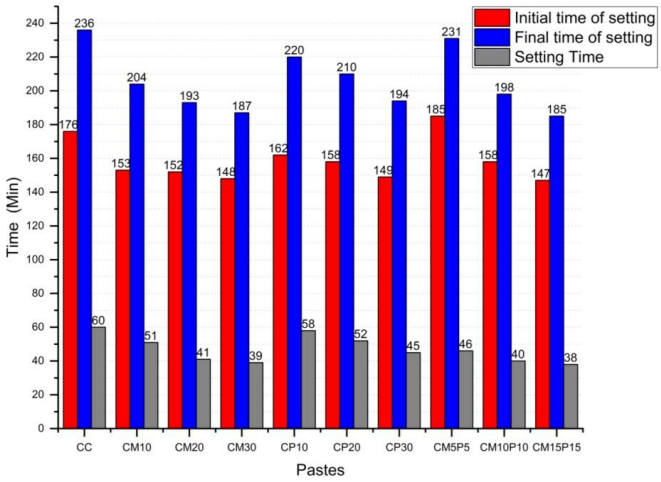

Fig. 7 - Setting time of cement with Vicat's needles.

Compressive strength

The compressive strength (CS) results of the control mortar and the nine mortars that contain modified cement, shown in Figure 8. The results obtained for the order of replacement 10% have very close values of CS compared to the control mortar, especially at long term (In the order of 60 MPA), with an advantage for the combination MM5P5 than the mortars MM10 and MP10; in other hands, at an early age, we note an advantage for MM10 and MM5P5 and a late of CS for MP10.

For the replacement rate with 20% SCMs, we note an advantage for MM20 and MM10P10 at both early age and long term, and the lowest values recorded for MP20, especially at an early age.

The best compressive strength results of mortars containing modified cement with 30% replacement of CEMI with CM and NP are noticed for MM30 (46 MPA), for the combination MM15P15 (42.5 MPA). The lowest results for this rate are saved for MP30 (40 MPA).

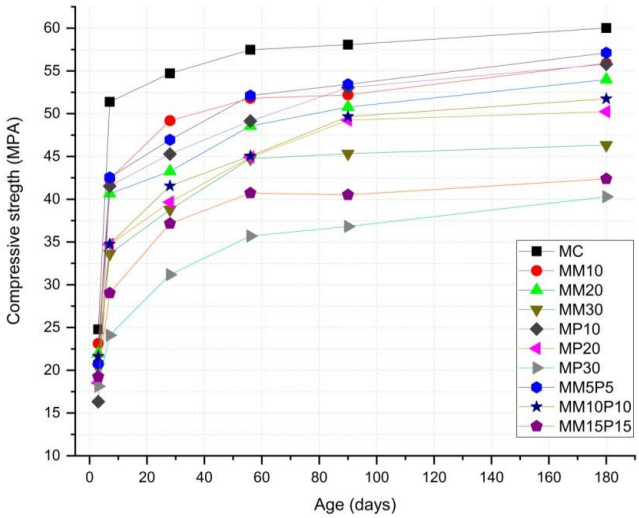

Fig. 8 - The mortar's Compressive strength Results.

These results indicate that CM presents a good pozzolanic reactivity than natural pozzolan, as noted in works cited in the literature [16-19]. However, the strengths of CM did not exceed the results of MC in the long term, as proved in the previous.

These good compressive strength results obtained of mortars containing a combination of CM and NP can be related to the increases the probability of lime and calcium hydroxide reaction

by two types of reactive silica with variables degrees of finesse, which explains a higher compressive strength of the combination compared than CM or NP alone, with more reactivity at an early age compared to NP and a similar mechanical behavior at later age.

These results improve the feasibility of the combination between CM and NP, especially for CM5P5 and CM10P10 at an early and later age that is good for the formwork striking times, which encourages us to think about developing new formulations based on these components for the development of high-performance mortars.

The low CS results obtained for mortars contained a rate of replacement of 30%, compared to the results cited previously can be related to the high “E/C” ratio, these formulations can be proposed in masonry and plastering of walls.

These results are not perfectly similar to those of O. Belaribi and O. Safer [16, 17]; for those, the compressive strengths of the mortars containing the calcined mud are better than that of the long-term control mortar. Moreover, this can be explained by the use of superplasticizers, which reduce water consumption, participate in the excellent placement and densification of mortars structures that reduces the porosity of the mortars and increase the compressive strength of the mortars.

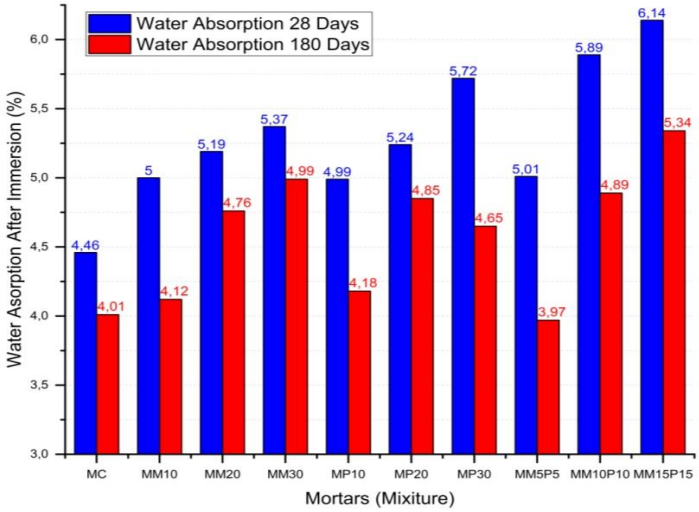

Fig. 9 - Water absorption of mortars after immersion.

Water absorption after immersion

As seen in Figure 9, we noticed that mortars mixtures containing modified cement have a higher water absorption rate than control mortar at an early age due to the high E/C ratio mixtures that increase porosity.

The rates of water absorption decrease in the long term, especially for mortars containing SCMs, which is related to the consumption of lime and calcium hydroxide by reactive silica due to a pozzolanic reaction that fills pores, decrease porosity, higher density and compressive strength, the mortars MM10, MP10, and MM5P5 present similar values to the control mortar with a slight advantage for MM5P5 mortar mixtures.

This test is a simple and good indicator of liquid transfer properties. It confirms the properties mentioned in the bibliography that the particles CM and NP enhance the compacity and decrease the porosity of mortars, which are beneficial for durability and resistance to acid attacks.

This test has never been developed on these materials and even rare works that have been used on mortars. Compared to the work of R. Aswin Maria Sebal [31], who worked on the water absorption after immersion on the mortars containing the rubber, it obtained higher values than ours, explained by the high mortars' porosity.

Hydrochloric acid attack

In normal curing conditions, the variation mass increases from 0.9% to 1.4% in 180 days and decreases in a volume less than 4.5% that happens in the first ten days, with an increase in apparent density of all mortars between 1% to 5.6% in 180 days (Figure 10).

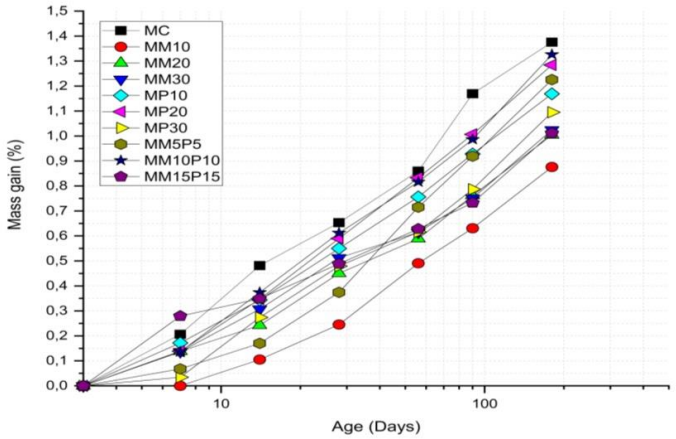

(a)

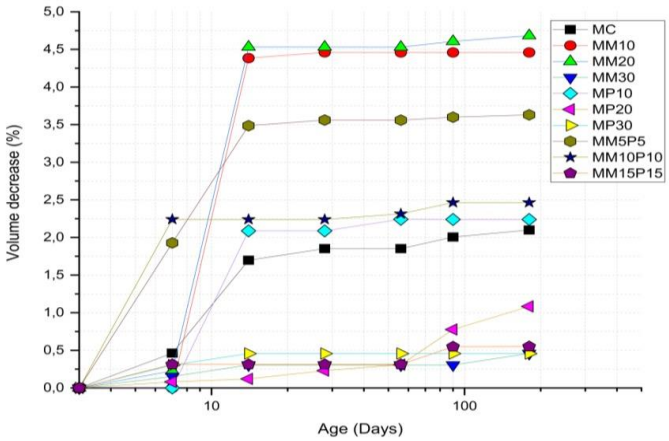

(b)

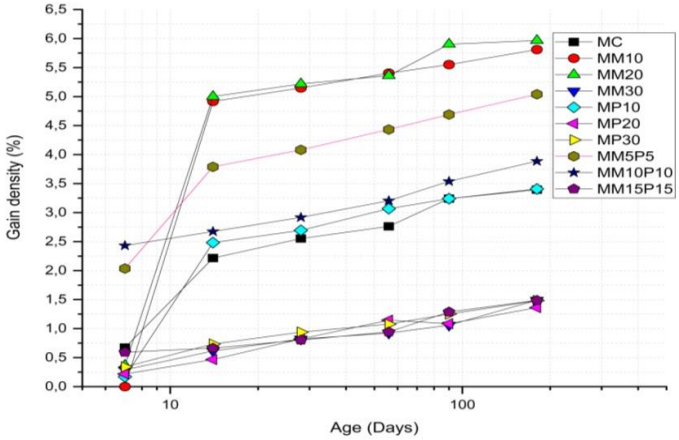

(c)

Fig. 10:- (a) Mass gain in normal curing, (b) Volume loss in normal curing, (c) Density gain of mortars in normal curing.

Figure 11 shows the mass loss of different mortars exposed to acid HCl 5% during 15 weeks; in the first five weeks, MM10, MM20, MP10, MP20, MM5P5 save lower mass loss values than MC, those same mortars continue to resist better than control mortar at the 10th week with MP30, MM10P10, and MP15P15 except MM30 that save a value of mass loss higher than MC. After 15 weeks of exposure to HCl 5%, all mortars containing SCMS resist better than the control mortar, and the best values of mass loss were given by MP20, MP10, MM5P5, MM10, and MM15P15 with values between 33.29% to 40.40 % compared to 58.01% of mass loss of the control mortar (Figure 14).

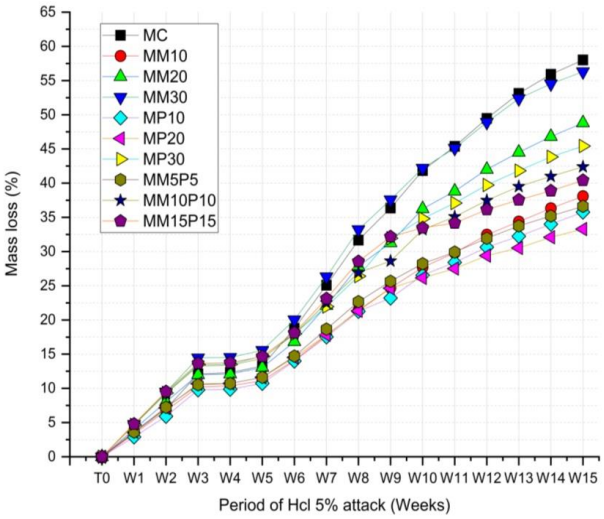

Fig. 11 - Mass loss of mortars exposed to hydrochloric acid 5%.

These results are related to lime and calcium hydroxide consumption, responsible for mass loss after reacting with HCl acid. For mortars with modified cement, especially MP20, MP10, MM5P5, MM10, and MM15P15, lime and CH are better consumed with reactive silica-rich CM and NP, increasing CSH rate and filling pores that delay the HCl attack [6, 22]. This result improves and completes the work of O. Belaribi [17], who used the calcined mud as supplementary cementitious materials to Postpone HCl attack.

The high resistance of natural pozzolana against HCl acid attacks has improved the ability of mortars based on combinations to resist this type of attack. These results agree with other studies conducted by several researchers showing the benefits of natural pozzolan and fly Ash enhancing the resistance to the hydrochloric acid attack [34-35].

We can report that the MM15P15 mortar resists against HCl acid attack despite its low compressive strength (compared to the control mortar), related to its high E/C ratio. To avoid this problem, it suffices to develop this mixture using admixture to reduce the quantity of water and a good particle's placement.

The volume loss of mortars after 15 weeks of exposure with HCl is illustrated in figure 12; we can note that the variation in the volume of mortars is similar to the variation in the mass of the same mortars that improves the results obtained previously.

The reduction in volume is principally due to the reaction between HCl and the CH, which produces a soluble chloride of calcium CaCl2, which is harmful to the cement matrix and facilitates the decomposition of CSH and CAH [22] and secondary to the liquid transfer properties of mortars that facilitates the infiltration of acid into mortars, unlike SCMs-based mortars, this process is slow.

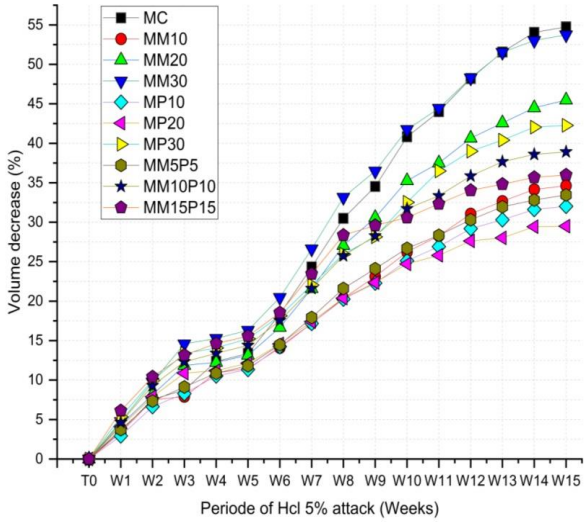

Fig.12 - volume loss of mortars exposed to hydrochloric acid 5%.

Figure 13 presents the results of examination during the exposure to HCl 5% for fifteen weeks. In the first five weeks, the values of density decrease were low, almost stable, after five weeks, we noticed a rise in the rate of density decrease than before, after ten weeks, the rate of density decrease became higher, especially for the control mortar that gave the higher value of density decrease compared to mortars containing modified cement.

These results are principally related to the decomposition of mortar structures that vary from a mortar to another and secondary to the porosity [6]; the mortars MM5P5 present the lowest density decrease value highest values are saved for the mortars MC, MM15P15, and MM20.

The high-density decrease of MM15P15 and MM20 is also due to the high values of water absorption that facilitate the infiltration of acid into mortars and eases the decomposition of CSH and CAH.

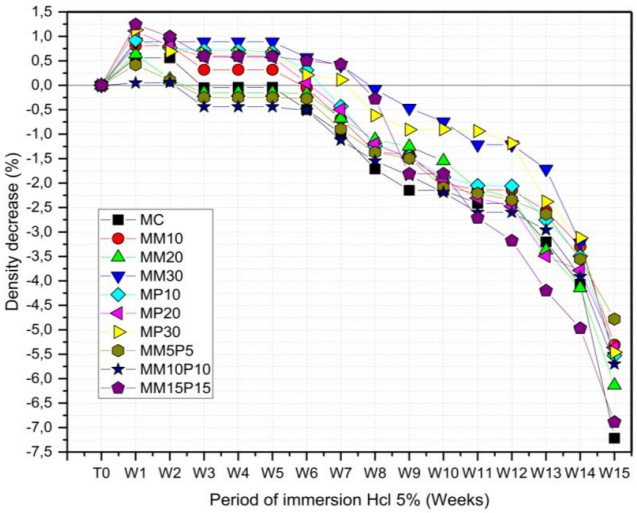

Fig.13 - Density decrease of mortars exposed to hydrochloric acid 5%.

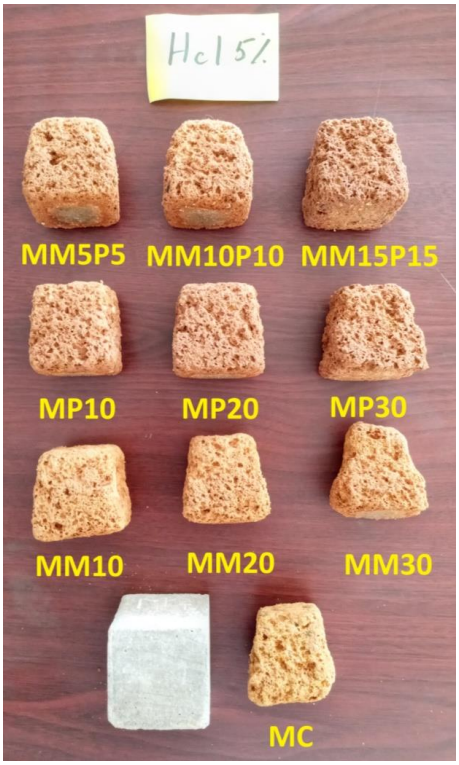

Fig. 14 - The ten mortars after 15 weeks exposed to HCl 5%.

CONCLUSION

At the end of this work, we can summarize it in the following notes:

The calcined mud of the Chorfa dam records a higher water demand than cement grains and is slightly higher than the NP due to the irregularity of CM grains and the higher finesse particles [6, 18], while the combination CM-NP maintains a similar behavior as the NP alone.

The setting time of the pastes containing SCMs used decreases proportionally with the cement replacement rate, especially for CM, which is comparable with the works cited in the literature [16-17], which is beneficial for formwork striking times and concrete works in the cold weather [6]. Also, we note that the combination CM-NP decreases the setting time with similar values compared to NP alone.

The compressive strength results of mortars with SCMs are lower at an early age, especially the NP, and comparable to MC at long term (60 MPA), especially for mortars MM5P5, MW10, MP10, MM10P10, and MW20 (53 to 57 MPA).

At a young age, the combination between calcined mud and natural pozzolan achieves compressive strength values higher than natural pozzolan alone, which is beneficial for fast formwork striking times.

The combination CM-NP is realizable, economic (until 30% of reduction in clinker), and more advantageous, this is due to the variable types of reactive silica of both CM and NP with two finesses degrees, that higher the probability of lime and calcium hydroxide consumption, more than each one of them alone (CM or NP).

Mortar with modified cement has a higher water absorption rate than MC at an early age due to the high E/C ratio that increases porosity. The rates of water absorption decrease in the long term for mortars with SCMs, by filling the voids and compensating the higher porosity noticed at an early age by lime and hydroxide calcium consumption (pozzolanic reaction), higher density, and compressive strength in the long term, that is beneficial for durability [6].

After exposure to HCl 5% until 15 weeks, we notice that the best mortars that showed better mass loss values are MP20, MP10, MM5P5, MM10, and MM15P15, with values between 33.29% to 40.40 % compared to 58.01% of mass loss of MC. This variety is due to the reactive

silica's lime and calcium hydroxide consumption rate; for mortars with modified cement, Cao and CH are better consumed with reactive silica-rich CM, increase CSH rate and fill the voids that are beneficial to HCl acid resistance.

The mortars MM5P5 and MM10P10 present comparable compressive strength values than MC and better resistance to HCl attack; we propose that they be developed concrete with high performance.

The MW15P15 is characterized by good resistance to HCl attack. Still, a higher water demand, lower compressive strength, and a higher water absorption rate encourage its development in the future by using admixtures to enhance the compressive strength and decrease porosity.

The variation in the volume of mortars is similar to the mass loss of the same mortars exposed to HCl attacks.

The high results of density decrease of MC, MM15P15, and MM20 are principally related to the decomposition of mortar structures that vary from a mortar to another and are secondary to the high-water absorption [6].

ACKNOWLEDGEMENTS

Foremost, I would like to acknowledge and give my warmest thanks to everyone who helped and encouraged me in carrying out this work. I also wish to express my sincere gratitude to all the staff members of Abd el Hamid IbnBadis University (UMAB), especially the team of Laboratory “LMPC” & “LCTPE.” They rendered their help during the period of my project work.

REFERENCES

[1] Agency I E., 2021. Net-Zero by 2050-A Roadmap for the Global Energy Sector.
[2] Pedraza J, Zimmermann A, Tobon J, Schomäcker R, Rojas N., 2021. On the road to net zero-emission cement: Integrated assessment of mineral carbonation of cement kiln dust. Chemical Engineering Journal, Vol. 408:127346. https://doi.org/10.1016/j.cej.2020.127346.
[3] Benhelal E, Shamsaei E, Rashid M I., 2021. Challenges against CO2 abatement strategies in cement industry: A review. Journal of Environmental Sciences, Vol. 104: 84–101. https://doi.org/10.1016/j.jes.2020.11.020.
[4] Lothenbach B, Scrivener K, Hooton R D., 2011. Supplementary cementitious materials. Journal of Cement and Concrete Research, Vol. 41: 1244–1256. https://doi.org/10.1016/j.cemconres.2010.12.001.
[5] Scrivener K, Martirena F, Bishnoi S, Maity S., 2018. Calcined clay limestone cement (LC3). Journal of Cement and Concrete Research, Vol. 114: 49 56. https://doi.org/10.1016/j.cemconres.2017.08.017.
[6] Newman J, Choo B S., 2003. Advanced Concrete Technology-Constituent Materials. (Elsivier Butterworth-Heinemann)
[7] AFNOR., 2012. NF EN 197-1 Composition, specifications and conformity criteria of common cement.
[8] FESTA J. DREUX G., 2007. New guide of concrete and its constituents.
[9] ALGERIAN STANDARD., 2003. NA 442, Composition, specifications and conformity criteria of commencement.
[10] JORA A., 2016. Official Journal of the Algerian republic number 27: 11–22.
[11] GICA Algeria cement factory official web. 2021.https://www.gica.dz .
[12] Algeria 360 (Algerian daily). promoting the use of pozzolan in construction techniques (researchers)., 2014.
[13] Liberty (Algerian daily). The Béni-Saf SPMC aims to produce 500,000 tons of pozzolana, 2010.
[14] Remini B., 2010. The water problem in northern Algeria. Larhyss Journal, Vol. 8: 27–46.
[15] Semcha A., 2006. Valorization of dredging sediments: Application in construction and public works, Fergoug dam case. (Thesis).
[16] Safer O, Belas N, Belaribi O, Belguessmia K, Bouhamou N E, Mebrouki A, 2018. Valorization of Dredged Sediments as a Component of Vibrated Concrete: Durability of These Concretes Against Sulfuric Acid Attack. International Journal of Concrete Structures and Materials,Vol. 12. https://doi.org/10.1186/s40069-018-0270-7.
[17] Belaribi O., 2015. Durability of Self Compacting Concretes based on the mud and pozzolan. (Thesis).

[18] Belguesmia K, Belas N, Amiri O, Leklou N., 2018.Influence of treated sediment substitution percentage on workability, strength, and porosity of SCC. Journal of materials and engineering structures, Vol. 5: 47–55.
[19] Taieb F, Belas N, Belaribi O, Belguesmia K, Hadj Sadok R., 2018.Influence of the calcinated mud on the kinetics of semiadiabatic hydration and the mechanical properties of Self-Compacting Concrete. Journal of Sciences & technologie, 35–41.
[20] Laoufi I, Laoufi L, Senhadji Y, Benazzouk A., 2019. Study of Mortars Made with Natural and Artificial Pozzolans. Journal of materials and engineering structures, Vol. 6: 427–442.
[21] Senhadji Y, Escadeillas G, Mouli M, Khelafi H, Benosman., 2014. Influence of natural pozzolan, silica fume, and limestone on strength, acid resistance, and microstructure of mortar. Journal of Powder Technology, Vol. **10**. https://doi.org/10.1016/j.powtec.2014.01.046.
[22] Mohit M, Ranjbar A, Sharifi Y., 2021. Mechanical and microstructural properties of mortars incorporating ceramic waste powder exposed to the hydrochloric acid solution. Journal of Construction and Building Materials, Vol. 271: 121565. https://doi.org/10.1016/j.conbuildmat.2020.121565.
[23] AFNOR., 2011. NF P 18-545-Aggregates - defining elements, conformity, and coding., 2011.
[24] AFNOR., 2016. NF EN 196-1 - Methods of testing cement., 2016.
[25] AFNOR., 2017. NF P 18-452 -Concretes — Measuring the flow time of concretes and mortars using a workability meter.
[26] AFNOR., 1987. NF P15-437- Hydraulic binders - Testing technics - Characterization of cement by fluidity measurement under mortar vibration.
[27] ASTM., 2012. C 267 - Standard Test Methods for Chemical Resistance of Mortars, Grouts, and Monolithic.
[28] AFNOR., 2017. NF EN 196-3- Methods of testing cement-part 3: Determination of setting time and soundness.
[29] AFNOR., 2019. NF EN 12390-7- Testing hardened concrete — Part 7: Density of hardened concrete.
[30] Taoukil D, El meski Y, Lahlaouti M, lhassane, Djedjig R, El bouardi A., 2021. Effect of the use of diatomite as partial replacement of sand on thermal and mechanical properties of mortars. Journal of Building Engineering, Vol. **42**: 103038. https://doi.org/10.1016/j.jobe.2021.103038.
[31] ASTM ., 2008. C642-06- Standard Method for Density, Absorption, and Voids in Hardened Concrete.
[32] Maria R A., Sakthieswaran N., Babu O G., Gaayathri K K., 2021. Effect of micro silica and ground granulated blast furnace slag on the performance of rubberized mortar. In: Proceeding Materials Today, edited by Vijayan V, Lee Chang Chuan (The Elsevier Journal), Vol **37**: 1014–1018. https://doi.org/10.1016/j.matpr.2020.06.278.
[33] Ghrici M, Kenai S, Meziane., 2006. Mechanical and durability properties of cement mortar with Algerian natural pozzolana. Journal of Materials Science, vol. 41(21): 6965–6972. https://doi.org/10.1007/s10853-006-0227-0
[34] Siad H, Mesbah H A S, Bernard K, Khelafi H, Mouli M., Influence Of Natural Pozzolan On The Behavior Of Self-Compacting Concrete Under Sulphuric And Hydrochloric Acid Attacks. Comparative Study. Arabian Journal for Science and Engineering, vol. 35 (1): 183–195.

CIVIL ENGINEERING JOURNAL

Article no. 8

THE CIVIL ENGINEERING JOURNAL 1-2022

FINITE ELEMENT ANALYSIS OF MECHANICAL PROPERTIES OF SPECIMEN WITH UHPC AND STUD CONNECTOR

Long Liu, Songqiang Wan, Shuwen Yao, Xinzhen Zhao and Jinyan Ma

Anyang Institute of Technology, the west end of Huanghe Avenue, Anyang 455000, China;20160913@ayit.edu.cn

ABSTRACT

UHPC is different from ordinary concrete for mechanical properties. To study the stress state of stud connector when UHPC is used to strengthen RC beam and its influence on bearing capacity of the strengthened beam, in this paper, ABAQUS was adopted first to simulate the push-out test of stud to verify accuracy of the finite element model. The nonlinearity of materials and contact conditions was considered in the model, and then three parameters including concrete strength, stud length and stud diameter were studied. Results showed the finite element model established by surface to surface contact method was possible to simulate the force and failure of the stud connector. UHPC could improve the bearing capacity of the stud specimens obviously, and the length of stud had little effect on bearing capacity of stud while failure of the stud may occur if length of the stud was too small. The increase of stud diameter could improve bearing capacity of elastic working stage.

KEYWORDS

Push out test, UHPC, Stud connector, Finite element, Reinforcement

INTRODUCTION

Ultra high performance concrete (UHPC) is considered as one of the most important innovative cement-based engineering materials in last 30 years. Compared with ordinary concrete, UHPC has better mechanical properties, its compressive strength is for three to six times and tensile properties for five to eight times that of the ordinary concrete. Since UHPC was put forward for the first time in 1990s, UHPC has developed rapidly, its components and performance has been improved, and its price has been gradually reduced, making it more and more widely used [1]. In recent years, researches on UHPC is mainly focused on how to make full use of its performance characteristics to achieve purpose of structural form innovation and provide basis for the large-scale promotion and application of UHPC [2]. Because of its ultra high tensile and compressive strength, as well as good ductility and durability, UHPC has unique advantages in all kinds of civil engineering structures, especially in bridge engineering, the way UHPC repairs and strengthens ordinary reinforced concrete beams has been recognized by more and more civil engineers and scholars [3]. Figure 1 is a new reinforced concrete beam strengthened by UHPC and CFRP proposed by the author. UHPC and oncrete beam are connected by a peg at the top, and traditional CFRP rod is glued to concrete beam at the bottom.

Stud is the most researched and applied shear connector currently, which can well bear the shear force on the connecting surface in UHPC reinforcement of existing Bridges. Stud connectors are suitable for industrial production because of their simple manufacturing and low cost [4]. However, stud is an isotropic material with the same strength and stiffness along the intended direction, with large deformation, good ductility and little impact on reinforcement placement in concrete slabs, which is widely used as shear connectors in bridge reinforcement [5].

Many research has been carried out on mechanical properties of stud connectors at home and abroad. Qing-hua han et al introduced the extended finite element method into calculation and analysis of composite beam, established the analysis model and simulated whole process of shear stud from crack beginning to fracture failure [6].Tian Qixian et al. studied the use of UHPC for bridge deck pavement, analyzed different length and diameter ratios of shear studs by push-out test and finite element analysis, and focused on the static performance of short studs[7].

Aiming at the new structure that UHPC is used for reinforcement, this paper adopts method of simulating studs in ABAQUS to carry out finite element analysis on push-out test of stud. By nonlinear finite element analysis model verified by push-out test results, three parameters of different concrete strength, stud length and stud diameter were studied to find out influence of three parameters on load-bearing capacity, failure and slip amount of push-out specimen, providing a theoretical basis for wide application of UHPC in beam reinforcement.

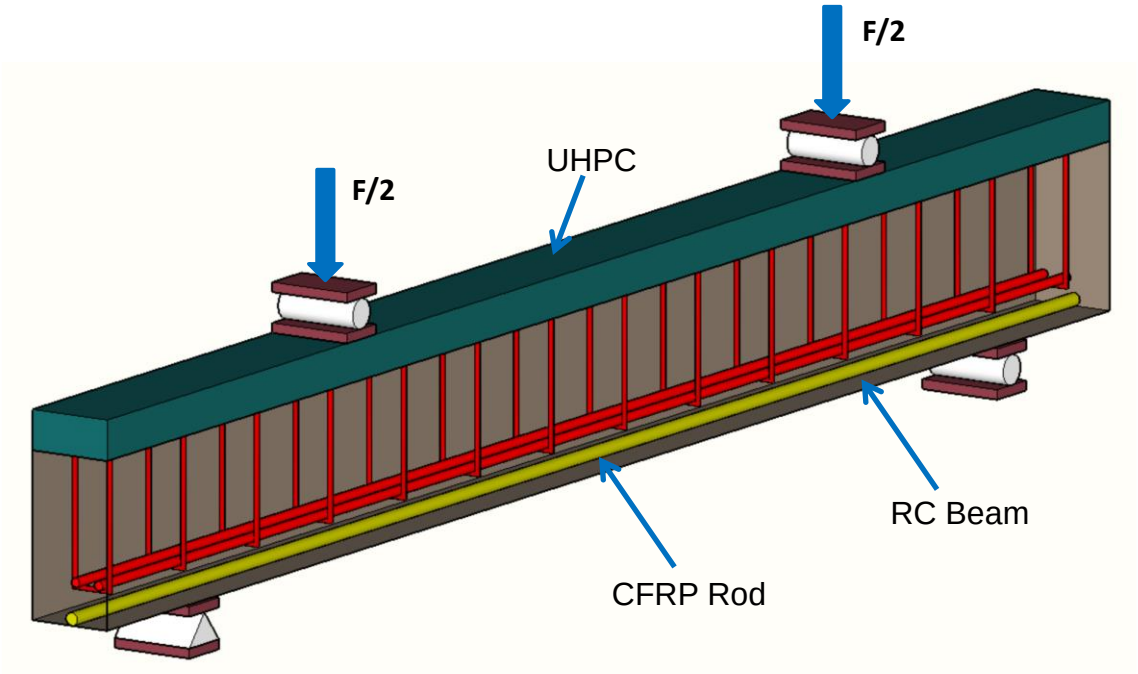

Fig. 1 - RC beam strengthened by UHPC and CFRP Rod

Verification of Finite element model

The reliability of finite element simulation analysis is effected by many factors, such as material constitutive relationship, contact action quality, load boundary condition, element type, mesh technique, loading, etc. [8]. Improper analysis modeling or assumptions may even lead to errors in analysis results. Therefore, to ensure the reliability of following parameter studies, the model verification of push-out test of the stud in literature [9] was carried out to ensure the reliability of the finite element model.

(1) Test overview

In reference [9], length, width and height of concrete of SS-1 were 460mm, 400mm and 460mm respectively. Two studs were welded horizontally on the outside I-shaped steel flange plate, arranged symmetrically on both sides. The studs were 22mm in diameter, 200mm in length and 150mm in spacing. Specific size of the specimen was shown in Figure 2.

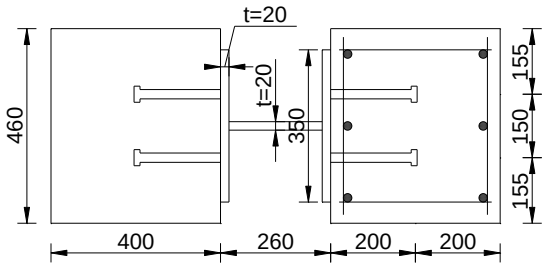

(a) Plan

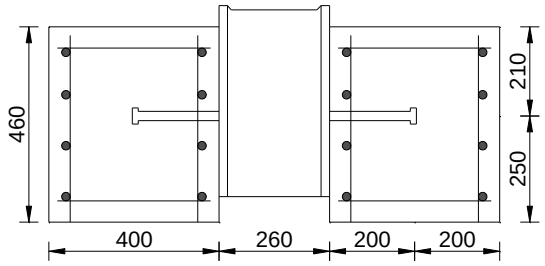

(b) Elevation

Fig. 2 - Structure diagram of the ejector specimen (mm)

(1) The constitutive relationship

The compressive strength of the high-strength concrete cube (150mm×150mm×150mm) used in the specimen was 72MPa, and the constitutive relationship was based on the curve recommended in the Code for Design of Concrete Structures (GB50010-2015) [10]. Stress-strain curve under uniaxial compression could be determined according to formula (1) and formula (2):

$$\sigma = (1 - d_c) E_c \varepsilon \tag{1}$$

$$d_c = \begin{cases} 1 - \dfrac{\rho_c n}{n - 1 + x^n} & x \le 1 \\ 1 - \dfrac{\rho_c}{\alpha_c (x-1)^2 + x} & x > 1 \end{cases} \tag{2}$$

Where, $\rho_c = \dfrac{f_c^*}{E_c \varepsilon_c}$, $n = \dfrac{E_c \varepsilon_c}{E_c \varepsilon_c - f_c^*}$, $x = \dfrac{\varepsilon}{\varepsilon_c}$, E_c is elastic modulus of concrete; α_c is reference value of the descending section of stress-strain curve under uniaxial compression of concrete； f_c^* is the uniaxial compressive strength of concrete； ε_c is the peak compressive strain of concrete corresponding to uniaxial compressive strength f_c^*； d_c is the damage evolution parameter of concrete under uniaxial compression.

$$\sigma = (1 - d_t) E_c \varepsilon \tag{3}$$

$$d_t = \begin{cases} 1 - \rho_t (1.2 - 0.2 x^5) & x \le 1 \\ 1 - \dfrac{\rho_t}{\alpha_t (x-1)^{1.7} + x} & x > 1 \end{cases} \tag{4}$$

Where, $\rho_t = \dfrac{f_t^*}{E_c \varepsilon_t}$, $x = \dfrac{\varepsilon}{\varepsilon_t}$, α_t is reference value of the descending section of the uniaxial tensile stress-strain curve of concrete； f_t^* is the uniaxial tensile strength of concrete； ε_t is the

peak tensile strain of concrete corresponding to uniaxial tensile strength f_t^* ; d_t is evolution parameter of uniaxial tensile damage of concrete.

Diameter of the welded nails was 22mm, the yield strength was 367MPa, the tensile strength was 480 MPa, and the elastic modulus was 210000MPa. The material properties of stud had an important influence on the results of push-out test. In this paper, a three fold line model was adopted [11], which was first elastic, then entered yield stage and finally failure stage. Stress-strain curve of stud is shown in Figure 3.

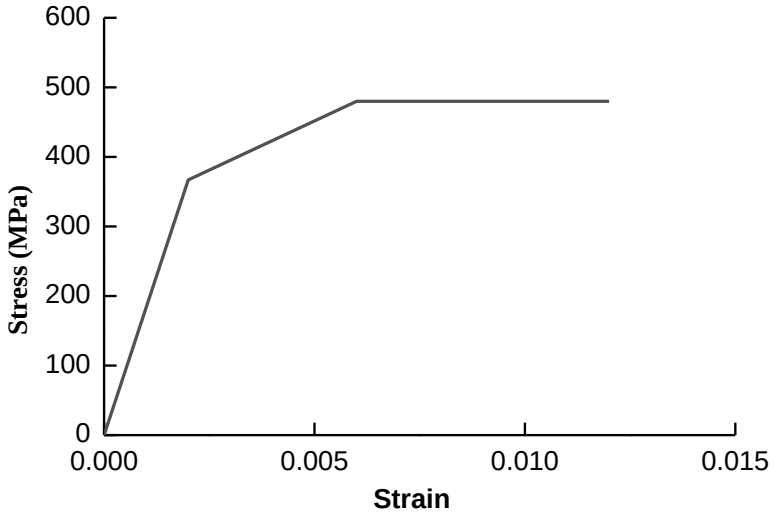

Fig. 3. - Stress - strain curve of stud

(3) Model establishment

According to the geometric symmetry, boundary symmetry and load symmetry of the extruded sample, a quarter part of the extruded sample was modeled. Studs and I-shaped steel members were created in the same part, while concrete and steel bars were created separately. In the model, concrete, stud and I-shaped steel were simulated by C3D8R three-dimensional eight-node reduction integral element, and steel bar was simulated by T3D2 three-dimensional two-node truss element. When assembling each member, reinforcement was placed inside concrete as a built-in unit to ensure reinforcement member nodes were bound to relevant nodes of the concrete member. The contact friction was simulated by creating contact unit pairs between concrete and stud, and rigid contact was simulated by creating contact unit pairs between concrete and I-shape. 1/4 finite element model of the extruded specimen is shown in Figure 4.

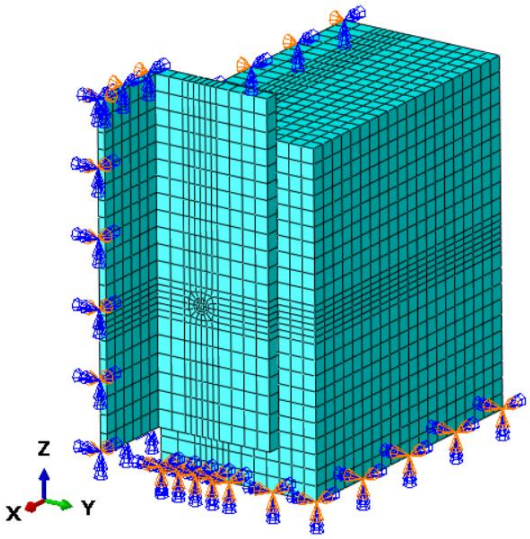

Fig. 4.- Finite element model of 1/4 of the specimen

(4) Boundary conditions

Boundary conditions of the model were set by mechanical symmetry adjustment. The bottom concrete surface was restricted in all three directions with a fully fixed boundary. Concrete and I-shaped steel adopt symmetrical boundary conditions on the symmetry plane of the X-axis and Y axis, which meant that points in the plane could not move along normal direction of the plane of symmetry, but could rotate in the plane.

(5) Contact relationship

In the finite element model, surface to surface contact method was used to simulate contact between concrete and I-shaped steel and between concrete and studs. Compared with common nodes or built-in elements, this simulation method could simulate relative slip between concrete and studs more accurately, and the contact stress was more consistent with the load [12]. It was assumed the contact properties of the two contact surfaces of concrete and I-shaped steel, concrete and studs were the same. The normal behavior adopted the default hard contact to ensure no penetration of component nodes. The tangential behavior adopted penalty friction, assumed the friction coefficient of the contact surface was 0.3, surface of I-shaped steel and studs was selected as the main contact surface, and the surface of concrete was taken as the secondary contact surface.

Finite element model result

Figure 5 shows load-slip curves gained from the finite element analysis results and test results of the test specimens. Finite element analysis results are consistent with the test results. The load-slip curves are mainly divided into elastic and plastic working stages, and the elastic working stage accounts for about 50% of the ultimate bearing capacity of the studs. In elastic working stage, slip of stud is small and load-slip curve is almost straight. Slip of stud in the test curve and finite element curve is about 0.3mm. In plastic working stage, slip amount of studs increases rapidly, shear stiffness of stud gradually degrades. When slip amount is about 7.5mm, the test specimen and finite element model reach the maximum load of 786.87kN and 783.20kN respectively. Then it enters failure stage, and shear stiffness of stud degrades rapidly. The test load value decreases to about half of the maximum value, and the finite element load value decreases to about 75% of the maximum value. Because the introduction of contact nonlinearity makes the calculation convergence difficult, but it does not affect bearing capacity of the model.

The results show both the test results and the finite element analysis results end with shear failure of studs, and the deviation between the experimental values and the calculated values is less than 10%, showing the finite element model with the face-to-face contact method is reliable for parameter study of bolt push-out test.

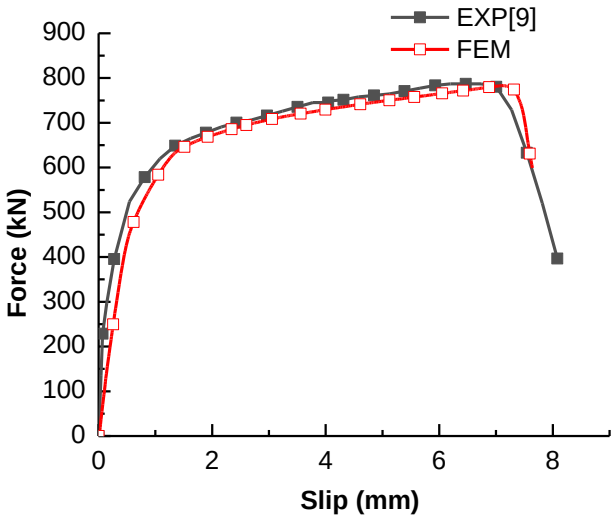

Fig. 5 - Comparison of load-slip curves between finite element calculation and test results

Parameter study

Based on the experimental verification of the material constitutive relationship and contact algorithm in the finite element model, finite element model of concrete and stud used for parameter study were established. The contact action, boundary conditions and element types were used in the same way as the finite element verification model. 11 finite element studies of stud connectors, numbered ST-1 to ST-11, were carried out. Sizes of each specimen were the same as those of the finite element verification model, and the main variation parameters were concrete strength, stud diameter and stud length. Specimens and their main parameters are shown in Table 1. In Table 1, d is diameter of stud, l is length of stud, f_{cu} is axial compressive strength of concrete, and f_s is yield strength of stud.

Tab. 1 - Main parameters of specimens

Specimen No.	*d*/mm	*l*/mm	Concrete	f_{cu}/MPa	f_s/MPa
ST-1	16	200	UHPC	140.3	367
ST-2	19	200	UHPC	140.3	367
ST-3	22	200	UHPC	140.3	367
ST-4	25	200	UHPC	140.3	367
ST-5	22	50	UHPC	140.3	367
ST-6	22	100	UHPC	140.3	367
ST-7	22	150	UHPC	140.3	367
ST-8	22	250	UHPC	140.3	367
ST-9	22	200	C40	36.8	367
ST-10	22	200	C60	38.5	367
ST-11	22	200	C80	50.2	367

(1) Concrete strength

Existing studies have shown concrete strength directly affects bearing capacity and failure of composite members [13]. When concrete strength grade is low, bearing capacity depends on concrete strength, and the failure form is mainly compression failure of concrete. As concrete strength increases to a certain level, bearing capacity depends on ultimate tensile strength of stud. To study load-slip between UHPC and ordinary concrete in the push-out test, C40, C60 and C80 ordinary concrete were selected for comparative analysis with UHPC.

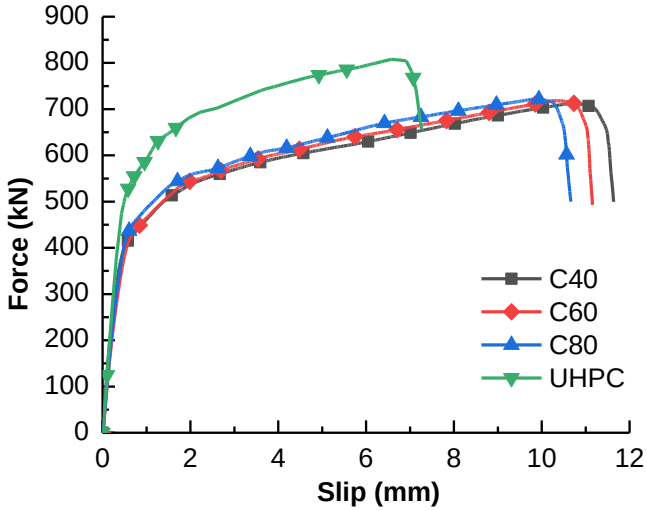

Fig. 6 - Load-slip curves of concrete with different strengths

Figure 6 shows load-slip curves of specimens pushed out with four different strengths of concrete. As can be seen from Figure 6, load-slip curves of three kinds of ordinary concrete are close to each other. With improvement of concrete grades, bearing capacity of specimens remains unchanged, and the maximum loads of ST-9, ST-10 and ST-11 are 712.2kN, 718.5kN and 721.8kN respectively. Stiffness of ST-3 of UHPC specimen is obviously greater than that of ordinary concrete specimens. In elastic working stage, maximum load of ST-3 is about 450 kN, which is about 20% higher than that of ordinary concrete. Slip amount of each specimen is the same. In plastic working stage, the maximum load of UHPC specimen can reach 807.8kN, about 1.13 times of ultimate bearing capacity of ordinary concrete specimen, and slip amount is obviously less than that of ordinary concrete specimen, only about 60% of it.

(2) Stud length

The length of stud connectors should not be too short, studs may be damaged when pulled out. In Design Standard of Steel Structure (GB50017-2017) [14], it is clearly stipulated the ratio of stud length L to stud diameter D must be greater than 4. In this paper, stud specimens with lengths of 50mm, 100mm, 150mm, 200mm and 250mm were selected to calculate the influence of length of stud on its bearing capacity and slippage. Figure 6 shows bearing capacity of composite members with the same diameter and different stud length.

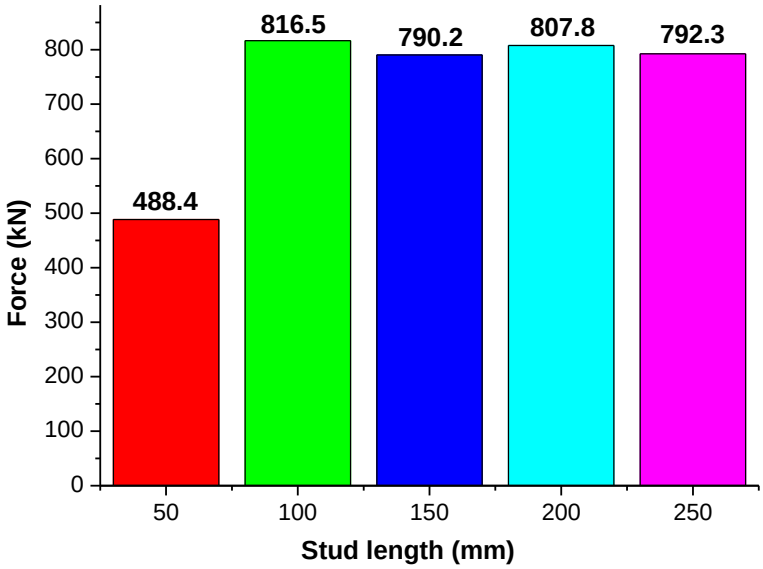

Fig. 7 - Influence of different stud lengths on load capacity

As shown in Figure 7, when length of stud is 50 mm, bearing capacity of composite components is only 188.4 kN, at this time, concrete around stud has reached ultimate compressive strain. Studs are pulled out and damaged, while other composite members with different lengths of studs have the same load-bearing capacity, and the small range of numerical changes is caused by different local meshing of the finite element model. Results of finite element numerical analysis show the design is reasonable to prevent failure of stud pulling out in composite members under requirement the ratio of stud length l to stud diameter d in code [14] is greater than 4.

(3) Stud diameter

Parameters that have important influence on the shear bearing capacity between UHPC and the stud combination members are cross-sectional area and tensile strength of stud. When tensile strength of bolt was kept unchanged, four studs diameters of 16mm, 19mm, 22mm and 25mm were selected to carry out parameter study. The calculation results are shown in Figure 8. Influence of different stud diameters on bearing capacity in elastic working stage is shown in Figure 9.

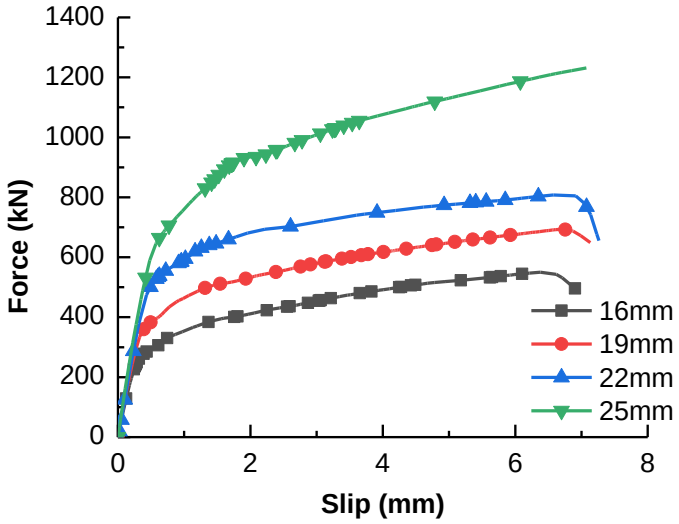

Figure 8 Load-slip curves of different stud diameters

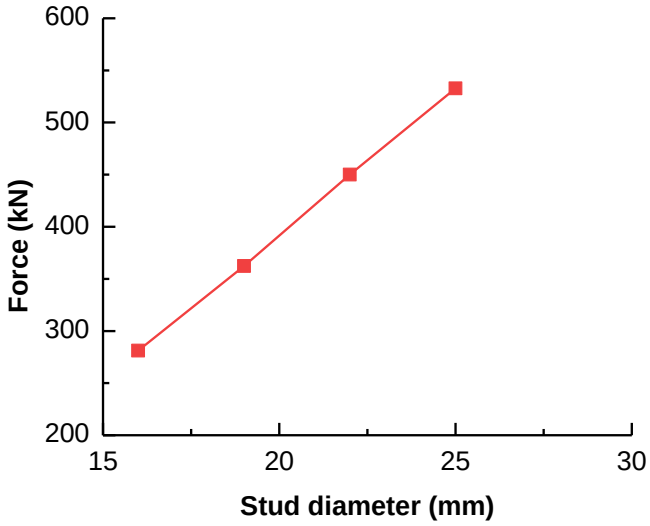

Fig 9 - Influence of different stud diameters on bearing capacity in elastic working stage

Diameter of stud has a great influence on elastic working stage of the load-slip curve. Compared with specimen with diameter of 16mm, the maximum load of the specimen with diameter of 19mm, 22mm and 25mm increases by 30%, 60% and 90% respectively in the elastic working stage, which shows an linear increase, but slip amount remains the same. Diameter of stud has little effect on the slope of load-slip curve in elastic working stage. From comparison of plastic development stages of load-slip curves of different diameter specimens, it can be seen the larger the stud diameter is, the higher the ultimate load will be. Except the slope of load-slip curve is slightly larger when stud diameter is 25mm, four curves remained parallel in plastic development stage, which is mainly because UHPC does not fail in plastic development stage, and load-slip is mainly affected by ultimate tensile strength of stud.

CONCLUSION

Through verification of push-out test of ABAQUS simulated stud connectors, variation rule of bearing capacity between UHPC and stud connector was further studied, and the following conclusions were drawn:

(1) The calculated results fit well with measured values by using surface-to-surface contact method to simulate contact between stud and concrete, and the deviation between calculated values and tested values is less than 10%, which shows the finite element simulation of the force and failure of stud connectors by using the surface-to-surface contact method is feasible.

(2) The adoption of UHPC with higher compressive strength can significantly improve bearing capacity of composite members. The maximum load is about 1.13 times of bearing capacity of ordinary concrete composite members, and slippage is less than that of ordinary concrete composite members obviously, which is only about 60%.

(3) Length of stud has little influence on bearing capacity of the composite components. However, if stud length is too small, it will lead to stud pulling out failure. It is reasonable to adopt stud as UHPC shear connectors according to requirement, and ratio of stud length to diameter should be greater than 4.

(4) With increase of stud diameter, the maximum load in elastic working stage increases obviously, but slippage remains unchanged. Stud diameter has little influence on development of load and slip amount in plastic development stage.

ACKNOWLEDGEMENTS

This study is supported by two key funds: 1) Science and technology planning project of Henan Province, China (222102320040); 2) Science and technology planning project of Anyang, Henan Province, China (2022C01GX038).

REFERENCES

[1] Xu Xiuying, Jia Ying, Shi Guosong. Application analysis of ultra high performance fiber concrete in highway bridge reinforcement [J]. Highway engineering, 2020,45 (04):92-95+135.
[2] wang J, wang J, wang J, et al.effect of concrete structure on the performance of ultra-high performance concrete [J]. International journal of Bridges, 2019,47 (02):2.
[3] Zhang Yang, Shi Jianqun, Shao Xudong. Experimental study on flexural behavior of UHPC bolted key-tooth joint beam [J]. Highway engineering, 2019,44 (03):1-5+26.
[4] Yang Weipeng, Li Chengjun, Song Xiaoming, Zhou Zhixiang. Experimental study on shear bearing capacity of prefabricated stud shear connectors [J]. Railway construction, 2019,59 (06):38-42.
[5] Shi Weihua, Chen Like, Chen Di. Journal of hunan university of science and technology (natural science edition), 2019,34 (01):28-35.
[6] Han Qinghua, Wang Yihong, Xu Jie, Xing Ying. Progress in building steel structures, 2015,17 (01):36-41.
[7] Tian Qixian, Du Xinxi. Experimental study on pushing out short stud of high-performance concrete composite pavement [J]. Bridge construction, 2016,46 (01):40-46.
[8] Yuan Weining, An Zhonghai, Zhang Xu. Simulation analysis of push-out test of stud based on ANSYS [J]. Industrial buildings, 2009,39 (S1):503-505+607.
[9] Su Qingtian, Han Xu, Ren Fei. Journal of tongji university (natural science), 2014,42 (07):1011-1016.
[10] Ministry of Housing and Urban-Rural Development, PRC. Code for Design of Concrete Structures: GB50010-2015 [S]. Beijing: China Architecture and Building Press, 2015.
[11] Nguyen H T, Kim S E.Finite element modeling of push-out tests for large stud shear connectors[J]. Journal of Constructional Steel Research, 2009,65 (10-11):1909-1920.
[12] Shi Chencheng, Wu Jingshu, Zhang Zeping, Ren Guopeng. Nonlinear Finite Element Analysis of Bending-shear Properties of Steel Plate Concrete Slab Based on ABAQUS [J]. Industrial construction, 2015,45 (09):7-12.
[13] Wang Jinfeng, Zhang Aiping, Wang Wenhao. Journal of zhejiang university (engineering science), 2020,54 (11):2076-2084.
[14] Ministry of Housing and Urban-Rural Development, PRC. Steel structure design standard: GB 50017 -- 2017 [S]. Beijing: China Architecture and Building Press, 2018.

CIVIL ENGINEERING JOURNAL

Article no. 9

THE CIVIL ENGINEERING JOURNAL 1-2022

UBLOX F9P FOR GEODETIC MEASUREMENT

David Zahradník, Zdeněk Vyskočil and Štěpán Hodík

Czech Technical University in Prague, Faculty of Civil Engineering, Department of Geomatics, Thákurova 7, Praha 6, Czech Republic; david.zahradnik@fsv.cvut.cz zdenek.vyskocil@fsv.cvut.cz, *stepan.hodik@sv.cvut.cz*

ABSTRACT

This article brings knowledge of the settings of the Ublox ZED-F9P device, which will allow to use this receiver to build-up a simple low-cost GNSS device. The settings for the rover and base station functions are different and need to be done very accurately. A wiring schema of the Ublox receiver with the Arduino system is presented, which as a whole device will enable the full functionality of the GNSS receiver as it is known from commonly used commercial devices. Ublox receiver was tested for accuracy and solution stability, results are shown in the article. The goal of this is to create devices usable for teaching students of our department as users or developers of applications using GNSS technologies.

KEYWORDS

Low-cost device, GNSS, Ublox, Raspberry PI, GSM module

INTRODUCTION

GNSS receivers are often used while teaching the field of geodesy and geoinformatics, either for the purpose of training the operator or as a source of data for other terrestrial measurements and other applications. GNSS technology is evolving rapidly in both the user and space segments. Receivers (the brand is not intentionally mentioned here) purchased fourteen years ago still work (after replacing GSM modems), but are technologically obsolete, cannot receive signals from Galileo or Beidou and generally have only few channels.

The motivation for creating our own GNSS equipment is the obvious possibility of operating a functional receiver for a fraction of the price at which a professional instrument can be purchased from a commercial seller of surveying equipment. The benefit is, of course, the uninhabited know-how that entails the assembly of the device. These instruments are created as a part of graduate projects at our department in cooperation of students and teachers. Assembling our own receivers on the basis of functioning GNSS boards is therefore a challenge for our research potential and at the same time an opportunity to keep the instrumentation for teaching at a functional and modern state.

This paper aims to bring the key information for users from the ranks of surveyors and surveyors who have decided to go their own way and build their receiver whether for economic or other reasons. We have an ambition to provide instructions for important settings but we do not create step-by step instructions since it is possible to find procedures on forums, YouTube, etc.

Many research teams are involved in the development of devices based on low-budget platforms. The closest to our activity is testing of RTK solution of two Ublox Zed F9P on short baseline [1]. Ublox modules are mostly used for solving position of cars and drones. Data from Ublox module are inputs for Kalman filter beside data from IMU [2], [3], [4] and [5].

In the article there is tested a Ublox ZED-F9P with ANN-BN-00 antenna by position accuracy, signal-to-noise ratio and position confidence. Low-cost GNSS receivers as Ublox achieve the same

position accuracy as professional receiver outside urban area. Position accuracy 1cm + 1ppm mentioned by the manufacturer was proved in RTK mode, see [6].

Multiple antenna with Ublox F9P was tested on the roof without multipath error. Low-cost antennas are comparable to professional geodetic antennas. Position accuracy by testing is less than 5mm for 40 min session, see [7].

One of the goals was to test the Ublox ZED-F9P GNSS module in various ways so that it can be confirmed that it is a receiver with centimetre accuracy. Comparison test was performed with a commercial GNSS receiver. Low-cost GNSS receivers have been analyzed and tested in various applications [8], [9], [10], [11], [12] and [13].

Our motivation for this paper is construction low-cost GNSS for teaching purposes. Students will be able to fully understand the functionality of GNSS receiver. Also, user will have full control over GNSS receiver so the black box problem will be dismissed.

METHODS AND MATERIAL

Two GNSS receivers were built for easy usage, because each type of GNSS measurement needs specific setting of Ublox module. The type of GNSS receiver comes from needs of a measurement. First GNSS receiver RTK was created for a land measuring and control points for areal photogrammetry. Second GNSS receiver is for long time observation. It will be used for landscape monitoring in places, where there is a risk of thievery or damage so the expensive professional receiver is excluded.

Construction of receiver RTK

GNSS receiver RTK is built for fast terrestric measurement and getting coordinates of control points for areal photogrammetry. The item will be used by students on practical work in terrain. GNSS receiver will be also used on drone or balloon for measuring in a forest, so the receiver must be almost weightless. The idea is to put receiver above the trees so the fix solution will be compute. Together with the measuring device, a smartphone application was developed for store measurements (RTK, Static), stakeout points and display of the current state of reception of satellite signals [14].

GNSS receiver RTK contains Ublox ZED-F9P, Bluetooth module HC-05, GSM module Arduino MRK 1400 and radio module Xbee PRO SS. Each component except Ublox F9P works as an input device of RTCM correction. Bluetooth module transfers data between the mobile device and the GNSS module. GSM module communicates with NTRIP client to send RTCM correction to GNSS module. Setup of the GSM module is by default prepared for the Czech permanent station network CZEPOS and it uses the nearest permanent station service RSM-RTK (valuable). For this service is it needed to send GGA message to NTRIP caster. Service must know approximate position of GNSS receiver for finding nearest permanent station. When GNSS receiver is turned on, it doesn't know its position. GSM module must wait until the GNSS receiver estimates an approximate position.

Radio module is for long distance usage, where Bluetooth module fails. Radio module can also communicate with own GNSS base station for a long baseline. All communication channels use the UART and 115 200 baudrate. High value of baudrate is better for the fastest communication between devices. Lower value of baudrate caused error buffer communication. GSM module does not contain two UART ports, which is resolved by using the SoftwareSerial library that replicates this functionality on other digital pins.

A power bank or Li-pol battery is used for the power supply. Input must be 5V and at least 2A. High current is needed by GSM module while connecting to network. After successful connection the high level of current decrease to few milliamperes.

RGB led serves as a visual control of GNSS status. It is connected to GSM module. Colour is changing by separate information from GGA message. Ublox ZED-F9P is configurable through Ublox software u-center. Modul is connected to PC with USB. The proper configuration can be seen in Table 1 and it is done on "View-Configuration View" application window.

Tab. 1 - GNSS receiver RTK configuration

Configuration view tab	Setting parameter 1	Setting parameter 2	Value
PRT (Ports)	UART1	Protocol In	RTCM3
		Protocol Out	NMEA
	UART2	Protocol In	RTCM3
		Protocol Out	NMEA
NMEA (NMEA Protocol)	Mode flags	High Precision	TRUE
MSG (Messages)	Messages	GxGGA	UART2
		GxGST	

Functionalities of GSM module were written in software Arduino IDE. For Arduino MKR-GSM, wiring private library was used. GSM module can connect to NTRIP client and send RTCM correction to Ublox. Module also control RGB LED to visualise GNSS status. The connection of the individual components is shown in the Figure 1 and sample PCB board of prototype in the Figure 2. Radio module Xbee PRO SS is configurable through software XCTU. Xbee shield or other device must be used for connection with pc.

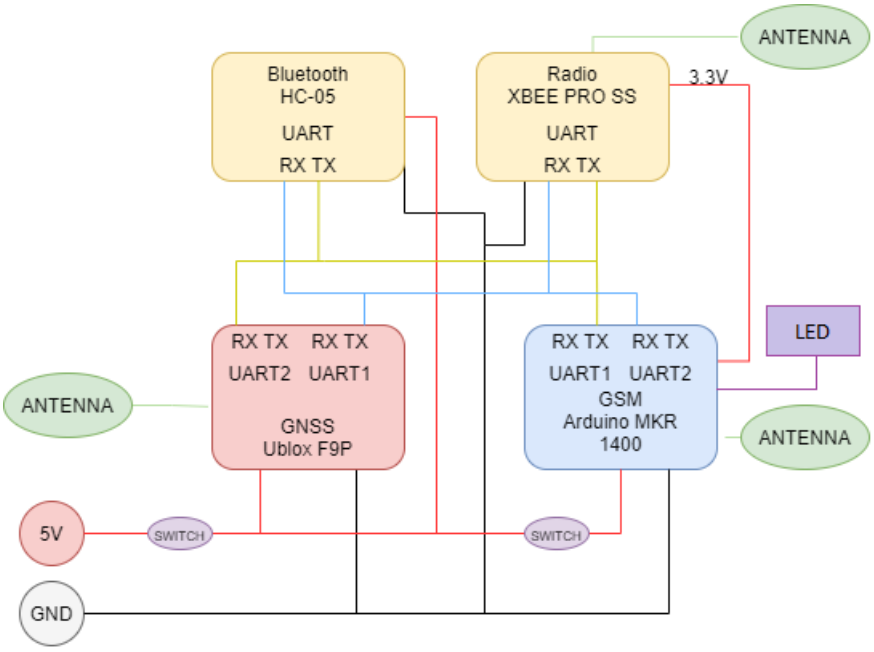

Fig. 1 – GNSS RTK receiver connection schema

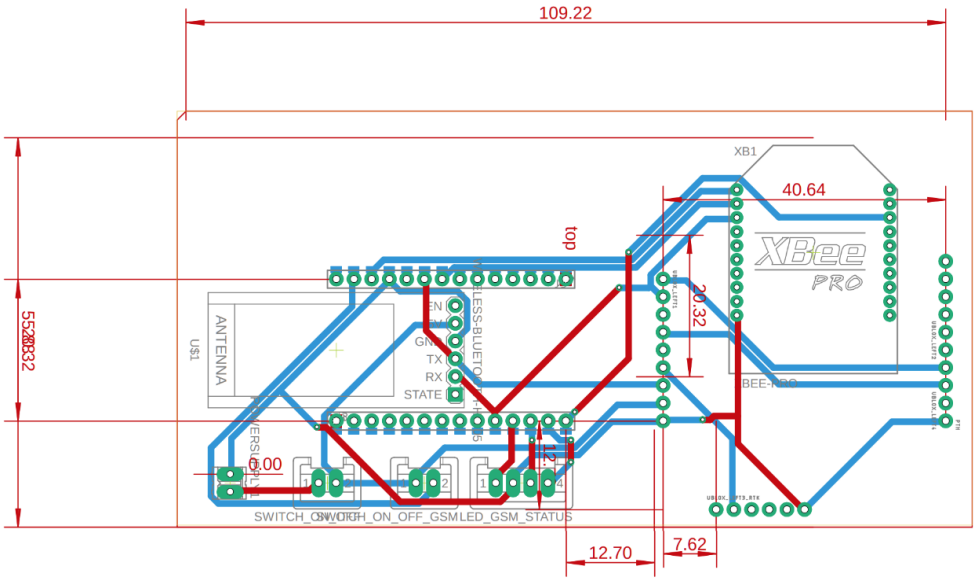

Fig. 2 - PCB layout of GNSS receiver board

Construction of receiver STATIC

GNSS receiver for static method is based on Ublox ZED-F9P and simple minicomputer Raspberry Pi (4th generation computer used). Those are connected via USB since the Ublox appears in the Raspbian linux system as a COM port. The Ublox output is setup according the Table 2 and so the Raspberry receives just raw measurement from the GNSS module. The data are converted to RINEX every hour using rtklib convertor and then stored to proper directory. One hour data file (separates by GNSS time) with measurement rate 1HZ containing observation of four GNSS systems has about 10MB according to the number of satellites in view.

The same time when the RINEX file is store to SD card of the Raspberry, it is also sent to all connected data storage peripheries (USB discs). The second variant of the control software is to push the data file to ftp server. The setup of ftp and also all possible setup (conversion frequency etc.) are in control software python file script.

Tab. 2 - GNSS receiver STATIC configuration

Configuration view tab	Setting parameter 1	Setting parameter 2	Value
PRT (Ports)	UART1	Protocol In	RTCM3
		Protocol Out	UBX+NMEA+RTCM3
	USB	Protocol In	RTCM3
		Protocol Out	UBX+NMEA+RTCM3
NMEA (NMEA messages)	Mode flags	High Precision	TRUE
MSG (Messages)	Messages	RXM-RAWX	USB, UART1
		GxZDA	USB, UART1

Receiver for static method is generally prepared for 12V power supply from car battery, it has DC step-down convertor which provides stabile 5V power supply for Raspberry and also Ublox. In the variant of the receiver connected to Ethernet, there is a USB cable for direct 5V

power supply from the phone charger. This variant has no USB connector on the box but RJ45 for connection to the ethernet.

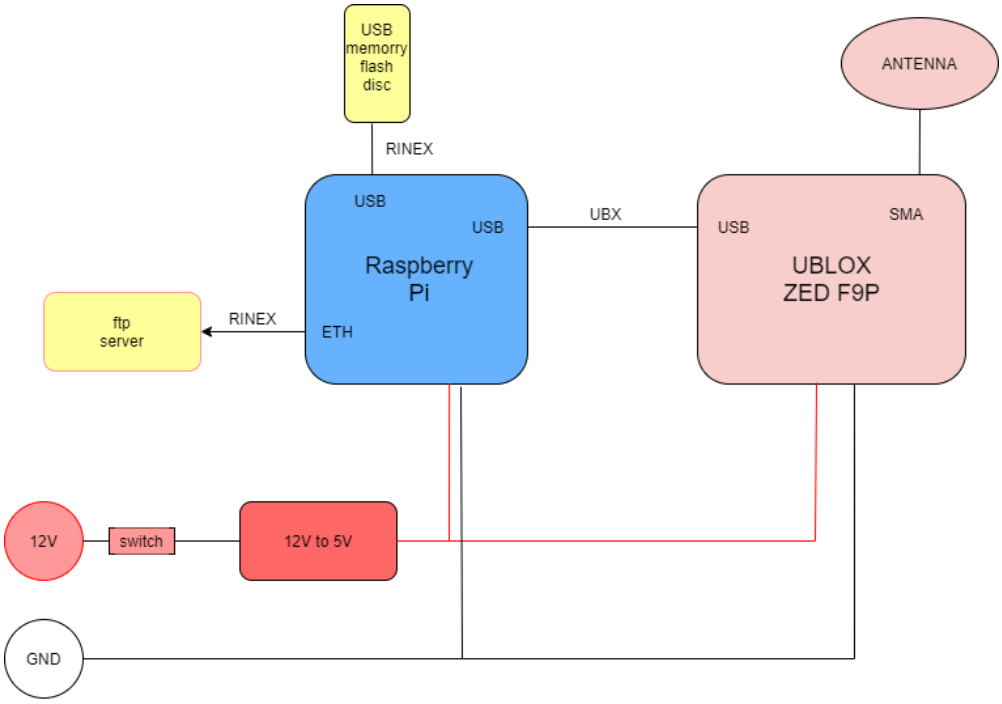

Fig. 3 - GNSS Static receiver schema

RESULTS

Testing STATIC receiver

The test verified the position of the antenna phase center. The test consisted of observing the change in the position of the antenna coordinates when the antenna was rotating around the vertical axis. A rotating device was designed, which allows automatic rotation with the antenna at a set time. The device consisted of a stepper motor and control unit, the motor was controlled by an Arduino Nano microcontroller with real-time module data (see Figure 4). The test itself lasted 24 hours, the measurement was divided into 24 stages after one hour of observation. After each hour determined by the real-time module, an engine command was sent via the Arduino Nano microcontroller to rotate 15 degrees of stepper motor. So in 24 hours the engine returned to original position. The measurement took place on the roof of the Faculty of Civil Engineering of the Czech Technical University.

Fig. 4 – Device for automatic rotation - Antenna and stepper motor (left) Control unit of stepper motor, Arduino Nano and real time clock module (right)

The data were processed like static GNSS method in the Leica Infinity software using data from the nearest permanent station - CZEPOS CPRG. The results were 24 coordinates, the plot of which can be seen in Figure 5. It is visible that there is no trend of phase centre shift, the resulting coordinates are completely random. It can therefore be concluded that the phase centre is in the material centre of the antenna. The resulting mean position error was 14 mm [15].

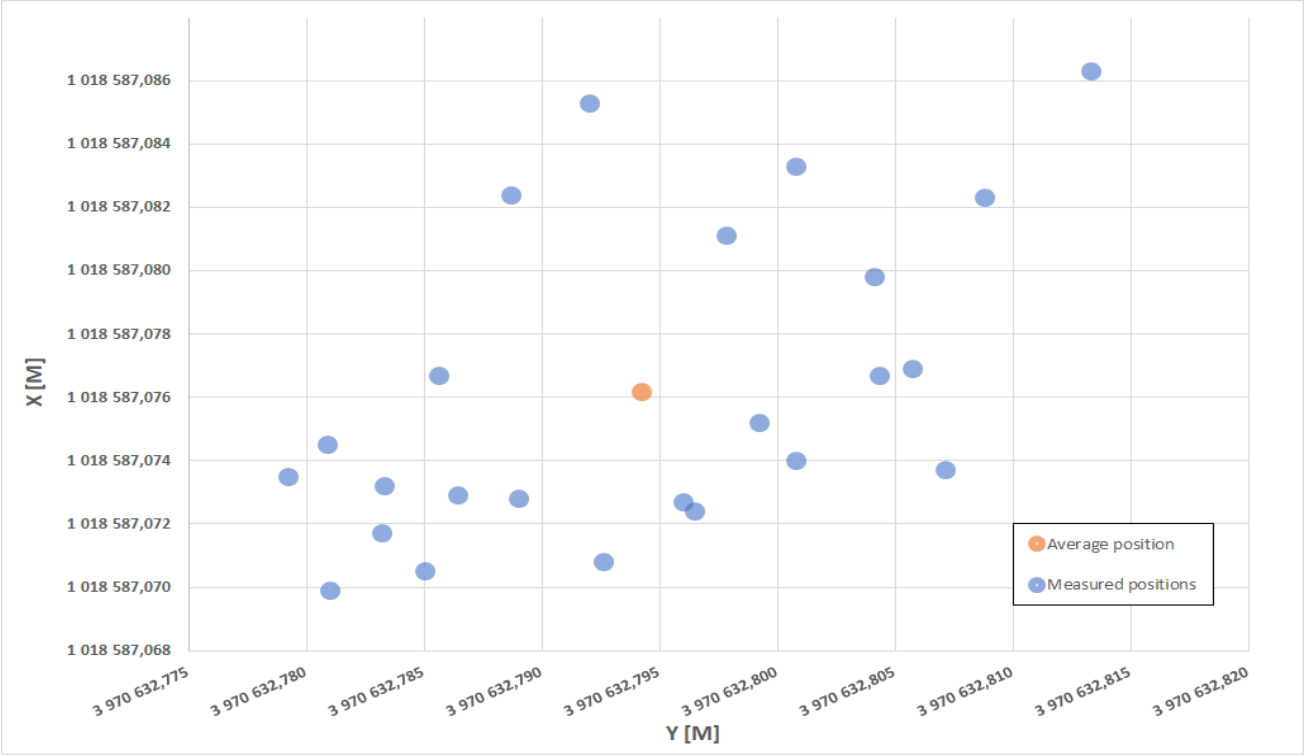

Fig. 5 - Phase centre position using low cost Ublox antenna [15]

Testing RTK receiver

The following parameters were determined during testing, the average time to find a fixed solution and the mean position error of all successive measurements were determined. The receiver antenna was fixed in the same position during the test to prevent accidental displacement. Then 50 measurements with 10-second observation were performed, in which the time of finding a fixed solution and the coordinates of the antenna were recorded. Between measurements, the antenna was covered with aluminium foil to prevent the input of all signals to the antenna, thus making it impossible to determine a fixed solution. After exposing the antenna, the time of finding a fixed measurement was measured. The result is an average time to find a fixed solution of 5 seconds and a mean position error 5 mm between measurements.

CONCLUSION

When testing the Ublox ZED-F9P module and the ANN-BN antenna, the accuracy of the device declared by the manufacturer was verified. The module can be used in surveying. The mean position error is 1 cm + 1ppm, when measured with Ublox ZED-F9P and ANN-BN antenna.

The Ublox ZED-F9P can be configured in various ways. The module can be used as a base and as well as a rover. The module supports RTK method measurements. The whole system is small and therefore inconspicuous. Therefore, it allows continuous measurement without the supervision of an authorized person, for example when measuring slope displacements. The module can be covered with a camouflage tarpaulin to make it as unobtrusive as possible. If someone stole the module, it would not be a big finantial loss. The price of the module and its accessories is about 500 USD.

We currently want to replace previously used GNSS receivers with the Ublox modules. Current GNSS receivers (Topcon HiPer Plus) are outdated and do not support data collection from Galileo and Beidou navigation systems. At the same time, the user interface does not allow complete control over the management of the receiver. This makes it a bit impossible to explain to students the principle of operation of the GNSS receiver in teaching.

With the Ublox module, the measurement principle with a GNSS receiver can be explained with a live demonstration. Students can configure the Ublox measurement module themselves and understand the process flow. Thanks to this, they can work with any GNSS receiver in practice. If the basic principle of setting up a base or NTRIP client is understood, they can deal with a lot of problems with electronics without the help of service. These devices are functional prototypes, but they do not aim to replace commercial devices from brands such as Leica, Trimble, etc. Their advantage lies in the low price and compact dimensions, and thanks to this they can be used in various applications.

The main disadvantage of these modules is that there are only few applications with which the module can be configured, or record measured data and most of them are only available on a PC. It is for these reasons that the GNSS controller application was developed at the department, which enables static measurement, RTK measurement (NTRIP client) and also stakeout imported or measured points. This application was further supplemented with measurement support in the national reference system S-JTSK.

Fig. 6 - Prototype of GNSS receiver

ACKNOWLEDGEMENTS

This work was supported by the Grant Agency of the Czech Technical University in Prague, grant No. SGS21/054/OHK1/1T/11

REFERENCES

[1] Hamza,V. Testing Multi-Frequency Low-Cost GNSS Receivers for Geodetic Monitoring Purposes.Sensors2622020,20, 4375.

[2] Lu,L. Performance Analysis of Positioning Solution Using Low-Cost Single-Frequency U-Blox Receiver264Based on Baseline LengthSensors2019,19, 4352.

[3] Rover, S.; Vitti, A. GNSS-R with Low-Cost Receivers for Retrieval of Antenna Height from Snow Surfaces266Using Single-Frequency ObservationSensors2019,19, 553.

[4] Feng, X.; Zhang, T.; Lin, T.; Tang, H.; Niu, X. Implementation and Performance of a Deeply-Coupled GNSS279Receiver with Low-Cost MEMS Inertial Sensors for Vehicle Urban Navigation Sensors 2020, 20, 3397.

[5] Elmezayen, A.; El-Rabbany, A. Ultra-Low-Cost Tightly Coupled Triple-Constellation GNSS PPP/MEMS-Based INS Integration for Land Vehicular Applications. Geomatics 2021, 1, 258-286. https://doi.org/10.3390/geomatics1020015

[6] Wielgocka, N.; Hadas, T.; Kaczmarek, A.; Marut, G. Feasibility of Using Low-Cost Dual-Frequency GNSS Receivers for Land Surveying. Sensors 2021, 21, 1956. https://doi.org/10.3390/s21061956

[7] Hamza, V.; Stopar, B.; Sterle, O. Testing the Performance of Multi-Frequency Low-Cost GNSS Receivers and Antennas. Sensors 2021, 21, 2029. https://doi.org/10.3390/s21062029

[8] X. Dong and W. Chen, "Research and Implementation of Dual-Frequency Precise Point Position Based on U-blox F9P," 2020 5th International Conference on Computer and Communication Systems (ICCCS), 2020, pp. 604-608, doi: 10.1109/ICCCS49078.2020.9118607.

[9] Cina, A.; Piras, M. Performance of Low-Cost GNSS Receiver for Landslides Monitoring: Test and Results. Geomat. Nat. Hazards Risk 2015, 6, 497–514.

[10] Jackson, J.; Davis, B.; Gebre-Egziabher, D. A Performance Assessment of Low-Cost RTK GNSS Receivers. In Proceedings of the 2018 IEEE/ION Position, Location and Navigation Symposium (PLANS), Monterey, CA, USA, 23–26 April 2018; pp. 642–649.
[11] Semler, Q.; Mangin, L.; Moussaoui, A.; Semin, E. Development of a Low-Cost Centimetric GNSS Solution for Android Apllications. Int. Arch. Photogramm. Remote Sens. Spat. Inf. Sci. 2019, XLII-2/W17, 309–314.
[12] Günter, J.; Heunecke, O.; Pink, S.; Schuhbäck, S. Developments towards a low-cost GNSS based sensor network for the monitoring of landslides. In Proceedings of the 13th FIG International Symposium on Deformation Measurements and Analysis, Lisbon, Portugal, 12–15 May 2008.
[13] Mahato, S.; Shaw, G.; Santra, A.; Dan, S.; Kundu, S.; Bose, A. Low Cost GNSS Receiver RTK Performance in Forest Environment. In Proceedings of the 2020 URSI Regional Conference on Radio Science (URSI-RCRS), Varanasi, India, 12–14 February 2020; pp. 1–4.
[14] Hodik,S. Development of low-cost GNSS device, Master's Thesis, 2019,http://hdl.handle.net/10467/83537
[15] Sikola,J. Testing GNSS module Ublox 9 generation Master's Thesis,2020,http://hdl.handle.net/10467/88561

CIVIL ENGINEERING JOURNAL

Article no. 10

THE CIVIL ENGINEERING JOURNAL 1-2022

DESIGN AND RESEARCH OF ELECTRIC BRICK CONVEYING TROLLEY IN UNFIRED BRICK FACTORY

Li Lin

Chengde Petroleum College, Department of Construction Engineering, Shuangqiao District, Chengde City, China; lw19871026@126.com

ABSTRACT

Under the background of building energy saving society, unfired bricks emerge as the time requires. The unfired bricks need to be conveyed to the maintenance site after being pressed and moulded, a lot conveying equipment in unfired brick factory especially small brick kilns at present are still unsteady and inefficient. In order to improve the production efficiency and conveying efficiency, the scheme of electric brick conveying trolley is put forward. This paper is centered on the design of electric brick conveying trolley. Firstly, the shortcomings of existing brick conveying equipment and the areas needing improvement are expounded, the main research contents and the main structure scheme are put forward. Secondly, specific design is carried out including structure design of main frame and loading carriage, calculation and selection of lifting system including motor, reducer and chain, calculation and selection of driving system including motor and chain, selection and design of steering system and braking system. Finally, finite element analysis(FEA) of bearing components is carried out and the design is summarized. The electric brick conveying trolley designed in this paper has the advantages of energy saving, environmental protection, high conveying efficiency and simple operation. It has broad application prospects in the future

KEYWORDS

Unfired brick, Brick conveying trolley, Electric drive, FEA

INTRODUCTION

There are approximately 80,000 brick kilns in China. It was estimated that China produced 340 billion bricks in 2012[1]. Over the past 30 years, great changes have taken place to the development of green building materials. Under the background that the Chinese government strongly encourages the development of new building materials for energy conservation, environmental protection and waste utilization [2], unfired bricks appear which use fly ash, cinder, coal gangue, tailings, chemical slag or natural sand, coastal mud (one or more of the above raw materials [3-7]) as the main raw materials without high-temperature calcination. It is mainly made of industrial waste residue and other materials. It does not need sintering in the manufacturing process and meet the use requirements only by curing at room temperature. It is very environmentally friendly building material, meanwhile the performance of unfired brick is

excellent: light weight, high strength and good heat and sound insulation performance.

After being pressed and formed by the unfired brick machine, the unfired brick needs to be cured to meet the use requirements in plant conveying. At present, there are still many small and medium-sized brick plants, which have different types of brick conveying equipment, including handcart, truck, forklift and so on [8-9]. Some uncontrollable factors such as vibration of these equipment during conveying will greatly affect the quality of unfired bricks. These brick conveying equipments have the disadvantages of time-consuming, laborious, high labor intensity, low conveying efficiency, low automation level and high brick crushing rate [10-11]. These disadvantages greatly limit the production efficiency and affect the quality to a great extent. The manufactured products have rough process and poor performance. It is in urgent need of adjustment and innovation.

Up to now, many brick making factories are already running with high level of mechanization and automation for proportioning, mixing, pressing and forming [12-13], in plant transportation, normal temperature maintenance and stacking. As to the conveying equipment, automatic stacking and conveying system has been used to transport non-cured or cured unfired bricks. The system is controlled by programmable logic controller, frequency converter and so on with stable startup process, fast transportation speed and high production efficiency [14]. There are also shortcomings as to the high investment, large floor spaces and complicate devices and software which are far beyond ability of small brick making plants.

Therefore, according to the special situation of China's unfired brick making industry, a new type of brick conveying equipment need to be developed for small and medium-sized brick plants to improve the conveying efficiency of unfired bricks. According to the design in this article, the energy is supplied by the storage battery. The principle of the brick conveying car effectively combines the work of forklift and stacking machinery [15]. It adopts the design of special loading carriage, so as to reducing conveying vibration and noise, brick making cost and workers' labor intensity, improving producing efficiency and product quality and saving energy. At the same time, it also responds to the call of national energy conservation and environmental protection.

OVERALL STRUCTURE DESIGN

Vehicle layout and design parameters

The electric brick conveying trolley adopts electric driving mode and three-wheel form. The rear single wheel is the driving wheel and the steering wheel, and the front two wheels are respectively fixed on the frame. The loading carriage is placed in the main frame at the front of the vehicle, the driver's seat is in the middle and upper part of the vehicle, the battery and lifting motor are in the middle and lower part of the vehicle, and the rear of the vehicle is the driving wheel and driving motor. The driver's position in the middle and upper part can make it easier for the driver to observe the loading of unfired bricks and road conditions, so as to facilitate the driver's control of the vehicle. The loading carriage is electrically driven and lifted by the lifting chain driven by the lifting mechanism. The steering mechanism adopts mechanical steering mode and the braking mode adopts front wheel belt braking. The energy supply device of the brick conveying trolley is a battery pack.

The main technical parameters of the brick conveying trolley are shown in Table 1.

Tab. 1: Main technical parameters

Technical indicators	Values and units
equipment weight	700kg
Loading weight	800kg
External dimension	≤2000×1900×1300mm
Battery	Capacity-140ah，more than 5 batteries
Loading capacity	Standard brick 6 plates
Lifting speed	0.2m/s
Vehicle speed	2m/s
Standard brick size	240×115×53mm

Overall design scheme

The main frame is a frame structure, which is mainly welded and connected by steel plate, welded square pipe and angle steel. The frame structure is used to place the loading carriage. A limit rod needs to be designed on the loading carriage to limit the shaking of the loading carriage. An intermediate shaft needs to be set on the upper part of the frame to transmit the torque output by the reducer to realize the lifting of the loading carriage.

The loading carriage is divided into two parts: the main body of the loading carriage and the hinged support plates on both sides of the bottom layer. The loading carriage is welded by rectangular pipe and angle steel, and the front-end opening is designed to facilitate loading and unloading of unburned bricks. The bottom support plate and the main body of the loading carriage are hinged, so that when the unfired bricks are unloaded, the bottom support plate can be opened to both sides, and the lower unfired bricks can support the upper unfired brick support plate, so as to enable the brick conveying trolley to unload the unfired bricks smoothly. The lifting chain is firmly connected with the loading carriage by bolts.

The lifting mechanism is mainly composed of motor, reducer, transmission chain, intermediate shaft and lifting chain, which is controlled by forward and reverse switch and speed regulating handle. The driving mechanism is composed of reduction motor, sprocket, chain and wheel. These components are fixed in the rigid structure. The rigid structure is hinged with the steering handle by pull rod. The driver rotates the handle to control the steering wheel to realize vehicle turning. Considering that the design speed of the brick transport trolley is low and the required braking torque is small, and the brake requirements are low, the manual braking mode is adopted. The brake lever and the brake pedal are connected together by pull rod and hinged to realize the driver's control over the vehicle speed. The overall structural layout is as shown in Figure 1.

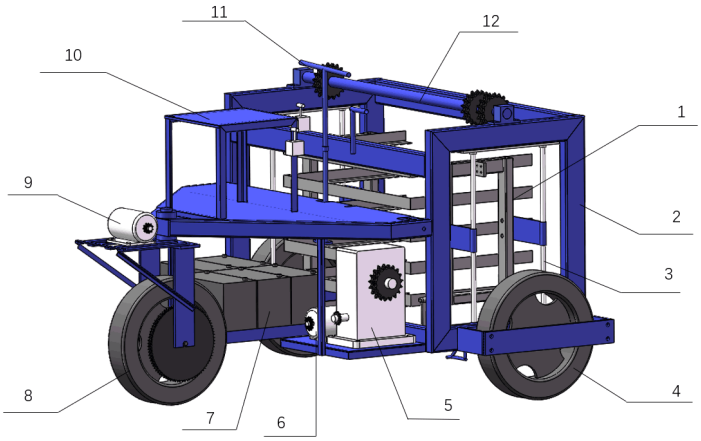

1- Loading carriage, 2- Main frame, 3- Limit lever,4- front wheel,5-decelerator,6-motor for Lifting,7-battery,
8-steering wheel, 9-drive motor, 10- Driver's seat, 11- Steering handle, 12- Intermediate shaft
Fig.1 - General layout of brick conveying trolley

Maintenance and use requirements

Before using the electric brick conveying trolley, the battery needs to be fully charged to meet the needs of one day. Do not use the battery until it is completely dead before charging. Long term wrong use of the battery will shorten its service life, reduce its capacity and shorten its working time. When the trolley is placed in an open and dry place, the charger needs to be ventilated for recharging. In addition, in actual use, each chain needs to be lubricated regularly, and the lubrication cycle depends on the actual use.

When in use, it is necessary to turn on the main power switch manually. The steering handle in front of the driver is used for vehicle steering. The rotation direction of the steering handle is the same as that of the vehicle. The right front of the floor of the brick conveying trolley is the vehicle brake pedal, which is used by the driver to control the vehicle brake. The forward and reverse switch on the right side of the driver's seat controls the forward and reverse rotation of the drive motor. The handle on the right side of the steering handle is used to adjust the speed of the drive motor. When the brick cart needs to travel, the driver needs to confirm the handle position of the forward and reverse switch. The forward and reverse switch at the front left of the steering handle is used to control the forward and reverse rotation of the lifting motor, and the fixed speed regulating handle at the front right is used to control the speed regulation of the lifting motor. During the loading of unburned bricks, the loading carriage needs to be lowered to a suitable position. The driving direction of the brick transport trolley must be parallel to the direction of the sidelines on both sides of the unburned brick support plate, and the unburned brick position needs to be located in the middle of the brick transport trolley. The driving position can be determined with the help of external references. When unloading the unburned bricks, a relatively flat ground shall be selected to ensure that the unburned bricks will not dump after being unloaded, resulting in unnecessary losses. The physical drawing of the whole vehicle is as shown in Figure 2.

Fig. 2 - Physical drawing of the whole vehicle

In actual use, it is necessary to properly protect key parts such as battery and motor to prevent damage caused by sundries such as rain. In this design, a thermal relay is set in the circuit to protect the motor. However, in actual use, if sundries jam the chain, resulting in abnormal noise or failure to work, the driver needs to cut off the main circuit switch to repair the vehicle, so as to ensure that it can be used again after troubleshooting.

DESIGN AND CALCULATION OF KEY COMPONENTS

Design and calculation of loading carriage

The loading carriage is very important in the design of the brick conveying trolley, because it directly supports the unfired brick support plate. The structural design of the loading carriage will greatly affect the quality of the unfired brick. In the process of pressing and forming the unfired brick, the mixed raw materials are loaded into the mold and pressed on the unfired brick support plate by the unfired brick machine, Then, the palletizing device is used for palletizing [16-17]. After palletizing, there is no gap between each plate of unfired bricks. If only the lowest supporting plate is lifted for conveying, the vibration and extrusion during conveying will greatly affect the quality of unfired bricks and increase the brick crushing rate.

The loading carriage in this design is mainly composed of the main carriage on the fifth floor and the hinged support plates on both sides of the sixth floor, as is as shown in Figure 3 and Figure 4. The hinge mode is adopted so that when the unfired brick is removed, the support plate at the lowest layer can be opened to both sides through the action of the limit device, as is shown in Figure 5. In this way, the loading carriage can continue to descend, so that the lower layer of unfired bricks supports the upper layer of unfired bricks. When the top layer of unfired bricks is completely pressed on the next layer of non-fired brick, the support plates on both sides of the loading carriage are completely separated from the unfired brick support plate, which is no longer effective. Then driving the brick conveying trolley backward will meet the requirements of easy loading and unloading, time-saving and labor-saving [18-21]. The unfired bricks are stacked automatically when they are unloaded.

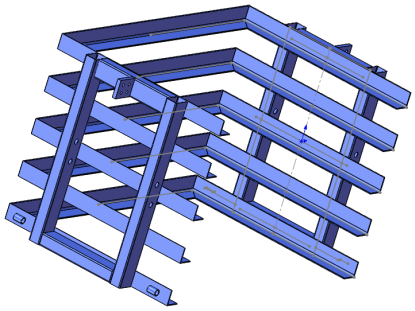

Fig. 3 - Loading carriage body

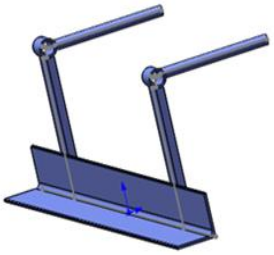

Fig. 4 - Hinged support plate

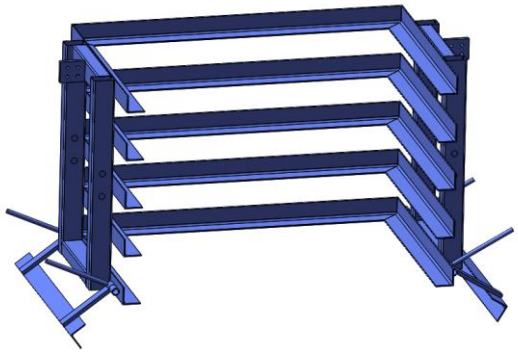

Fig. 5 - Overall loading carriage

In this design, the loading carriage adopts a U-shaped structure with a front-end opening welded by stainless steel welded square pipe and angle steel, and the front-end opening design is used to facilitate the loading or unloading of unburned bricks. Support plates are set on both sides of the loading carriage to support the unfired brick support plate, and the distance between each two layers of support plates is greater than the height of unburned bricks placed on the pallet, so that there is a gap between each two layers of unfired bricks, so as to avoid squashing of unfired bricks.

The internal dimension of the loading carriage is determined by the size of unburned brick, the thickness of unburned brick support plate and the loading capacity. The brick transport trolley mainly transports the ninth five-year plan standard bricks, and the standard brick size is

240X115X53mm. The supporting plate adopts the size of 900, which is mostly used in brick factories at present 900X600X35mm PVC supporting plate, the supporting plate is placed horizontally, and the loading capacity is 6 plates. The support plate of the upper five layers is fixed by stainless steel welded square pipe, and the connection method is welding. The support plate of the sixth layer is hinged with the upper five layers for loading and unloading. The upper part of the loading carriage is welded with two pieces, with a length of 180mm and a specification of 100 × 7 flat steel plate. The flat steel plate is firmly connected with the lifting chain by bolts to realize the lifting action of the loading carriage.

Holes are arranged on the stainless steel welded square tubes on both sides to install the limit device of the loading carriage, and the limit rod is arranged on the main frame to reduce the horizontal vibration of the loading carriage and only produce the movement in the vertical direction relative to the main frame. This design uses the unique structure of angle steel as the support plate. Each layer of non-fired bricks in the loading carriage is supported by angle steel. The gap between each layer of non-fired bricks in the upper five layers is set as 20mm, and the gap between the sixth layer and the upper layer is set as 30mm. The specification of angle steel is L50X50X3mm. The specification of stainless steel welded square pipe is 40X60X2.0mm. Then the internal length of the loading carriage is 600+ 30=630mm and the width is 900+2X15=930mm. The external dimension is 633mm length, 1096mm width and 818mm height.

Design and calculation of main frame

At present, all vehicles with load-bearing body have a frame as the frame of the whole vehicle. Most parts and assemblies of the vehicle are fixed on the frame through various connection methods, including engine, body panel, transmission and steering system, passenger seat and other related parts. The frame plays a role of fixing and supporting these components and assemblies, and it bears the effects of various forces inside and outside the vehicle.

We shall design the structural form of the main frame according to the layout position, installation form and use requirements of various parts of the vehicle. During the operation of the vehicle, the change of loading or road conditions may lead to the deformation of the frame. The deformation of the frame may affect the normal operation of various components or affect the driving safety of the vehicle. Therefore, in order to overcome these frame deformations that are not conducive to the normal operation of the vehicle, we need to ensure that the stiffness and strength of the frame meet the use requirements. At the same time, in order to improve the overall lightweight level of the vehicle and save energy, the frame mass should be as small as possible.

On various special vehicles, various special devices are also directly or indirectly installed on the vehicle chassis frame (hereinafter referred to as the main frame). The main frame is also the main bearing component of special devices on special vehicles [22]. In this design, we directly or indirectly install the lifting mechanism, loading carriage, battery pack and driving mechanism on the frame, and the frame is the main bearing component. At the same time, it also fixes the vehicle steering system, driver's seat, braking system and other relevant operating mechanisms, as is shown in Figure 6, which ensures the stability and steering flexibility of the

vehicle when driving.

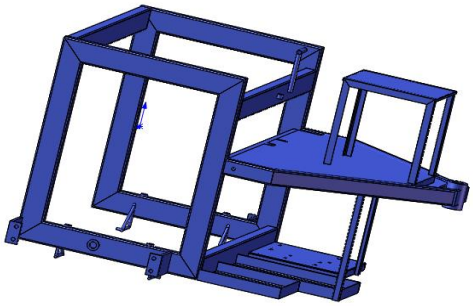

Fig - 6 Main frame structure

Stainless steel welded square pipe is widely used in various construction machinery because of its unique advantages: when the weight of components is equal, stainless steel welded square pipe has better torsion and flexural strength; And it has many specifications and models, which can provide users with a variety of choices. Angle steel can form various stress components of different shapes and sizes with various structural steels according to the actual required structures. It can also be used as a rigid connecting part between components. It also has good weldability, elastic deformation capacity and stiffness strength in practical use. Therefore, angle steel is widely used in various mechanical components and building structures. Therefore, the main frame of the special brick transport trolley is mainly welded by stainless steel welded square pipe, angle steel and steel plate.

The main frame is made of stainless steel welded square tubes with a specification of 50X100X3mm. Angle steel specification: L50X50X3mm. The main frame at the front end of the vehicle is in a frame structure to place the loading carriage and play a supporting role, and there is no cross beam under the front end of the vehicle to facilitate the loading and unloading of bricks without burning. A frame and platform structure welded by angle steel and steel plate are arranged below the middle of the frame to place the battery pack, lifting motor and reducer. The driver's seat and vehicle control device are equipped above the middle so that the driver can better observe and control the vehicle. The rear steering wheel and drive motor of the vehicle are fixed in the rigid structure and connected with the main frame through tapered roller bearings.

The height of the main frame mainly depends on the full load height and lifting distance of the loading carriage. According to the design of the above loading carriage, the full load height of the loading carriage is 818mm. The lifting distance depends on the distance between each layer of unburned bricks and the upper layer in the loading carriage and the ground height of the lowest layer of unburned bricks during full load transportation. It is designed from the above: the distance between each of the upper 5 plates is 20mm, and the distance between the sixth plate and the upper plate is 30mm. During full load transportation, in order to make the brick conveying trolley has certain trafficability, the distance between the lowest supporting plate and the ground is tentatively determined as 200mm. So the frame height is 950mm. The width of the frame mainly depends on the width of the loading carriage. The width of the loading carriage designed by the loading carriage is 1096mm, and the working space for lifting chain and transmission chain is reserved, the external width of the main frame is 1472mm. The distance between the

middle floor of the vehicle and the lower cross beam is determined by the size of the reducer, taking 500mm. The driver's seat is fixed on the floor in the middle of the vehicle. The seat is 400mm high, 400mm long and 400mm wide. The horizontal distance between the front end of the seat and the upper cross beam is set as 300mm as the driver's operation space.

Design and calculation of storage battery

Electric vehicles have become the inevitable direction of the future development of the automotive industry, which depends on the unique advantages of zero emission of electric vehicles. The driving energy of electric vehicles mainly comes from electric energy storage devices such as rechargeable batteries or super capacitors loaded on the vehicle. This energy supply mode determines the advantage that electric vehicles do not emit any harmful gases and particles into the atmosphere. At the same time, the electric energy of the power plant comes from the capture of various natural energy sources, such as coal, nuclear energy, tidal energy, wind energy, light energy, heat energy, etc. even if the power plant uses coal as fuel to obtain electric energy, it can still have relatively higher efficiency, which means that using electric energy can save limited oil resources. In addition, the brick truck driven by diesel engine brings inevitable vibration transmitted to the main frame, which will greatly increase the brick breaking rate. Therefore, using battery as energy supply device is the best energy supply scheme for brick truck. Under the background of the depletion of oil resources and the state's strong support for the development of electric vehicles, the electric vehicle industry has developed rapidly, and the battery industry has also developed rapidly. The developing power sources mainly include sodium sulfur battery, nickel hydrogen battery, nickel cadmium battery, lithium battery, fuel cell, flywheel battery, etc. The research and rapid development of power battery has laid a solid power foundation for the development of pure electric vehicles. In contrast, the development of lead-acid battery has a history of more than 100 years [23]. So far, the technology of lead-acid battery has become mature after continuous development and improvement.

Nowadays, lead-acid battery is the most widely used in the automotive industry, because it has been developed for many years and has a separate power battery type. This battery has the advantages of large instantaneous discharge current and can discharge at a large current all the time. Compared with the other types of power batteries, it has mature technology, stable discharge voltage and reliable performance [24], It allows deep discharge, can be recycled, and can be used in a wide temperature range. In practical use, the use requirements are low and the maintenance method is simple. In actual production, it can be mass produced with low production cost, simple structure, low price and higher cost performance.

Therefore, under the comparison of these batteries, lead-acid battery is the best choice for the energy supply device of brick conveying trolley. According to the requirements of the project, the capacity is 140ah. It is proposed to select 5 lead-acid batteries with rated voltage of 12V and capacity of 140ah. The size of the battery is 360 × one hundred and seventy-two × 253, each weighing 30kg.

Design and calculation of lifting system

The design adopts the scheme of chain drive lifting. The chain drive is not easy to slip, the transmission is more accurate, reliable, high transmission efficiency, and can adapt to the harsh environment of humidity, high temperature and dust. The lifting system is a special lifting device designed for the actual use requirements of the brick transport car. The lifting motor is driven by the battery to convert the electric energy into mechanical energy. The speed reducer is decelerated and the loading carriage loaded with unburned bricks is lifted through chain drive. The transmission diagram of lifting system is as shown in Figure 7. The flowchart of lifting system design process is as shown in Figure 8. According to the main frame design, the lifting motor and worm gear reducer are fixed on the frame structure or platform under the middle of the vehicle, and the connection method is bolt fastening connection. The lifting motor drives the input shaft of the worm gear reducer to rotate through the chain drive. After the worm gear reducer reduces the speed and increases the torque, the intermediate shaft placed above the main frame is driven to rotate through the transmission chain. The sprocket used for the transmission chain and the lifting chain are fixed on the intermediate shaft to make the lifting chain move, to realize the lifting or lowering action of the loading carriage.

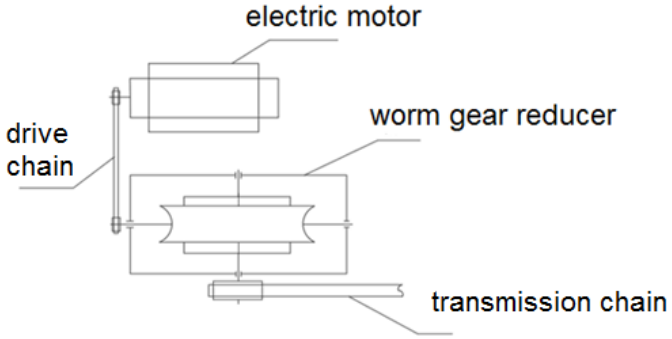

Fig. 7 - Lifting system transmission diagram

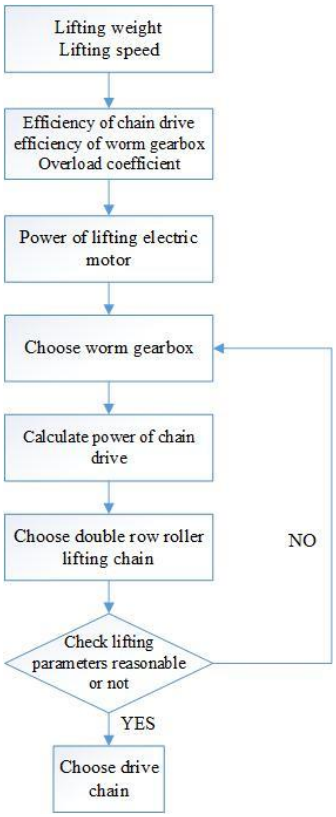

Fig. 8 - Flowchart of Lifting system design process

According to the design requirements, the lifting mass is 800kg. According to the mechanical design manual, the chain transmission efficiency is 0.96, the transmission efficiency of worm gear reducer is 0.9, and the overload coefficient is tentatively 1.3.

$$P = FV = 1600\text{W} \quad (1)$$

$$P_N = 1.3P/0.96/0.9 = 2407\text{W} \quad (2)$$

In the formula, gravity of the lifted unburned brick F is set as 8000N. The lifting speed V is set as 0.2m/s according to the design requirements.

It is proposed to select the lifting motor with the power of 2500W and the rated voltage of 60V according to the requirements of the subject. Subject to the requirements of the reducer reduction ratio, size and lifting speed, the DC series excitation reduction motor with horizontal foot installation, self-cooling, rated voltage of 60V and rated power of 2500W is finally selected as the lifting motor, and the motor reduction ratio is 5:1, The rated speed of the motor is 3000r / min, the output speed is 600r / min, the rated torque of the motor is 9.2N • m, and the output torque is 46N • m.

Reducer is often used in various power transmission systems. The main types include gear reducer, worm reducer, gear worm reducer and planetary gear reducer. These types of reducers have their own characteristics. Among them, gear reducers are most widely used because of their high transmission efficiency. Single-stage gear reducers are mainly used in occasions where the transmission ratio is less than 8. Simultaneous interpreting of the two-stage gear reducer can be divided into expansion, shunt and coaxial. The overall size of the single stage

gear reducer is smaller than that of the same gear ratio, but there are some disadvantages such as uneven load distribution and uneven bearing capacity.

The reduction ratio of single-stage worm reducer is generally suitable for occasions with a reduction ratio of 10 ~ 70, and its input and output shafts can be distributed at right angles, which can change the direction and height of power transmission. Its main feature is that the input and output shafts have a variety of layout forms, and can only transmit power in one direction, and self-locking will be realized in the reverse direction. The reduction ratio of gear worm reducer is generally not less than 35, and its principle is equivalent to two-stage reduction of gear reduction and worm reduction. It has two layout forms: worm drive at the high-speed stage and gear drive at the high-speed stage. Both have unique advantages: the latter has compact structure, small overall size, the former has high efficiency and less energy loss. Compared with the above reducers, planetary gear reducer is famous for its small volume, high precision, high transmission efficiency and wide speed regulation range. Therefore, it is widely used in all kinds of motor transmission systems.

According to the actual use requirements in the design, the electric brick transport trolley plans to select a 25:1 worm reducer. According to the output speed of the lifting motor of 600r / min, the output speed of the reducer is 24r / min. If the number of custom sprocket teeth is the same, z = 17, according to the formula as below.

$$P_C = \frac{K_A P}{k_z k_p} \leq P_0 \tag{3}$$

In the formula, P_C means calculated power of chain drive, P_0 means rated power, *P* means nominal transmission power, the power of lifting motor is set as 2500W, K_A means working condition coefficient, it is set as 1.3 from table 2, k_Z means small sprocket number factor, it is set as 0.887 from table 3, k_p means row number coefficient, it is set as 1.7 from table 4.

From the calculation, we get $P_0 \geq 2155W$, together with $n_1 = 24r/\min$, By look-up table ,16A type double row roller chain is chosen as transmission chain and lifting chain. The lubrication method is manual periodic lubrication.

Tab. 2 - Working condition coefficient

Load type	Working machine	Power machine		
		internal-combustion engine Hydraulic transmission	Electric motor or steam turbine	internal-combustion engine mechanical drive
Steady load	Liquid mixer, Medium and small centrifugal blower, Light conveyor, centrifugal pump	1.0	1.0	1.2
Medium load	Medium cranes and hoists, agricultural machinery, Food machinery, grinder	1.2	1.3	1.4
Large impact	construction machinery, Mining machinery, Forging machinery, Punch, Shearing machine, Vibrating machinery	1.4	1.5	1.7

Tab. 3 - Small sprocket number factor

Z	9	11	13	15	17	19	21	23	25
K_z	0.446	0.554	0.664	0.775	0.887	1.00	1.11	1.23	1.34

Tab. 4 - Multi row chain coefficient

Row number	1	2	3	4	5	6
K_P	1	1.7	2.5	3.3	4.0	4.6

$$\mathrm{d} = \frac{P}{\sin(180°/z)} \tag{4}$$

In the formula, P means Selected roller chain pitch, it is set as 25.4mm, Z means number of teeth of sprocket, it is set as 17.

From the calculation, we can get sprocket indexing circle diameter $d = 138mm$, perimeter of dividing circle is 434mm, number of sprocket teeth is the same, the intermediate shaft speed is $24r/\min$.

Lifting speed $V = 0.434\text{m} \times 24\text{r/min} = 0.1736\text{m/s}$.

Torque check:

$$T_1 = 46 \times 25/ \ (0.138/2) = 14417\text{N} \tag{5}$$

$$T_2 = 14417 \times 0.9 \times 0.96 = 12456\text{N} > 8000\text{N} \tag{6}$$

Then the reduction ratio of lifting motor and worm gear reducer meets the requirements. The model of worm gear reducer is determined as WPA-120-1/25-A according to the input shaft power, reduction ratio, input and output shaft position. The reducer base is 320mm long and 230mm wide, the whole machine is 430mm high, the input shaft diameter is 30mm, the length is 65mm, and the keyway size is 8 X 4； The diameter of output shaft is 45mm, the length is 85mm, and the size of keyway is 14 X5.5.

The lifting motor drives the worm reducer through chain drive. The selection of this drive chain is based on the following formula:

$$P_C = \frac{K_A P}{k_z k_p} \leq P_0 \tag{7}$$

In the formula, P_C means calculated power of chain drive, P_0 means rated power, *P* means nominal transmission power, the power of lifting motor is set as 2500W, K_A means working condition coefficient, it is set as 1.0 from table 2, k_Z means small sprocket number factor, it is set as 0.775 from table 3, k_p means row number coefficient, it is set as 1.0 from table 4.

From the calculation, we get $P_0 \geq 3266W$, together with $n_1 = 24r/\min$, By look-up table ,08A type single row roller chain is chosen as transmission chain. The lifting motor is used as the power source to drive the operation of the worm gear reducer.

According to the above calculation, the total mass of moving parts up and down $m = 880kg$, Rated power of lifting motor $P = 2500W$, Output speed $n = 600r/\min$, Reduction ratio of worm reducer $i = 25$, Efficiency of worm gear reducer $\eta = 0.9$, Number of sprocket teeth $z = 17$, Sprocket ratio $i = 1$, Double row chain type number 16A, Check the mechanical design manual for chain minimum tensile strength $F = 111.2KN$, pitch $p = 25.4mm$.

Average speed of sprocket $n = 24r/\min$, The average speed of the chain is according to the following formula:

$$\text{V} = \frac{Pzn}{60} \times 10^{-3} = 0.17m/s \tag{8}$$

In the formula, P means Chain pitch, z means number of sprocket teeth, n means average speed of sprocket.

The tension of chain tight edge is according to the following formula:

$$F_t = \frac{P\eta}{V} = 13235.3N \quad (9)$$

In the formula, P means Lifting motor power, η means transmission efficiency of worm gear reducer, V means average chain speed.

Chain speed $V = 0.6m/s$, it is low speed chain drive, The main failure form is the static tension fracture of the chain, so it is calculated according to the static tension strength and the safety factor S is checked.

$$S = \frac{F_u}{K_A F_t} = 6.46 \geq [S] \quad (10)$$

In the formula, minimum tensile strength of chain $F_u = 111.2KN$, tight edge tension of chain drive $F_t = 13235.3N$, Working condition coefficient $K_a = 1.3$, refer to the mechanical design manual, allowable value of chain static strength safety factor $[s] = 4-8$, tension on Chain $F_a = 8800\,N$.

The safety factor of static tension is based on the following formula:

$$S_T = \frac{F_u}{K_A F_a} = 9.7 \geq [S] \quad (11)$$

According to the above check calculation, the strength of the selected 16A double row roller chain meets the requirements.

In order to realize the lifting or lowering action of the loading carriage, the switch, speed control handle and motor controller should be installed in the circuit. In the process of working, the failure of the lifting device of the brick carriage may cause the motor to be blocked and damaged. The protection measures for the motor are to set the thermal relay in the circuit. The control of the forward and reverse switch can realize the positive and negative rotation of the motor, so as to lift or lower the loading carriage.

Design and calculation of driving system

The drive system of electric vehicle plays the role of effectively connecting the power storage system and the driving wheel and converting the form of energy. Since the brick conveying car adopts battery power supply, it needs to be driven by motor. There are three types of transmission after the motor generates power: belt transmission, transmission chain transmission and transmission shaft transmission. Belt transmission relies on the friction between belt and pulley for power transmission. In contrast, belt transmission has the lowest cost and is very simple to install and maintain, but the belt must be tensioned during transmission. Otherwise, it is easy to slip and affect the transmission effect. The transmission shaft has high transmission efficiency, stable and reliable performance and large power transmission. It is mostly used in heavy-duty vehicles, but there are installation angle requirements in practical use.

Chain transmission is widely used. The same transmission efficiency is high, maintenance is simple, transmission is more accurate, and can adapt to humid, dusty and other harsh service environments. Due to the limitation of installation space and cost, the way of chain transmission is selected in this subject. The driving system uses battery power to drive the motor to generate power, and the power is transmitted to the driving wheel by chain transmission and deceleration to drive the vehicle.

The maximum total mass of the whole vehicle is 1500kg (sum of equipment weight and loading weight), the friction coefficient of most brick factory pavement is taken as 0.025[25], The design speed is 2m/s. According to the design requirements and mechanical design manual, the chain transmission efficiency is set as 0.96, overload factor is set as 1.5.

$$\mathrm{F} = \mu \mathrm{mg} = 375\mathrm{N} \tag{12}$$

$$\mathrm{P} = \mathrm{FV} = 750\mathrm{w} \tag{13}$$

$$P_N = 750 \times \frac{1.5}{0.96} = 1172\mathrm{w} \tag{14}$$

The motor power is bigger than P_N, A DC series excitation reduction motor with self- cooling is chosen and the horizontal foot is installed. Rated voltage is 60V, Rated power is 1300W, reduction ratio is 5.2:1, rated speed of the motor is $3200\,r/\min$, Output speed is $625\,r/\min$, Rated torque is $3.8N \cdot m$, Output torque $19.76N \cdot m$.The flowchart of driving system design process is as shown in Figure 9.

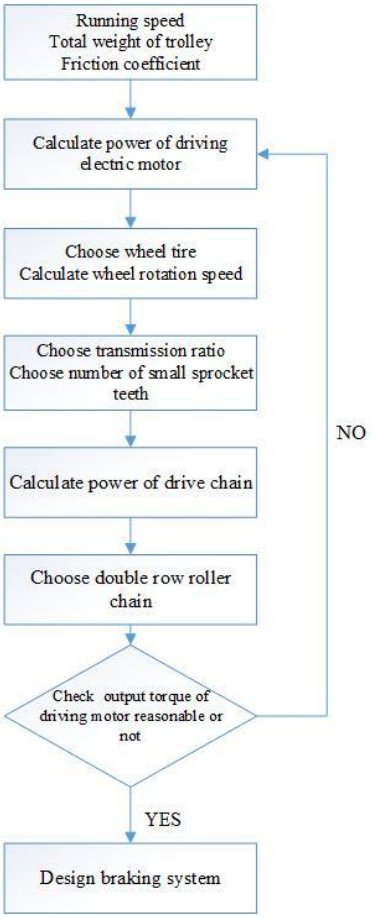

Fig. 9 - Flowchart of driving system design process

The driving motor of the brick transport trolley drives the rear wheel through chain drive. According to the weight of the whole vehicle and referring to the road conditions of most brick factories, it is proposed to select 4.5 R12 radial steel wire tire, which has a section width of 114mm, a diameter of 545mm and a circumference of 1.7m. Tire pressure: 600kpa, normal use; Tire pressure 650kpa, rated load 0.8t; Tire pressure 700KPA, rated load 1.0T. According to the design speed $2m/s$, tire circumference 1.7m, Available wheel speed $1.18r/s = 70.59r/\min$, determine the transmission ratio $615/70.59 = 8.71$ according to the speed of the driving motor and the driving wheel, transmission ratio is set as 9, Set the number of pinion teeth as Z_1=9, so the number of teeth of large sprocket is Z_2=81, according to the formula:

$$P_C = \frac{K_A P}{k_z k_p} \le P_0 \tag{15}$$

In the formula, P_C means calculated power of chain drive, P_0 means rated power, *P* means nominal transmission power, the power of lifting motor is set as 2500W, K_A means working condition coefficient, it is set as 1.0 from table 2, k_Z means small sprocket number factor, it is set as 0.446 from table 3, k_p means row number coefficient, it is set as 1.7 from table 4.

From the calculation, we get $P_0 \ge 2229W$, together with $n_1 = 615r/\min$, By look-up table ,08A type double row roller chain is chosen as transmission chain with the pitch $p = 12.7mm$.

Diameter of indexing circle of two sprockets according to formula:

$$\mathrm{d} = \frac{P}{\sin(180°/z)} \tag{16}$$

From the calculation, we can get $d_1 = 37.1$, $d_2 = 325.6$, Torque check according to formula

$$T = \frac{FR}{i\eta} \tag{17}$$

The drive motor requires the least torque $T_1 = 11.83N \cdot m$, the rated torque of the drive motor is $T_2 = 19.76N \cdot m$, so the motor meets the requirements.

In order to realize the forward and backward of the brick conveying trolley, it is necessary to connect the reverse forward switch, speed regulating handle and motor controller in the driving circuit to control the forward and reverse rotation of the driving motor. Similarly, in order to prevent the motor from blocking and damaging the motor due to the failure of the transmission mechanism, it is also necessary to connect the thermal relay. All the chains used in the bricks

transportation car are shown in Figure 10.

Fig. 10 - All the chains used in the bricks transportation car

Design of steering system

In this design, the rear single wheel is the steering wheel, and the load is mainly in front of the vehicle. Considering the economic and simple and reliable practical requirements, the brick conveying trolley adopts mechanical steering [26]. The steering control device is directly hinged with the transmission device without a steering gear, that is, the rigid structure of the fixed steering wheel is hinged with the steering handle through the pull rod, so as to realize the driver's function of controlling the forward direction of the vehicle, as is shown in Figure 11. The steering handle and the shaft in the rigid structure of the steering are connected with the main frame through bearings. The mechanical steering system is simple and reliable, easy to maintain, and is more suitable for the service conditions of unfired brick plants.

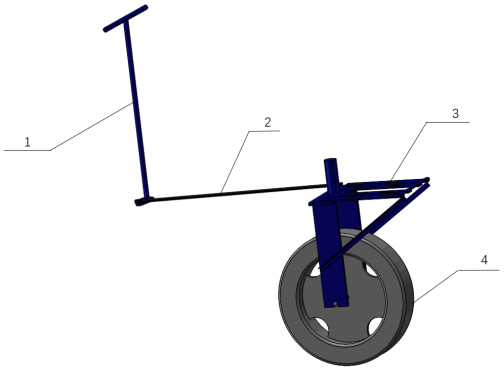

1- Steering handle, 2 - Steering tie rod, 3- Steering rigid structure, 4- Steering wheel
Fig. - 11 Steering system schematic

Design of braking system

The belt brake is composed of a brake drum and a brake belt that can rub with the circumferential surface of the brake drum. When the vehicle needs braking, the brake belt is stretched and contracted to contact the brake drum to generate friction and produce braking

effect. It can be divided into simple belt brake, differential belt brake and comprehensive belt brake. These three types have simple and compact structure. The utility model has the advantages of easy loading, unloading and maintenance and large braking torque. However, its heat dissipation is poor, and the rotation direction of the brake drum will affect the braking force generated by the simple type and differential belt type, which limits its application range. Belt brakes are mostly used in occasions requiring compact structure [27]. The action diagram of integrated belt brake is shown in Figure 12.

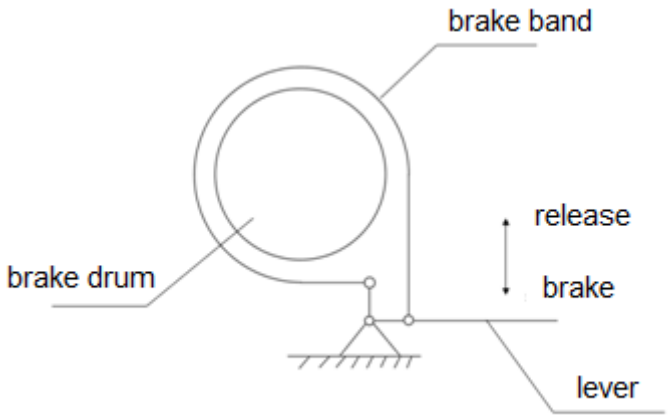

Fig. 12 - Working principle diagram of belt brake

In this design, the design speed of the brick conveying trolley is 2m/s, which belongs to low-speed operation and requires less braking force. Therefore, the requirements for the braking device are low and limited by the size of the installation space. In order to achieve the characteristics of energy conservation, environmental protection, durability and simple operation, this design selects the comprehensive belt brake and manual braking system. The brake lever in the integrated belt brake is hinged with the brake pedal through the pull rod, and the driver can control the braking of the vehicle through the pedal.

FINITE ELEMENT ANALYSIS OF BEARING PARTS

In order to check bearing capacity of the loading carriage and main frame, check the strength of the part, verify the structure design is reasonable or not, the deformation process is simulated and the parameters are obtained with the help of finite element analysis software ANSYS. The load curve of the loading carriage, the deformation process of main frame, the stress field, the strain field, and velocity field can be analyzed and summarized, through which the deformation principles can be known. The reaction force of the brick plates and loading carriage, the stress distribution of each part of main frame can be calculated.

Finite element analysis method

The basic steps of finite element problem solving can be divided into: firstly, the physical properties and solving region of the solving model are defined according to the actual problem.

Then the solution model is discretized, that is, the finite element mesh of the solution model is divided [28]. Obviously, the more detailed the mesh is, the closer the approximate solution of the discrete model is to the exact solution, and the more accurate the solution of the model is. At the same time, it brings the disadvantage of increasing the amount of calculation. Finite element mesh generation plays an extremely important role in finite element analysis. The next step is to determine the control method and state variables.

A physical problem to be solved can generally be expressed by a set of equations containing the boundary conditions of the state variables of the physical problem. Then, the element derivation is carried out, and an appropriate approximate solution is set for a certain element, that is, the formulation of the finite element is derived. Then, the final assembly solution, that is, all finite element final assembly forms the total matrix joint equations of the discrete model. The last step is to solve the simultaneous matrix equations and explain the results.

Finite element analysis can be divided into three basic stages: pre-processing, General Assembly solution and post-processing. The pre-processing is to establish the solution model and mesh it. The post-processing is to collect the solution and analyze and evaluate it, so that users can easily extract the obtained information and understand the calculation results more intuitively.

Finite element analysis results

In the finite element analysis, it is necessary to select the materials of the main bearing components, import the assembled assembly into ANSYS, and then mesh the whole assembly. In this process, it is necessary to select the appropriate mesh size to ensure the accuracy of the analysis results. Then add loads and constraints to the assembly to ensure that the loads and constraints are added correctly, and then conduct finite element analysis of the assembly.

As follows, Table 5 shows the names of the materials selected for the structure, and Table 6 shows the load constraints imposed on the bearing structure and the properties of the table. Figure 13 is the schematic diagram of meshing, Figure 14 is the stress diagram in the analysis results.

Tab. 5: Selected material properties

Material name	Q345
Material density	7.85E+03kg/m³
Elastic modulus	2.06E+11N/m³
Poisson's ratio	0.280
yield strength	345Mpa

Tab. 6 - Loads, constraints and attributes

Load type	Force
Load value	8000N
Number of constraint faces	5

Grid size	20mm
Number of grids	72429

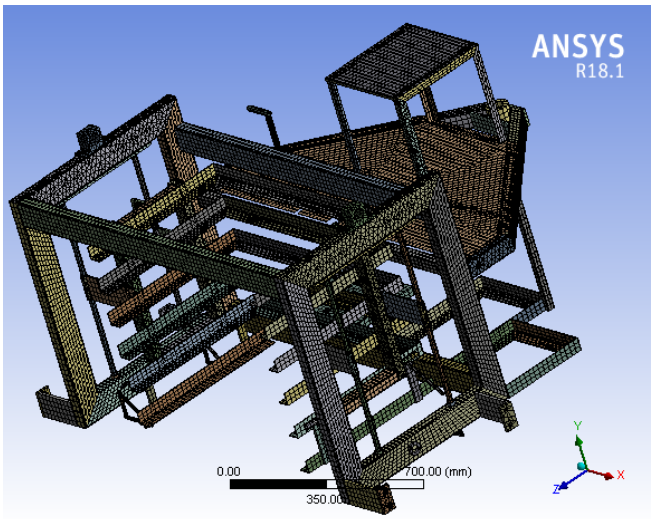

Fig. 13 - Meshing of the loading carriage

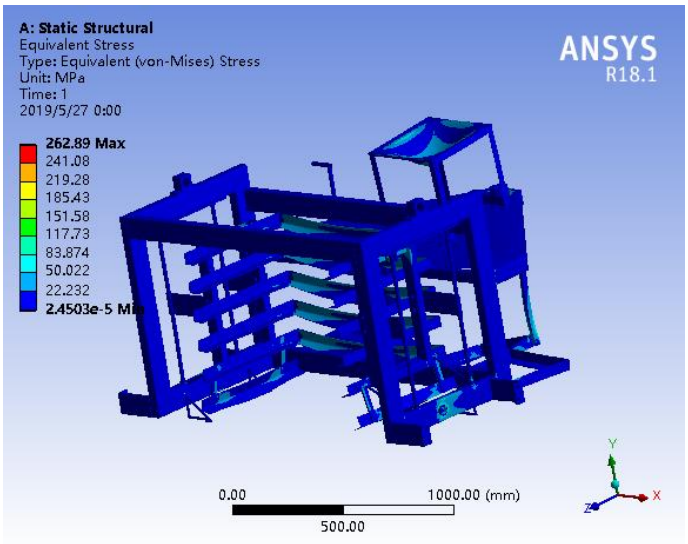

Fig. 14 - Stress contour of the loading carriage

The finite element analysis results show that the deformation and stress of the support beam of the loading car are large, max stress 241.08MPa, meet design requirements.

CONCLUSION

The designed brick conveying trolley is fully electric. The power consumption is as low as 5-7 KW·h. It takes 8-10 hours to get the battery full charge. There is a gap between the upper and lower layers when conveying bricks, the vibration amplitude is small. Therefore there will be few brick breaking problems. Loading capacity reaches 4-5 boards continuous working 14-16

hours after full charge. It reduces brick breaking rate and conveying cost than common diesel brick truck.

With the advantages of simple operation, little noise, energy saving and simple structure. One person can drive the trolley easily, which greatly reduces labor force, labor intensity and production cost, improves production efficiency and increases brick factory profit. It is an excellent ideal equipment for unfired brick factory which is suitable for various types of unfired brick types for integrating the work of the stacking machine and the forklift. It is suitable for different brick machines and brick plates of different sizes for users to choose. If there are brick machines and brick plates of special sizes, the factory only needs to change the loading carriage.

The characteristics of the brick conveying trolley are as follows:

(1) No damage to the quality of brick blank: the set of equipment automatically palletizes and lifts. During operation, each brick has a gap, which does not press, squeeze, lean or twist, and does not damage the brick.

(2) Green environmental protection: the trolley is driven by electric energy, without noise, vibration, oil pollution and carbon dioxide emission.

(3) Simple operation, The operation of brick conveying trolley has been simplified to the operation of the steering wheel, lever and button, and one person can complete the work task very easily.

(4) Stable power output, reliable performance and longer service life.

(5) Simple control system: it adopts continuously speed change, handle throttle control, brake power-off protection device.

ACKNOWLEDGEMENTS

Special thanks to National Science Foundation of the Ministry of Education of China, I would like to thank Research Institute of Sinopec Petroleum Machinery Co., Ltd and Chengde Petroleum College for their support.

REFERENCES

[1] Chen, Y., Du, W., Zhuo, S., Liu, W., Liu, Y., Shen, G., Wu, S.,Li,J., Zhou,B., Wang,G., Zeng,E., Cheng,H., Liu,W., Tao,S., Stack and fugitive emissions of major air pollutants from typical brick kilns in China. Environmental Pollution 224(2017)421-429. http://dx.doi.org/10.1016/j.envpol.2017.02.022

[2] Zheng Juaner, Wu Cifang. Research on the current situation, potential and policy design of building energy conservation in China[J]. Chinese Soft Science, 2005(5): 64,76-80.

[3] Zhao,P., Zhang,X., Qin,L., Zhang,Y., Zhou,L., Conservation of disappearing traditional manufacturing process for Chinese grey brick: Field survey and laboratory study. Construction and Building Materials 212(2019)531-540.
https://doi.org/10.1016/j.conbuildmat.2019.03.317

[4] Ganzone,G., Frano,R., Sumini,M., Troiani,F., Dismantling of the graphite pile of Latina NPP: Characterization and handling/removal equipment for single brick or multi-bricks. Progress in Nuclear Energy 93(2016)146-154.

http://dx.doi.org/10.1016/j.pnucene.2016.08.010

[5] Taurino,R., Ferretti,D., Gattani,L., Bozzoli,F., Bondioli,F., Lightweight clay bricks manufactured by using locally available wine industry waste, Journal of Building Engineering 26(2019)100892. https://doi.org/10.1016/j.jobe.2019.100892

[6] S. Elavarasan, A.K. Priya, V.Kavin Kumar, Manufacturing fired clay brick using fly ash and M-Sand, Materials Today: Proceedings 37(2021)872-876.
https://doi.org/10.1016/j.matpr.2020.06.042

[7] Lan,J., Zhang,S., Mei,T., Dong Y., Hou,H., Mechanochemical modification of electrolytic manganese residue: Ammonium nitrogen recycling, heavy metal solidification, and baking-free brick preparation, Journal of Cleaner Production 329(2021)129727. https://doi.org/10.1016/j.jclepro.2021.129727

[8] Liu,L., Cheng,X., Miao,X., Shi Y., Zhang,M., Guo,M., Cheng,F., Zhang,M., Preparation and characterization of majority solid waste based eco-unburned permeable bricks, Construction and Building Materials 259(2020)120400.
https://doi.org/10.1016/j.conbuildmat.2020.120400

[9] Zhao,Y., Liang,N., Chen,H., Li,Y., Preparation and properties of sintering red mud unburned road brick using orthogonal experiments, Construction and Building Materials 238(2020)117739. https://doi.org/10.1016/j.conbuildmat.2019.117739

[10] A.Seco, J.Omer, S.Marcelino, S.Espuelas, E.Prieto, Sustainable unfired bricks manufacturing from construction and demolition wastes, Construction and Building Materials 167(2018)154-165. https://doi.org/10.1016/j.conbuildmat.2018.02.026

[11] Wang,W., Gan,Y., Kang,X., Synthesis and characterization of sustainable eco-friendly unburned bricks from slate tailings, Journal of Materials Research and Technology 2021;14:1697-1708. https://doi.org/10.1016/j.jmrt.2021.07.071

[12] Peng,Y., Peng,X., Yang,M., Shi,H., Wang,W., Tang,X., Wu,Y, The performances of the baking-free bricks of non-sintered wrap-shell lightweight aggregates from dredged sediments, Construction and Building Materials 238(2020)117587.
https://doi.org/10.1016/j.conbuildmat.2019.117587

[13] Zhao,H., Gou,H., Unfired bricks prepared with red mud and calcium sulfoaluminate cement: Properties and environmental impact, Journal of Building Engineering 38(2021)102238. https://doi.org/10.1016/j.jobe.2021.102238

[14] V. Gupta, H. K. Chai, Y. Lu, S. Chaudhary, A state of the art review to enhance the industrial scale waste utilization in sustainable unfired bricks, Construction and Building Materials 254(2020)119220.
https://doi.org/10.1016/j.conbuildmat.2020.119220

[15] D. E. Quesada, M. A. Felipe, M. J. Fuentes, Biomass bottom ash waste and by-products of the acetylene industry as raw materials for unfired bricks, Journal of Building Engineering 38(2021)102191. https://doi.org/10.1016/j.jobe.2021.102191

[16] Li, X., Gu, H., Huang, A., Fu, L, Bonding mechanism and performance of rectorite/ball clay bonded unfired high alumina bricks, Ceramics International 47(2021)10749-10763. https://doi.org/10.1016/j.ceramint.2020.12.191

[17] S, Masuka., W, Gwenzi., T, Rukuni., Development, engineering properties and potential applications of unfired earth bricks reinforced by coal fly ash, lime and wood aggregates, Journal of

Building Engineering 18(2018)312-320, https://doi.org/10.1016/j.jobe.2018.03.010

[18] L, Lang., B, Chen., Y, Pan., Engineering properties evaluation of unfired sludge bricks solidified by cement-fly ash-lime admixed nano-SiO_2 under compaction forming technology, Construction and Building Materials 259(2020)119879.
https://doi.org/10.1016/j.conbuildmat.2020.119879

[19] D. Muheise, S. Pavia, Properties of unfired, illitic-clay bricks for sustainable construction, Construction and Building Materials 268(2021)121118.
https://doi.org/10.1016/j.conbuildmat.2020.121118

[20] J.E. Oti, J. M. Kinuthia, Stabilised unfired clay bricks for environmental and sustainable use, Applied Clay Science 58(2012)52-59. doi:10.1016/j.clay.2012.01.011

[21] H. A. Gawwad, A. M. Rashad, M.S. Mohammed, T. A. Tawfik, The potential application of cement kiln dust-red clay brick waste-silica fume composites as unfired building bricks with outstanding properties and high ability to CO_2-Capture, Journal of Building Engineering 42(2021)102479. https://doi.org/10.1016/j.jobe.2021.102479

[22] Si Jingping. Refitting analysis and design key points of special purpose vehicle sub frame [J]. Inner Mongolia Highway and transportation, 1997 (1): 28-29.

[23] Wu Xingmin. New energy vehicle[M]. Beijing: Beijing University of Technology Press, 2018,14.

[24] Rubal Dua, Kenneth White, Rebecca Lindland. Understanding potential for battery electric vehicle adoption using large-scale consumer profile data[J]. Energy Reports,2019,5.

[25] Qiu Xuanhuai. Mechanical design[M]. Fourth Edition. Beijing: Higher Education Press, 2011,280.

[26] Shi Wenku. Automobile structure[M]. Sixth Edition. Beijing: People's Communications Press,2013, 291.

[27] Wang Wangyu. Automobile design[M]. Beijing: Machinery Industry Press, 2004, 219.

[28] Hu Fucai, Zhou Yong. Finite element analysis and experimental study of belt brake[J]. Hoisting and transportation machinery, 2007(8): 80-82.

CIVIL ENGINEERING JOURNAL

Article no. 11

THE CIVIL ENGINEERING JOURNAL 1-2022

PRELIMINARY RESULTS OF GAMMA-RAY SPECTROSCOPY FOR DETECTION OF SNOW WATER EQUIVALENT IN JIZERA MOUNTAINS

Abigail Klejchová[1], Michal Dohnal[1] and Miroslav Tesař[2]

1. *Czech Technical University in Prague, Faculty of Civil Engineering, Thákurova 7, Prague 6, Czech Republic*
2. *Czech Academy of Sciences, Institute of Hydrodynamics, Pod Paťankou 5, Prague 6, Czech Republic*

ABSTRACT

The snow water equivalent is an important snow characteristic as it provides hydrologically relevant information about the amount of water stored in the snowpack. The experimental catchment in the Jizera Mountains was equipped with the gamma-ray spectroscope CS725. The sensor uses emitted electromagnetic signals of isotopes ^{40}K and ^{208}Tl to remotely and continuously measure the snow water equivalent. Two winter seasons, 2018-2019 and 2019-2020, were monitored, and the obtained data were analyzed together with the complementary measurements available (snow depth, precipitation, air temperature). The sensor was tested in contrasting conditions of the precipitation-rich winter period 2018-2019 and the mild winter period 2019-2020. Our measurement showed that the SWE values derived from both isotopes are very similar and logically correspond well with the other measurements at the site. As far as we know, the first use of the sensor in the Czech Republic has proven usability in the conditions of the temperate montane catchment.

KEYWORDS

Snow water equivalent, Snow depth, Montane catchment, Temperate climate

INTRODUCTION

Precipitation measurement during winter is much less frequent, both in time and space, than in summer. However, careful monitoring of snow depth and the equivalent depth of water on the ground if all snowfall melted (snow water equivalent, SWE; [1]) is of significant importance in hydrology. Information about the snow water equivalent in the snowpack is essential for water management and water engineering authorities. The maximum value of SWE affects the groundwater replenishment in the spring and water availability for crop growth in the vegetation season. Flood protection also benefits from knowing the maximum value of SWE. Continuous measurement of snow water equivalent is still sparse [2], and new measurement techniques are welcome.

Spectroscopy as a tool for measuring snow water equivalent and soil moisture has been available for decades [3], [4]. The successful use of electromagnetic radiation for SWE measurement is based on the sufficient difference between attenuation of gamma-radiation of water and soil (typically by factor 1.11). Techniques primarily differ in the type of gamma radiation detected and/or by the type, number, and sensor position. Recently, techniques that use two neutron sensors - one above the snowpack and the second directly on the ground - were described (e.g., [5]). These

techniques detect gamma radiation from the soil/bedrock. Another technique (e.g., [6]) also benefits from two sensors, but sensors detect background cosmic gamma radiation.

In contrast, the CS725 (Campbell Scientific, Inc.) detects electromagnetic radiation from soil/bedrock and uses a single sensor, significantly decreasing acquisition and maintenance costs [7]. Choquette et al. [8] studied the performance of the CS725 and highlighted the need for on-site calibration of the CS725 sensor to obtain reliable and precise data. They described a calibration method and considered saturated soil moisture to be the most sensitive parameter with the most significant impact on the correct determination of SWE. The method of Choquette et al. [8] proved to provide snow water equivalent values with an accuracy of about 90% compared to manual readings.

Smith et al. [9] compared two automated SWE measurement sensors (CS725 and SSG1000, Sommer GmbH) and periodic manual SWE measurements concerning possible poor soil moisture calibration, spatial variability of snow cover, or ice layers in the snowpack. Excellent accuracy has been achieved between automated and manual measurements (in general, correlations were higher than 0.9). For the CS725 sensor, problems mainly occurred with sandy soil and the melting period, when the sensor may not distinguish frozen water in the soil from the unmelted snow.

The present study evaluates continuous snow water equivalent measurement by the gamma-ray spectroscope CS725. Two consecutive winter periods (2018-2019 and 2019-2020) are examined. Special attention is paid to analyses of transient changes during snowmelt in the spring.

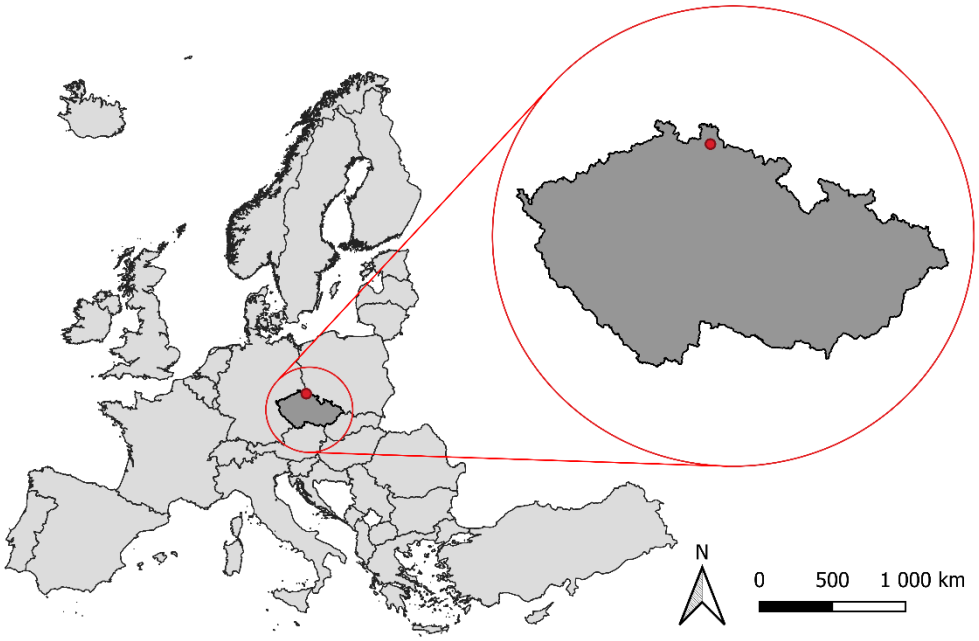

Fig. 1 – Jizera Mountains in the Czech and European context.

MATERIAL AND METHODS

The sensor is located at a mountain meadow in the Jizera mountains, called Nová Louka (50.813611N, 15.158611E; altitude of 778.6 m a. s. l.). It is situated in the north of the Czech Republic, in the district of the city Jablonec nad Nisou (Figure 1). The site has a long history of measurement [10] and it is characterized by high precipitation totals (e.g., the highest national 24-hour total). Nowadays, an automatic meteorological station is operated by the Institute of

Hydrodynamics of the Czech Academy of Sciences. The meteostation is situated in the gently inclined area (about 9 percent) exposed to the northeast (Figure 2). The station is equipped with a set of sensors for complete meteorological and climatic measurements. In the present study, data from a weighing rain gauge MRW 500 (Meteoservis v.o.s.) and standard air temperature and humidity sensor RVT11 (Fiedler AMS s.r.o.) are used. Weighing rain gauge provided accurate precipitation intensity; actual air temperature allowed to distinguish rain and snow; and air humidity facilitated fog detection. The site was found to be well suited for the measurement of SWE by detecting electromagnetic radiation from bedrock, i.e., sufficient radiation levels of ^{40}K and ^{208}Tl.

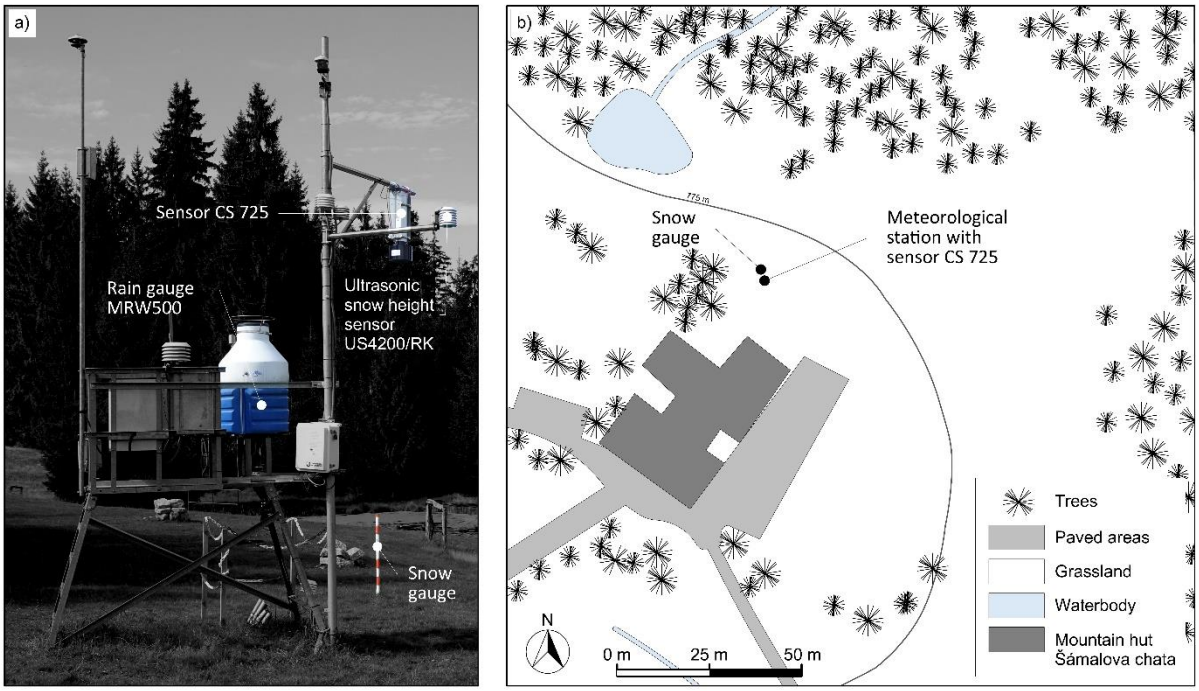

Fig. 2 - Meteorological station of the Institute of Hydrodynamics of the AS CR at locality Nová Louka.

Snow water equivalent measurement

The CS725 sensor was developed by Institute de recherche d'Hydro-Québec (IREQ, Varennes, Qc, CANADA) for the determination of the water equivalent of the snowpack [11]. The sensor has a scintillator of a thallium-doped sodium iodide crystal optically coupled to a photomultiplier tube [7]. The crystal detects the net terrestrial gamma radiation naturally emitted by isotopes ^{40}K and ^{208}Tl present in soil/bedrock. The signal emitted by dry soil and in the absence of snow or water above ground is considered a constant background value [8]. The attenuation of the gamma signal then varies with the presence of water between the radiation source and the sensor. Therefore, gamma radiation is attenuated by the presence of snowpack. The number of detected electromagnetic signals is summed up four times per day, and the resulting value is together with the background value used for *SWE* calculation [9], [8]:

$$SWE = \frac{-1}{\beta} * \ln\left[N * \frac{(1+1.11*SSM)}{N_0}\right] - (0.001165 * H) \quad (1)$$

where β is attenuation coefficient [cm^{-1}], N is the number of radiation counts recorded per period of time [6h^{-1}], N_0 is the number of radiation counts emitted by a dry soil in the absence of snow

or water above [$6h^{-1}$], *SSM* is saturated soil moisture [-], and *H* is sensor height above the ground surface [cm].

The sensor uses a threshold (factory pre-set value of 5 mm) that decides how the SWE is calculated. Above that threshold, SWE is calculated independently for both attenuations (SWE_K and SWE_{Tl}). Below this threshold, when there is a danger of patchy snow cover and the calculation could be affected by the soil moisture, a different approach is used based on the ratio of the two attenuations (SWE_{ratio}), which, although not as accurate, removes soil moisture from the expression.

The bottom edge of the sensor is installed at the height of 3.53 m above the ground. The sensor is equipped with a lead collimator, which prevents the counting of gamma radiation emitted from sources not in the target area [9]. The bottom edge of the collimator is 3.45 m above the ground. The collimator limited the field of view to 120 degrees [7]. Therefore, the sensor at the Nová Louka site detects gamma radiation from an area of approx. 117 m^2.

Snow depth monitoring

Snow depth is measured by an ultrasonic sensor (US4200/RK, Fiedler AMS s.r.o.) and alternatively detected from the camera record (BCC100, Brinno Inc.), which is focused on the snow gauge. The camera record was available from the end of March 2019. The ultrasonic sensor and snow gauge are located within the detection area of the SWE sensor, approximately 2 m apart in the horizontal direction.

Monitoring intervals

The snow depth, weighing rain gauge, air temperature, and humidity sensor are monitored at 15-minute intervals. The camera record is comprised of a sequence of 1-hour images. The CS725 sensor provided six-hour averages of SWE. Once a month, the sensors are checked for functionality and maintenance.

RESULTS AND DISCUSSION

Snow water equivalent

To study the performance of the CS725, two winter periods, 2018-2019 and 2019-2020, were examined. The SWE values obtained from the sensor are shown in Figure 3. The snow cover was present from December to the beginning of April in both periods. Nevertheless, these periods differ significantly. The maximum value of SWE was about 365 mm in the winter period of 2018-2019, while it was only 88 mm in winter 2019-2020 (based on attenuation of the ^{40}K isotope). During 2019-2020, several accumulation phases and thawing episodes were observed. While the season 2018-2019 was characterized by a single accumulation peak only. The overall character of SWE measurement also reflected the air temperatures and amount of precipitation in both periods. In 2018-2019 almost twice as much precipitation occurred, and temperatures were significantly lower (by about -1.02°C on average), often day-long below 0°C.

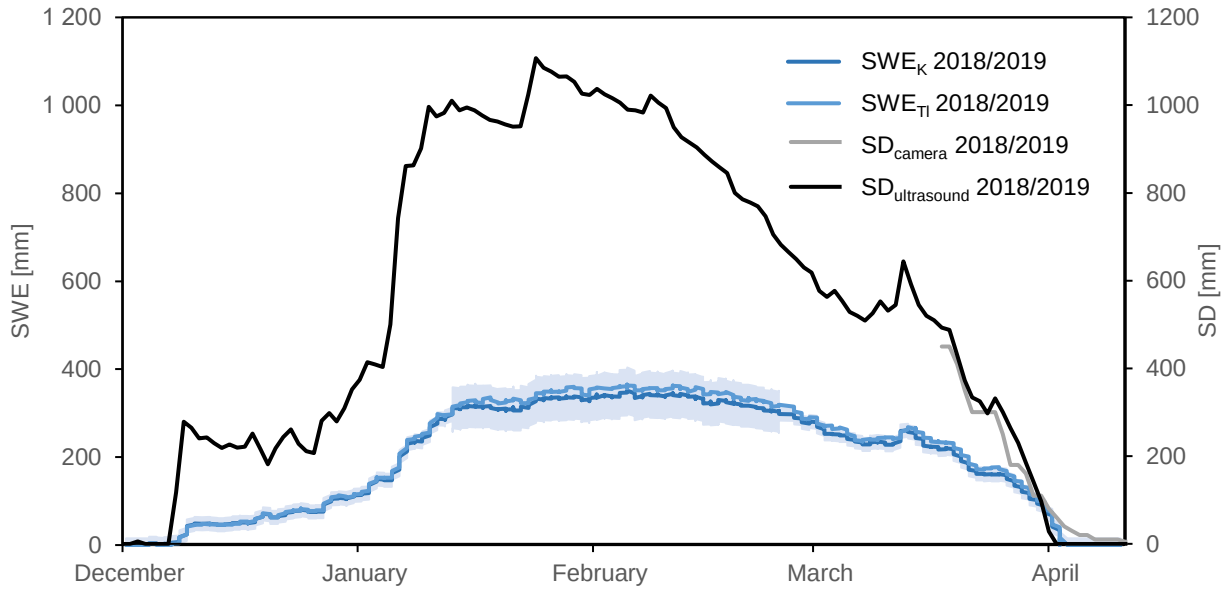

Fig. 3 - Snow water equivalent (SWE) measured by sensor CS725 and snow depth (SD) measured by ultrasound sensor and detected from the camera record at the Nová Louka site in winter period 2018-2019. SWE_K and SWE_{Tl} stand for snow water equivalent values determined based on attenuation of gamma radiation emitted by isotopes ^{40}K and ^{208}Tl. The shaded area represents a factory specified accuracy of the CS725 sensor.

Attenuations of electromagnetic signals emitted by both isotopes (^{40}K and ^{208}Tl) provide a similar course of SWE (Figure 3, Figure 4). Registered differences were up to 30 mm and dependent on the actual SWE values (i.e., higher values yield higher differences between SWE_K and SWE_{Tl}). The absolute majority of the time, the differences were within the accuracy range specified by the manufacturer. Generally, the SWE values derived from isotope attenuation with the higher counts (usually emitted by isotope ^{40}K) are considered more reliable [12], [9]. At the Nová Louka site, the detected hourly totals of emitted electromagnetic signals in the period without snow cover were about 40 000 h^{-1} and 9 000 h^{-1} for ^{40}K and ^{208}Tl, respectively. Therefore, the values based on isotope ^{40}K attenuation are regarded as more accurate in our study.

The course of the snow depth is similar to the snow water equivalent (Figure 3, Figure 4). However, snow water equivalent in the period 2018-2019 demonstrates a considerably wider peak (Figure 3) associated with the gradual settling and compacting of snow, which is not reflected in the value of SWE. The differences in the snow depth obtained from the ultrasonic sensor and camera could be attributed to the snow cover spatial variability. Specifically, the average relative difference between ultrasonic sensor and camera daily average readings comprises 25% for the fragment of period 2018-2019 (Figure 3) and 35% for the whole winter period 2019-2020 (Figure 4). It is obvious that the spatial variability is more pronounced in the case of the winter period with a small amount of snow (2019-2020) and a large number of accumulation-melting cycles.

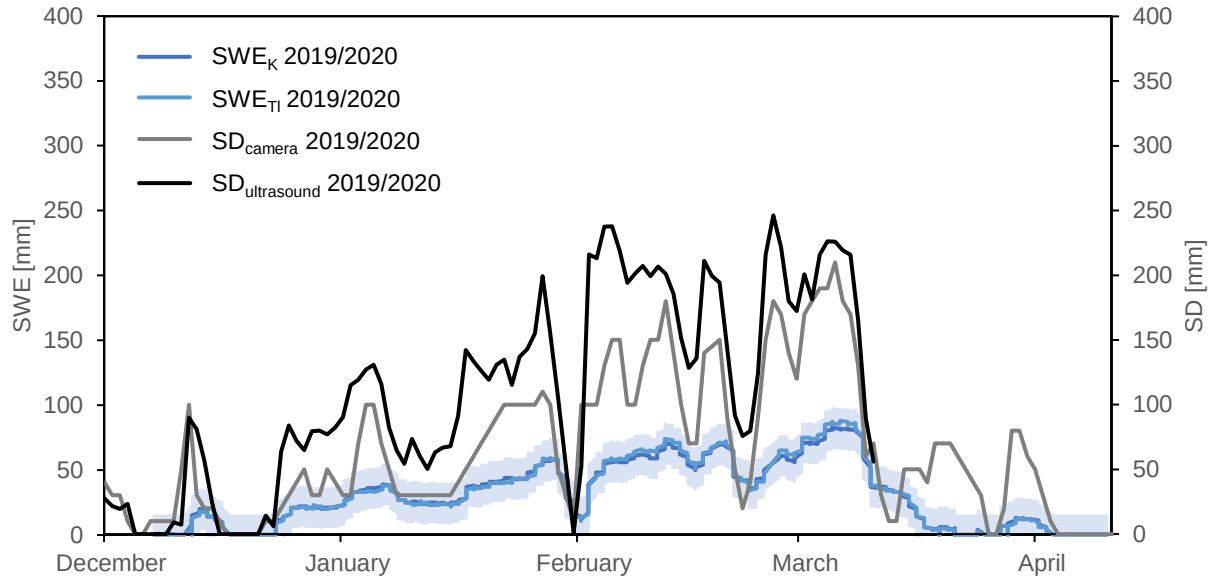

Fig. 4 - Snow water equivalent (SWE) measured by sensor CS725 and snow depth (SD) measured by ultrasound sensor and detected from the camera record at the Nová Louka site in the winter period 2019-2020. SWE_K and SWE_{Tl} represent snow water equivalent values determined based on attenuation of gamma radiation emitted by isotopes ^{40}K and ^{208}Tl. The shaded area represents a factory specified accuracy of the CS725 sensor.

Thawing snow and transient snow-rain situations

Due to the spatial variability, it is possible that even if the snow cover is still lying on some spots, the sensor evaluates the integral SWE value = 0 mm. Therefore, the calculated SWE value should be carefully analyzed, especially during periods of thawing snow and transient snow-rain situations.

Figure 5 shows a series of images capturing the soil surface under the sensor in April 2019, when the snow cover started to melt. In the first two days (April 4 and 5), the air temperature is above freezing point overnight, and the afternoon temperature peaks exceed 13°C. Although other days during the night it freezes and the thawing of snow slows down, high daytime temperatures cause even the remaining snow to disappear within six days (Table 1).

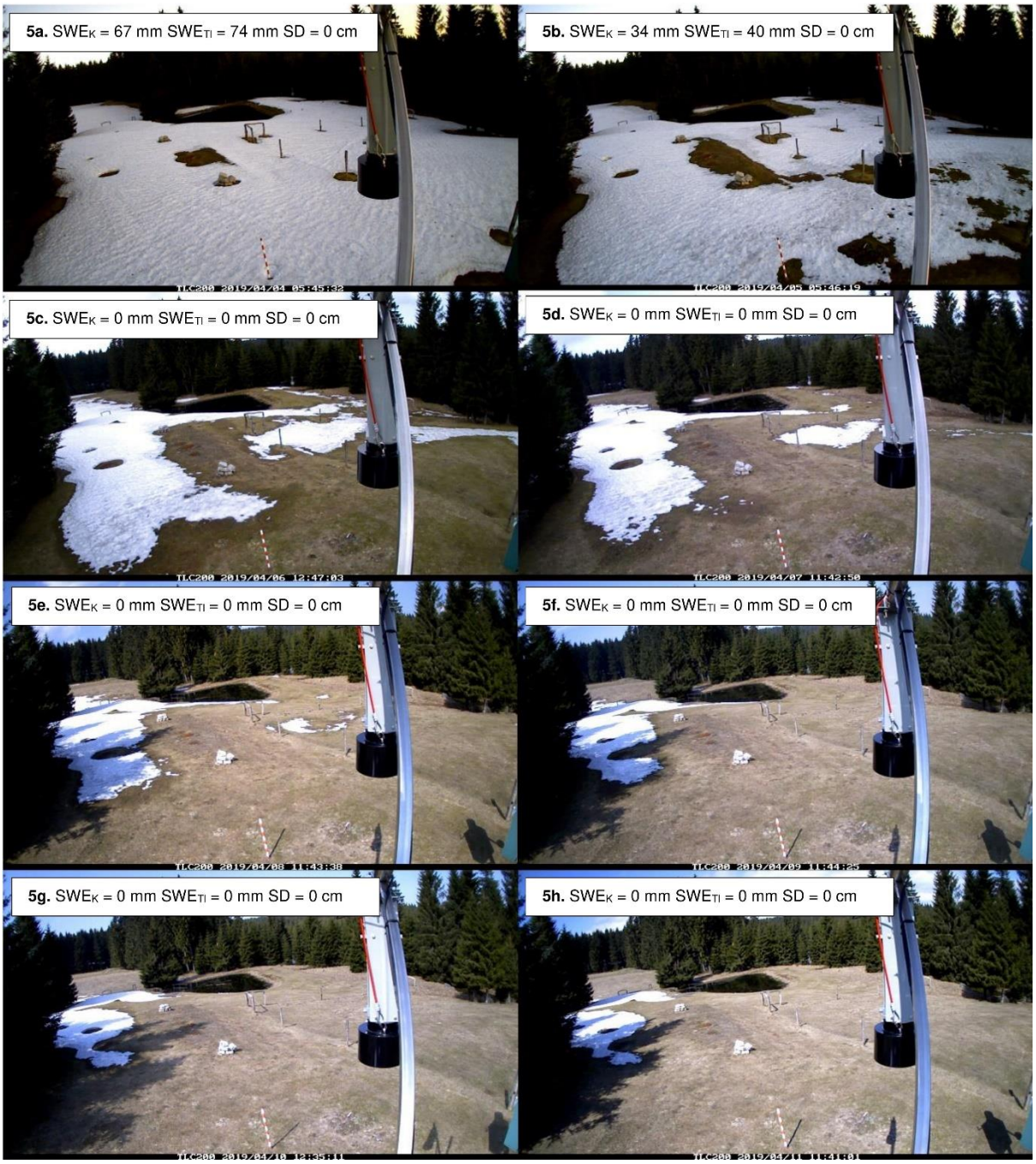

Fig. 5 - Soil surface under the CS725 sensor on April 04-11, 2019. SWE_K and SWE_{Tl} stand for snow water equivalent values determined based on attenuation of gamma radiation emitted by isotopes ^{40}K and ^{208}Tl.

The surface is covered with a discontinuous snow cover in the first two days (April 4-5). In this situation, the sensor evaluated the SWE_K to be 67 mm and SWE_{Tl} = 74 mm. At the same time, the SWE_{ratio} value independent of soil moisture was 43 mm (see Tab. 1) and corresponded better to the captured site conditions (Figure 4). On April 5, the difference, i.e., the influence of shallow soil moisture, was even more important, SWE_K = 34 mm and SWE_{ratio} = 15 mm. The snow melted even more intensively in the following days, and the sensor evaluated the SWE values as 0 mm. It is also

clear from the camera record that only fragments of snow cover remain on the site outside the sensor's range.

Tab. 1 - Snow characteristics and air temperatures for selected days in April 2019. SWE_{RATIO} is used when the threshold value is exceeded, and the SWE determination is affected by soil moisture.

Fig. 5	*a*	*b*	*c*	*d*	*e*	*f*	*g*	*h*
April 2019	*4*	*5*	*6*	*7*	*8*	*9*	*10*	*11*
SWE_{RATIO} (mm)	*43*	*15*	*0*	*1*	*-5*	*-5*	*-11*	*-12*
T_{min} (°C)	*5.1*	*0.1*	*-1.6*	*-2.7*	*-2.0*	*-2.5*	*-4.3*	*-2.2*
T_{max} (°C)	*13.8*	*15.4*	*16.8*	*15.3*	*15.1*	*13.4*	*8.4*	*3.4*

In contrast, the series of images in Figure 6 show the transient period at the beginning of the winter season 2019/2020. It freezes all day for the first four days of the December period, and snow is deposited. Subsequently, warming occurs, precipitation is mixed, and temperatures are stable above freezing (see Table 2).

A thin layer of new snow from December 11 to December 13 is obviously at the limit of the sensor's detectability (SWE_{TI} and SWE_{K} equal to zero, and SWE_{ratio} from -4 to 10 mm). The increasing snow cover and its snow water equivalent value are captured more reliably in the following days. By December 16, temperatures had already reached above freezing all day, which was reflected in the thawing of the snow cover (up to 24 mm per day) and the decrease in SWE in the next days.

Tab. 2: Snow characteristics and air temperatures for selected days in December 2019.

Fig. 6	*a*	*b*	*c*	*d*	*e*	*f*	*g*	*h*
December 2019	*11*	*12*	*13*	*14*	*15*	*16*	*17*	*18*
SWE_{RATIO} (mm)	*5*	*10*	*-4*	*9*	*25*	*27*	*20*	*14*
T_{min} (°C)	*-4.2*	*-5.3*	*-3.3*	*-0.9*	*-2.1*	*1.1*	*1.5*	*-1.7*
T_{max} (°C)	*-1.2*	*-2.6*	*-1.0*	*-0.2*	*2.9*	*4.7*	*6.8*	*7.6*

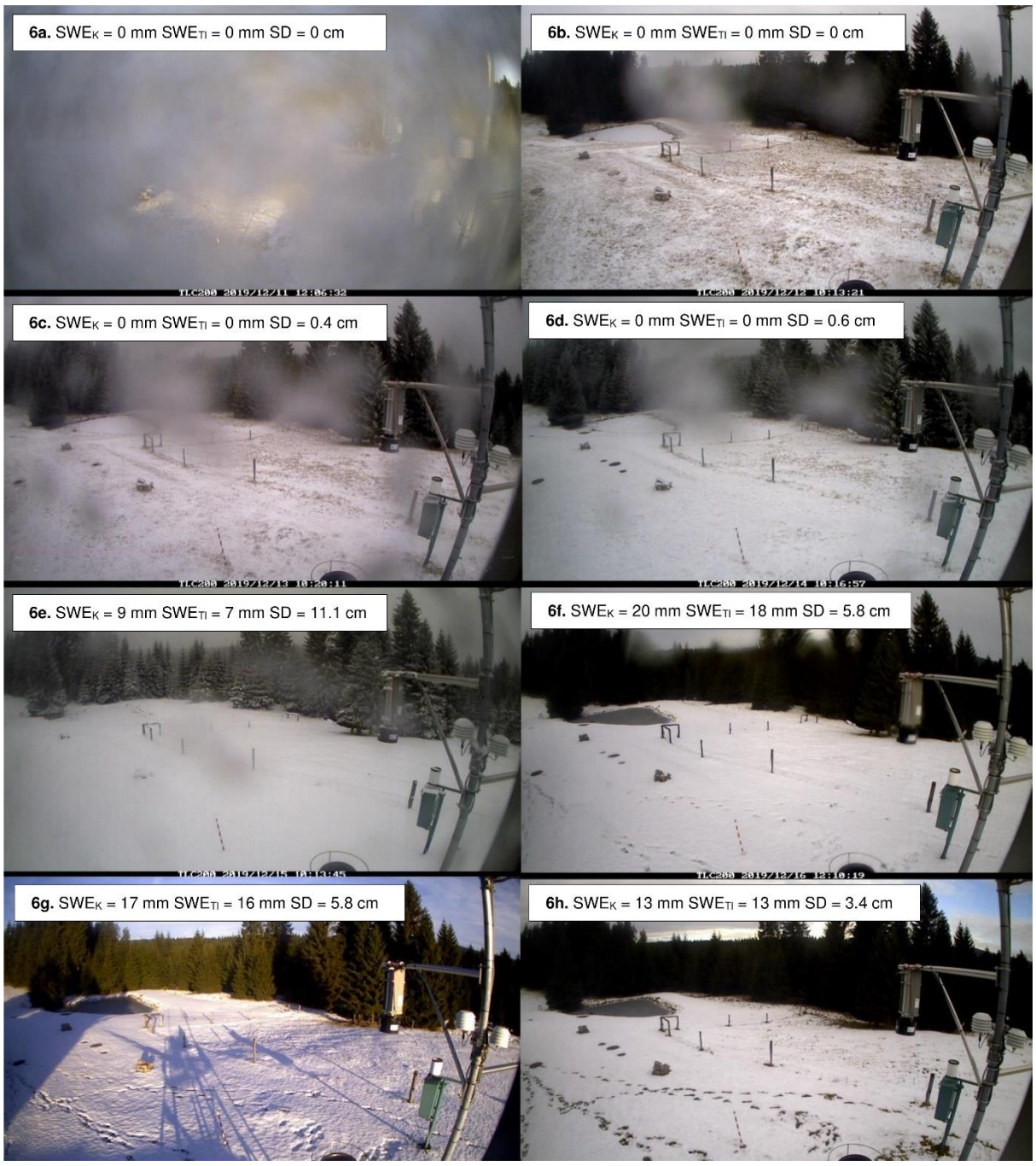

Fig. 6 - Soil surface under the CS725 sensor on December 11-18, 2019. SWE_K and SWE_{Tl} stand for snow water equivalent values determined based on attenuation of gamma radiation emitted by isotopes ^{40}K and ^{208}Tl.

CONCLUSIONS

In the present study, continuous snow water equivalent measurement by the gamma-ray spectroscope CS725 was evaluated. Two consecutive winter periods (2018-2019 and 2019-2020) were examined. Natural conditions allowed the sensor to be tested in contrasting circumstances: during the winter period 2018-2019 with the maximum value of SWE of about 365 mm and during the mild winter period 2019-2020 with the peak value of 88 mm.

Our measurement showed that the SWE values derived from both isotopes ^{40}K and ^{208}Tl are very similar. Detected differences could be attributed to the different background radiation levels available in the soil/bedrock. Because of the higher level of ^{40}K at the site, SWE values derived from this isotope are considered more accurate.

The CS725 gamma-ray spectroscope has proven usability in the conditions of the temperate montane catchment. The conditions at the beginning (when continuous snow cover is forming) and at the end of winter (during intense snowmelt when patchy snow cover occurs) require special attention.

ACKNOWLEDGMENTS

This study was supported by the Czech Science Foundation, project No. 20-00788S. In preparing this work, the infrastructures acquired within the projects OPVV - ERDF CZ.02.1.01/0.0/0.0/16_017/0002626 "Modernisation of the infrastructure of the doctoral study programmes in water management and environmental engineering" and Project Strategy AV21, Programme Water for Life were used.

REFERENCES

[1] Pomeroy J.W., Brun E., 2001. Physical properties of snow. In: Jones H.G., Pomeroy W.J., Walker D.A., Hoham R.W. (eds) Snow ecology: an interdisciplinary examination of snow-covered ecosystems. Cambridge University Press. Cambridge, UK, pp 45-118.

[2] Koch, F., Henkel, P., Appel, F., Schmid, L., Bach, H., Lamm, M., et al., 2019. Retrieval of snow water equivalent, liquid water content, and snow height of dry and wet snow by combining GPS signal attenuation and time delay. Water Resources Research, 55, 4465–4487.

[3] Grasty R., 1982. Direct snow-water equivalent measurement by air-borne gamma-ray spectrometry. Journal of Hydrology, 55(1-4): 213-235.

[4] Ducharme, P., Houdayer, A., Choquette, Y., Kapfer, B., Martin, J. P., 2015. Numerical Simulation of Terrestrial Radiation over a Snow Cover. Journal of Atmospheric and Oceanic Technology [online]. ISSN 0739-0572, 1520-0426.

[5] Wada, M., Kodama, M., Kawasaki, S., 1977. Method of determining the water equivalent depth of snowfall using neutrons of cosmic rays. US patent 4,047,042.

[6] Condreva, K.J., 1997. Method for detecting water equivalent of snow using secondary cosmic gamma radiation. United States: N. p.

[7] Choquette, Y., Lavigne, P., Ducharme, P., Houdayer, A., Martin J. P., 2010. Apparatus and method for monitoring snow water equivalent and soil moisture content using natural gamma radiation. US patent 7,800,051 B2.

[8] Choquette, Y., Ducharme, P., Rogoza, J., 2013. CS725, an accurate sensor for the snow water equivalent and soil moisture measurements. International Snow Science Workshop Grenoble – Chamonix Mont-Blanc France

[9] Smith, C. D., Kontu, A., Laffin, R., Pomeroy, J. W., 2017. An assessment of two automated snow water equivalent instruments during the WMO Solid Precipitation Intercomparison Experiment. The Cryosphere [online]. ISSN 1994-0424.

[10] Munzar, J., Ondráček, S., 2010. Historický srážkový rekord z Jizerských hor z roku 1897 dodnes nepřekonán. Sborník Severočeského Muzea. ISSN 0375–1686.

[11] Campbell Scientific, Inc., 2012. Guide of manufacturer CS725 Snow Water Equivalency Sensor. Campbell Scientific Ltd.

[12] Kirkham J.D., Koch I., Saloranta T.M., Litt M., Stigter E.E., Møen K., Thapa A., Melvold K., Immerzeel W.W., 2019. Near Real-Time Measurement of Snow Water Equivalent in the Nepal Himalayas. Front. Earth Sci. 7:177.

CIVIL ENGINEERING JOURNAL

Article no. 12

THE CIVIL ENGINEERING JOURNAL 1-2022

A NEW METHOD TO CONTROL THE REGIONAL STRATA MOVEMENT OF SUPER-THICK WEAK CEMENTATION OVERBURDEN IN DEEP MINING

Guojian Zhang[1], Guangli Guo[2], Wei Wei[3], Sifeng Zhang[4] and Guobiao Yao[5]

1. *School of Surveying and Geo-informatics, Shandong Jianzhu University, Ji'nan 250101, China & Post-doctoral Workstation of Technology Research Institute in Shandong Energy Group Co. LTD., Ji'nan 250101, China & School of Environmental Science and Spatial Informatics, China University of Mining and Technology, Xuzhou 221116, China; 24155@sdjzu.edu.cn*
2. *School of Environmental Science and Spatial Informatics, China University of Mining and Technology, Xuzhou 221116, China; guo_gli@126.com*
3. *Technology Research Institute in Shandong Energy Group Co. LTD., Ji'nan 250101, China;*
4. *School of Transportation Engineering, Shandong Jianzhu University, Ji'nan 250101, China; sddxzsf@sdjzu.edu.cn*
5. *School of Surveying and Geo-informatics, Shandong Jianzhu University, Ji'nan 250101, China; yao7837005@sdjzu.edu.cn*

ABSTRACT

In the western of China, the deep mining area with super-thick and weak cementation overburden is vast, sparsely populated and the ecological environment is extremely fragile. With the large-scale exploitation of deep coal resources, it is inevitable to face green mining problem, whose essence is the surface subsidence control. Therefore, it is necessary to study the control technology for the regional mining based on the evolution law of subsidence movement and energy-polling of super-thick and weak cementation overburden, and put forward the economically design scheme that can control strata movement and surface subsidence in a certain degree. Based on the key strata control theory, this paper puts forward the subsidence control scheme of partial filling -partial caving in multi-working face coordinated mining, and further studies its control mechanism through the numerical simulation and then analyzes the control effect of the strata movement and energy-polling in the fully caving mining, backfill mining, wide strip skip-mining and mixed filling mining method etc., the following conclusions are detailed as follows: (1) The maximum value of energy-polling occurs on the coal pillars or on both sides of goaf. With the width of goaf, the maximum value of energy-polling increases in a parabola. (2) In the partial filling-partial caving multiple working faces coordinated mining based on the main key stratum, the stress distribution of the composite backfill in the filling working face is parabolic, and it is high on both sides and low in the middle. Moreover, in the composite backfill, the stress concentration degree of a outside coal pillar is greater than that of the inside coal pillar. (3) The control mechanism of partial filling-partial caving harmonious mining based on main key layer structure is the double-control cooperative deformation system, formed by the composite backfill and the main and sub-key layers structure. They jointly control the movement and energy accumulation of overlying strata by greatly reducing the effective space to transmit upward, and absorb the wave subsidence trend of the overburden until it develops into a single flat subsidence basin. (4) Considering the recovery rate, pillar rate, area filling rate, technical difficulty and subsidence coefficient etc., the partial filling-partial caving multiple working faces coordinated mining based on the main key stratum is the most cost-effective mining method to control surface subsidence. This paper takes a guiding role in

controlling the regional strata movement and surface subsidence of deep mining with super-thick and weak cementation overburden.

KEYWORDS

Deep filling mining, Regional control, Key stratum, Numerical simulation

INTRODUCTION

With the westward development of China economic strategy, Ordos coalfield has become an important area where supplies the country's energy needs. It has simple geological structure and abundant deep coal resources, which is suitable for large-scale mining with high intensity. At present, many scholars have studied on the strata movement of deep mining in Ordos coal field, and achieved certain results. For example, Wang [1] and Lin [2] studied the movement law of weak cementation overburden of deep single working face mining by means of physical simulation and numerical simulation method, and believed that the control effect of super-thick weak cementation sandstone was the reason for the small surface subsidence. By analyzing the surface measured data of Yingpanhao Coal mine, Zhang believed that the main reasons for the abnormal characteristics of the overburden movement were that the dip direction did not reach sufficient mining and the super-thick weak cementation sandstone has a strong control effect [3]. Gong used multi-borehole strata data to construct intensive 3D numerical model to study the movement law of super-thick weak cementation sandstone in deep mining, and results show that Zhidan group sandstone has a strong control effect, which makes the surface subsidence smaller under the same mining conditions [4]. In addition, he also studied the influence of joint and block size on the motion law and failure characteristics of the super-thick weak cementation sandstone [5]. Ning found that the periodic pressure of working face is closely related to the breaking law of main roof and key stratum in Nalinhe coal mine [6]. Wang carried out in-depth research on the occurrence mechanism and prevention of typical dynamic disasters in deep mining, and believed that the fracture of low-hard stratum and high thick sandstone was one of the main causes resulting in rock burst and mine quake [7]. The writer uses similar material simulation method to study the failure law of super-thick weak cementation sandstone, and results show that it has a larger limit span and strong control effect, and its failure characteristics are "arch shell - beam - half arch shell - step" [8]. In the meanwhile, the numerical simulation method is used to study the compound effect of super-thick weak cementation sandstone, and explored the influence law of its spatial location and thickness on the failure characteristics and energy accumulation of the overburden [9].

The above research shows that the high intensity mining of coal resources in deep mining area of Ordos coal field is faced with many problems. With the mining depth increasing and the mining scope expanding in Ordos coalfield, rock burst, mine earthquake and other disasters occur frequently caused by the special strata movement and energy accumulation of the super-thick weak cementation sandstone, and the serious surface subsidence leads to the deterioration of ecological environment. These phenomena have become a serious problem restricting the large-scale continuous mining of coal mines. Therefore, it is necessary to study a kind of efficient, safe and green mining technology to control the strata movement and energy accumulation of super-thick sandstone and alleviate mine quake and surface subsidence disaster.

The current normally used subsidence control technologies mostly include surface subsidence control technologies with filling bodies as the core and surface subsidence control technologies with coal-rock bodies as the core. Strip mining and goaf filling mining are presently frequently used approaches for controlling surface subsidence. The principle of strip mining is to divide the coal seam into regular shapes, mining one and leaving one, and the remaining coal pillars can bear the load of the overlying strata, thereby controlling the surface movement and deformation. In other aspect, backfill mining is to control the surface deformation by filling the mined-out area with filling bodies, reducing the sinking space. The research on the control

mechanism of these two means has been relatively mature and has been extensively applied in eastern mining areas.

In addition, with coal pillar-overburden structure collaborative deformation, researchers have sequentially proposed coal pillar compression and indentation theory [10], rock beam hypothesis [11], plate theory [12-14] and other rock control theories. Plate theory suggests that surface subsidence is composed of coal pillar compression deformation, overburden compression deformation and plate deflection. Meanwhile, it is believed that the synergy of coal pillars and plates has effectively controlled surface subsidence. With the increase of mining depth, the question of coal pillar-overburden structure coordinated deformation in deep mining has gradually changed from the issue of coal pillar-roof cooperative deformation to the problem of coal pillar-high control layer cooperative deformation, and coal pillar stability question has gradually changed from the issue of the stability of coal pillar itself to the overall stability of coal rock pillar structure, which is often affected by adjacent or multiple working faces (goafs). Scholars such as Chen Junjie [15], Guo Weijia [16,17], Zhang Ming [18] and Jiang Fuxing [19] have performed substantial researches on the stability of coal pillars in deep strip mining and the control of subsidence mechanism.

In terms of backfill mining, the Xiaotun Mine, Daizhuang Mine and other mining areas applied paste materials as filling materials for longwall filling mining. Huafeng Mine and Quangou Mine utilized general working face gangue to fill the goaf to liberate coal resources under the building (structure) and to reduce the amount of solid waste exiting the well [20]. Dongping Mine, Jisan Mine and other mining areas adopted solid-bakcfill mining technology to liberate a large amount of coal resources under the building and consumed significant solid waste [21-23].

With regard to the combination of strip mining and backfill mining, Guo Guangli proposed to apply the equivalent replacement theory and adopt the method of ‘Gradually taking ‘. First, the narrow strip was implemented, and then the narrow strip goaf was injected. The idea of slurry filling ultimately achieves the purpose of recovering the remaining coal pillars [24]. Zhang Huaxing suggested the wide strip mining method of " Large mining width-wide retention width-goaf filling", offering a new idea for liberating the deep coal resources of "three under" [25,26]. Li Xiushan and Zhang Xinguo took Daizhuang coal mine as an instance to investigate the feasibility of using paste as a filling material and adopting filling technology to recover strip coal pillars. The outcomes indicate that the filled paste has strong stability and can replace coal seam to bear the overburden load [27,28]. With Gaozhuang as an example, Hou Xiaosongexplored the feasibility of pillarless mining in practice. The study gave that backfilling the roadway with gangue concrete grout can be utilized to recover the coal pillars between the roadway and the channel while ensuring the stability of the surrounding rock. This method further reduces the waste of resources and improve the resource utilization rate [29]. Zhang Xinguo learned the mining mode of driving the roadway in the strip coal pillars and filling and recovering the strip coal pillars based on Xuchang coal mine. The research indicated that although the safety factor is reduced after the roadway is driven in the middle of the strip coal pillars. However, the composite backfill formed by the roadway gangue and the remaining coal pillar still has a strong bearing capacity and can effectively control surface deformation [30].

From the above researches, the current investigation on the control of surface subsidence largely focuses on the coal mining of “three under“in the east, while the research on the regional rock movement and its control of the super-thick weak cementation overburden in deep mining in the western of China is rarely mentioned. The "three-under" coal mining surface subsidence control method can be employed to control the regional strata movement in deep mining of the western super-thick weak cementation overburden, but the deep mining area of the western super-thick weak cementation overburden is wide and sparsely populated. The control plan of "three under" will generate substantial waste of coal resources and high filling costs.

Thus, this paper combines the movement law and energy evolution of super-thick weak cementation overburden in deep mining, and proposes an economical design plan that can control the regional movement to a certain extent.

Evolution law of energy-polling of super-thick weak cementation overburden in deep mining

The existing results suggest that when the mining area is small and the surface is in an extremely inadequate mining state, the surface subsidence of the super-thick weak cementation overburden is noticeably smaller. With the continuous expansion of the mining area, the overburden has a sudden and jumping sinking phenomenon. Thus, during the movement of the overlying strata, energy-polling and release must exist. According to the analysis of the energy-polling and evolution characteristics of the super-thick weak cementation overburden, this chapter describes a reasonable mining plan in combination with the law of movement and failure characteristics of the super-thick weak cementation overburden, thereby reducing the dynamic strength and surface damage degree. This mining plan provides a reference for the layout of the working face in the deep mining area, facing the control of regional strata movement.

This section chiefly applies elastic energy as the representative quantity to learn the evolution law of energy-polling of super-thick weak cementation overburden in deep mining.

Based on Ref. 31, when coal and rock mass damage is not considered, the releasable elastic energy can be expressed as the following formula:

$$U^e=\frac{1}{2}\sigma_1\varepsilon_1^e+\frac{1}{2}\sigma_2\varepsilon_2^e+\frac{1}{2}\sigma_3\varepsilon_3^e \tag{1}$$

Where：ε_i^e is the total elastic strain in the three principal stress directions, $\varepsilon_i^e=\frac{1}{E_i}\left[\sigma_i-\vartheta_i\left(\sigma_j+\sigma_k\right)\right]$, ϑ_i is the poison's ration.

Substituting the expression ε_i^e into Eq. (6-1), Eq. (6-2) can be obtained [32]:

$$U^e=\frac{1}{2}\left\{\frac{\sigma_1^2}{E_1}+\frac{\sigma_2^2}{E_2}+\frac{\sigma_3^2}{E_3}-\vartheta\left[\left(\frac{1}{E_1}+\frac{1}{E_2}\right)\sigma_1\sigma_2+\left(\frac{1}{E_2}+\frac{1}{E_3}\right)\sigma_2\sigma_3+\left(\frac{1}{E_1}+\frac{1}{E_3}\right)\sigma_1\sigma_3\right]\right\} \tag{2}$$

For damaged rock mass, unloading of rock mass will have an impact on the elastic modulus:

$$E_i=a_iE_0 \tag{3}$$

Where, E_0 is the initial elastic modulus when the unit body is not damaged, and a_i is the reduction coefficient.

Assuming that the poison's ratio "ϑ" is not affected by rock damage, substituting Eq. (3) into Eq. (2), we can get:

$$U^e=\frac{1}{2E_0}\left\{\frac{\sigma_1^2}{a_1}+\frac{\sigma_2^2}{a_2}+\frac{\sigma_3^2}{a_3}-\vartheta\left[\left(\frac{1}{a_1}+\frac{1}{a_2}\right)\sigma_1\sigma_2+\left(\frac{1}{a_2}+\frac{1}{a_3}\right)\sigma_2\sigma_3+\left(\frac{1}{a_1}+\frac{1}{a_3}\right)\sigma_1\sigma_3\right]\right\} \tag{4}$$

For the convenience of calculation, the paper ignores the influence of unloading damage on the elastic modulus and Poisson's ratio, then Eq. (4) can be expressed as Eq. (5) [33]:

$$U^e=\frac{1}{2E_0}\left[\sigma_1^2+\sigma_2^2+\sigma_3^2-2\vartheta(\sigma_1\sigma_2+\sigma_2\sigma_3+\sigma_1\sigma_3)\right] \tag{5}$$

In this paper, a three-dimensional numerical model (4500m in length, 4500m in width, 763m in height) is built, and the bottom boundary of the model is selected as the constrained boundary (a=b=c=0, a is the displacement in the x direction, b is the displacement in the y direction, and c is the displacement in the z direction), the top is the free, and the left and right boundaries are constraint in the horizontal direction. The working face width is 300m, the strike distance is 2500m, the section coal pillar is 25m, and 8 working faces are continuously mined.

According to Eq. (5), the post-processing program is developed with Fish language to extract the energy value in the FLAC3D numerical model. Then, the energy value was imported into Tecplot10.0 software for display. Next, with the help of such post-processing program, the

energy-polling evolution law in the movement of super-weak cementation overburden in deep mining is analyzed, such as the energy-polling distribution characteristics in Figures 1 and 2.

In Figure 1, the energy-polling was dominated by the compression strain energy after mining the first working face (working face 2101). The compression strain energy in the Zhidan group sandstone was released slightly, and the Zhidan group sandstone was not destroyed. The Zhidan group sandstone and the overburden above it were bent synchronously.

In Figure 2, the maximum energy-polling is 1300kJ after the second working face was mined, which occurs near the section coal pillar. At this time, the energy-polling is still mainly dominated by compressive strain energy. The compressive strain energy-polling occurs in the upper part of Zhidan Group sandstone above the goaf. This is because stronger tensile failure occurs far from two sides of the goaf in Zhidan Group sandstone. Then, larger bending deformation and compression occurs in the upper strata. The overburden subsided sharply, and its load further transferred to both sides of the goaf, and the energy-polling of the coal walls on both sides of the goaf continued to increase.

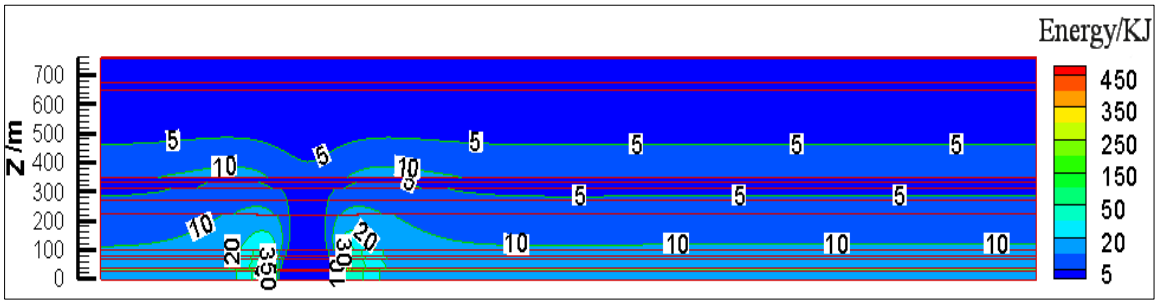

Fig. 1 - Energy-polling distribution characteristics when one working face was mined

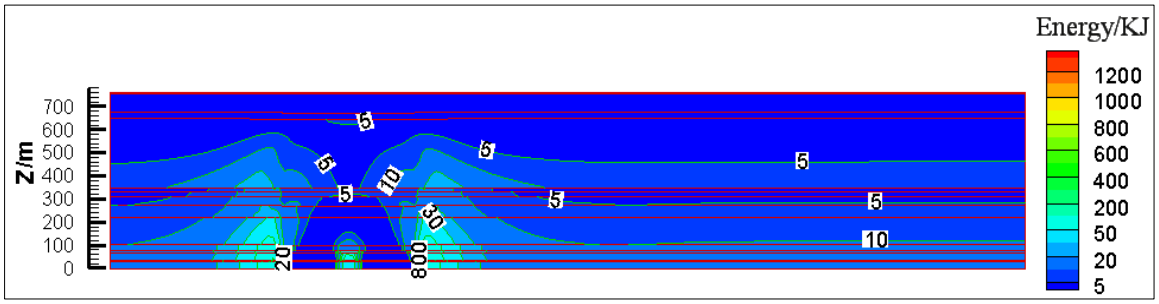

Fig. 2 - Energy-polling distribution characteristics when two working faces were mined

In order to visually analyze the relationship between the maximum energy-polling value and the mining width, the maximum energy-polling value in different mining width is calculated. The relationship between the mining space and the maximum energy-polling value is drawn, and the relationship between the goaf width and the maximum surface subsidence is depicted, as shown in Table 1 and Figure 3.

Tab. 1 - Statistical table of maximum subsidence and energy-polling values

Mining width/m	300	625	950	1275	1600	1925	2250	2575
subsidence/mm	295	1499	3689	4849	4899	5154	5295	5400
Energy accumulation/KJ	450	1300	3400	4500	5000	6000	6500	7000

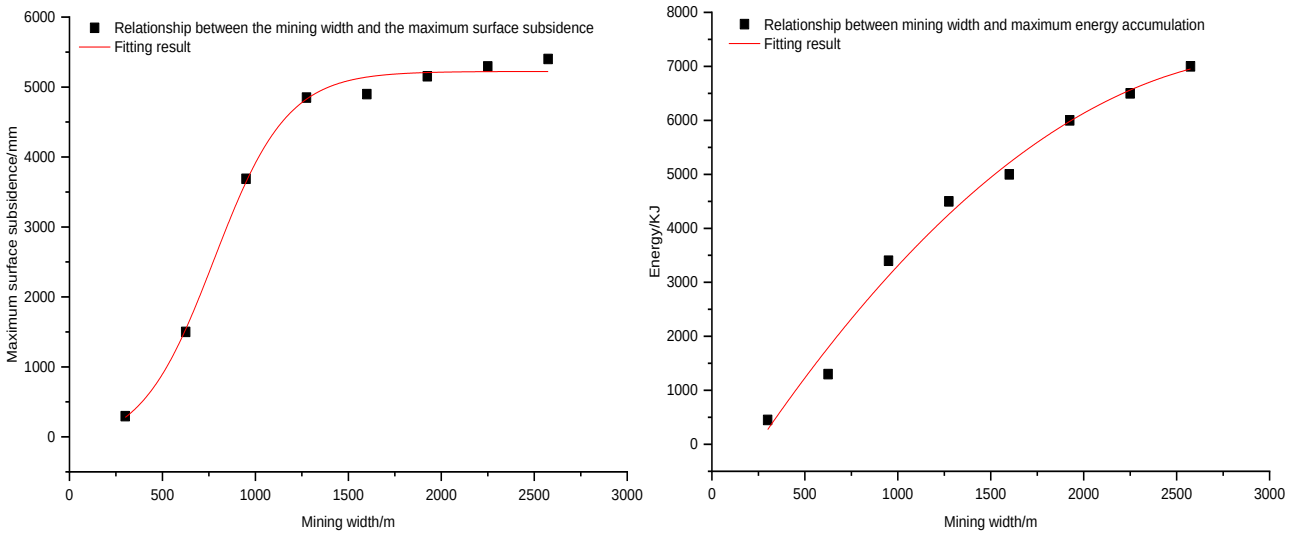

(a) Mining width and maximum subsidence (b) Mining width and maximum energy

Fig. 3- Functional relationship between mining area and maximum surface subsidence and energy-polling values

Based on Figure 3 (a), as mining width increases, the maximum surface subsidence value gradually increases. According to the outcomes of Origin fitting, it can be seen, that the mining width is related to the maximum surface subsidence as a Boltzmann function, the correlation coefficient R_2=0.993, x is the mining width, and the corresponding mathematical relationship is as follows:

$$W_{max}=5223-\frac{5379}{1+e^{\frac{x-777}{196}}} \quad (6)$$

According to Figure 3 (b), as the goaf width increases, the maximum energy-polling progressively increases. From the results of Origin fitting, it can be seen, that the goaf width has a parabolic correlation with the maximum energy-polling, the correlation coefficient R_2=0.984, x is the goaf width, the corresponding mathematical relationship is as follows:

$$Energy_{max}=5.49x+0.001x^2-1293.5 \quad (7)$$

From comparison, it can be found that although the mining width expands, the corresponding maximum surface subsidence value and the maximum energy-polling also increase, but the mathematical relationship between the goaf width and the maximum surface subsidence is significantly different from the mathematical relationship between the goaf width and the maximum energy-polling.

Control plan of regional strata movement of super-thick weak cementation overburden in deep mining

Based on the characteristics of energy accumulation and failure law of overlying strata of super-thick weak cementation overburden in deep mining, the paper proposes a method of partial filling-partial caving multiple working faces coordinated mining based on the main key stratum, thereby reducing the strength of the rock dynamics and surface damage degree in the overburden, which are shown in Figure 4.

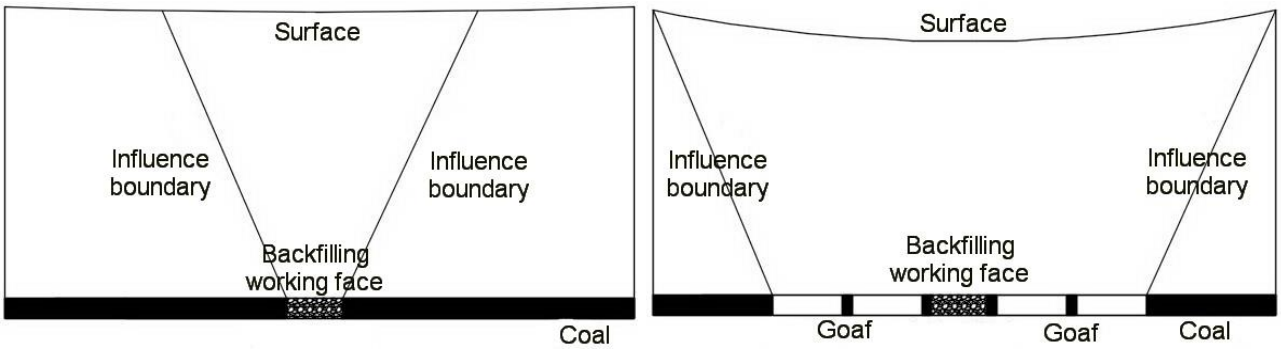

（a）Backfilling （b）Caving mining

Fig. 4 - Schematic diagram of partial filling-partial caving harmonious mining design scheme based on main key layer structure

First, the relevant literature can be referred to establish the physical and mechanical parameters of the gangue filling area [34], and verify the model parameters by the principle of equivalent mining height [35].

Tab. 2 - Physical and mechanical parameters of the backfill

Mechanical parameter	Bulk /Gpa	Shear /Gpa	Friction angle/(°)	Cohesion /Mpa	Density /(kg/m3)	Poisson
Coal	1.35	0.587	6	8.89	1210	0.31
Gangue filling area	0.21	0.095	28	2	1500	0.3

Then, this paper use FLAC3D numerical simulation analysis software to carry out a method of partial filling-partial caving multiple working faces coordinated mining based on the main key stratum, a three-dimensional numerical model was established to mine 8 working faces continuously. The model and excavation parameters are shown in Table 3:

Tab. 3 - Excavation sequence of partial filling-partial caving harmonious mining based on main control layer structure

Mining sequence	Working face	X direction/m	Y direction/m	Mining method
Second stage	2201	750~1050	750~3250	Caving mining
	2202	1075~1375	750~3250	Caving mining
First stage	2203	1400~1700	750~3250	Backfilling
Second stage	2204	1725~2025	750~3250	Caving mining
	2205	2050~2350	750~3250	Caving mining
First stage	2206	2375~2675	750~3250	Backfilling
Second stage	2207	2700~3000	750~3250	Caving mining
	2208	3025~3325	750~3250	Caving mining

From numerical simulation analysis, the stress distribution characteristics of the partial filling-partial caving multiple working faces coordinated mining based on the main key stratum are shown in Figure 5:

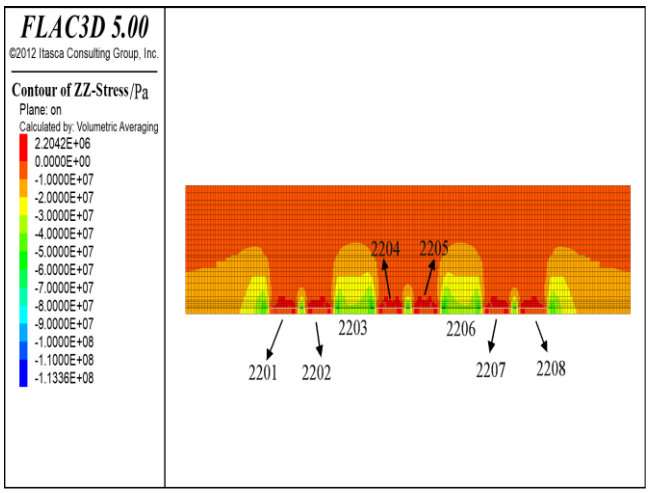

(a) Vertical stress contour of longitudinal section

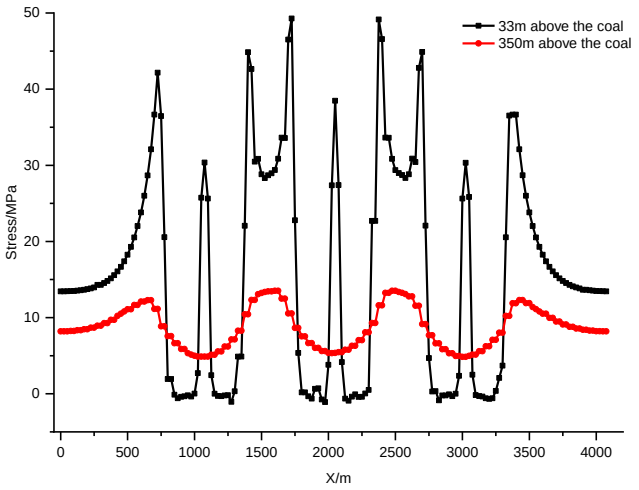

(b) Vertical stress in some strata

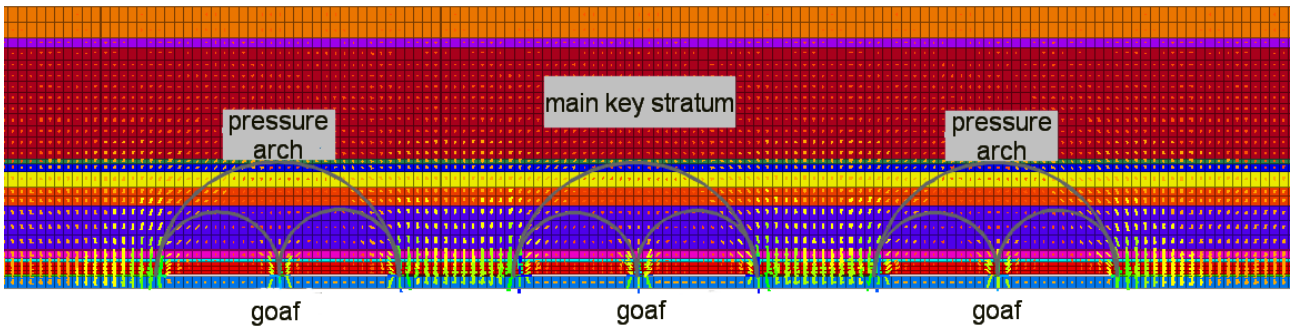

(c) Distribution diagram of pressure arch

Fig. 5 - Stress field distribution diagram of partial filling-partial caving harmonious mining based on main key stratum structure

It can be seen from Figure 5 (a) that the composite filling structure formed by the filling working face and the section coal pillar divides the entire mining area into three independent insufficient mining spaces, and acts as a wide isolated coal pillar to support the overburden load. Each independent goaf is composed of two caving working faces. After a single working face mined, the upper rock mass breaks and collapses, forming a caving fractured zone. The sub-critical stratum restricts the caving fractured zone from continuing to develop upward. The load of the sub-key stratum and its overlying strata is transferred to both sides and concentrated, forming a pressure arch in the middle-low part of the sub-key stratum. After two consecutive working faces are mined, the caving fractured zone continues to develop upwards, and the load of the main key stratum and its overlying strata is transferred to both sides and concentrated on the coal walls of both sides of the goaf, forming a large stress arch under the main key stratum. Meanwhile, a bimodal small pressure arch is formed above a single working face, and the dome develops slightly upwards, as shown in Figure 5 (c).

From Figure 5 (b), the stress distribution of the composite backfill is parabolic, high on both sides and low at the middle, and the internal stress of the composite backfill reaches 49.3MPa, which is slightly larger than the external 44.9MPa. The maximum vertical stress of coal pillars in composite backfill is greater than the maximum vertical stress of 42.2MPa on the coal walls of the goaf sides. The vertical stress of coal pillar between the working face 2204 and the working face 2205 is 38.5 MPa, and the vertical stress of coal pillar between the working faces 2201 and 2202, and the vertical stress of coal pillar between the working faces 2207 and 2208 is 30.4 MPa. The load of the overlying strata is transferred to both sides along the stress arch, and a stress release zone is formed above the goaf. The vertical stress distribution at the bottom of the main key stratum is wavy, with the maximum value of 13.5MPa and the minimum value of 4.86MPa.

In order to more intuitively analyze the strata movement in different buried depth in the method of partial filling-partial caving multiple working faces coordinated mining based on the main key stratum, the movement data of 104m, 350m, 650m above the coal seam and the surface are got and plotted as Figure 6. It can be seen from Figure 6 that as the height from the coal seam increases, the wave-shaped sinking trend gradually eases, but it still develops to the surface. This wave-shaped sinking is related to factors such as the goaf width and the width of the backfill working face.

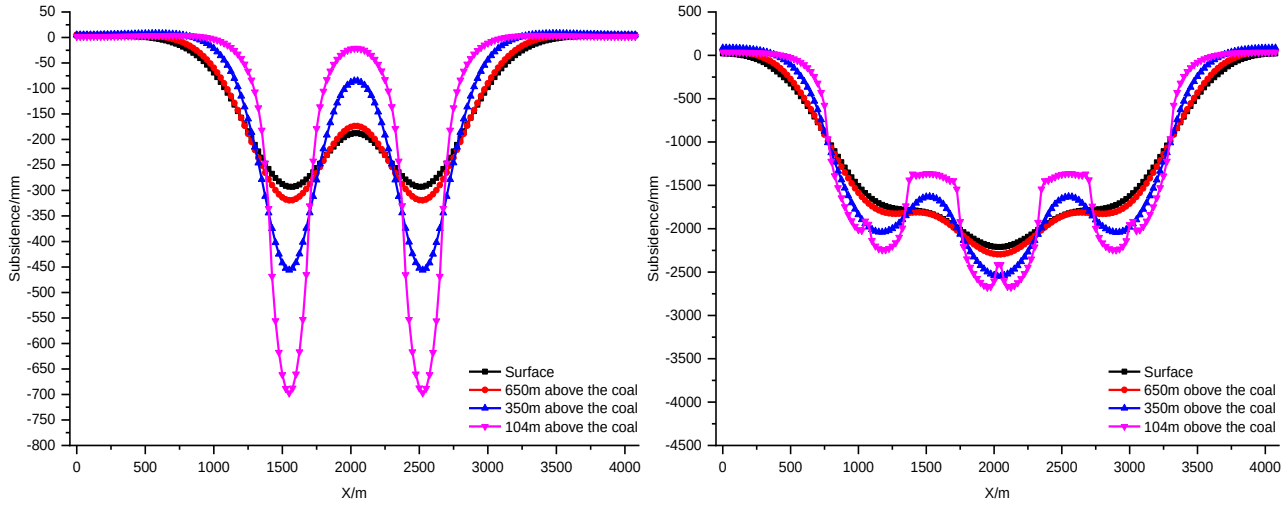

（a）Backfilling （b）Caving mining

Fig. 6 - Strata subsidence curve in different depth caused by partial filling-partial caving harmonious mining based on main key layer structure

Comparative analysis of the control effect of strata movement and energy-polling in different mining approaches

To verify the superiority of the partial filling-partial caving multiple working faces coordinated mining based on the main key stratum, full caving mining, full filling mining, wide strip mining, mixed filling mining, large mining width-wide retention width are simulated respectively, the corresponding mining plan is indicated in Table 4.

The corresponding three-dimensional numerical model can be established based on the mining plans in Table 4, and the surface subsidence value and horizontal movement value can be calculated, and the corresponding deformation curve diagram can be drawn in Figure 7. According to Eq. (5), the energy accumulation value in the corresponding numerical model can be extracted, and the corresponding energy-polling distribution feature map can be drawn through Tecplot10.0 drawing software, as shown in Figure 8.

Tab. 4 - Scheme design of different mining ways

Mining method	Width of caving working face	Width of backfilling working face	Filling ratio	Strike length	Coal pillar width
Full caving mining	300	0	0%	2520	30
Full backfill mining	0	300	80%	2520	30
Wide strip mining	300	0	0%	2520	30
Mixed backfill mining	300	300	80%	2520	30
Large mining width-wide retention width	630	0	0%	2520	30
Partial filling-partial caving in Multi-working face coordinated mining based on main key stratum	630	300	80%	2520	30

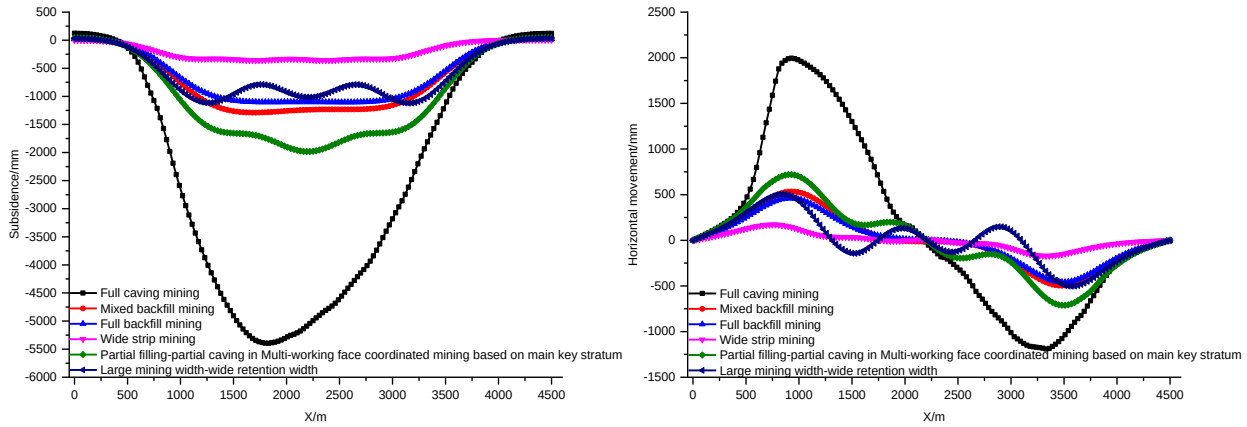

(a) Surface subsidence curve (b) Horizontal movement curve

Fig. 7 - Surface movement and deformation curve of different mining ways

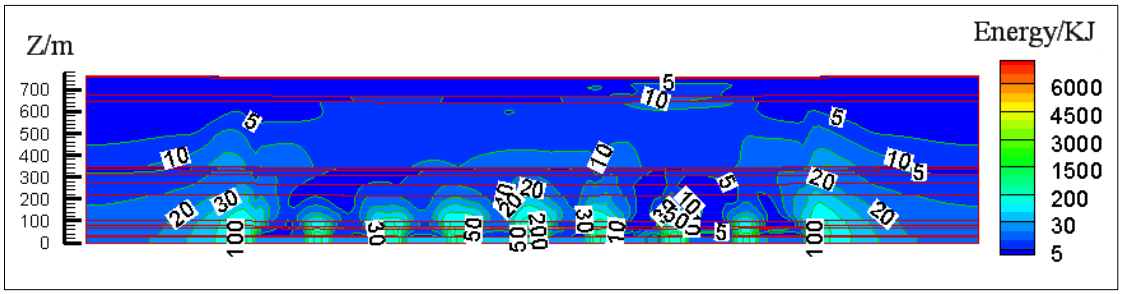

(a) Full caving mining

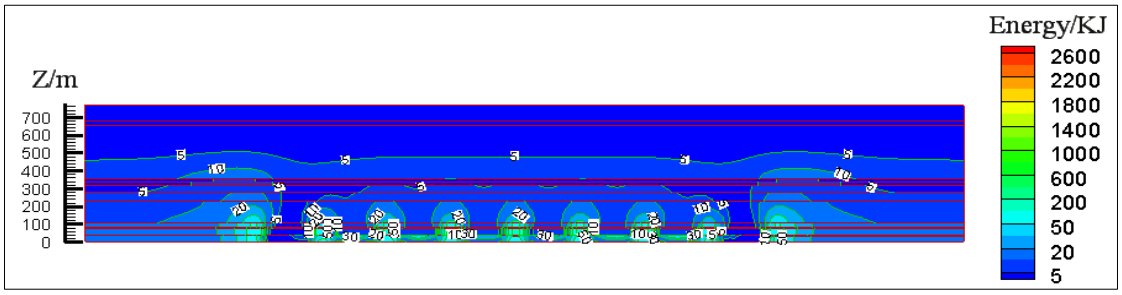

(b) Full backfill mining

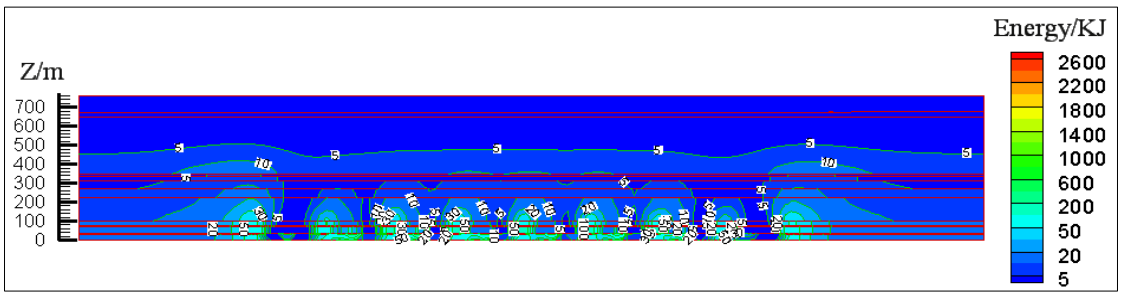

(c) Mixed backfill mining

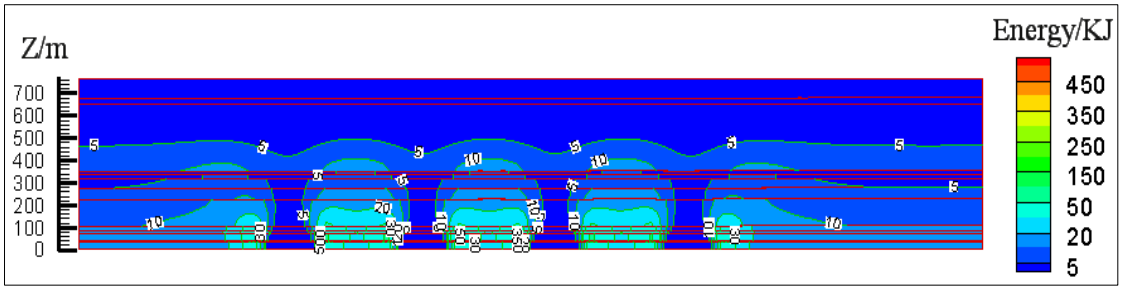

(d) Wide strip mining

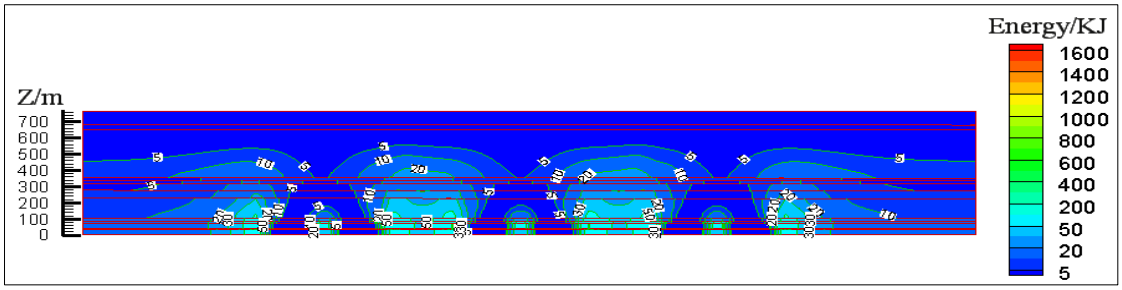

(e) Large mining width-wide retention width

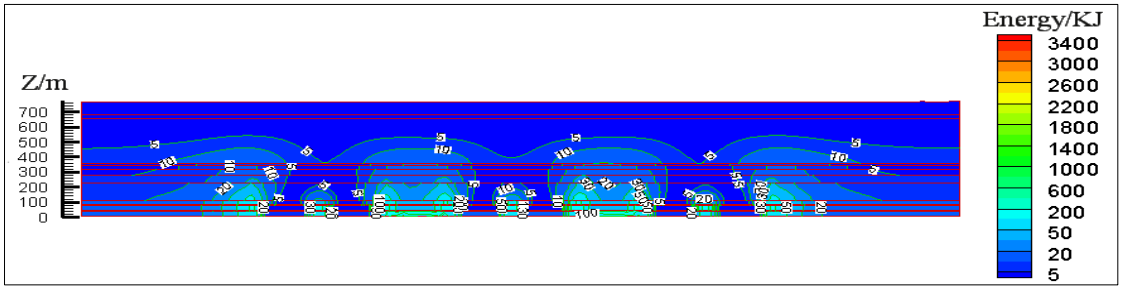

(f) Partial filling-partial caving in multi-working face coordinated mining based on main key stratum

Fig. 8 - Energy-polling distribution characteristics of different mining methods

To visually analyze the surface subsidence and energy-polling of different mining means, the corresponding filling rate, recovery rate, coal pillar rate, maximum surface subsidence value and maximum energy accumulation value can be extracted and calculated (Table 5).

Tab. 5 - Statistical table of surface subsidence and energy-polling extreme values in different mining methods

Mining method	Maximum subsidence /mm	Maximum energy/KJ	Filling Subsidence coefficient ratio	Area filling ratio	recovery ratio	Rate of coal pillar
Full caving mining	5394	6000	0.9	0%	92%	8%
Full backfill mining	1101	2600	0.18	92%	92%	8%
Wide strip mining	357	500	0.06	0%	46%	46%
Mixed backfill mining	1289	2600	0.21	46%	92%	8%
Large mining width-wide retention width	1122	1600	0.19	0%	69%	31%
Partial filling-partial caving in multi-working face coordinated mining based on main key stratum	1983	3400	0.33	31%	92%	8%

In Table 5, from the reduction effect of the surface subsidence, it has following relationship: wide strip mining>full backfill mining>large mining width-wide retention width>mixed backfill mining> partial filling-partial caving in multi-working face coordinated mining based on main key stratum > full caving mining. From the control effect of the energy-polling, it has following relationship: wide strip mining>large mining width-wide retention width> full backfill mining = mixed backfill mining> partial filling-partial caving in multi-working face coordinated mining based on main key stratum> full caving mining. It can be assumed that the recovery rate and coal pillar rate reflect the utilization degree of coal resources, the area filling rate reflects the coal mining cost, and the subsidence coefficient reflects the damage of the ecological environment to a certain extent. With comprehensive considerations, mixed backfill mining, partial filling-partial caving in multi-working face coordinated mining based on main key stratum are the most cost-effective. Mixed backfill mining is to realize mining and backfilling at the same working face, which is technically difficult. Thus, partial filling-partial caving in multi-working face coordinated mining based on main key stratum is the most cost-effective mining method for controlling surface subsidence.

Control mechanism of partial filling-partial caving in multi-working face coordinated mining based on main key stratum

Practice and theoretical researche are both shown that the surface subsidence generated by coal mining does not completely conform to the random medium theoretical model of granular medium, and is closely related to the structural characteristics and lithology of the overlying strata. In particular, when the overlying strata contains multiple strong and thicker strata, the movement of the overlying strata will be divided into multiple strata movement groups, causing the overlying strata and the surface movement and deformation to show its own obvious particularity. To explain the mechanical behavior of hard stratum, researchers have successively proposed the key stratum theory, the plate theory and the bearing layer theory.

The super-thick weak cementation overburden in Yingpanhao Coal Mine contains two layers of thick sandstone, but the strata is soft in lithology, and its movement law is different from ordinary soft strata and hard strata. The existing mechanical theory cannot fully explain its movement mechanism. Even so, Figure 5 (c) shows that the double-layer thick sandstone has obvious control effect on the overburden movement. The key stratum theory can be used to explain its movement mechanism to a certain extent. Although partial filling-partial caving in multi-working face coordinated mining based on main key stratum is similar to the method of deep wide-strip mining, there is the essential difference between the bearing mechanism of the large-width isolation coal pillar and the composite support (filling body and section coal pillar). Figure 9 shows the control mechanism of partial filling-partial caving in multi-working face coordinated mining based on main key stratum.

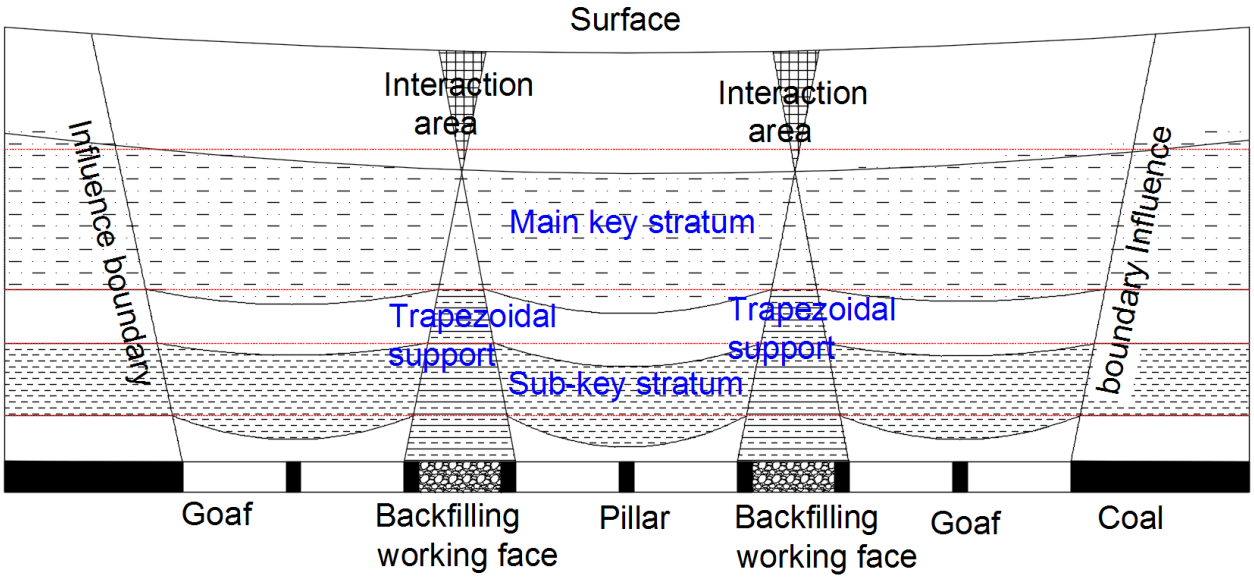

Fig. 9 - Schematic diagram of control mechanism of partial filling-partial caving in multi-working face *coordinated mining based on main key stratum structure*

In partial filling-partial caving in multi-working face coordinated mining based on main key stratum, the composite support and main key strata (main key strata and sub key strata) forms a dual control system of coordinated deformation, which step by step realizes the control of the movement of the overlying strata: The sub-key strata is close to the coal seam, which directly limits the damage height of the overlying strata and reduces the effective sinking space for upward transmission. The chief key stratum limits the upward transmission of the wave-shaped sinking basin, causing the overlying stratum to be a single gently sinking basin. The detailed cooperative control mechanism is as follows:

When the partial filling-partial caving in multi-working face coordinated mining based on main key stratum is completed, the goaf, formed by the double caving working face, loses the support of the coal body, and the overburden damage height develops to the bottom of the main key stratum. Due to the large size of the working face, although the overburden strata on the filling working face are supported by filling bodies, the overburden strata also have a damage in a certain degree. And, due to the limitation of the sub-critical strata, the overburden failure height only developed to the middle and lower parts of the sub-critical strata. The filling working face and caving working face of the mining area are arranged periodically to make the section of the overlying strata form a multi-peak hole structure. The filling working face and the strata above it form a trapezoidal support to separate adjacent goaf. Multiple trapezoidal supports jointly support the main key stratum and can continue to bear the load of the overlying strata. Under the action of its own flexural rigidity and inverted trapezoidal support, the sub-key stratum effectively blocks the upward transmission of the sinking space and diminishes the movement space of the overlying strata. Under the combined action of its own flexural rigidity and the trapezoidal support, the main key stratum further reduces the sinking amplitude, and the wave-shaped sinking trend is blocked or absorbed by the main key stratum when it is transmitted upward.

Judging from the simulation results of similar materials in Ref. 34, when single working face mining or even two-woking face was mined, the sub-critical stratum will block a large amount of effective subsidence space in its lower caving zone and fractured zone, which greatly reduces the sinking space of the overlying strata. From the numerical simulation results in Fig. 11(c), the multimodal pore failure structure is the stress transfer path inside the overburden. The main critical stratum itself and the overlying strata load transfer the stress to the trapezoidal support through the multimodal pore structure. Finally, it acts on the composite support of the filling working face and the section coal pillars, thereby forming multiple stress arches to support the overlying strata together.

CONCLUSION

From the investigation of energy-polling evolution law of the super-thick weak cementation overburden in deep mining, this work proposes an approach for the control of regional strata movement and energy-polling of the super-thick weak cementation overburden, and compares the control effect with other mining methods. Results confirms the superiority of the partial filling-partial caving in multi-working face coordinated mining based on main key stratum and reveals its control mechanism. The following findings are attained：

(1) According to the elastic energy theory, the energy-polling evolution law of super-thick weak cementation overburden in deep mining is analyzed. The maximum energy-polling occurs on both sides of the goaf or on the section coal pillars, and the maximum energy-polling increases parabolically with the mining width.

(2) In the partial filling-partial caving in multi-working face coordinated mining based on main key stratum, the stress distribution of the composite filling body is parabolic, with high on both sides and low in the middle. The inside coal pillars of the backfilling working face has a greater stress concentration.

(3) Numerical simulation methods are employed to investigate the control effects of strata movement and energy-polling in mining methods such as full caving mining, full backfill mining, wide strip mining, and mixed backfill mining. From the reduction effect of surface subsidence, it follows: wide strip mining>full filling mining>large mining width-wide retention width>mixed backfill mining>partial filling-partial caving in multi-working face coordinated mining based on main key stratum >full caving mining. From the energy-polling control effect, it has the following effect: wide strip mining> large mining width-wide retention width >full backfill mining=mixed backfill mining> partial filling-partial caving in multi-working face coordinated mining based on main key stratum>full caving mining. With comprehensive consideration, the partial filling-partial caving in multi-working face coordinated mining based on main key stratum is the most cost-effective.

(4) In the partial filling-partial caving in multi-working face coordinated mining based on main key stratum, a dual control system of coordinated deformation was generated by the composite support and main key strata (main key strata and sub key strata), step-by-step achieving the control of the overlying strata movement. The sub-key stratum structure blocks the height of the overburden damage and greatly reduces the effective space upward transmission. The main key stratum structure further reduces the effective space upward transmission, and absorbs the wave-shaped sinking trend of the overburden until it develops into a single and gentle sinking basin.

ACKNOWLEDGEMENTS

The authors gratefully acknowledge the financial support from the National Natural Science Foundation Item (Grant No.: 51974292).

REFERENCES

[1] Wang B., 2017. Study on the Strata and Surface Movement Regular of the Weakly Cemented Rock High Intensity Mining, Master's thesis, China University of Mining and Technology, Xuzhou, China.
[2] Lin Y.K., 2018. Study on the Surface and Strata Movement Regular of Mining under the Hugely Thick Sand—Illustrated by the Case of Yingpanhao Mine, Master's thesis, China University of Mining and Technology, Xuzhou, China.
[3] Zhang G.X, Fang Z., Han J., et al., 2019. Measurement Study of the Surface Movement Characteristics of the First Mining Working Face in Yingpanhao Coal Mine, Metal Mine, no.10, pp. 81-86.
[4] Gong, Y.Q., Guo G.L., and Wang L.P., et al., 2022. Numerical Study on the Surface Movement Regularity of Deep Mining Underlying the Super-Thick and Weak Cementation Overburden: A Case Study in Western China, Sustainability, vol.14, no. 3: 1855.

[5] Gong, Y.Q., Guo, G.L., and Zhang, G.J., et al., 2021. A Vertical Joint Spacing Calculation Method for Udec Modeling of Large-Scale Strata and Its Influence on Mining-Induced Surface Subsidence, Sustainability, vol.13, no.23, 13313.
[6] Ning J., 2020. Study on the Fracture Characteristics and Roof Control of Overlying Strata in the Deep Mining Area of Ordos. PhD thesis, China University of Mining and Technology (Beijing), Beijing, China.
[7] Wang, B., Jiang, F. and Wang C., et al., 2019. Experimental Study on the Width of the Reasonable Segment Pillar of the Extremely Soft Coal Seam in the Deep Mine. Geotechnical and Geological Engineering, vol.37. no.6, pp. 4947-4957.
[8] Zhang G.J., Guo G.L. and Lv Y.N., et al., 2020. Study on the Strata Movement Rule of the Ultra-thick and Weak Cementation Overburden in Deep Mining by Similar Material Simulation: A Case Study in China, Mathematical Problems in Engineering, vol.2020. pp. 1-21.
[9] Zhang G.J., Guo G.L. and Shen S.K., et al., 2021. Numerical Simulation Study of the Strata Movement Rule of Deep Mining with the Super-Thick and Weak Cementation Overburden: A Case Study in China, Mathematical Problems in Engineering, vol.2021, pp.1-20.
[10] Kukutsch R., Kajzar V. and Waclawik P., et al., 2016. Use of 3D Laser Technology to Monitor Coal Pillar Deformation, Coal Operator's Conference Coal, pp. 109-117.
[11] Zhao Y., Wang S. and Zou Z., et al.,2018. Instability Characteristics of the Cracked Roof Rock Beam under Shallow Mining Conditions, International Journal of Mining Science & Technology, vol. 28, no.3, pp. 437-444.
[12] Li X., Liu C. and Liu Y., et al., 2017. The Breaking Span of Thick and Hard Roof Based on the Thick Plate Theory and Strain Energy Distribution Characteristics of Coal Seam and Its Application, Mathematical Problems in Engineering, vol. 2017, pp. 1-14.
[13] Cao Z., Du F. and Xu P., et al., 2015. Control Mechanism of Surface Subsidence and Overburden Movement in Backfilling Mining based on Laminated Plate Theory, Computers Materials & Continua, vol.53, no.3, pp. 175-186.
[14] Yu L. and Liu J., 2015. Stability of Interbed for Salt Cavern Gas Storage in Solution Mining Considering Cusp Displacement Catastrophe Theory, Petroleum, vol. 1, no.1. pp. 82-90.
[15] Chen J.J., Zhou Y.F. and Yuan Z.L., 2005. Discussion on the Change Rule of Protective Coal Pillar Size under Deep Mining Condition, Law of National Mining Subsidence and the Proceedings of the "Three Under" Coal Mining Academic Conference, pp. 78-79+75.
[16] Guo W.J, Wang H.L. and Liu Z.P., 2015. Coal Pillar Stability and Surface Movement Characteristics of Deep Wide Strip Pillar Mining, Journal of Mining & Safety Engineering, vol. 32, no.3, pp. 369-375.
[17] Guo W., Wang H. and Chen S., 2016. Coal Pillar Safety and Surface Deformation Characteristics of Wide Strip Pillar Mining in Deep Mine, Arabian Journal of Geosciences, vol.9, no.2, pp. 1-9.
[18] Zhang M., Jiang F.X. and Li J.Z., et al., 2018. Stability of Coal Pillar on the Basis of the Co-deformation of Thick Rock Strata and Coal Pillar, Rock and Soil Mechanics, no.2, pp. 1-10.
[19] Jiang F.X., Wen J.L., and Bai J.S., et al., 2018. Rock Burst Risk in Surrounding Abscission Layer of Overlying High Key Strata in Deep Mining Mines, Journal of China University of Mining & Technology, no.1, pp. 40-47.
[20] Gao M.T., Zhang M. and Zhou M., 2012. Study and Practice on the Technology of Filling Mining in Xin Wen mining area, Applied Mechanics and Materials, pp. 2892-2896.
[21] Ma L. and Ding Z.W., 2011. The Application Research on Backfill Mining Technology of Gangue for Coal Pillar Mining in Xingtai mining village, Advanced Materials Research,pp. 225-231.
[22] Zhu X.J., Guo G.L. and Zha J.F., 2014. Surface Subsidence Caused by Solid Backfilling Mining, Disaster Adv, vol. 7, no.3, pp. 59-66.
[23] Zhang Q., Zhang J.X. and Kang T., et al., 2015. Mining Pressure Monitoring and Analysis in Fully Mechanized Backfilling Coal Mining Face-A Case Study in Zhai Zhen Coal Mine, Journal of Central South University, vol. 22, no.5, pp. 1965-1972.
[24] Guo G.L., Wang Y.H. and Ma Z.G., 2004. A New Method for Ground Subsidence Control in Coal Mining, Journal of China University of Mining & Technology, no.2, pp. 26-29.
[25] Zhang H.X. and Guo A.G., 2006. Study on the Influencing Factors of Surface Subsidence in Wide Strip Filled Full Column Mining[J]. China Coal Industry, no. 6., pp. 56-57.
[26] Zhang H.X. Li X.G. and Liu D.M., 2002. Full-pillar Extraction by Wide Working Face Layout in Partial Mining, Journal of Mining And Strata Control Engineering, no.2, pp. 16-18+25.
[27] Li X.S., Cao Z. and Liu C.M., et al., 2012. Study on Surface Subsidence of Strip Coal Pillar and Gangue Gypsum Filling Mining, Coal Engineering, no.4, pp. 85-87.
[28] Zhang X.G., Jiang X.Y. and Jiang N., 2012. Research and Application of Coal Gangue Paste Packing in Daizhuang mine, China Mining Magazine, vol. 21, no.4, pp. 82-86.

[29] Hou X.S., 2011. No Pillar Mining Practice in Gaozhuang Coal Mine, Shandong Coal Science and Technology, no.1, pp. 88-89.
[30] Zhang X.G., Jiang X.Y. and Jiang N., 2013. Study on Coal Rejects Backfill Mining Mode in Xuchang Mine, Coal Engineering, no.1, pp. 12-14+18.
[31] Boresi A. P., Schmidt R. J. and Sidebottom O. M., 1985. Advanced mechanics of materials, New York et al.: Wiley.
[32] Xie H.P., Ju Y. and Li L.Y., 2005. Criteria for Strength and Structural Failure of Rocks Based on Energy Dissipation and Energy Release Principles, Chinese Journal of Rock Mechanics and Engineering, vol. 24, no.17, pp. 3003-3010.
[33] Wang H.W., Jiang Y.D., and Zhao Y.X., et al., 2013. Investigation on Mechanism of Energy Explosion During Extraction of Island Longwall Panel, Chinese Journal of Rock Mechanics and Engineering, vol. 32, no.11, pp. 2250-2257.
[34] Gong P., 2018. Surrounding Rock Deformation Mechanism and Application for Gob-Side Entry Retaining in Deep and Large Height Coal Seam with Fully Mechanized Gangue Backfilling Mining, PhD thesis, China University of Mining and Technology, Xuzhou, China.
[35] Guo G.L., Zhu X.J. and Zha J.F., et al., 2014. Subsidence Prediction Method Based on Equivalent Mining Height Theory for Solid Backfilling Mining, Transactions of Nonferrous Metals Society of China, vol. 24, no.10, pp. 3302-3308.

CIVIL ENGINEERING JOURNAL

Article no. 13

THE CIVIL ENGINEERING JOURNAL 1-2022

EXAMINED AND ANALYSIS OF EMPIRICAL SEISMIC DAMAGE OF WORKSHOP BUILDING

Si-Qi Li[1,2,3], Yong-Sheng Chen[4] and Hong-Bo Liu[3,5*]*

1. *Longjian Road and Bridge Co., Ltd., No. 109, Songshan Road, Harbin City, China; lisiqi@hlju.edu.cn*
2. *School of Transportation Science and Engineering, Harbin Institute of Technology, Harbin City, China*
3. *School of Civil Engineering, Heilongjiang University, No.74, Xuefu Road, Harbin City, China; hongboliuhlju@126.com*
4. *Institute of Engineering Mechanics, China Earthquake Administration, No.29, Xuefu Road, Harbin City, China; chenys@iem.ac.cn*
5. *Key Laboratory of Functional Inorganic Material Chemistry (Heilongjiang University), Ministry of Education, No.74, Xuefu Road, Harbin City, China*

ABSTRACT

To deeply explore the typical damage characteristics and vulnerability characteristics of workshop buildings (WBs) in actual earthquakes, empirical field reconnaissance and observation of WBs damaged to varying degrees in the Mw 8.0 earthquake in Wenchuan County, Sichuan Province, China, on May 12, 2008, were conducted. The investigation results indicated that the typical seismic damage forms of industrial buildings in multiple intensity regions were: local and overall collapse, column cracking and crane beam displacement, failure and cracking of walls, and damage of supporting and connecting members. Field investigation pictures of typical seismic damage were provided. According to different typical failure characteristics, the seismic damage mechanism and seismic capacity were analysed, and measures and suggestions to improve the seismic ability of industrial buildings with different material categories were conducted. The conclusions can provide a necessary reference for the revision of the seismic code of industrial plants and the seismic intensity scale of China.

KEYWORDS

Workshop Building, Empirical Seismic Damage Observation, Analysis of Typical Failure Characteristics, Failure Analysis, Seismic Damage of Components

INTRODUCTION

Earthquakes of different intensities significantly impact the natural environment and infrastructure, which will commonly cause traffic blocking and buildings stock failure [1], especially damage to artificial structures. A large amount of empirical seismic damage observation data indicates that many casualties and property losses are caused by the failure or serious damage of engineering structures. Therefore, to improve the ability of structures to resist earthquakes of different intensities, deeply studying the seismic capacity and vulnerability characteristics of engineering structures has critical engineering and practical significance.

Empirical structural seismic damage investigation and vibration model analysis can effectively evaluate the seismic damage of building structures under different intensity levels. Sun et al. [2] and Qu et al. [3] conducted damage analysis and statistics on the seismic damage

investigation data of structures (reinforced concrete structure (RC), masonry structure (MS), and wood structure) in the Lushan earthquake in China, and empirical seismic vulnerability analysis considering this earthquake was provided. Li et al. [4-8] investigated and analysed the actual seismic damage of MS, RC, and bottom frame seismic wall masonry structures (BFSWMSs) damaged to varying degrees in the Wenchuan earthquake in China, compared the vulnerability in combination with a variety of coupling influence factors, and established an empirical seismic damage vulnerability probability demand model considering multiple intensity regions. Bagheri et al. [9] and Miglietta et al. [10] conducted an experimental study on the structural model under a strong medium earthquake considering the structural seismic response system, and the relationship model between impact and floor ductility high-rise structures under specific ground motions was analysed.

With the gradual development of factory manufacturing, WB has been extensively used in different regions. This type of structure has the characteristics of a large bay, flexible spatial layout, and strong applicability and is especially suitable for the production and manufacture of large objects. However, owing to the seismic action of different intensity levels, WB has suffered many degrees of earthquake damage, which has seriously affected industrial production and even threatened people's life safety and property loss. Palanci et al. [11] investigated single-story prefabricated industrial buildings in Turkey using probability and statistics methods, conducted inelastic and time history analysis combined with typical WB and produced a vulnerability curve model considering the ground peak acceleration parameter. A two-level fuzzy comprehensive evaluation method was proposed by Sun and Zhang [12], which can be used for seismic damage assessment and risk analysis of single-layer reinforced concrete industrial plants. Casotto et al. [13] analysed the vulnerability model of RC prefabricated industrial buildings that suffered typical damage in northern Italy, conducted regression analysis considering the cumulative percentage parameters of different failure states, and obtained the vulnerability function model under the influence of varying strength modulus. Wang et al. [14] utilized ABAQUS analysis software to establish a finite element model of a single-layer brick column factory building and performed dynamic response and failure mechanism analysis.

The relevant research mentioned above mainly focuses on the empirical seismic damage investigation and model analysis of a single WB, such as damage investigation of a single structure, 3D finite element model, and shaking table test. It has achieved a great deal of scientific research results. However, by analysing the failure characteristics of a single typical WB, it is difficult to effectively grasp the typical seismic damage characteristics of WB in the overall seismic region to a certain extent. Therefore, to effectively grasp the typical seismic damage characteristics of WB structures, based on the empirical structural seismic damage observation data of the Wenchuan Mw 8.0 earthquake on May 12, 2008 [4-8], this study analyses and summarizes the typical damage characteristics of WB in the overall survey region and puts forward measures and methods to effectively improve the seismic capacity of WB according to different damage characteristics.

BRIEF INTRODUCTION OF STRUCTURAL DAMAGE INVESTIGATION IN WENCHUAN EARTHQUAKE

On May 12, 2008, a magnitude 8.0 earthquake occurred in Wenchuan County, Sichuan Province, China, causing a large number of casualties and property losses. After the earthquake, the China Earthquake Administration quickly organized a field seismic damage reconnaissance team to investigate structural seismic damage on various structures in 33 cities and villages [5] [7]. The author and relevant personnel of the investigation team participated in the investigation. They carried out a field actual seismic damage investigation on 18480 building structures in different intensity regions according to the seismic intensity distribution map (as reported in Figure 1 [15], China seismic code (GBJ11-89, GB50011-2001, and GB50011-2010) [16][17][18], and China seismic intensity scale (GB/T17742-2020, CSIS-20) [19], including all building samples (7099 buildings)

investigated in Dujiangyan city. The structural categories investigated in the earthquake region are diversified. Table 1 summarizes the main categories of building structures in the investigated region.

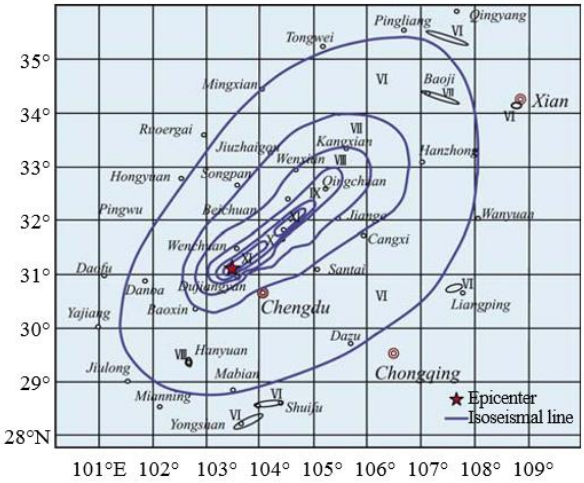

Fig. - 1 Macrointensity map of Wenchuan earthquake in China [5][15]

Tab. 1 - Type of structure investigated in the actual earthquake region

Category	WB	Other
	Masonry industrial building, single-story concrete of workshop, the single-story steel frame of the workshop, single (multiple) story RC of industrial workshop, RC industrial plant with masonry infilled wall, single-story masonry industrial plant	RC, MS, BFM, Brick wood structure, and adobe structure

According to the field seismic damage investigation of various structures, the WB of the steel frame is less damaged in different intensity regions, and a certain number of masonry WB are subjected to different degrees of seismic damage. The damage to the RC structure is relatively light, the MS after seismic design shows good seismic performance, and the deterioration of the BFM is relatively heavy due to the inconsistency of the structural stress system. The damage to brick wood and adobe structures is relatively significant. It is worth noting that WB structure types show diversified characteristics, and the seismic damage is more significant in different intensity areas. To relatively accurately and comprehensively grasp the typical damage characteristics of this type of structure, the investigation and analysis of typical seismic damage of WB should be considered.

ANALYSIS OF EMPIRICAL SEISMIC DAMAGE CHARACTERISTICS OF WB

With the rapid and sustainable development of the global industry and manufacturing industry, the demand for industrial plant buildings (WBs) in various industries has increased significantly. Single-story industrial plant buildings are the main structural form of plant buildings in different industrial areas in China. The investigation data of the empirical seismic damage of the Wenchuan earthquake indicated that WB built with different materials suffered various degrees of seismic damage and caused substantial economic losses. The field structural seismic damage reconnaissance team investigated and analysed the seismic damage of the overall and local components of WB in multiple intensity regions. The damage forms mainly include local and overall

structural failure, column cracking and crane beam displacement, wall failure and cracking failure, and seismic damage of support and connecting components. The structural form and category is divided into reinforced concrete bent column workshop, steel structure workshop, brick column workshop, frame bent workshop, and steel-concrete composite structure workshop. This study analyses the failure characteristics and mechanisms according to the empirical seismic damage and types mentioned above.

Local or overall structural failure

The investigation team found that in the high-intensity area, due to the relatively weak stiffness and strength at the connection between the precast beam and column, the beam was seriously displaced or even fell under the reciprocating action of ground motion, resulting in local collapse. In addition, individual brick plants experience an overall collapse in the multi-intensity region, owing to their brittle materials and weak vertical and horizontal constraints, as depicted in Figure 2. It should be considered to properly strengthen the connection between the crane beam and corbel, improve the integrity of longitudinal and transverse stressed members, and reasonably set diagonal bracing members to enhance lateral stiffness to coordinate the overall deformation of the structure. Structural members composed of multiple materials should be avoided, the lateral force resistance of the structure should be reasonably increased, and the seismic effect of the structure should be inproved.

(a) Local collapse of RC industrial building

(b) Collapse of MS industrial building

(c) Failure of steel structure industrial building

(d) Failure of roof slabs and beams in an industrial building

(e) Overall failure of MS and steel frame industrial building

(f) Failure of upper transverse beam and plate of industrial building

Fig. 2 - Overall and local failure of WB

Column cracking and crane beam displacement

The seismic damage of the WB column was typical in the investigation work. The failure forms were: oblique and transverse cracking of the column (column head, column body, and column base), cracking of the concrete corbel root, cracking at the variable section, and cracking at the column beam joint, as illustrated in Figure 3. Owing to the column ends (top and bottom) being generally subjected to large horizontal earthquakes, a the large shear force was generated and led to shear failure. The failure of the column body was characterized by transverse cracking, local compression, and crisp crushing, resulting in a short column effect, and cracking failure was caused by the coupling effect of bending and tension. Shear or crushing cracking often occurs at the variable section of the concrete column (corbel). Because this position was at the variable section of the column, it caused sudden changes in stress and force transmission coupled with insufficient strength and stiffness, resulting in cracking failure.

(a) Cracking failure of the RC column head

(b) Oblique cracking failure of RC frame column

(c) Transverse cracking failure of the brick column

(d) Cracking failure of the lower part of the brick column

(e) Cracking and failure of corbel root

(f) Crushing cracking failure of corbel end

(g) Longitudinal displacement of crane beam

(h) Vertical cracking failure of crane beam

Fig. 3 - Seismic damage of columns and crane beams

In addition, it was found in the investigation that some column and beam joints produce plastic hinges and crack damage. Individual crane beams cause the corresponding displacement due to insufficient longitudinal restraint. The columns of different materials should be checked in strict

accordance with the seismic design requirements to ensure that they have sufficient seismic capacity. Reasonably improve the ductility to reach the plastic state and still have a certain bearing capacity and deformation capacity when working. Properly control the section shape of a variable column and the ratio of the section area and linear stiffness of the upper and lower columns. The corbel should be subjected to strict seismic checking calculations of stiffness, strength, and ductility, and the lateral stiffness should be reasonably designed to avoid the increase in seismic force caused by too short a transverse period due to improper design.

Cracking and failure of the wall

Walls are a vital enclosure component of WB, which can avoid the adverse impact of natural environmental factors on the structural system, ensure the normal use of WB, and play the role of enclosure and blocking space. According to the field investigation of empirical seismic damage, most of the retaining walls are self-supporting brick walls, with relatively small shear and bending resistance and insufficient seismic capacity. Under the reciprocating action of longitudinal ground motion, it is easy to produce a "whiplash effect," resulting in outward inclination of the top and local or overall collapse, as demonstrated in Figure 4.

(a) Failure of Maintenance wall (gable)

(b) Local collapse of building a wall of RC bent workshop

(c) Overall wall failure of maintenance wall

(d) Local collapse of maintenance wall

(e) Collapse of upper maintenance wall

(f) Partial failure of upper maintenance wall

Fig. 4 - Seismic damage of maintenance wall

In the low and medium-intensity regions, some walls show transverse and oblique cracking failure, especially at the door and window openings caused by stress concentrations, as depicted in Figure 5.

(a) Cracking of wall between windows

(b) Oblique cracking of wall

(c) Cracking of inner wall

(d) Cracking and damage at the door opening

Fig. 5 - Crack and damage of maintenance wall

WB's stress system is a bent or frame structure system. The maintenance wall is a nonstructural member. It first fails with beams and columns, which protects the bearing capacity of the main structure to a certain extent, plays the role of "the first line of defense," and has positive seismic significance. The necessary design should be conducted in strict accordance with the code for seismic design of building structures, the essential description of the wall structure design, the seismic checking calculation of tie joints, the connection between the wall and structural members should be strengthened to coordinate its stiffness and mass distribution, and the seismic performance of the wall should be further included in the seismic checking calculation of WB.

Seismic damage of supporting and connecting members

The practical setting of X-type and horizontal support and connection can improve the lateral stiffness of WB to a certain extent to improve its seismic performance. In the field seismic damage investigation, it is found that the yield of supporting and connecting members is relatively significant. When subjected to an earthquake, the roof truss and roof system produce a large horizontal inertial force, resulting in more considerable pressure and tension on the support members. In addition, the support system suffers buckling or failure due to insufficient stiffness and connection strength, as depicted in Figure 6.

It is necessary to consider the essential aseismic checking of the X-type supporting system and appropriately increase its stiffness and lateral force resistance. Strengthen the joint strength between the vertical and horizontal connecting members and the main structure to have the same deformation coordination ability. However, the buckling or failure of the X-brace consumes part of the seismic capacity to a certain extent and has a certain protective effect on the main structural system.

(a) Buckling of X-brace

(b) Failure of horizontal contact

Fig. 6 - Seismic damage of supporting and connecting members

Basically intact

During the field investigation, it was found that a large amount of light steel structure WB and constrained brick WB after seismic design were basically intact, as illustrated in Figure 7. It is worth noting that even in the high-intensity regions, a certain number of light steel structures WB and brick WB after seismic design were still undamaged.

(a) Light steel workshop

(b) Steel structure workshop

(c) Steel frame workshop

(d) Brick workshop with seismic design

Fig. 7 - Basically intact of WB

The main reason was that the light steel structure has a strong overall deformation capacity, light material texture, and relatively small inertial force. After the seismic design, the brick WB has the seismic structural measures of ring beam and connecting column so that its seismic capacity can be further improved. In new construction or reinforcement projects, priority should be provided to the use of light steel structure WB and brick WB structure category with seismic design to ensure that the structural design and construction are performed in strict accordance with the seismic code.

CONCLUSION

WB structures have attracted much attention as a widely used structure type worldwide. This type of structure has suffered many degrees of seismic damage in different levels of earthquakes, which directly affects human safety and property damage. In this study, employing the WB damage of the empirical seismic damage investigation of the Wenchuan earthquake on May 12, 2008, in China as the research case, the damage characteristics and mechanism analysis are performed for the local or overall failure of the structure, the damage of columns and crane beams, the seismic damage of retaining walls and the damage of supports and connections. The following opinions and suggestions are obtained:

1. It should be considered to prioritize the selection of light steel structure roof systems in different intensity regions, reasonably reduce the self-weight of the structure, reduce the support system, and avoid the failure of connecting structure and load-bearing structural components.

2. Reasonably strengthen the structural connection of local joints to ensure the connection strength and stiffness of the corbel and roof truss system. A light steel structure plate should be considered for skylight frames.

3. A steel structure or RC column should be preferentially selected as the vertical stress system for the single-story plant to reasonably ensure the ductility of the components. Ensure that the lateral stiffness of the column is suitable for the section size and avoid the increase in seismic force caused by the shortening of the structural period.

4. Priority should be given to the use of lightweight precast wallboards as enclosure structures. In strict accordance with the seismic code, the effective connection between the retaining wall and the column and beam is strengthen, and the integrity of the structure is improved.

5. It is suggested to use X-braced steel members with relatively good energy dissipation and deformation capacity to improve the lateral force resistance of WB and the seismic resistance of the whole structure.

The results of this study can provide necessary references for the empirical seismic damage investigation and evaluation of WB structures, the revision of seismic codes, and seismic intensity scales in the future.

ACKNOWLEDGMENTS

The basic data used in this paper are from the Dujiangyan city seismic damage field observation team of the Institute of Engineering Mechanics (IEM), CEA. I would like to express my sincere gratitude to them. In addition, the research described in this paper was financially supported by the Basic Scientific Research Business Expenses and Scientific Research Projects of Provincial Colleges and Universities in Heilongjiang Province (2021-KYYWF-0044), Science Foundation of Heilongjiang Province (E2018060), Scientific Research Fund of Institute of Engineering Mechanics, China Earthquake Administration (Grant No. 2019A02), and Key Laboratory of Functional Inorganic Material Chemistry (Heilongjiang University), Ministry of Education.

REFERENCES

[1] Li, S. Q., Liu, H. B. and Chen, Y.S. 2021 “Vulnerability models of brick and wood structures considering empirical seismic damage observations”, Structures, Vol. 34, 2544–2565.

[2] Sun, B. T., Spencer, B. F., Yan, P., Chen, X., Zhang, G. X. 2019 “Analysis of the Seismic Vulnerability of Buildings in the Lushan Ms7.0 Earthquake in the Sichuan Province of China”, Journal of Earthquake Engineering. DOI: 10.1080/13632469.2019.1692742

[3] Qu, Z., Dutu, A., Zhong, J., Sun, J. 2015 “Seismic damage of masonry infilled timber houses in the 2013 M7.0 Lushan Earthquake in China”, Earthquake Spectra, Vol. 31, No. 3, 1859-1874.

[4] Li, S. Q., Yu, T. L., Chen, Y. S. 2019 “Comparative analysis of the empirical seismic vulnerability of typical structures in multiple intensity zone”, Archives of Civil Engineering, Vol. 65, No. 3, 167-183.

[5] Li, S. Q., Yu, T. L., Chen, Y. S. 2021 “Comparison of macroseismic intensity scales by considering empirical observations of structural seismic damage”, Earthquake Spectra, Vol. 37, No. 1, 449-485.

[6] Li, S. Q., Yu, T. L., Jia, J. F. 2019 “Empirical seismic vulnerability and damage of bottom frame seismic wall masonry structure: A case study in Dujiangyan (China) region”, International Journal of Engineering, Transactions C: Aspects**,** Vol. 32, No. 9, 1260-1268.

[7] Li, S. Q., Chen, Y. S. 2020 “Analysis of the probability matrix model for the seismic damage vulnerability of empirical structures”, Natural Hazards, Vol. 104, No. 1, 705-730.

[8] Li, S. Q., Yu, T. L., Jia, J. F. 2019 “Investigation and analysis of empirical field seismic damage to bottom frame seismic wall masonry structure”, International Journal of Engineering, Transactions B: Applications, Vol. 32, No. 8, 1082-1089.

[9] Bagheri, G., Ashtari, P., Behnamfar, F. 2021 “Rigid-Plastic Analysis of Seismic Resistant T-Frame considering Moment-Shear Interaction”, Shock and Vibration, 8844039.
[10] Miglietta, M., Damiani, N., Guerrini, G. Graziotti, F. 2021 “Full‐scale shake‐table tests on two unreinforced masonry cavity‐wall buildings: effect of an innovative timber retrofit”, Bulletin of Earthquake Engineering Vol.19, No. 6, 2561–2596.
[11] Palanci, M., Senel, S. M., Kalkan, A. 2017 “Assessment of one story existing precast industrial buildings in Turkey based on fragility curves”, Bulletin of Earthquake Engineering, Vol. 15, No. 1, 271-289.
[12] Sun, B. T., Zhang, X. 2020 “Research on the safety assessment of RC workshop buildings in earthquake site based on the fuzzy comprehensive evaluation”, Structural Concrete, 1-18.
[13] Casotto, C., Silva, V., Crowley, H., Nascimbene, R., Pinho, R. 2015 “Seismic fragility of Italian RC precast industrial structures”, Engineering Structures, Vol. 94, 122-136.
[14] Wang, M., Sun, B. T., Yan, P. 2014 “Seismic damage predictions and antiseismic performance researches of single-story brick column workshops in Lushan Ms7.0 Earthquake”, Applied Mechanics and Materials, Vol. 638-640, 1842-1847.
[15] Yuan, Y. F. 2014 “Impact of intensity and loss assessment following the great Wenchuan Earthquake”, Earthquake Engineering and Engineering Vibration, Vol. 7, No. 3, 84-93.
[16] GBJ11-89, 1989, Specifications for antiseismic construction design, China.
[17] GB50011-2001, 2001, Code for seismic design of buildings, China.
[18] GB50011-2010, 2010, Code for seismic design of buildings, China.
[19] GB/T17742-2020, 2020, Chiese seismic intensity scale, China.

CIVIL ENGINEERING JOURNAL

Article no. 14

THE CIVIL ENGINEERING JOURNAL 1-2022

A KNOWLEDGE MAPPING ANALYSIS OF DIGITAL PHOTOGRAMMETRY RESEARCH USING CITESPACE

Yongquan Ge, Yingchun Liu and Xiaodong Liu

Shandong Jianzhu University, College of Surveying and Geo-Informatic, Fengming Road 1000, 250101 Jinan, Shandong, China; ge39953@163.com, 1781632516@qq.com

ABSTRACT

In order to clearly understand the current status and application trends of digital photogrammetry domestic and overseas research, taking the core journals of Web of Science (WoS) as the data source, using bibliometric methods and CiteSpace to carry out statistical analysis of the relevant literature of digital photogrammetry research. The results show that since 2011, the research literature on digital photogrammetry has shown a steady growth year by year. Digital photogrammetry is most closely related to the three disciplines of geology, earth science integration, and physical geography; countries such as the United States, the United Kingdom, Italy, and China publish the most papers, and these countries have strong research capabilities. Lane S.N. and Chandler J.H. have been shared with a high number of citations, who are representative scholars in this field; Digital photogrammetry contains multiple research directions. This article studies the research frontier and trend analysis of digital photogrammetry through keyword co-occurrence analysis and mutation detection analysis.

KEYWORDS

Web of Science, WoS, Knowledge mapping, CiteSpace, Digital photogrammetry, Document metrology, Visual analysis

INTRODUCTION

Photogrammetry is a field of geodesy, and it originated with very similar approaches from the pioneering works of Laussedat in France [1] and Meydenbauer in Germany [2] about 10 years apart, i.e. around 1860 and 1870, respectively [3]. Laussedat was the first to use photographic images for topographic surveys as early as 1861 [1]. In 1867, Meydenbauer used his photogrammetric cameras to record metric images from the town church and also a sector of the terrain for topographic purposes [4].

Digital photogrammetry is based on the basic principles of digital imaging and photogrammetry. It uses computer technology, digital image processing, image matching, pattern recognition and other multidisciplinary theories and methods to extract the geometric and physical information of the subject digitally expressed [5]. With the emergence of new sensors, digital photogrammetry has been further developed, such as post assisted aerial triangulation, information extraction combined with lidar images, etc. Digital photogrammetry has the potential to solve many current problems more effectively, and it will be further developed. Therefore, it is necessary to clearly understand the research status of digital photogrammetry at home and abroad, grasp the research trends of digital photogrammetry and study the development of digital photogrammetry.

From the perspective of visualization, this paper uses the method of generating knowledge map to intuitively display the research status and hot spots in the field of digital photogrammetry in recent years, in order to help scholars grasp and analyse the development trend of this discipline more accurately, and provide scientific reference for subsequent research.

DATA AND METHODS

This section should describe in detail the study material, procedures and methods used.

Data sources

Taking the web of science core collection database as the data source, the period is limited from 1900 to December 2020, the language is limited to English, and the literature type is limited to article and review After that, 939 related literatures were obtained.

research method

CiteSpace developed by Professor Chen Chaomei of Drexel University, is one of the most characteristic and influential information visualization analysis software developed under the background of scientometrics, data and information visualization [6]. It can not only provide the mining of citation space, but also provide the co-occurrence analysis function among other knowledge units, such as the cooperation among authors, institutions regions and countries [7]. In this paper, CiteSpace v.5.7.r2 (64 bit) is used as a visualization tool to draw a series of related knowledge maps and analyze the research status and trends of digital photogrammetry.

RESULTS AND ANALYSIS

Time series analysis of literature output

As shown in Figure 1, the overall trend of literature in the field of digital photogrammetry retrieved by WoS is gradually increasing. Searchable literature in WoS was first published in 1991 and reached the peak of literature growth rate in 1995. Because of the influence of covid pandemic in 2020, the annual number of published papers reached a maximum of 87 in 2019. From 1991 to 2000, 89 literatures were published in the field of digital photogrammetry, accounting for only 9% of the total. From 2001 to 2010, 272 literatures were published, accounting for 29% of the total. From 2011 to 2020, 577 literature was published in this field, accounting for 62% of the total, which is 6.5 times the published literature in 1991-2000. Especially since 2011, the number of related research literature has been steadily increasing. The rise of literatures numbers is accompanied with the rise of journal numbers, as Figure 2 shows. The number of people continues to increase, except for the influence of the covid pandemic in 2020.

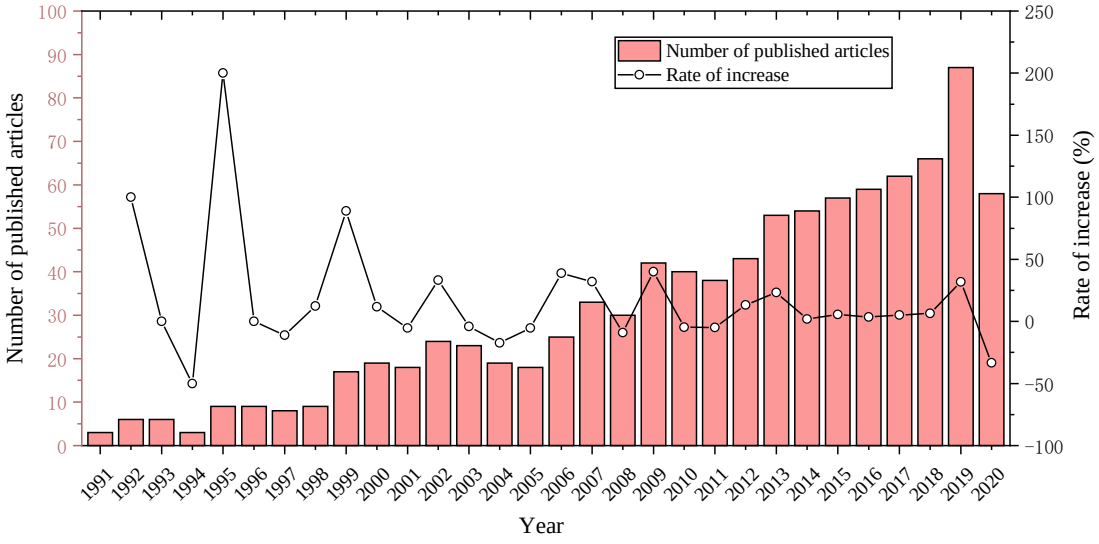

Fig. 1 – Number and growth trend of published literature year by year

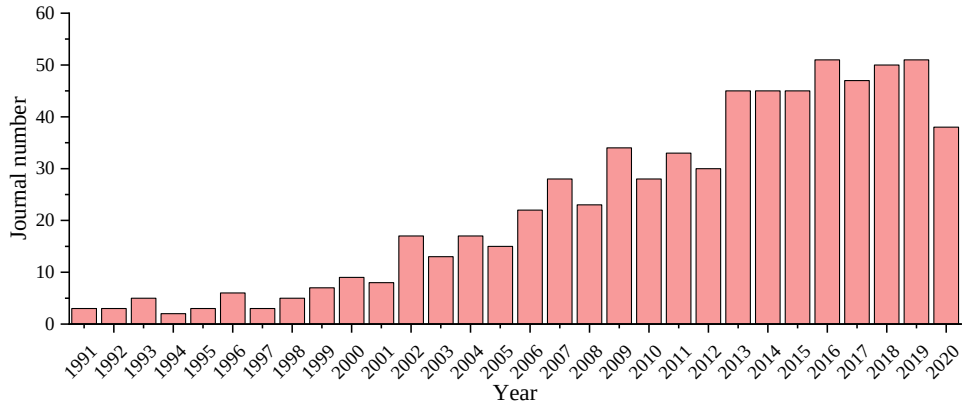

Fig. 2 – Number of journals in which articles are published

Main publishing subjects

The node selects the category, and uses CiteSpace to analyze 939 literatures, finally obtains 136 subject categories. The top 10 discipline categories and the relative number are shown in Figure 3, respectively. It can be seen that the most published papers in digital photogrammetry are geology, geoscience synthesis and physical geography.

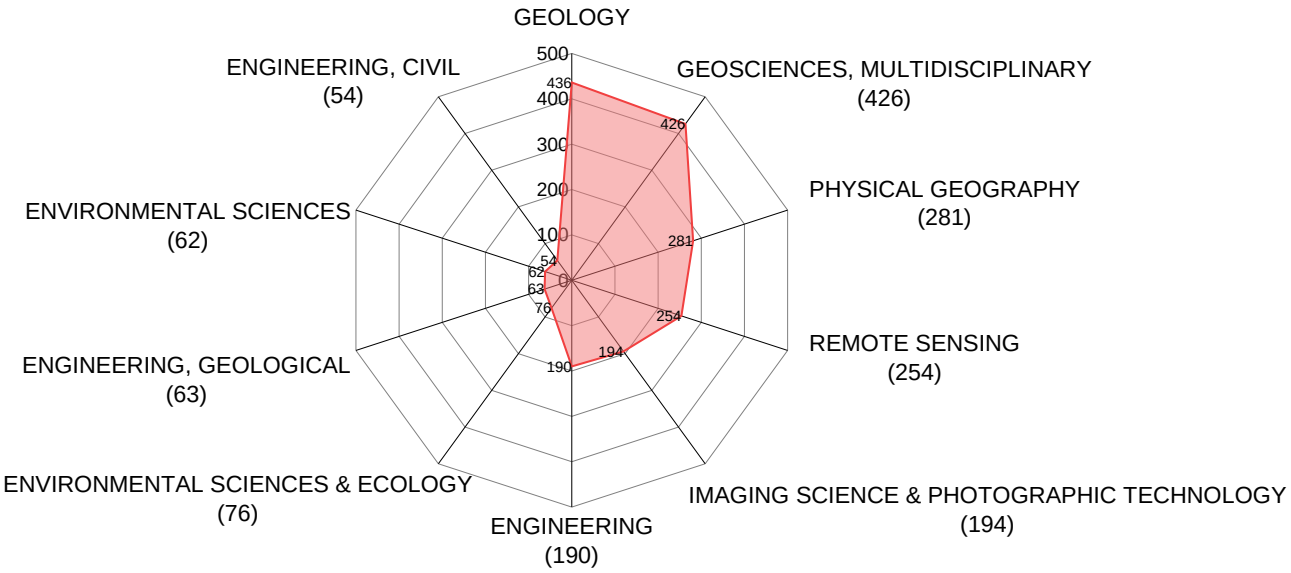

Fig. 3 – Top 10 subjects of digital photogrammetry

Main published journals and co-cited journals

By using the literature analysis function of NoteExpress, the obtained data are shown in Table 1.

Tab. 1 - Top 10 journals with the largest number of literatures on Digital Photogrammetry

Journals	Article number	Countrys
PHOTOGRAMMETRIC RECORD	77	UK
EARTH SURFACE PROCESSES AND LANDFORMS	58	UK
ISPRS JOURNAL OF PHOTOGRAMMETRY AND REMOTE SENSING	40	NED
REMOTE SENSING	36	SUI
PHOTOGRAMMETRIC ENGINEERING AND REMOTE SENSING	35	USA
GEOMORPHOLOGY	27	NED
INTERNATIONAL JOURNAL OF REMOTE SENSING	21	UK
JOURNAL OF CULTURAL HERITAGE	17	FRA
ENGINEERING GEOLOGY	16	SUI
WATER RESOURCES RESEARCH	9	USA

It can be seen that the high-quality literatures published in the field of digital photogrammetry mainly focus on the Photogrammetric Record, Earth Surface Processes and Landforms and ISPRS Journal of Photography and Remote Sensing. These journals are mainly concentrated in the United States, the United Kingdom, the Netherlands, Switzerland and France. The cited journal node is selected, and CiteSpace is used to analyze the journal co-citation, and the obtained data shown in Figure 4 and Table 2

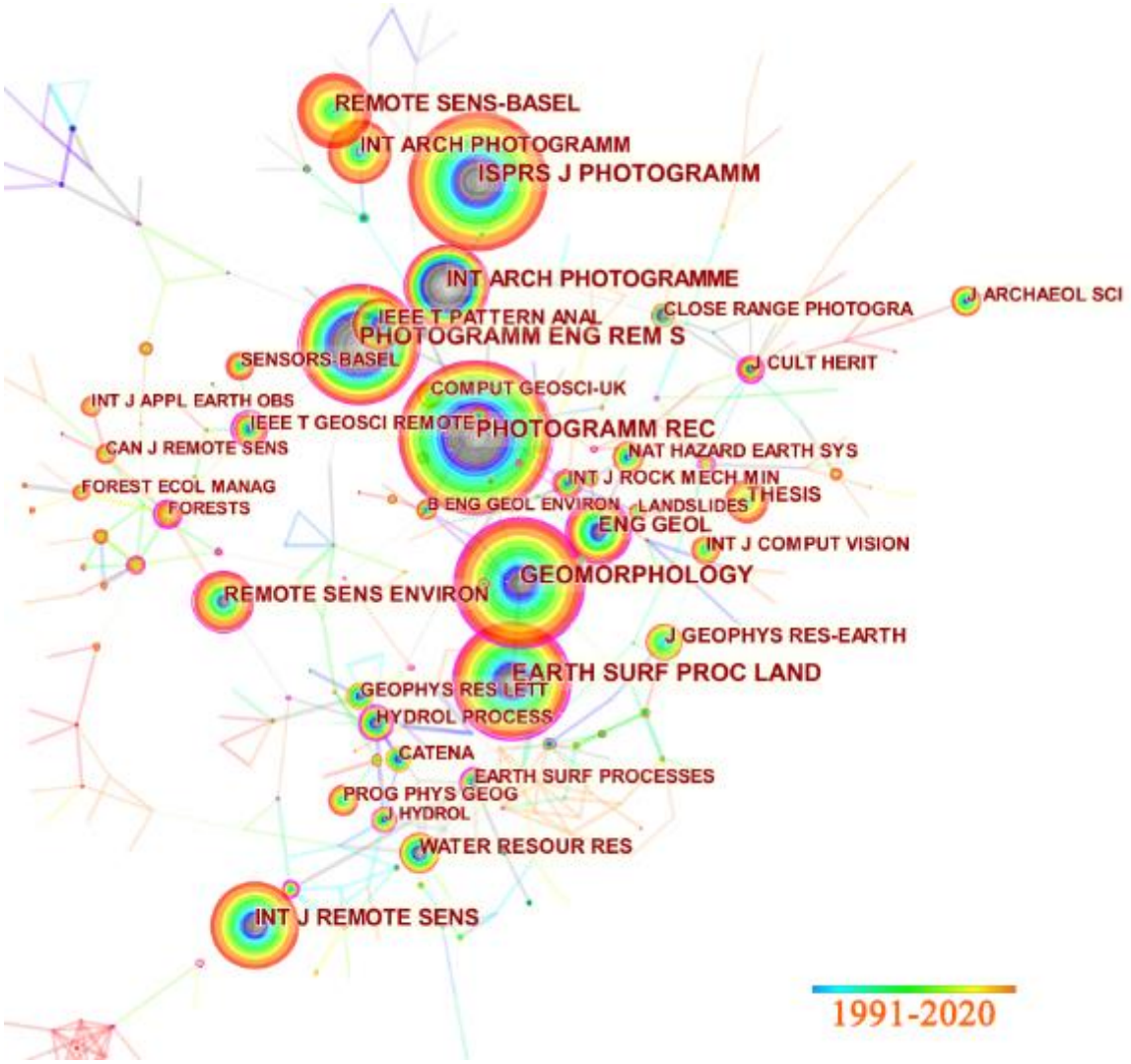

Fig. 4 – Knowledge map of co-cited journals

Tab. 2 - The top 10 journals cited most frequently in digital photogrammetry research

Journals	Article number	Countrys
PHOTOGRAMMETRIC RECORD	353	UK
ISPRS JOURNAL OF PHOTOGRAMMETRY AND REMOTE SENSING	337	UK
GEOMORPHOLOGY	294	NED
PHOTOGRAMMETRIC ENGINEERING AND REMOTE SENSING	289	USA
EARTH SURFACE PROCESSES AND LANDFORMS	263	UK
INTERNATIONAL JOURNAL OF REMOTE SENSING	213	UK
INTERNATIONAL ARCHIVES OF PHOTOGRAMMETRY AND REMOTE SENSING	205	GER
REMOTE SENS-BASEL	170	SUI
ENGINEERING GEOLOGY	150	SUI

It can be seen that the journals with the largest number of citations are mainly concentrated in the United Kingdom, the United States, Switzerland and the Netherlands. To sum up, journals with certain international influence in the field of digital photogrammetry are mainly in the United States, the United Kingdom, the Netherlands and Switzerland.

Main sending countries

To obtain the co-occurrence network by CiteSpace, Taiwan, people R China are merged into China, Scotland, England, UK, North Ireland and Walls are merged into the UK, the result as shown in Figure 5. Each node represents a country, the size of the node represents the frequency of occurrence. The larger the node represents the higher the frequency of occurrence, that is, the more published literature. The connection between nodes represents the co-occurrence strength, the coarseness of the connection is the closer the cooperative relationship is, otherwise, the more distant the connection is. The larger the diameter of the node is, the greater the influence of the node in this field. It can be seen from Figure 4 that the USA, the UK, China, Italy, Germany and Switzerland have a certain influence in the field of digital photogrammetry.

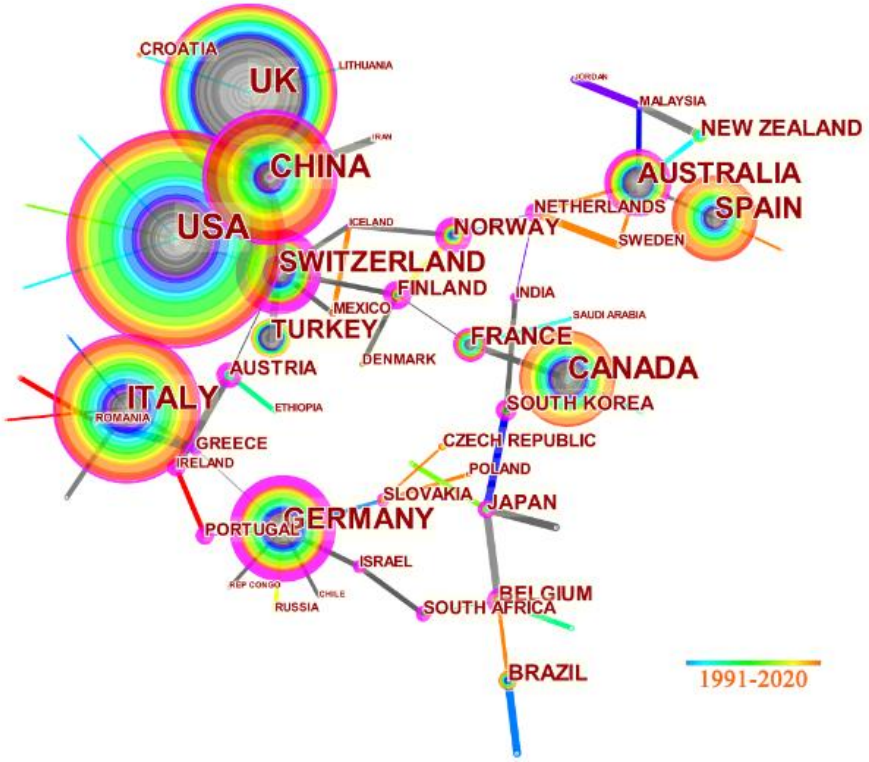

Fig. 5 – National knowledge map of digital photogrammetry research

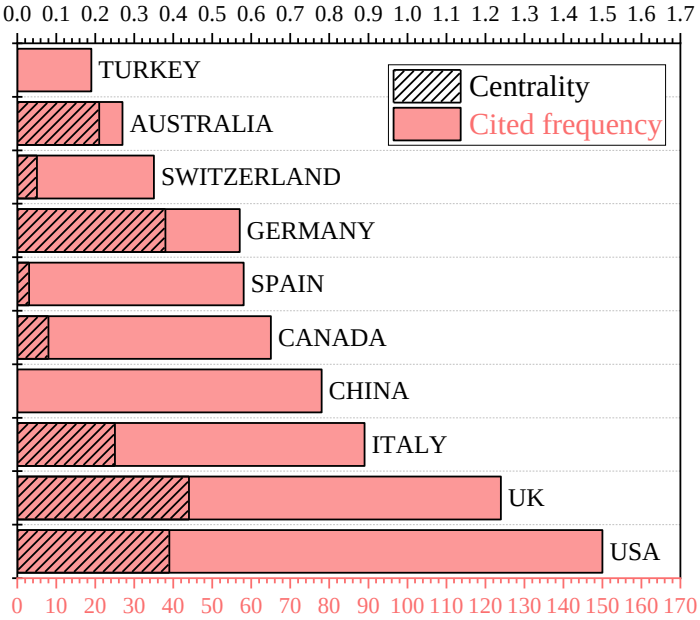

Fig. 6 – Distribution of major countries in Digital Photogrammetry

As shown in Figure 6, scholars who published digital photogrammetry literature mainly concentrated in the United States (153 articles), the United Kingdom (128 articles), Italy (102 articles), China (93 articles) and Canada (77 articles). The most central countries are the United Kingdom (0.44), the United States (0.39), Spain (0.38), Italy (0.25) and Australia (0.21). It can be seen that in the field of digital photogrammetry, scholars from the United States, the United Kingdom and Italy have published many papers, and the literature has a certain international influence. Although Chinese and Canadian scholars have certain advantages in the number of publications in the field of digital photogrammetry, the international influence of the literature is weak on the whole. In contrast, Australian scholars have published in the field of digital photogrammetry Although the literature is not dominant in quantity, it has a strong international influence on the whole.

Major co-authors

By using cited author analysis function in CiteSpace, the co-citation knowledge map of co-cited authors is obtained, as shown in Figure 7. The top 10 co-cited authors ranking, as shown in Table 3 The results showed that Lane S.N. (Institute of Earth Surface Dynamics, University of Lausanne, Switzerland) and Chandler J.H. (Former Professor of Geomatics, Loughborough University, UK) were the most frequently cited authors with 150 and 147 times respectively, which were in the first echelon; Westby M.J. and Remondino F. were more than 80 co-cited, which were in the second echelon; James M.R., Butler J.B., Brasington J., Sturzenegger M. and Kraus K. has been cited more than 70 times, which is in the third echelon. These authors form the core author group of digital photogrammetry research, and have made great contributions to the related research of digital photogrammetry. Further study of the literature shows that the core authors' research mainly focuses on Photogrammetry or remote sensing technology such as digital photogrammetry, lidar, high-resolution satellite remote sensing [8]. In order to carry out geomorphic change research [9] and Hydraulic Research [10,11] With the development of computer vision technology, some scholars combine it with photogrammetry technology, carry out image matching through SFM [12] or MVS (Multiview-stereo) and other algorithms [13,14], and establish three-dimensional models of geomorphology and historical monuments [15] such as river channels [16]. Some scholars use digital photogrammetry for slope monitoring, [17,18] and deformation monitoring of common structures [19,20,21].

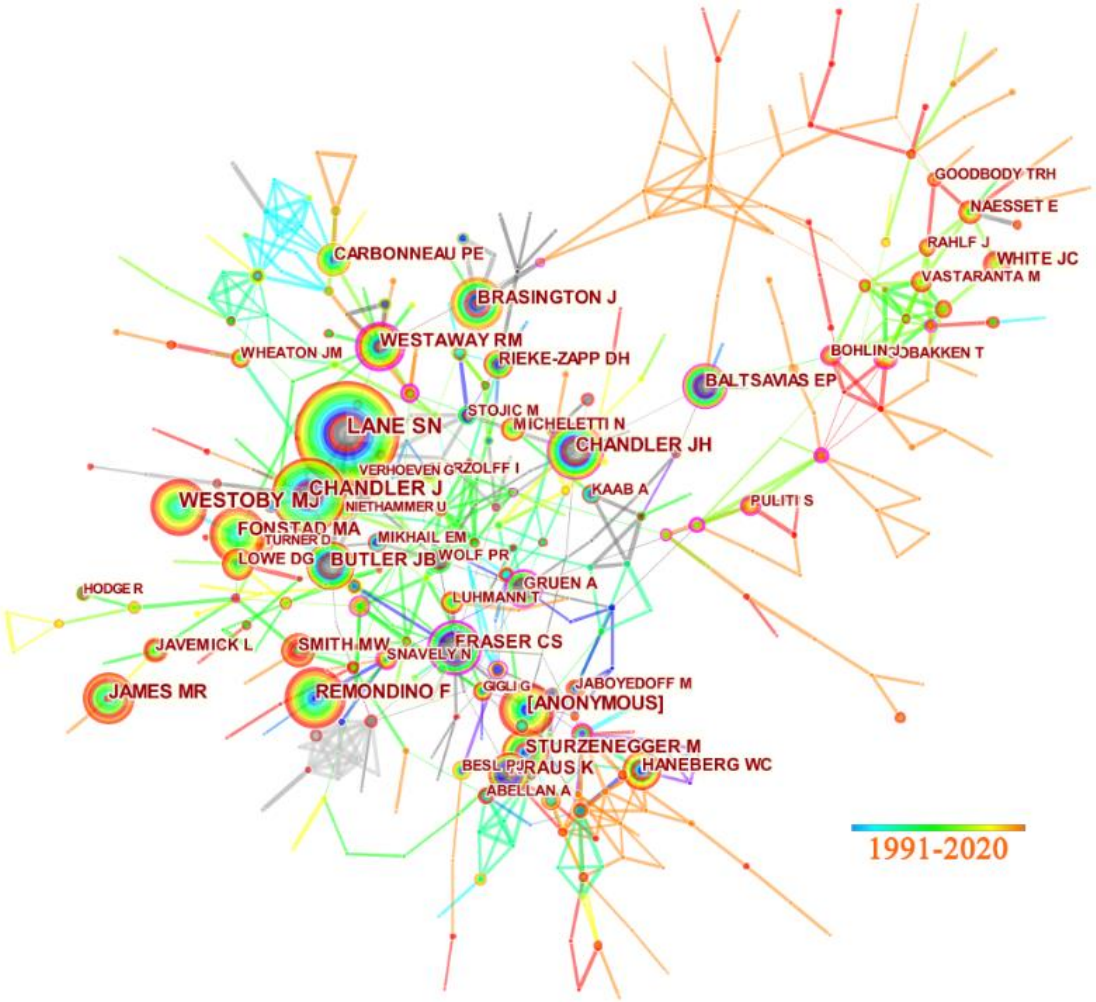

Fig. 7 – Co-citation and co-visualization of digital photogrammetry

Tab. 3: Top 10 co-cited authors of digital photogrammetry

Co-citation times	Authors
150	Lane S.N.
147	Chandler J.H.
96	Westoby M.J.
83	Remondino F.
76	James M.R.
75	Butler J.B.
73	Brasington J.
73	Sturzenegger M.
71	Kraus K.
69	Fraser C.S.

Keyword analysis

The keyword map is more conducive to scholars' analysis of research hotspots and the evolution of hot spots [23]. The relevant research papers on digital photogrammetry from 1991 to 2020 were collected, and the keyword statistics of retrieved literatures were conducted by CiteSpace. The top 20 high-frequency keywords of digital photogrammetry research were obtained as shown in Table 4

Tab. 4: Top 20 high-frequency keywords of digital photogrammetry research

Rank	Freq	Keywords	Rank	Freq	Keywords
1	327	digital photogrammetry	11	45	laser scanner
2	196	photogrammetry	12	45	point cloud
3	85	accuracy	13	41	topography
4	81	structure from motion	14	34	surface
5	78	lidar	15	31	landslide
6	68	unmanned aerial vehicle	16	26	remote sensing
7	63	model	17	25	documentation
8	60	digital elevation model	18	24	low cost
9	50	system	19	22	morphology
10	48	erosion	20	22	reconstruction

In order to further understand the relationship and closeness of high-frequency keywords, the co-occurrence analysis of keywords and the research frontier trend analysis were carried out.

Co-occurrence analysis of key words

Keyword co-occurrence analysis is to use mathematical algorithms and econometric methods to conduct data statistics and cluster analysis on literature keywords and subject words, to obtain hot topics and frontier trends in a certain field. Through the visualization function of CiteSpace, the co-occurrence knowledge map of high-frequency keywords in digital photogrammetry is generated (Figure 8). It can be seen that digital photogrammetry and SFM are the two centres of the whole network and they occupy the core position. Around these two cores, there are two closely related groups:

Digital photogrammetry and unmanned aerial vehicle (UAV) are formed the group of high-frequency keywords, such as vehicle, erosion, digital elevation model and landslide, involves geology, geomorphology and earth science. It reflects that digital photogrammetry has some applications in the field of geological geomorphology. Topographic change detection is a powerful tool in geomorphology, which can link the rates, patterns, processes and impacts of erosion and deposition. It is often applied to the study of processes such as river dynamics [24]. Airborne and land-based lidar is a standard tool for quantifying geomorphic changes. Although the data quality is high, it has disadvantages of poor current situation, high cost and inconvenient scanning. With the development of Unmanned Aerial System (UAS) technology, photogrammetry technology based on UAS, with its superior convenience and economy, is increasingly used to generate high-resolution topographic maps for the study of topographic changes [25].

The group is composed of SFM, photogrammetry, topography, low cost, terrestrial laser scanning and other core high-frequency keywords, involving geomorphology, computer vision and surveying and mapping. The SFM algorithm supports the generation of topographic maps from randomly oriented and distributed photos from uncalibrated cameras [26]. With the rapid development of computer vision, there is a method that can calculate the internal and external azimuth angle elements of a camera by taking a group of photos. These data can be used to measure

the same name image points in overlapping photos and generate 3D point clouds [16]. Lidar can carry out high-precision and high-resolution measurement with high accuracy [27]. However, although the data quality is reliable, there are obvious defects in the research of lidar change detection: the land-based lidar instrument is expensive, in many cases, due to the limited field of vision, it is necessary to scan from multiple locations to obtain sufficient coverage; airborne lidar measurement is not economical, and frequent measurement is usually not feasible, which leads to the poor reality, unable to respond quickly to sudden geomorphic events. The SFM algorithm based on digital photogrammetry can quickly generate digital elevation model, and it is easy to operate and has a high degree of automation. However, the accuracy of the SFM algorithm depends on image resolution. It is also related to the image quality, image distortion, vegetation and surface characteristics, as well as the number, distribution and accuracy of ground control points [28]. How to improve the accuracy and stability of the SFM algorithm is still a hot issue.

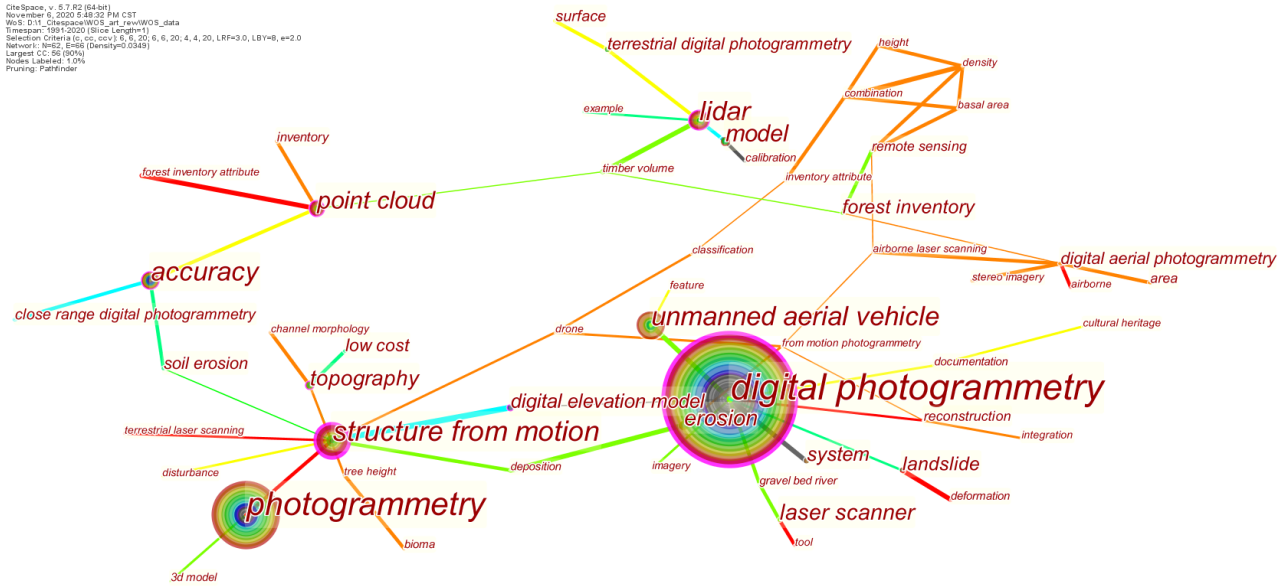

Fig. 8 – Visualization knowledge map of key words co-occurrence in Digital Photogrammetry

Research frontier and trend analysis

The research of digital photogrammetry is a process of gradual evolution. According to the co-occurrence analysis of keywords, it is found that the research content of digital photogrammetry is still expanding. In order to further study and determine the research hotspots of digital photogrammetry, the mutation detection analysis method in CiteSpace is used to obtain the co-occurrence network mutation words of key words in digital photogrammetry (Figure 9) From 1999 to 2010, the mutation intensity of DEM and accuracy are 6.3588 and 6.55 respectively, and "accuracy" refers to the accuracy of DEM. It shows that the research in this period mainly focused on obtaining the original data digital surface model for establishing digital elevation model through digital photogrammetry, and the accuracy of the established digital elevation model was studied in depth. As one of the "4D" products, digital elevation model, its most valuable data source is aerial photogrammetry, which belongs to the category of digital photogrammetry. Through aerial photogrammetry, a large area of original data of DEM can be obtained, to meet the requirements of data current situation [29]. In this period, there were also three-dimensional digital photogrammetry, anthropometry and reliability, which indicated that scholars had realized the advantages of non-contact measurement of digital photogrammetry, and carried out application research on anthropometry combined with three-dimensional digital photogrammetry technology. The mutation time of "anthropometry" lasted from 2003 to 2012, indicating that digital photogrammetry technology had a period of research boom in the field of anthropometry in the early 20th century, and the main researchers were Seth M. Weinberg [30] and Thomas J.J. Maal [31].

From 2011 to 2016, the research focused on rockfall, soil erosion and river accumulation. Kristen L. cook used the images collected by UAV equipped with digital cameras to study the geomorphic changes caused by the spring monsoon in the middle of the Da'an River Canyon in Western Taiwan Province through the SFM algorithm. The experiments show that the accuracy of the SFM point clouds largely depend on the surface characteristics of the measured objects [32]. Baptiste Marteau et al. Applied the SFM algorithm to the field of river restoration, and the experiments show that the digital elevation model generated by the SFM technology can easily determine the geomorphic changes of the river channel over time, and evaluate the spatial changes of erosion and concentration [8]. It can be seen that digital photogrammetry was widely used in geomorphology during this period.

From 2017 to 2020, the mutation intensity of forest inventory, motion recovery structure and unmanned aerial vehicle (UAV) were 6.5264, 13.4714 and 14.071, respectively, which indicated that the main research objects of digital photogrammetry in this stage were forest inventory, movement recovery structure and UAV. Forest resources survey is an important field of applied statistics, involving measurement, tree measurement, remote sensing, data processing and other technologies and methods, and is the only technical means to obtain forest resource information needed for decision-making at different forestry levels [33]. The emergence and rapid development of photogrammetry provide an economical and effective technical means for forest resource inventory. Compared with the traditional measurement methods, photogrammetry can be carried out simultaneously in a large range, which is not limited by the ground visibility conditions, and the measurement cost is relatively low. Especially in recent years, with the development of computer vision theory and efficient automatic feature matching algorithm, SFM 3D reconstruction technology is introduced into photogrammetry, which greatly improves the degree of automation of photogrammetry. The SFM method can automatically solve the position and pose of the camera and the three-dimensional spatial coordinates of the object by matching the same name features from the multi-view photos, which greatly improves the automation of photogrammetry. In addition, with the rapid development of low altitude remote sensing platforms such as small UAVs, they have been widely used in photogrammetry. Compared with the traditional satellite remote sensing platform and aviation platform, they have high data acquisition efficiency, flexible and fast operation mode and low cost. At the same time, because of their flying distance, large-scale and high-precision images can be obtained. The wide application of these low altitude platforms greatly improves the accuracy and efficiency of photogrammetry and greatly reduces the operation cost. At present, photogrammetry has been applied in many fields because of its advantages of low cost and high precision. The mutation intensity of digital aerial photogrammetry, lidar and tree height was high in this period, which reflected the main research means and research objectives in this period.

Keywords	Strength	Begin	End	1991 - 2020
digital elevation model	6.3588	1999	2003	
morphology	5.2483	2003	2012	
digital photogrammetry	7.5263	2004	2008	
Anthropometry accuracy	3.8602	2009	2013	
accuracy	6.55	2009	2011	
laser scanner	4.3891	2009	2013	
precision	4.2901	2010	2011	
reliability	5.522	2010	2012	
digital 3 dimensional photogrammetry	6.2951	2010	2013	
Rockfall	3.9906	2011	2015	
terrestrial digital photogrammetry	5.0144	2011	2015	
soil erosion	6.3706	2013	2017	
Close-range digital photogrammetry	4.2097	2014	2016	
point cloud	8.8161	2016	2020	
deposition	4.1243	2016	2018	
forest inventory	6.5264	2017	2020	
SfM	13.4714	2017	2020	
unmanned aerial vehicle	14.071	2017	2020	
Digital Aerial Photogrammetry	5.2911	2018	2020	
Lidar	4.1258	2018	2020	
Tree height	3.4451	2019	2020	

Fig. 9 – 21 mutation words in the field of digital photogrammetry from 1991 to 2020

CONCLUSION

This paper takes 939 papers about digital photogrammetry in the core database of web of science from 1991 to 2020 as the research object. With the help of the bibliometric method and information visualization analysis software CiteSpace, this paper studies the current situation and trend of digital photogrammetry research, and draws the following conclusions:

Since 2011, the number of research literatures published in the field of digital photogrammetry has increased steadily, but in 2020, the number of published literatures dropped.

Lane S.N. and Chandler J.H. have been cited for the most times. Together with Westby M.J., Remondino F. and other scholars, Lane S.N. and Chandler J.H. are the core authors in the field of digital photogrammetry and they have made certain contributions to the research of digital photogrammetry.

The United Kingdom, the United States and Italy have a certain international influence in the field of digital photogrammetry and are in an important position. At the same time, the academic journals that collect high-quality documents in the field of digital photogrammetry are mainly concentrated in the United States, the United Kingdom, the Netherlands, Switzerland and other countries. In the field of digital photogrammetry, the number of papers published in China ranks first in the world, with strong scientific research strength, however on the whole, the international influence of literature is weak.

From the co-occurrence analysis of key words and the trend analysis of research frontier, it can be seen that the application research of digital photogrammetry in the forestry field and the combination with computer vision and lidar technology have attracted the attention of scholars.

DISCUSSION

Knowledge map analysis visualizes and simplifies the development of digital photogrammetry. Because all the results presented in this article are based on the results retrieved on WoS at one point in time, this article has the following predictable shortcomings:

1. The papers retrieved by WoS are not invariable, and not all the papers retrieved by WoS are of high research value. However, in the section of "Time Series Analysis of Literature Output", we assume that all retrieved literature is regarded as equally important.

2. Due to high publishing costs and possible corporate or institutional competition, some papers need to be analyzed, but we cannot obtain them through WoS, so we have not analyzed them. In order to improve the reliability of data and results, it is recommended to further increase data sources and further filter the data.

REFERENCES

[1]. Polidori, L., "ON LAUSSEDAT'S CONTRIBUTION TO THE EMERGENCE OF PHOTOGRAMMETRY". The International Archives of the Photogrammetry, Remote Sensing and Spatial Information Sciences, 2020. XLIII-B2-2020: pp. 893-899.

[2] Albertz J . "A look back - 140 Years of "photogrammetry" - Some remarks on the history of photogrammetry". Photogrammetric Engineering & Remote Sensing, 2007, 73(5):pp.504-506.

[3]. Polidori, L., Words as tracers in the history of science and technology: the case of photogrammetry and remote sensing. Geo-spatial information science, 2021. 24(1): pp. 167-177.

[4]. Jörg Albertz,"Albrecht Meydenbauer– Pioneer of Photogrammetric Documentation of the Cultural Heritage", Proceedings 18th International Symposium CIPA 2001 Potsdam (Germany), September 18 - 21, 2001,pp.21-25.

[5] Zhang. Z. X., Digital photogrammetry, Wuhan University Press, Wuhan, 2012.

[6] Chen C.M., "CiteSpace II: Detecting and visualizing emerging trends and transient patterns in scientific literature", Journal of the American Society for Information Science and Technology, vol.57, no.3, pp.359-377, 2006-02-012006, doi:10.1002/asi.20317.

[7] Chen C.M., "Science mapping：a systematic review of the literature", Journal of Data and Information Science, vol.2, no.2, pp.1-40, 2017-01-012017, doi:10.1515/jdis-2017-0006.

[8] D. Poli, F. Remondino, E. Angiuli and G. Agugiaro, "Radiometric and geometric evaluation of GeoEye-1, WorldView-2 and Pleiades-1A stereo images for 3D information extraction", ISPRS J PHOTOGRAMM, vol.100, no., pp.35-472015, doi:10.1016/j.isprsjprs.2014.04.007.

[9] Lane S. N., Westaway R. M. and Hicks D. M., "Estimation of erosion and deposition volumes in a large, gravel-bed, braided river using synoptic remote sensing", EARTH SURF PROC LAND, vol.28, no.3, pp.249-2712003, doi:10.1002/esp.483.

[10] Chandler J. H., Shiono K., Rameshwaren P. and Lane S. N., "Measuring flume surfaces for hydraulics research using a Kodak DCS460", PHOTOGRAMM REC, vol.17, no.97, pp.39-612001, doi:10.1111/0031-868X.00167.

[11] Westoby M. J., Dunning S. A., Woodward J., Hein A. S., Marrero S. M., Winters K. and Sugden D. E., "Interannual surface evolution of an Antarctic blue-ice moraine using multi-temporal DEMs", EARTH SURF DYNAM, vol.4, no.2, pp.515-5292016, doi:10.5194/esurf-4-515-2016.

[12] M. J. Westoby, J. Brasington, N. F. Glasser, M. J. Hambrey and J. M. Reynolds, "'Structure-from-Motion' photogrammetry: A low-cost, effective tool for geoscience applications", GEOMORPHOLOGY, vol.179, no., pp.300-3142012, doi:10.1016/j.geomorph.2012.08.021.

[13] M. R. James and S. Robson, "Straightforward reconstruction of 3D surfaces and topography with a camera: Accuracy and geoscience application", Journal of Geophysical Research: Earth Surface, vol.117, no.F3, pp.n/a-n/a2012, doi:10.1029/2011JF002289.

[14] L. Javernick, D. M. Hicks, R. Measures, B. Caruso and J. Brasington, "Numerical modelling of braided rivers with Structure-from-Motion-Derived terrain models", RIVER RES APPL, vol.32, no.5, pp.1071-10812016, doi:10.1002/rra.2918.

[15] F. Remondino, "Heritage recording and 3D modeling with photogrammetry and 3D scanning", REMOTE SENS-BASEL, vol.3, no.6, pp.1104-11382011, doi:10.3390/rs3061104.

[16] F. Remondino, M. G. Spera, E. Nocerino, F. Menna and F. Nex, "State of the art in high density image matching", PHOTOGRAMM REC, vol.29, no.146, pp.144-1662014, doi:10.1111/phor.12063.

[17] M. Sturzenegger, D. Stead, J. Gosse, B. Ward and C. Froese, "Reconstruction of the history of the Palliser Rockslide based on Cl-36 terrestrial cosmogenic nuclide dating and debris volume estimations", LANDSLIDES, vol.12, no.6, pp.1097-11062015, doi:10.1007/s10346-014-0527-4.

[18] M. Brideau, M. Sturzenegger, D. Stead, M. Jaboyedoff, M. Lawrence, N. Roberts, B. Ward, T. Millard and J. Clague, "Stability analysis of the 2007 Chehalis lake landslide based on long-range terrestrial photogrammetry and airborne LiDAR data", LANDSLIDES, vol.9, no.1, pp.75-912012, doi:10.1007/s10346-011-0286-4.

[19] Ge Yongquan, Yu Chengxin, Liu Xiaodong and W. Ronghui, "Monitoring dynamic deformation of communication tower using photography dynamic monitoring system", IOP Conference Series: Earth and Environmental Science, vol.558, no.22020, doi:10.1088/1755-1315/558/2/022061.

[20] Yu C.X., Zhang G.J., Ding X.H., Zhao Y. and Guo G.L., "Monitoring dynamic deformation of shuttle steel shelves by digital photography", Civil Engineering Journal, vol.28, no.2, pp.136-150, 2019-01-012019, doi:10.14311/CEJ.2019.02.0012.

[21]. Ge Yongquan,Yu Xianzhi, Chen Mingzhi et al., Monitoring Dynamic Deformation of Building Using Unmanned Aerial Vehicle. Mathematical Problems in Engineering, 2021, pp.2657689, doi:10.1155/2021/2657689

[22]. Ge Yongquan, Yu Chengxin, Zhao Tonglong and Liu Xiaodong, Real-Time monitoring deformation of building using photography dynamic monitoring system. Civil Engineering Journal, 2021. 30(1), pp. 245-259,doi:10.14311/CEJ.2021.01.0018

[23] C. Yue, Chen Chaomei, L. Zeyuan, H. Zhigang and W. Xianwen, "Methodological functions of CiteSpace Knowledge Maps", Studies in Science of Science, vol.33, no.02, pp.242-253, 2015-02-152015

[24] M. R. James and S. Robson, "Straightforward reconstruction of 3D surfaces and topography with a camera: Accuracy and geoscience application", J GEOPHYS RES-EARTH, vol.117, no.F030172012, doi:10.1029/2011JF002289.

[25] Colomina I. and Molina P., "Unmanned aerial systems for photogrammetry and remote sensing: A review", ISPRS J PHOTOGRAMM, vol.92, no., pp.79-972014, doi:10.1016/j.isprsjprs.2014.02.013.

[26] Westaway R. M., Lane S. N. and Hicks D. M., "The development of an automated correction procedure for digital photogrammetry for the study of wide, shallow, gravel-bed rivers", EARTH SURF PROC LAND, vol.25, no.2, pp.209-2262000

[27] Michel Jaboyedoff, Thierry Oppikofer, Antonio Abellán, Marc-Henri Derron, Alex Loye, Richard Metzger and Andrea Pedrazzini, "Use of LIDAR in landslide investigations: A review", NAT HAZARDS, vol.61, no.1, pp.5-28, 2012-01-012012, doi:10.1007/s11069-010-9634-2.

[28] Cook, Kristen L., "An evaluation of the effectiveness of low-cost UAVs and structure from motion for geomorphic change detection", GEOMORPHOLOGY, vol.278, no., pp.195-2082017, doi:10.1016/j.geomorph.2016.11.009.

[29] Zhu Qing, Li Zhilin, Gong Jianya and Sui Haigang, "On "Updating and Building of 1:1000 Digital Elevation Model" in China", Jour nal of Wuhan Tech nical Univ ersity o f Surv eying a nd Mapping, no.02, pp.3-5, 1999-06-251999

[30] Weinberg Seth M., Naidoo Sybill, Govier Daniel P., Martin Rick A., Kane Alex A. and Marazita Mary L., "Anthropometric precision and accuracy of digital three-dimensional photogrammetry: Comparing the Genex and 3dMD imaging systems with one another and with direct anthropometry", J CRANIOFAC SURG, vol.17, no.3, pp.477-483, 2006-05-012006, doi:10.1097/00001665-200605000-00015.

[31] Thomas J.J. Maal, Bram van Loon, Joanneke M. Plooij, Frits Rangel, Anke M. Ettema, Wilfred A. Borstlap and Stefaan J. Bergé, "Registration of 3-Dimensional facial photographs for clinical use", J ORAL MAXIL SURG, vol.68, no.10, pp.2391-24012010, doi:10.1016/j.joms.2009.10.017.

[32] Cook K. L., "An evaluation of the effectiveness of low-cost UAVs and structure from motion for geomorphic change detection", GEOMORPHOLOGY, vol.278, no., pp.195-2082017, doi:10.1016/j.geomorph.2016.11.009.

[33] Kangas and Annika, Forest inventory:methodology and applications, China Forestry Press, Beijing, 2010.

CIVIL ENGINEERING JOURNAL

Article no. 15

THE CIVIL ENGINEERING JOURNAL 1-2022

3D DIGITAL RECONSTRUCTION OF DEFUNCT RURAL BUILDINGS BASED ON ARCHIVAL SOURCES

Zdeněk Poloprutský[1], Eva Frommeltová[1], Josef Münzberger[1] and Kateřina Sedlická[2]

1. *CTU in Prague, Faculty of Civil Engineering, Department of Geomatics, Thákurova 2077/7, 166 29 Prague 6 - Dejvice, Czech Republic; zdenek.poloprutsky@fsv.cvut.cz*
2. *Institute of Ethnology, Czech Academy of Sciences, Na Florenci 3, 110 00 Prague 1, Czech Republic*

ABSTRACT

This paper deals with the specifics and working procedures for 3D digital reconstructions of defunct and altered buildings of vernacular architecture. Primarily, the resulting 3D models are intended to serve for general lay public in order to present and popularize vernacular architecture and for educational activities. Secondly, they can be used by professional public for the same purposes. The models are based on archival sources - archival 2D metric survey documentation (drawings and photographs), written sources. Another requirement is the possibility of presentation on the internet within a parallel developing web platform. SketchUp 2021 Pro software, extended by plug-ins, is used for the 3D modelling process.

KEYWORDS

3D modelling, Cultural heritage, Ethnology, SketchUp, Vernacular architecture, Virtual Open-air Museum

INTRODUCTION

Immovable cultural heritage monuments are important evidence of the development of human society in history. Just like in the past, these monuments around the world are threatened by devastation by human activity - war, terrorism, vandalism, changes in the social and cultural environment; as well as the forces of nature - weather conditions, fires, etc. For many immovable cultural monuments, it is too late, i.e. they were destroyed or defunct in the past. In some cases, it is possible to virtually reconstruct and visualize the destroyed monument using digital technologies. Various examples of destroyed cultural monuments and their subsequent 3D digital reconstruction are described in the professional literature.

A monument has been destroyed completely (1), but archival sources are available, see e.g. the Great Buddha of Bamiyan in Afghanistan[1] or the Great Bel Temple in the archaeological site of Palmyra in Syria[2]. A monument has been destroyed completely (2), but archival sources are available, and its immediate surroundings can be measurably documented, see e.g. the minaret of the Umayyad Mosque in the ancient city of Aleppo[3] or the civic tower of Sant' Alberto in Italy[4]. A monument has defuncted partially (3), while the existing torso can be measurably documented, see e.g. the Siegesburg Castle in Bad Segeberg in Northern Germany[5] or the ruins of Zvířetice Castle in Bakov nad Jizerou in the Czech Republic [6].

In addition to representative historical buildings of national importance, such as sacral buildings (churches, synagogues, mosques), mansions (castles and chateaux) or town buildings (town halls), the development of human society is also well captured in vernacular architecture. Vernacular architecture usually served immediate local needs and was limited by materials available in a particular area, thus reflecting local traditions and cultural practices. Traditional vernacular

architecture was mostly self-built, i.e. without the contribution of formally educated architects. Furthermore, it was usually based on the design skills and tradition of local builders[7]. In the environment of the Czech Republic, vernacular architecture has been a classic subject of interest for ethnology and other humanities, such as the history of art and architecture, for many decades[8–16].

Research on vernacular architecture is often based on surveys of existing rural buildings that are typical of a particular region. These surveys may be of different nature depending on their purpose and the erudition of researchers[17–19]. If time and money are available, it may be advantageous to use 3D laser scanning in combination with Close-range photogrammetry[20]. In the case of area research of vernacular architecture, it may be advantageous to use Geographic Information Systems (GIS)[16,21]. In the worst-case scenarios, this may be the last form of metric survey documentation of a building before its demise. In better case scenarios, the acquisition of metric survey documentation of the building is the first step towards its revitalization, e.g., in Open-air Museums[22,23], which have a long tradition in the cultural environment of the Czech Republic (since the end of the 19th century).

This paper deals with the specifics and working procedures for 3D digital reconstructions of defunct and altered buildings of vernacular architecture. Primarily, the resulting 3D models are intended to serve for general lay public in order to present and popularize vernacular architecture and for educational activities. Secondly, they can be used by professional public for the same purposes. Due to the fact that the application of modern computational methods to historical metric survey documentation allows its critical evaluation and reinterpretation in the context of current knowledge[24], it is possible to base the creation of 3D models on archival sources – archival 2D metric survey documentation (drawings and photographs), written sources. Another requirement is the possibility of presentation on the internet within a web platform developing in parallel.

VISKALIA – Virtual Open-air Museum of Vernacular Architecture

The project aims to (1) rescue the source of plans, drawings, and photographs of vernacular architecture in the Czech Republic which contain original ethnological data about the form, function and identity importance of vernacular architecture before its transformation into museum buildings, and (2) enable innovative access to this source by the public within a single platform. The implementation of the stated general objectives of the project will achieve the following[25,26]:

a) Creation of the Virtual Open-air Museum of Vernacular Architecture (VISKALIA) which will cover basic thematic, typological and geographic variability of this architecture in the Czech Republic. The VISKALIA will become a basic tool for studies and popularization of vernacular architecture in the online environment and electronic media and will be useable in education and training focused on issues related to cultural heritage.

b) Creation of a specialized public database and map outputs including plans and photographs and other documentation of vernacular architecture at the level of the Czech Republic, complemented by a maximum amount of ethnographic, historical and spatial metadata.

c) Access to the information on vernacular architecture by the public through an exhibition and publications.

d) Preservation and digitization of specific collection and archive sources of The Institute of Ethnology of the CAS and National Museum.

In the Viskalia project, 3D digital reconstructions of up to fifteen models of selected village architecture buildings are planned. To achieve this, complete background data will be collected, i.e. maps, plans, photographs, drawings, which are preserved in digitized collections, and which also represent (regionally, functionally, architecturally) the basic regional house types from the territory

of the Czech Republic. Models will be created with CAD tools, or BIM. In appropriate cases[1], the models will be supplemented with photographic surface textures. For the creation of 3D models, the basic criterion of the Level of Detail was determined, i.e. the resulting model must have visibly important and regionally specific structural elements of the building. The building models will be placed on a local digital terrain model in their immediate vicinity, to get a better idea of their relationship to neighbouring buildings, or to the given village settlement.

MATERIALS AND METHODS

In this section, the types of base materials are introduced. Their use is shown in 3D digital reconstructions of several models of completely or partially defunct or altered buildings of vernacular architecture. The used working procedures are also presented.

Archival sources

In our case, the archival sources consist mainly of metric survey documentation, which originated in the first half of the 1940s during the Protectorate of Bohemia and Moravia within its then borders. The so-called "Surveying event" was organized by the Czech Academy of Sciences and Arts and was attended by architects (a group of the Association of Architects) and students of closed universities, as well as students of the Vocational School of Applied Arts in Prague. Fieldworks yielded more than 2,000 sheets of plans, sketches and drawings of vernacular architecture, especially timbered buildings. Thanks to this event, research work in connection with the scientific interest in vernacular architecture and its values for the national cultural heritage could continue in the Protectorate period[8,27]. Another important source of information is the professional literature, that deals with vernacular architecture and reflects the scientific background in this field for the cultural environment of the Czech Republic[9–16,23].

The available archival metric survey documentation usually contains, considering the time of its creation, a relatively complex set of drawings, but its quality and completeness is variable. In general, complex 2D and 3D metric survey documentation should ideally operate on the principle of connected vessels. It should be possible to create a 3D model from the complex 2D metric survey documentation with the same Level of Detail as the underlying drawings. It should be possible to create a set of drawings from the 3D model, i.e. complex 2D metric survey documentation, in the same Level of Detail as the underlying 3D model. A comprehensive set of drawings should include at least:

[1] E.g. to improve the visual presentation of surface finishes of used building materials.

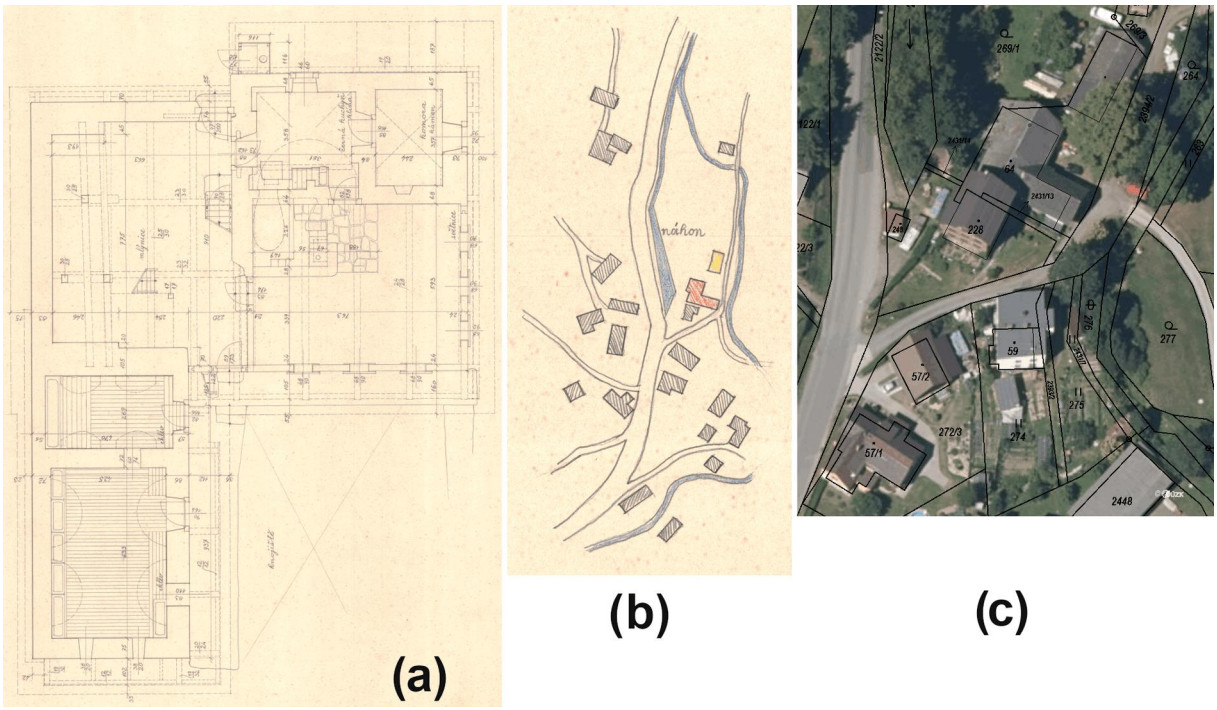

Fig. 1 – Example of archival floor plan (a) and comparison of archival situational sketch (b) with current cadastral map and aerial orthophoto (c), Kundratice, Semily District, Czech Republic

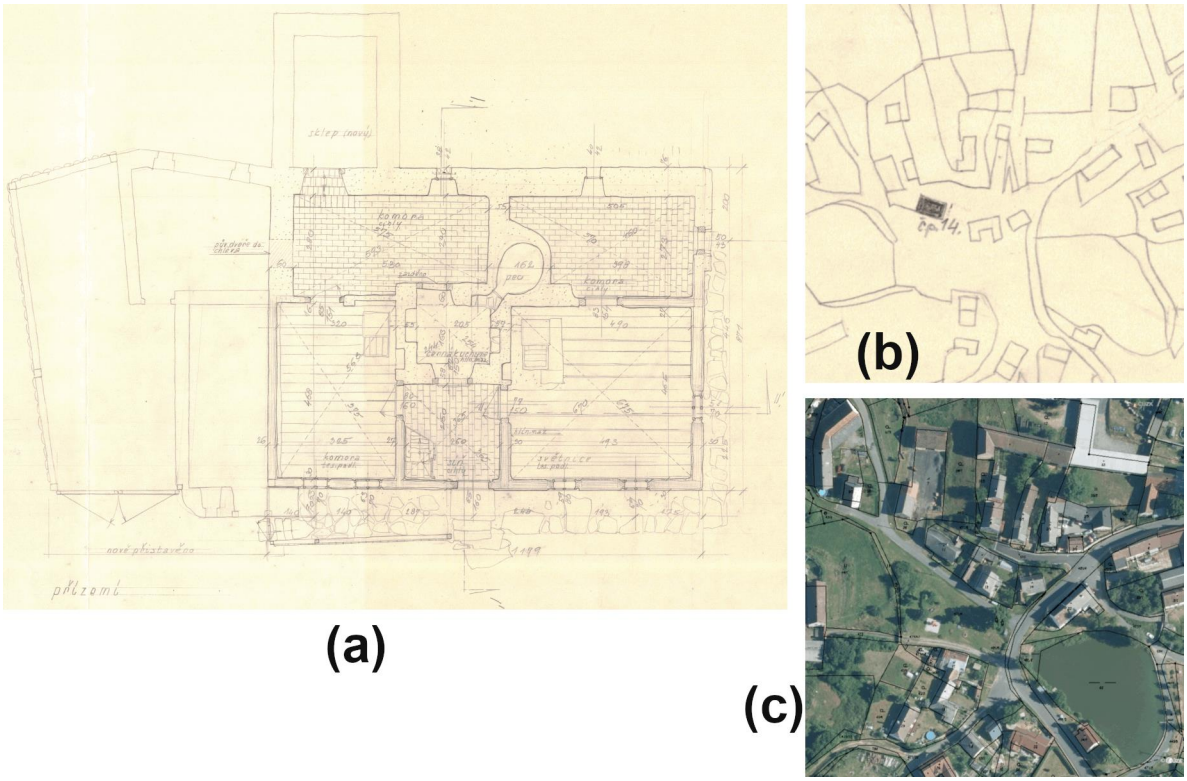

Fig. 2 – Example of archival floor plan (a) and comparison of archival situational sketch (b) with current cadastral map and aerial orthophoto (c), Petrovice, Domažlice District, Czech Republic

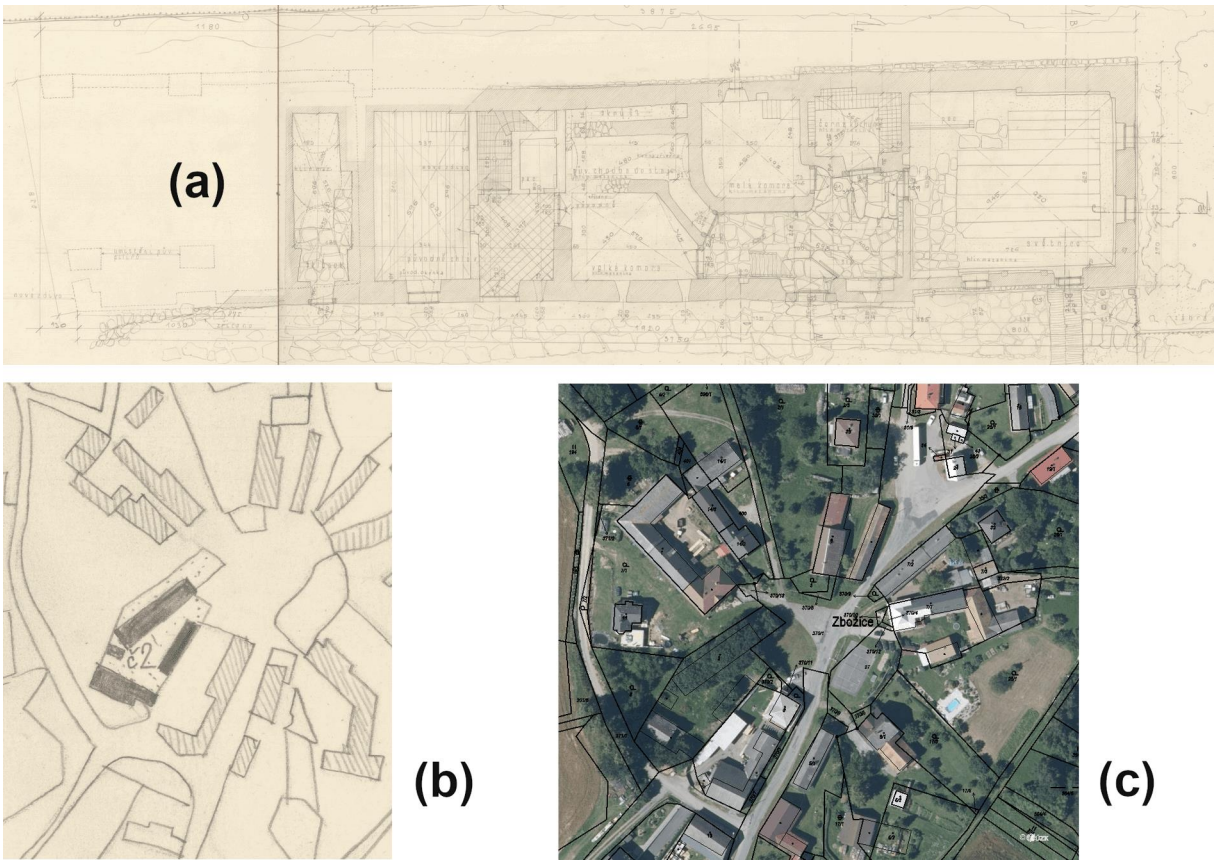

Fig. 3 – Example of archival floor plan (a) and comparison of archival situational sketch (b) with current cadastral map and aerial orthophoto (c), Zbožice, Havlíčkův Brod District, Czech Republic

1. Floor plans – should depict each floor of the building, including the attic with a depiction of the truss structure.
2. Vertical cuts – should depict the structure at least in a longitudinal and a transverse cut
3. Views – should depict views of individual facades, they can be effectively replaced by photographs.
4. Additional documentation – may contain exterior and interior photographs, situation plans, etc.

However, the archival metric survey documentation, which in this case serves as a starting point for 3D modelling, was not created for the purpose of spatial reconstruction of surveyed buildings. Logically, this leads to situations where the data lack spatial relationships, which is important to know during the process of 3D modelling. Then, these imperfections of archival plans must be supplemented from other information sources, usually based on analogies from other case studies.

For the exact geographical location of reconstructed buildings, archive situation plans or cadastral maps and current cadastral maps in combination with aerial orthophotos can be successfully used. In the current cadastral maps, the original boundaries of the plots are often still drawn, i.e. also perimeters of defunct buildings. These "echoes of the past" make it possible to locate the reconstructed buildings and determine their orientation towards the cardinal directions. Examples are shown in Figures 1–3.

The first building in Kundratice[2] (Figure 1) exists and is a protected monument. However, before the surveying in the 1940s, part of its construction disappeared, i.e. the so-called refrigerator for the mill wheel. The second building in Petrovice[3] (Figure 2) also exists. The basic mass is preserved, but it is assumed that there have probably been partial modifications to its construction. The third building in Zbozice[4] (Figure 3) has been destroyed. It was an enclosed village homestead with several buildings, see Figure 3, (b). I.e., a residential building in the north (Figure 3, (a)), cowshed in the east, a separate cellar, and a barn in the south. Examples of 3D models of reconstructed buildings are presented in Figures 6-8.

The process of 3D reconstruction

SketchUp 2021 Pro software[28] was chosen and used for the creation of 3D models. It can be used in many fields, especially in construction, and allows intuitive work directly in 3D space, where it allows quick creation of models and their presentation. Plug-ins available for this software can be a useful aid in 3D modelling in SketchUp. Following our pilot study[29], we mostly use the following plug-ins:

- CleanUp[3] – used to clean the model, e.g. from unnecessary edges or duplicate areas[30]. It contains a relatively wide range of elements that can be cleaned in the 3D model.
- RoundCorner – used to modify the edges of 3D objects, i.e. allows their bevelling or rounding[31]. It can be used, for example, to round the corners of the wall or to model the oval mass of the furnace, see Figure 4.
- TopoShaper – allows you to generate terrain from contours or from a point cloud. In our work, the possibility of creating terrain from a point cloud was used[32]. The plug-in generates terrain using Delaunay triangulation, with the network point density changing with altitude. The algorithm smoothes triangulation until the terrain is smooth enough. The smoothing angle can be set.

Historical constructions in the layers of the 3D model

For the 3D modelling process, a general system of 3D model layers based on the typology of historical building structures[13] was designed. The proposed system consists of twelve layers into which the individual building structures are divided. The system was designed so that when the visibility of individual layers is turned off and on, it is possible to comfortably view the entire model (especially the interior). It was also necessary to consider the fact that vernacular architecture can be very diverse in the number of used building structures. The structure of the proposed system can therefore be easily extended, e.g. according to used building material, floor-levels, etc., or simplified, e.g. for the purpose of presentation on the internet. The proposed system is described in detail in Table 1.

[2] Due to capacity reasons, the complete archive documentation could not be attached to the article, which is available from: http://zamerovaciakce.eu.cas.cz/tlokalita_popis.php?jmeno=&kr=Libereck% C3%BD &ok=Semily&lo=Kundratice&cp=60&trej=MIS

[3] Due to capacity reasons, the complete archive documentation could not be attached to the article, which is available from: http://zamerovaciakce.eu.cas.cz/tlokalita_popis.php?jmeno=&kr=Plze% C5%88sk %C3%BD&ok=Doma%C5%BElice&lo=Petrovice&cp=14&trej=MIS

[4] Due to capacity reasons, the complete archive documentation could not be attached to the article.

Fig. 4 – Example of using RoundCorner plug-in – existing object (left) and its 3D model (right)

Tab. 1: Comparison of historical structures and layer system for 3D model of a reconstructed building

ID	Historical construction	Layer name	Examples of layer naming
1	Walls - stone or brick	Walls	Walls_perimetric_material_floor-level
	Wooden walls		
	Clay and Layered clay		Walls_interior_material_floor-level
	Surface finishes		
2	Floors and tiles	Floors	Floors_material_floor-level
3	Ceilings	Ceilings	Ceilings_material_floor-level
	Vaulting		Ceilings_vaulting _material_floor-level
4	Staircases	Staircases	Staircases_material_floor-level
5	Railings and bars	Railings	Railings_material_floor-level
6	Roof trusses	Roofs	Roofs_trusses_material_floor-level
7	Roof covering		Roofs_covering_material_floor-level
8	Doors and gates	Doors	Doors_material_floor-level
9	Windows	Windows	Windows_material_floor-level
10	Terrain surface etc.	Terrain	Terrain_floor-level
11	Heating	Chimneys	Chimneys_material_floor-level
12		Furnaces	Furnaces_material_floor-level
-----	Ventilation, water and waste regime	-------	-------

Phases of 3D modelling

The creation of each 3D model consists of several phases. In all phases of 3D modelling in the SketchUp environment, it is advantageous to pay attention to the correct orientation of the surfaces[5].

In the first phase, a 2D floorplan of the building is vectorized in the initial working plane of the 3D model. Then, the floorplan is pulled into the space according to the height dimensions. In this way, the perimeter and interior walls are created. This is followed by the creation of floorings on the ground-floor. When creating floorings, it is important to find out whether the individual rooms on the ground-floor are height-shifted relative to each other. If so, it is necessary to take this into account when modelling the walls and floors on the ground-floor. This work process is also repeated when modelling other floor-levels of the building up to the attic-floor.

In the second phase, beams and a truss system are modelled. When modelling these parts, it is worth using clustering of surfaces into groups or components. This allows elements to be easily copied and prevents unwanted editing of already finished parts. The trusses are followed by the modelling of the roof and gables. The roof is usually created by a simply pulled-out surface, which is complemented by a texture according to the actual roofing of the building. Shields (squares) are often made of individual planks. The individual planks can be modelled separately or, to maintain the spatial impression, selected areas that represent the individual planks can be slightly pulled out or recessed. Another way to give the impression of a shield formed by individual boards is to use colours to create narrow spaces between imaginary boards and assign a different shade to them. This approach can also be used for the creation of timbered walls.

In the third phase, some elements of interior equipment and other types of structures are modelled, such as stairs, black kitchen equipment, furnaces, vaults, etc. These elements are usually only indicated in the archival plans, and for their modelling it is necessary to use other sources, such as existing period photographs of objects or professional literature dealing with vernacular architecture.

Due to the fact that in our case modellers[6] are not at the same time erudite architects or historians, the process of 3D modelling is based on cooperation of modellers with the staff of the Institute of Ethnology CAS. In this phase, the appearance of the reconstructed building is continuously revised and compared with analogous studies to capture the period appearance of the building as best as possible. Thanks to the consultations, it is also possible to resolve ambiguities arising from the imperfection of archival plans. This may be associated with additional modifications to previously modelled constructions.

In the fourth phase, digital terrain in the immediate vicinity of the building is modelled. For this purpose, Digital Terrain Model of the Czech Republic of the 5th generation (DMR 5G)[33] is used. ArcGIS Pro software[34] is used for editing and formatting DMR 5G data containing the given territory. Data editing consists of (1) import into ArcGIS Pro, (2) cropping of data to the required area, i.e. the nearest neighbouring building, and (3) export to DXF format. Then, data in DXF format are (4) imported into SketchUp software, where the TopoShaper plug-in is used.

In the fifth phase, a presentation of the 3D model on the internet is performed, which is to be implemented within a parallel-developed web platform. This process usually requires tailoring the 3D model to the used environment for the web presentation. In this case, it was a topological

[5] In SketchUp itself, the opposite orientation of the surfaces does not cause problems, but oppositely oriented surfaces can cause problems when exporting to other data formats, which are used for subsequent presentations of models on the internet. In SketchUp, it is possible to assign textures to both sides of any surface.

[6] I.e. creators of specific 3D models.

cleaning[7] of elements in the 3D model, or their geometric generalization, and the selection of suitable textures.

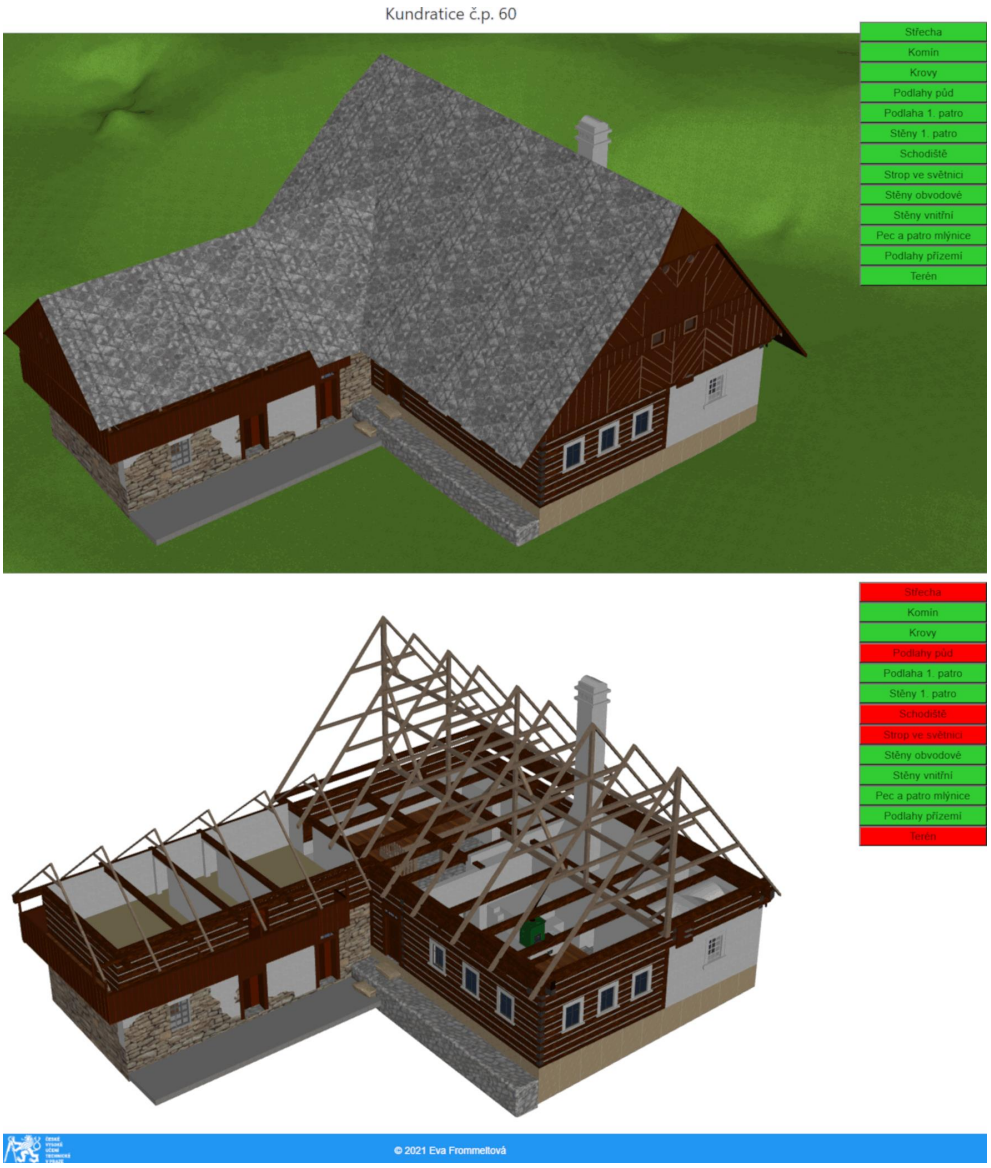

Fig. 5 - Example of visualization of 3D model in DAE format in Three.js interface including panel for displaying layers (in Czech language) – with all layers (top) and with selected layers activated (bottom)

Various technologies have been tested for visualization and presentation of the 3D model[29]. It is assumed that WebGL technology[36] will be used for 3D presentation on the internet, using the freely available JavaScript libraries Three.js[37] or Babylon.js[38], or using Coper Cube software[39]. Using one of these tools, interactive scenes should be created that allow the user to view the digital 3D model directly in a web browser. To view the exterior and interior of the building, the scenes must

[7] Within the 3D modelling process, the topology is understood in the same way as in the creation of maps, i.e. as *"defining the structure elements of geosystems based on their relationships connectivity (interconnection) and continuity (relative positions); map elements create topological structures consisting of nodes, edges, and walls"*.[35]

include a panel that allows individual layers of the 3D model to be turned on and off. An example of this solution is shown in Figure 5.

Another software used for visualization and presentation could be Lumion software[40], in which panoramic images of the object can be created. From the created images, it is possible to create a virtual tour complemented with text. The freely available Marzipano[41] JavaScript library can be used to create a tour.

RESULTS AND CONCLUSION

As part of the Viskalia project, several defunct buildings of vernacular architecture have already been reconstructed. Examples of three specific digital 3D models are shown in Figures 6 - 8 in the Appendices section. These figures present ongoing work results, their final form will be adapted for web presentation. In particular, the colour and textures of 3D models are currently illustrative, their final form is still under development.

The resulting 3D models digitally reconstruct the appearance of selected rural buildings based on preserved archival sources. The Level of Graphic Detail of 3D models corresponds to the Level of Detail of archive drawings. Details and finishes of building structures were usually modelled on the basis of views-plans or period photographs. In situations where archival metric survey documentation did not provide enough spatial information for 3D modelling, building structures and elements were modelled on the basis of analogous studies and customs of vernacular architecture. The resulting 3D models meet the specified criterion of level of detail in the introduction, i.e., the resulting model must have visibly important and regionally specific structural elements of the building. The models also represent (regionally, functionally, architecturally) selected regional house types from the territory of the Czech Republic.

This paper describes the specifics and working procedures for digital 3D reconstructions of defunct and altered buildings of vernacular architecture, which were realized within the project Viskalia. Primarily, the resulting 3D models are intended to serve for general lay public in order to present and popularize vernacular architecture and for educational activities. Secondly, they can be used by professional public for the same purposes. That is why they are based on archival sources - archival 2D metric survey documentation (drawings and photographs), written sources. The process of digital 3D reconstruction of each building is based on cooperation of modellers with the staff of the Institute of Ethnology CAS. The appearance of the reconstructed building is continuously revised and compared with analogous studies to capture the period appearance of the building as best as possible. Thanks to the consultations, it is also possible to resolve ambiguities during 3D modelling, which are the consequences of imperfections of archival plans. The resulting 3D models are made so that they can be presented on the internet within a parallel-developed web platform.

ACKNOWLEDGEMENTS

This work was supported by the Ministry of Culture of the Czech Republic from the Program for the Support of Applied Research and Development of National and Cultural Identity for the Years 2016-2022 (NAKI II), grant project "VISKALIA – Virtual Open-air Museum of the Vernacular Architecture ", No. DG20P02OVV003.

REFERENCES

[1] Gruen, A., Remondino, F., & Zhang, L. (2002). *Reconstruction of the great Buddha of Bamiyan, Afghanistan*. https://doi.org/10.3929/ETHZ-A-004655538

[2] Wahbeh, W., Nebiker, S., & Fangi, G. (2016). COMBINING PUBLIC DOMAIN AND PROFESSIONAL PANORAMIC IMAGERY FOR THE ACCURATE AND DENSE 3D RECONSTRUCTION OF THE DESTROYED BEL TEMPLE IN PALMYRA. *ISPRS Annals of the Photogrammetry, Remote Sensing and Spatial Information Sciences*, *III–5*, 81–88. https://doi.org/10.5194/isprs-annals-III-5-81-2016

[3] Pavelka, K., Šedina, J., Raeva, P., & Hůlková, M. (2017). MODERN PROCESSING CAPABILITIES OF ANALOG DATA FROM DOCUMENTATION OF THE GREAT OMAYYAD MOSQUE IN ALEPPO, SYRIA, DAMAGED IN CIVIL WAR. *ISPRS - International Archives of the Photogrammetry, Remote Sensing and Spatial Information Sciences*, *XLII-2/W5*, 561–565. https://doi.org/10.5194/isprs-archives-XLII-2-W5-561-2017

[4] Bitelli, G., Dellapasqua, M., Girelli, V. A., Sbaraglia, S., & Tinia, M. A. (2017). HISTORICAL PHOTOGRAMMETRY AND TERRESTRIAL LASER SCANNING FOR THE 3D VIRTUAL RECONSTRUCTION OF DESTROYED STRUCTURES: A CASE STUDY IN ITALY. *ISPRS - International Archives of the Photogrammetry, Remote Sensing and Spatial Information Sciences*, *XLII-5/W1*, 113–119. https://doi.org/10.5194/isprs-archives-XLII-5-W1-113-2017

[5] Deggim, S., Kersten, T. P., Lindstaedt, M., & Hinrichsen, N. (2017). THE RETURN OF THE SIEGESBURG –3D-RECONSTRUCTION OF A DISAPPEARED AND FORGOTTEN MONUMENT. *The International Archives of the Photogrammetry, Remote Sensing and Spatial Information Sciences*, *XLII-2/W3*, 209–215. https://doi.org/10.5194/isprs-archives-XLII-2-W3-209-2017

[6] Dvořák, V., Novák, V., & Šanda, M. (2017). *Zvířetice 3D intro*. https://www.youtube.com/watch?v=7faRMvVWRhk

[7] Wikipedia. (2021). Vernacular architecture. In *Wikipedia, the free encyclopedia*. https://en.wikipedia.org/w/index.php?title=Vernacular_architecture&oldid=1051057511

[8] Motyčková, D., & Sedlická, K. (2006). Činnost Národopisné komise při České akademii věd a umění v období protektorátu a její přínos k rozvoji oboru. In J. Pospíšilová & J. Nosková (Eds.), *Od lidové písně k evropské etnologii: 100 let Etnologického ústavu Akademie věd České republiky* (pp. 124–132). Etnologický ústav AV ČR Praha, pracoviště Brno ve spolupráci s Jiřím Plockem.

[9] Langer, J. (1997). *Co mohou prozradit lidové stavby: Lidové stavební tradice v severozápadních Karpatech a jejich kulturní funkce* (Vyd. 1). Ready.

[10] Mencl, V. (1980). *Lidová architektura v Československu*. Academia.

[11] Vařeka, J., & Frolec, V. (2007). *Lidová architektura: Encyklopedie* (2., přeprac. vyd.). Grada.

[12] Škabrada, J. (1999). *Lidové stavby: Architektura českého venkova*. Argo.

[13] Škabrada, J. (2003). *Konstrukce historických staveb*. Argo.

[14] Škabrada, J., & Ebel, M. (2014). *Chalupy v Čechách na historických stavebních plánech*. Argo.

[15] Pešta, J. (2003). *Encyklopedie českých vesnic: Vesnické památkové rezervace, zóny a ostatní památkově hodnotná vesnická sídla v Čechách*. Libri.

[16] Pešta, J. (2014). *Area research into vernacular architecture and rural settlements* (Professional and methodical publications). National Heritage Institute.

[17] Kmošek, J., Křenková, Z., & Bryol, R. (Eds.). (2016). *The Survey and Documentation of Vernacular Architecture Monuments* (1st ed.). Valašské muzeum v přírodě v Rožnově pod Radhoštěm, Spolek archaických nadšenců.

[18] Mira, J. A., Bevià, M., & Giner, J. (2020). CASTALLA (ALICANTE, SPAIN) VERNACULAR ARCHITECTURE: USE, LOSS, OBLIVION AND MEMORY. *The International Archives of the Photogrammetry, Remote Sensing and Spatial Information Sciences*, *XLIV-M-1–2020*, 73–80. https://doi.org/10.5194/isprs-archives-XLIV-M-1-2020-73-2020

[19] Poloprutský, Z. (2018). METRIC SURVEY DOCUMENTATION AS A BASIS FOR UNDERSTANDING THE DEVELOPMENT OF RURAL ARCHITECTURE. *Stavební Obzor - The Civil Engineering Journal*, *27*(1), 48–59. https://doi.org/10.14311/CEJ.2018.01.0005

[20] Castilla, F. J., Ramón, A., Adán, A., Trenado, A., & Fuentes, D. (2021). 3D Sensor-Fusion for the Documentation of Rural Heritage Buildings. *Remote Sensing*, *13*(7), 1337. https://doi.org/10.3390/rs13071337

[21] Domínguez-Ruíz, V., Rey-Pérez, J., & Rivero-Lamela, G. (2020). Contribution to the Knowledge of Cultural Heritage via a Heritage Information System (HIS). The Case of “La Cultura del Agua” in Valverde de Burguillos, Badajoz (Spain). *Sustainability*, *12*(3), 1141. https://doi.org/10.3390/su12031141

[22] Wikipedia. (2021). Skansen. In *Wikipedia, the free encyclopedia*. https://en.wikipedia.org/w/index.php?title=Skansen&oldid=1042162712

[23] Langer, J. (2005). *Evropská muzea v přírodě: Atlas památek*. Baset.

[24] Balletti, C., & Guerra, F. (2015). The survey of cultural heritage: A long story. *Rendiconti Lincei*, *26*(S1), 115–125. https://doi.org/10.1007/s12210-015-0411-8

[25] Technology Agency of the Czech Republic. (2021). *VISKALIA – Virtual open air museum of the vernacular architecture*. TA ČR Starfos. https://starfos.tacr.cz/en/project/DG20P02OVV003

[26] Herman, D. (2017). *Rozhodnutí Ministerstva kultury o přijetí projektů ve 2. Veřejné soutěži ve výzkumu, experimentálním vývoji a inovacích na rok 2018*. Ministerstvo kultury ČR. https://www.mkcr.cz/doc/cms_library/1-rozhodnuti-mk-o-prijeti-a-vyrazeni-z-vs-2018-7635.doc

[27] Etnologický ústav AV ČR. (2021). *Databáze Zaměřovací akce ČAVU*. http://zamerovaciakce.eu.cas.cz/

[28] Trimble. (2020). *SketchUp Pro Software: Create 3D Model Online*. SketchUp. https://www.sketchup.com/products/sketchup-pro

[29] Frommeltová, E. (2021). *Virtual open-air museum—Presentation of models of rural buildings* [Master thesis, CTU in Prague, FCE, Department of Geomatics]. http://hdl.handle.net/10467/96107

[30] ThomThom. (2021). *CleanUp³*. SketchUp Extension Warehouse. https://extensions.sketchup.com/extension/046175e5-a87a-4254-9329-1accc37a5e21/clean-up

[31] Fredo6. (2021). *RoundCorner v3.3a*. SketchUcation. https://sketchucation.com/plugin/1173-roundcorner

[32] Fredo6. (2021). *TopoShaper v2.6a*. SketchUcation. https://sketchucation.com/plugin/716-toposhaper

[33] Czech Office for Surveying, Mapping and Cadastre. (2010). *Geoportal ČÚZK: Access to map products and services*. http://geoportal.cuzk.cz/

[34] ESRI. (2021). *ArcGIS Pro*. 2D, 3D & 4D GIS Mapping Software. http://www.esri.com/software/arcgis-pro

[35] Terminological Commission of the Czech office for Surveying, Mapping a Cadastre. (2020). *Terminological Dictionary of Geodesy, Cartography and Cadastre*. Terminological Dictionary of Geodesy, Cartography and Cadastre. http://www.slovnikcuzk.eu/

[36] Wikipedia. (2021). WebGL. In *Wikipedia, the free encyclopedia*. https://en.wikipedia.org/w/index.php?title=WebGL&oldid=1045854911

[37] *Three.js: JavaScript 3D Library*. (2021). https://threejs.org/

[38] *Babylon.js*. (2021). https://doc.babylonjs.com/

[39] Ambiera. (2020). *CopperCube: Free easy to use 3D engine*. https://www.ambiera.com/coppercube/

[40] Act-3D. (2021). *Lumion 3D Rendering Software: Architectural Visualization*. https://lumion.com/

[41] *Marzipano: A 360° viewer for the modern web*. (2021). https://www.marzipano.net/index.html

APPENDICES

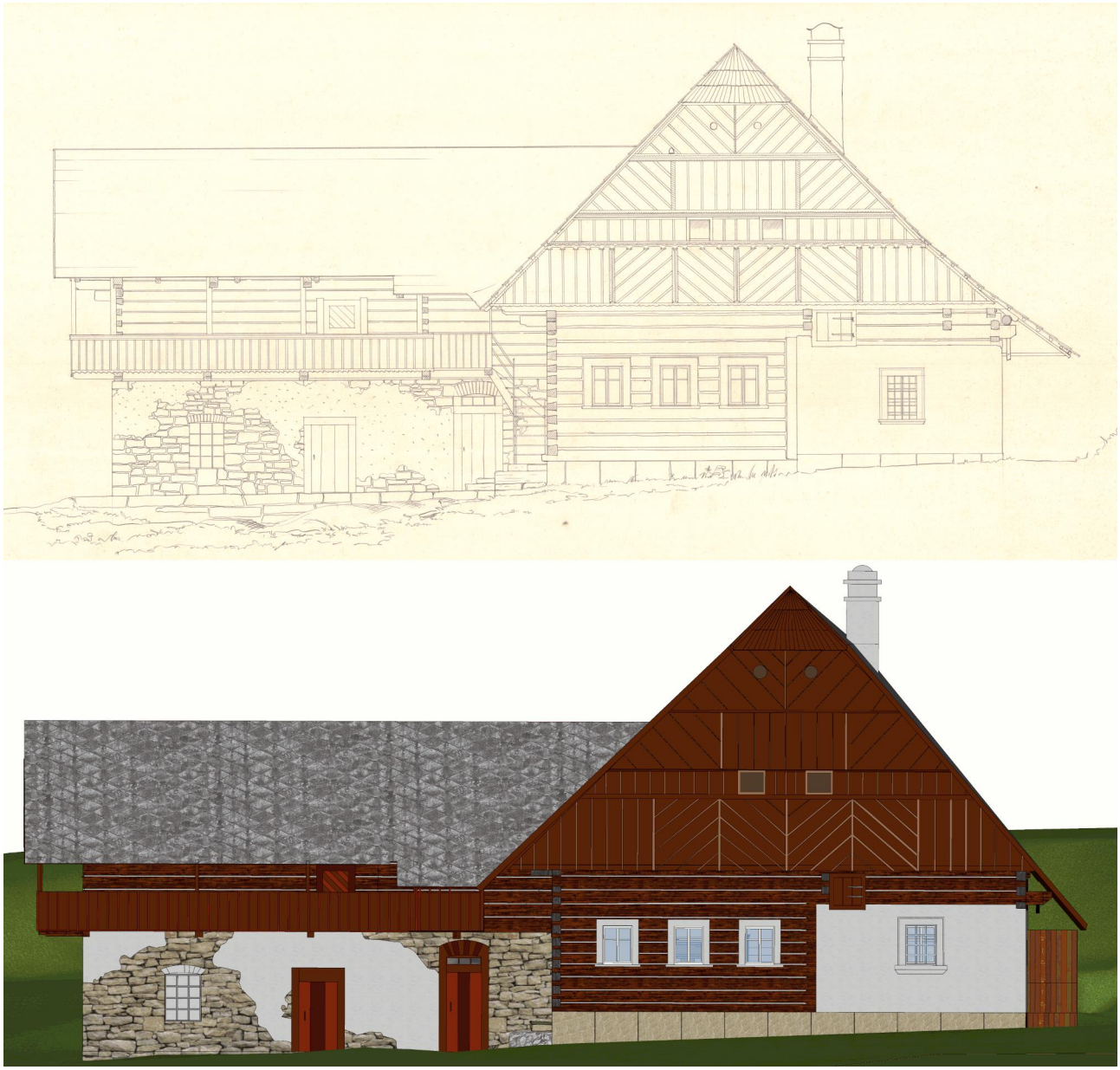

Fig. 6 - Comparison of the archival plan (above) with the corresponding view in the 3D model (below), Kundratice, Semily District, Czech Republic

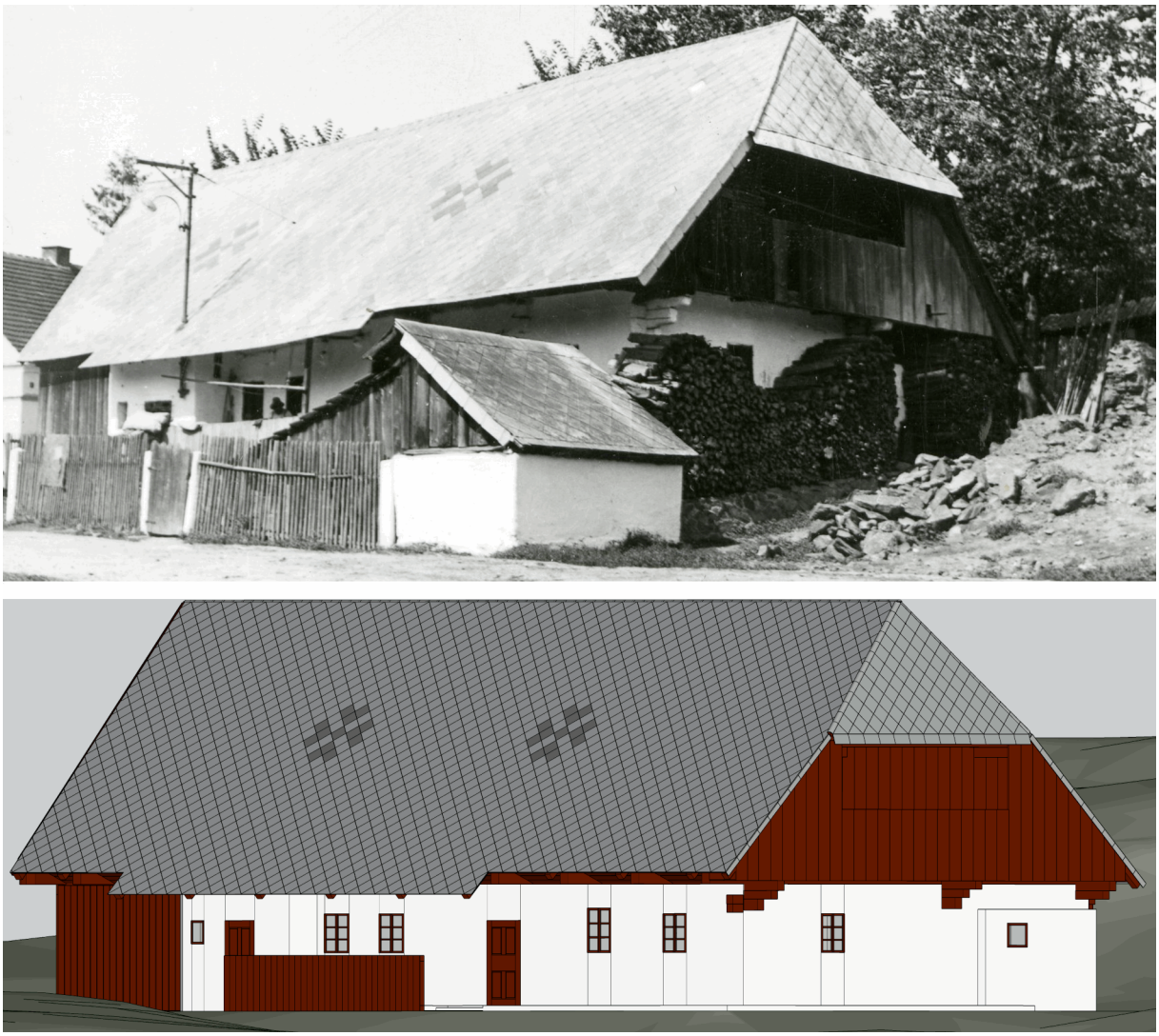

Fig. 7 - Comparison of archive photography (above) with the corresponding view in the 3D model (below), Petrovice, Domažlice District, Czech Republic

Fig. 8 - Comparison of archive photography (above) with the corresponding view in the 3D model (below), Zbožice, Havlíčkův Brod District, Czech Republic

CIVIL ENGINEERING JOURNAL

Article no. 16

THE CIVIL ENGINEERING JOURNAL 1-2022

EFFECT OF VARIOUS GROINS IN SERIES ON CHANNEL BED MORPHOLOGY: AN EXPERIMENTAL INVESTIGATION

Mohammed Alauddin, Rokshana Pervin and Md. Zakir Hasan

Department of Civil Engineering, Dhaka University of Engineering & Technology, Gazipur, Bangladesh, mauddin@duet.ac.bd

ABSTRACT

The alluvial rivers of Bangladesh being unstable keep changing their main course, bank lines, and so on. Groins are extensively used worldwide for shore protection from erosion, river navigation, and beach reclamation among many others. Improving the performance of groins is a crucial issue around the glove. Experimental investigations under clear water scour conditions have been carried out in this research to compare the performance of different groins in order to find out the suitable design for a groin. From the experimental runs, it is revealed that the groin models having different configurations behave differently. In the case of a solid I-shaped groin, a huge scour near the groin head and irregular bed pattern develops in the channel bed while L-head and hockey-shaped groins improve the channel response a bit leading to decreased scour. Moreover, the hockey-shaped groin attracts the flow, and thus requires a close groin installation. The scour hole for a combined groin is relatively very small. As the scour endangers the stability of the groin structure, it turns out to be the most suitable one.

KEYWORDS

Bank erosion, Combined groin, Deposition, Groin, Scour, Shore protection

INTRODUCTION

Most of the lowland rivers pass through alluvium plain which is highly susceptible to erosion and deposition because of its very dynamic nature. Various river training structures are being practiced in the rivers to stabilize the river channels, among which groins are extensively used all over the world [1] to [3]. These are artificial flow deflecting structures that are employed directly or indirectly in river engineering to protect the bank from erosion, to improve the navigability of channels, and to serve many additional purposes like land reclamation, an increase of aquatic habitats, and so on. These functions are provided by means of groins both in the river and coastal engineering [4]. The groin mainly diverts the direction of flow so that the flow velocity is significantly reduced in the groin area, and thereby bank erosion is minimized. Several parameters are needed to be considered in the installation of groins including groin length, groin angle towards the approaching flow, permeable or impermeable states, submerged or non-submerged states, spacing, and number of groins, among others [5].

The construction of groin structures that impede flow causes significant changes in flow patterns, sediment transport, and bed topography. Thus, it involves in the development of strong vortices near the groin head leading to scouring around the groin. Numerous experimental and numerical studies have been done so far to examine the flow patterns induced in the vicinity of groins, morphological changes that result from the interaction among groins, and so on. Due to inherent varieties associated with the configuration of groins, flow separation and recirculating length would be greatly different posing challenges for the applications of numerical models [6]. From an investigation on the effects of groins, it was found that the increase in discharge caused an increase

in the dimension of the scouring hole around the groin and an increase in the extent and thickness of sedimentation downstream of the groin [7]. Also, maximum scour depth shows an increasing trend with increasing Froude number. Through an investigation of scour-deposition mechanism around a series of spur dikes, it was concluded that the aspect ratio was a significant parameter that affected bed topography and flow behavior close to the structures [8]. A study on the flow field and bed topography being induced because of the interaction of groins of various alignments revealed that the groin modified with downstream aligned part performed better in improving navigation depth and bank protection as well [9]. From a comparison of the effect of a triangular groin with a rectangular one, it was concluded that the maximum scour hole depth and volume were smaller in the triangular spur dikes than in their rectangular counterparts [10]. An investigation on the effects of flow around a pile-group groin demonstrated that the staggered type groin functioned better compared to the in-line type in reducing flow towards the bank and turbulence around the structures [11].

The I-shaped impermeable groins are usually practiced to protect the bank from erosion. However, from this structure, the flow deviates highly from the river bank and a horizontal vortex in the recirculation zone forms that results in the local scour [12]-[15]. Thus, they cannot sustain long in many situations and cannot function properly. The L-head and hockey-shaped impermeable groins could minimize flow separation and the strong vortices near the groin tip which are responsible for a huge local scour. Although the permeable groins can allow flow through the structure which could eliminate the strong return currents, fully permeable groins cannot properly deflect the flow. Also, the flow near the bank occurs which could affect the bank if it is associated with the oblique flow. A combined groin (a combination of both permeable and impermeable parts in a groin structure) with an impermeable part near the bank could improve the flow field through a gradual deceleration of flow velocity towards the bank and develops a stagnant flow region near the bank line and thereby minimizes scour near groins [16]. In the present research, attempts are made to explore the effects of groin shape and groin permeability through experimental investigations. Four different groin models: I-shaped, L-head, hockey-shaped impermeable groins, and a combined groin are considered in this study. Thus, a suitable design of groins could be established whose performance would be better compared to others.

METHODS

Experimental setup

In this study, laboratory experiments are conducted in a straight concrete channel of dimension: 22.50 m x 1.52 m x 1.15 m with a sand bed of 0.30 m (Figure 1). Four sets of different groin models such as I-shaped (M-1), L-shape (M-2), hockey-shaped (M-3) impermeable, and a combined groin (M-4) containing six numbers in each set to install the groins in series are considered for assessing their performance. Solid groin models – I-shaped, L-shaped, and hockey-shaped groins are made with wooden planks of 2.5 cm thickness; the other combined groin is made of wooden plank for the impermeable part with 5.0 mm diameter steel sticks at different spacings of 7.0 cm@1.0 cm c/c and 11.0 cm @1.5 cm c/c for the permeable portion.

.

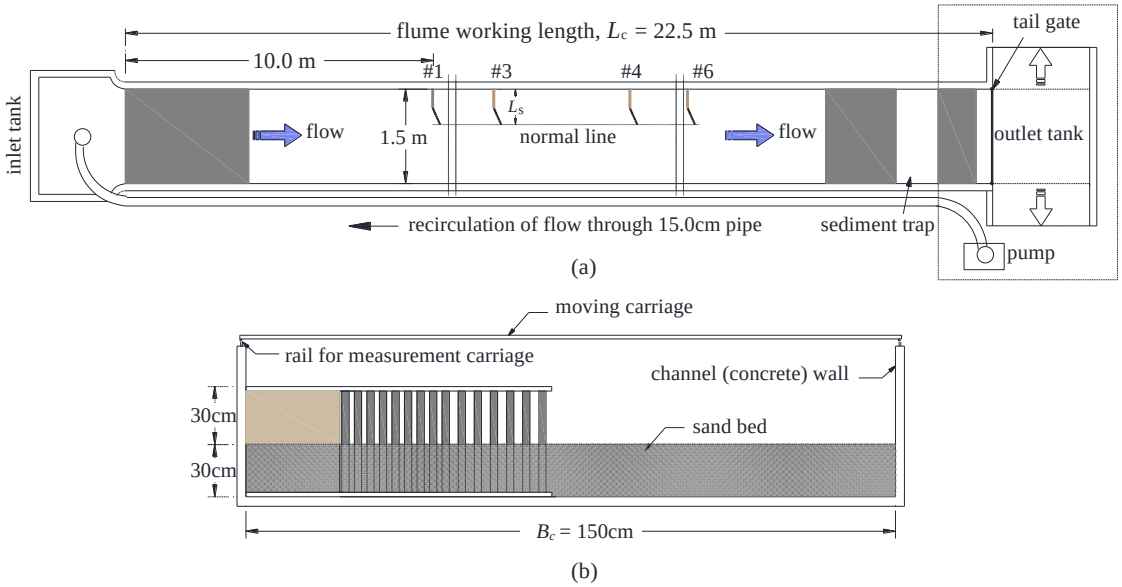

Fig. 1 – Laboratory channel: (a) Plan view; (b) Cross-section

The L-shaped and hockey-shaped solid groins are expected to improve the flow pattern compared to I-shape solid groin model. The part of a combined groin model near the main channel is made permeable to allow the flow through the structure to minimize the strong vortices near the groin head and to develop gradual deceleration of flow velocity towards the bank. The groin models used in the study are shown below (Figure 2).

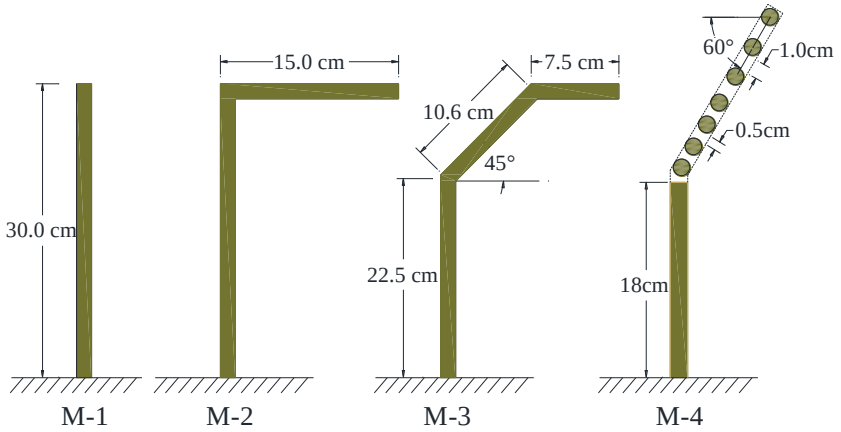

Fig. 2 – Groin models

The channel bed is prepared with fine sand with a thickness of about 30.0 cm. First, the sand is washed to remove silt and clay from this, and then this is placed on the channel bed and is levelled with a wooden scraper. A certain flow condition is considered in the study, and it was maintained the same for all the cases. The experiments are conducted under clear-water scour conditions. This scour occurs when the bed materials are not in motion before the control section. This condition is initiated in the channel when the shear stress being induced by the water flow does not exceed the critical shear stress of the bed material, and this is established after some trials. The depth of flow in the channel with the groins is kept constant. It is kept around 10.0 cm in the channel. This depth is controlled and adjusted by the tailgate set at the end of the channel. The discharge is measured by the flowmeter (0.03 m3/s) and the depth of flow in the channel is maintained the same for all the cases in the study.

Four different sets of groin models with six models in each set are utilized in the study and their effects on the channel being examined. The first model of each set is installed at a distance of 10.0 m from the upstream end, and the rest five models are placed at an interval of twice their length. The channel bed is carefully levelled using a wooden scraper to ensure surface regularities along the channel bed in order to consider this as the initial condition. The models are embedded in the sand bed so that 30.0 cm of its height goes under the sand bed.

Working procedure

In the beginning, the flow of water is run at a very low speed and allowed to enter the main channel slowly only to wet the sand bed, and after draining, the bed level is measured with a point gauge to find the initial bed level. Next, the flow is allowed to enter the channel gradually and the flow is increased by a check valve mounted in the discharge pipe to adjust the required flow. For each experiment, the flow runs up to 2.0 hours, till the depth of the scour hole near the first model does not increase, i.e., the equilibrium state is reached. Then, the flow is stopped and the channel bed is drained out before measuring the elevations of the final bed.

The effects of four different sets of groin models on the channel bed are evaluated based on scour-deposition patterns. In order to know the scour and deposition in the channel bed, the bed levels are measured before and after each experimental run with a point gauge. The bed level before each of the experimental runs, i.e., the initial bed level is measured at 10.0 cm grid points along both transverse and longitudinal directions in the groin area. However, after the experiments, this is measured at 5.0 cm intervals in the longitudinal direction and 2.5 cm intervals in the transverse direction to get the uneven condition of the surface well. In almost all the cases, the scour occurs at the end of the groin head in the impermeable groin cases, and at the end of the impermeable part in the case of a combined groin, where the magnitude of scouring varies with the different models. The maximum deposition is, however, observed immediately in the downstream of the scour hole in these experiments under clear water-scour conditions. Besides, erosion occurs in the main channel in different ways due to the diverted flow from the models. The channel showing the bed with four different groin sets before and after the experimental runs is shown in Figure 3.

(a) M-1

Fig. 3 – Initial bed (left) and final bed (right) with four different groin models

(b) M-2

(c) M-3

(d) M-4

Fig. 3 – Initial bed (left) and final bed (right) with four different groin models: (a) M-1, (b) M-2, (3) M-3, (4) M-4

DATA ANALYSIS

The bed level data of both the initial bed and final bed for each set of groin models are taken before and after the experimental runs. The change in bed level (Δz) is calculated to determine the effect of groins on channel bed, and bed profiles along transverse and longitudinal directions are determined. These analyses have been explained in the following sections.

Changes in bed topography

From the measured data of initial and final bed elevations, variation in the bed level due to the groins is calculated by taking their difference. The depth of scour near the groin head, and average deposition in the groin field are obtained from the bed level variation. Also, the changes in bed level

due to the groins are recognized in the channel after the groin field which vary from one model to another. The bed topographies due to the various groins are shown in the following figures (Figures 4-7).

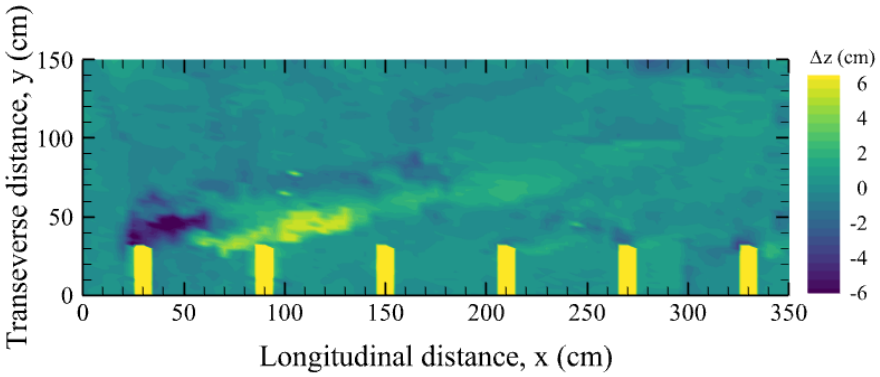

Fig. 4 – Model M-1 induced bed topography

The area of scour hole near the first groin model is more pronounced in the case of Model M-1 (Figure 4), and this is followed by siltation in the immediate downstream area. The sediments from the first scour hole have mainly accumulated here and cannot be transported downstream under the present flow conditions. However, the local scour is not visible in the next four groins downstream. But the scour near the groin is observed in the last groin as the flow is back on the same side where the groins are installed. This solid groin gives obstruction to flow fully causing a huge deviation of the flow that leads to flow separation and formation of strong eddies. Because the size and depth of scour hole near the first groin head are much higher. Also, the effect of the flow across the channel is wider and it is not even. The flow being obstructed by the solid groin does not follow a certain direction, and erosion in the channel bed is observed irregularly.

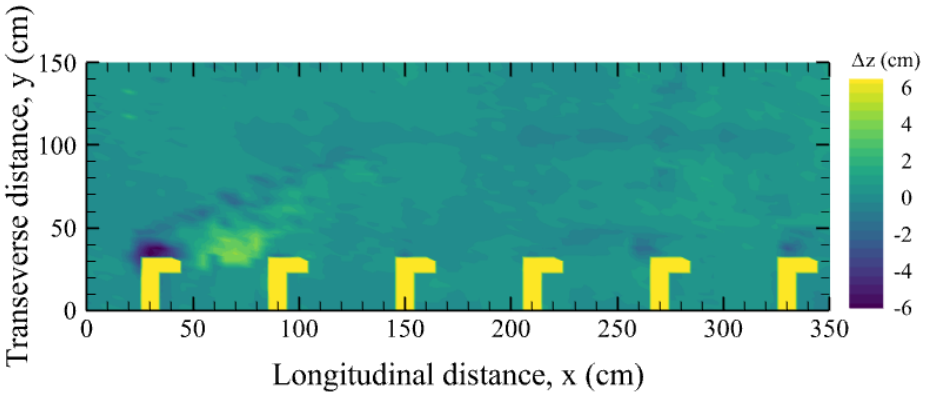

Fig. 5 – Model M-2 induced bed topography

The area of the scour hole in the L-head groin (Figure 5) is not as large as that is found in the solid straight groin. However, in this case, also more scours occur near the first groin compared to the downstream ones. Silt has accumulated in the downstream area of the scour hole in proportion to the first scour hole. The eroded area in the channel bed is influenced by the groins regular. Although the effect of this groin has gone quite far to the other side, it is still regular. As the water returns to the groin side, a little scour can be found near the groin of the downstream end which may be due to the reflected flow from the other bank.

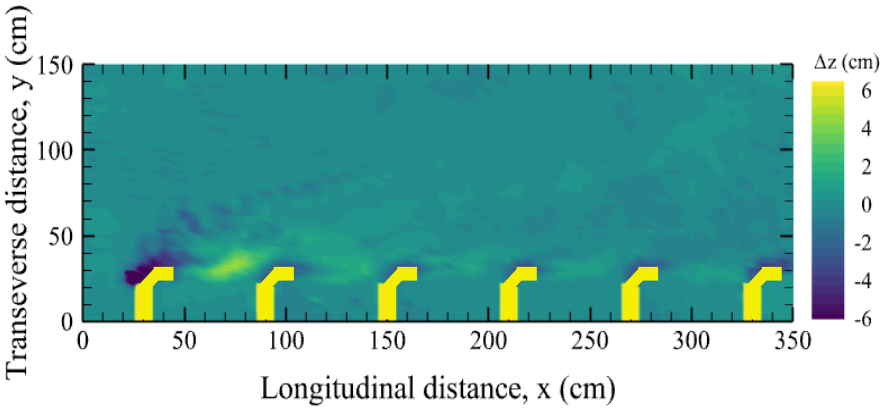

Fig. 6 – Model M-3 induced bed topography

In the case of Model M-3 (Figure 6), the hole in the first object covers a little more space than in the second. Due to its shape in the head, this groin does not deflect the flow too far. As a result, there are holes near every groin models. In this case, the main flow path passes close to the groin area. These groins do not make irregular paths, and the effect of the flow on the other side of the channel is not found at all.

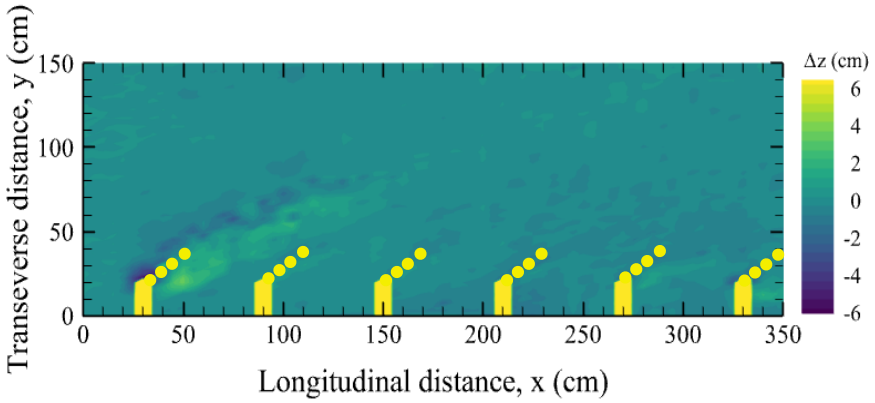

Fig. 7 – Model M-4 induced bed topography

In the case of the combined groin M-4 (Figure 7), since water can pass through the structure on the flow side, the flow is not obstructed much. As a result, the flow separation or the eddies is reduced, and scour in both area and depth is very few. When it flows through the first groin, its speed decreases and goes downstream with a low speed resulting in decreased ability to form scour in the downstream groins. So there are no scour holes near the downstream groins. There is no effect of these groins on the other side of the channel and no significant change is observed in the bed in other areas. In this case, the effect of the flow is greatly reduced.

Erosion-deposition pattern

To identify the changes in bed level, the bed profiles are taken along various sections in both longitudinal and transverse directions. Finally, the profiles found from different groin models have been compared to evaluate the effects of groin models having different shapes and configurations. The changes in bed level across the channel width at the location of the first groin are presented in the following figure (Figure 8). From the profile, bed level changes (Figure 8) are evident across the channel width for the first groin and the variation of the profiles due to the various groin models can be recognized. The highest effect can be noticed for the solid straight groin (M-1), where the local scour depth is observed that be maximum and then a relatively lesser effect can be observed in the case of the L-head groin (M-2). The scouring effect for the other two groin models (M-2 and M-3) has decreased significantly. Alignment and permeability could be attributed to the improved

response in these cases. For model M-1, the scour-prone zone can be recognized from 30.0 cm (groin tip) to 70.0 cm along the transverse direction, and 10.0 cm upstream of the groin section to 35.0 cm downstream (Figure 4). For model M-2, the scour-prone zone is found from 30.0 cm (groin tip) to 47.5 cm in the transverse direction, and 7.5 cm upstream to 12.5 cm downstream from the groin location (Figure 5). However, for model M-3, this area can be seen between 30.0 cm to 40.0 cm in the transverse direction and 10.0 cm upstream to 17.5 cm downstream as affected in the inclined part (Figure 6), and for model M-4, this area is between 22.5 cm to 37.5 cm from the channel side, and 5.0 cm upstream to 10.0 cm downstream from the groin position (Figure 8).

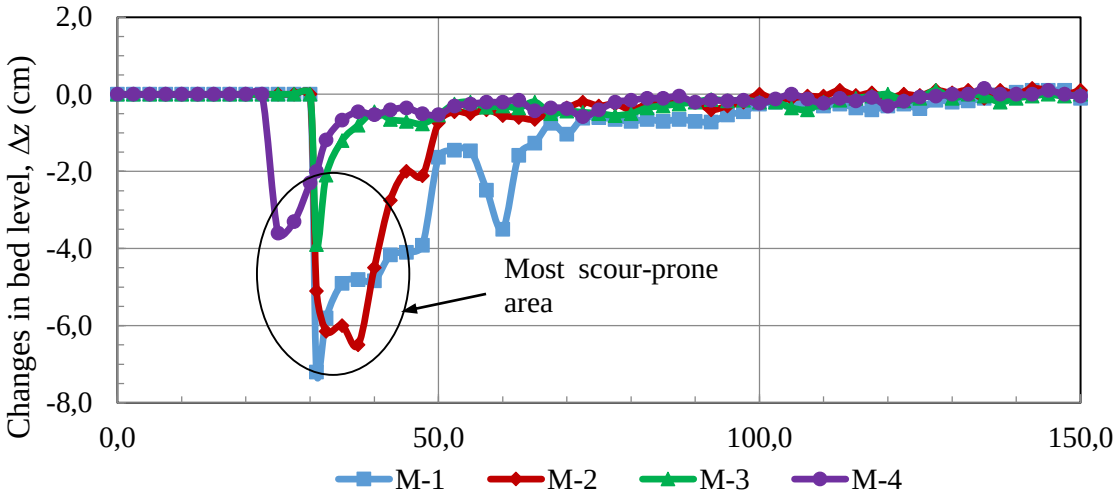

Fig. 8 – Bed level changes along the cross-section at the first groin

The maximum depth of scouring formed near the first groin-head due to various groin models is shown in the following figure (Figure 9).

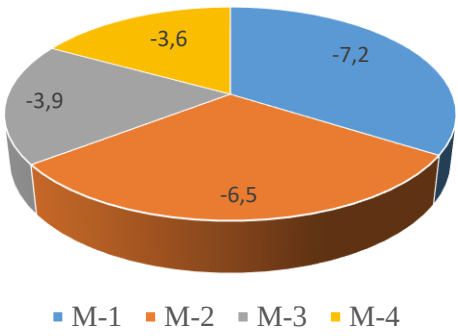

Fig. 9 – Maximum depth of scour due to various groin models

From the figure shown above, it can be found that the maximum value of scouring occurs for model M-1 and the minimum for model M-4. These values are 7.2 cm and 3.6 cm, respectively, i.e., the scour depth for the combined groin is reduced by 50%. The depth of the scour hole for M-2 is very close to that of M-1. But in the case of M-3, it is a bit more than M-4. The maximum scour depth for groin M-2 is 6.5 cm, and it is 3.9 cm for groin M-3. Also, the average depth of scour in the scour area is calculated for all the groin models. These values are 1.35 cm, 0.70 cm, 0.41cm, and 0.40 cm for the groin models of M-1, M-2, M-3, and M-4, respectively.

An average deposition in the groin field developed by various groin models is presented in the following figure (Figure 10).

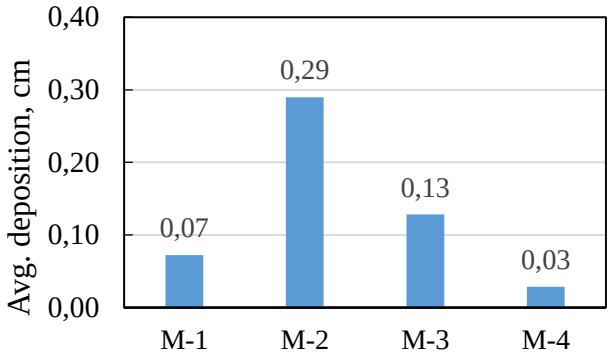

Fig. 10 – Average deposition in the groin field due to various groins

From the Figure shown above (Figure 10), the average deposition that occurs the groin field for different groin models can be observed differently. This is found maximum for the groin model M-2 and minimum is in case of M-4, and it is almost 10 times more than that of model M-4. Deposition from models M-1, M-2, M-3 and M-4 is found 0.07 cm, 0.29 cm, 0.13 cm and 0.03 cm, respectively. It is worth mentioning here that the experiments are conducted under clear water scour conditions, and even in the control area, the presence of suspended sediments is not significant. As a result, the deposition in the groin field does not truly reflect the natural flow environment as prevalent in the lowland river where the siltation of fine suspended sediment particles occurs in the slow flow zone of the groin field.

Discussions

From the figures presented above, the effect of the groin models on the channel bed is quite evident. Among these, the effect of the conventionally used groins, the solid straight one (M-1) is quite irregular. For large and irregular effects, there is an effect on a distant and some important installation, and no good channels are generated in a certain direction which could not be a good arrangement for navigation either. The scour near the other bank occurs, which might not be expected in many cases. The returned and oblique flow on the bank can be more dangerous as observed in the Jamuna River [17]. Also, for larger holes nearby, its stability can be assumed to be lower. Compared to Model M-1, the effect of the flow in the M-2 has been much more regular or even. Its stability is expected to be higher with a comparatively less scour depth. By conducting the flow through the space close to the groin area, a suitable channel for navigation can be found with Model M-3. However, since the flow returns quickly with a short distance, the distance from one of the continuously placed groins to the other does not show much. As a result, the return flow can come back resulting in an attack on the bank of the river or channel for which the groins have been provided.

In the combined groin (M-4), the flow does not come back towards the bank or side where the groins are placed leading to less scour in the vicinity. However, the concentration of flow in a certain direction may not be so good. Pointing to the permeable end of the groin towards downstream may point the flow somewhat in a certain direction, although this has not been observed under the low flow conditions in the present experiments. However, this arrangement can reduce the problem of debris flow to minimize the force from the debris and also can allow debris to flow along the downstream direction. In this case, there is lesser tendency to damage any important object placed on the far or other bank, and there is less chance for returning the flow that can affect the bank where the groins are installed. So, in this case, groins can be placed far away. Having a very few scour in the vicinity of the groin head, a combined groin could increase its stability and longevity. As a result, the costs of groin implementation for the protection of the river bank from erosion can be less.

Although a deeper channel cannot be recognized rightly under the present experimental conditions, its evolution can be marked relatively uniform along the definite direction in the case of downstream aligned groins (M-3 and M-4). The deeper portion of the main channel developed for M-1 is not found

uniform; while M-2 modifies the channel far better than M-1. Deposition in the groin field is not found significant in the experimental runs as the suspended sediment particles in the flow are very few, and the experiments are conducted under clear water scour conditions. The silt from the scour hole has accumulated in the downstream area as it cannot be transported under the prevailing flow conditions and available channel bed materials.

CONCLUSIONS

As the groin models with different configurations behave differently, the extent and distribution of erosion and deposition in the channel bed are different. From the changes in bed levels, i.e., erosion-deposition reflects from the channel bed due to the groins as discussed earlier and the following conclusions can be drawn.

In the case of solid I-shaped groin, as the flow is deviated, a huge, deep and large scour holes have formed near the groin structure. Also, the flow being deviated from the groin returns to the same bank get obstructed from the other bank, as recognized from the erosion and the channel that has been created is found irregular. The flow for L-head and hockey-shaped groins has improved compared to the first one as changes in bed level are found defined and regular, whereas the depth and size of scour holes near the groin have decreased. However, for the hockey-shaped groin, the flow is attracted towards the groin area, and thus groins are required to be placed closely in series. The flow has deviated slightly in the case of the combined groin as it allows flow through the structure, and flow separation is minimized resulting in a very few scour hole. As the scour endangers the stability of the groin structure, the stability of the groin can be expected to be higher in this case.

A major deposition of sediment occurs immediately in the downstream of the scour zone near the groin head. The formation of this scour hole can be attributed to the sediment deposition. The deposition measured in the groin field is found maximum for model M-2, and minimum for M-4. The deeper channel which provides navigation facilities does not show clearly in these present experiments; however, a defined path of flow towards the downstream direction is quite apparent for the downstream aligned groins (M-3 and M-4).

As the suspended sediment particles are not significantly present in the channel environment and the experiments are carried out under clear-water scour conditions, the deposition in the groin field does not properly show up. Therefore, when it comes to the question of stability, the combined groin shows better performance than others in terms of minimum scour near the groin tip.

ACKNOWLEDGEMENTS

This research was supported by University Grants Commission (UGC) under the Ministry of Education, Bangladesh through CASR, DUET. We would like to express our deepest appreciation for the generous support.

REFERENCES

[1] Richardson E.V., Stevens M.A. and Simons D.B., 1975. “The design of spurs for river training.” In XVIth, IAHR congress (pp. 382–388). Sao Paulo, Brazil.

[2] Pandey M., Ahmad Z., and Sharma P.K., 2018. “Scour around impermeable spur dikes: A review.” ISH J. Hydraul. Eng., 24(1), 25–44. doi:10.1080/09715010.2017.1342571

[3] Pandey M., Valyrakis M., Qi M., Sharma A. and Lodhi A.S., 2020b. “Experimental assessment and prediction of temporal scour depth around a spur dike.” Int. J. Sediment Res. doi:10.1016/j.ijsrc. 2020.03.015

[4] Sarveram H., Shamsai A. and Banihashemi M.A., 2012. Two-dimensional simulation of flow pattern around a groyne using semi-implicit semi-Lagrangian method. International Journal of Physical Sciences. 7, 2775-2783.

[5] J Kang H. Yeo S.K. and Ji U., 2011. Permeability effects of single groin on flow characteristics, Journal of Hydraulic Research. 49:6, 728-735.
[6] Quanhong L. and Pengzhi L., 2007. Numerical Simulation of Recirculating Flow Near a Groyne, The 2nd International Conference on Marine Research and Transportation, Ischia, Naples, Italy. 61-68.
[7] Mahmoud R. Eltoukhy and Neveen B.A., 2012. Effect of Groin Geometry on Scouring of Sandy River Beds Having 180o Bend, Civil Engineering Research Magazine, Al-Azhar University. 34(3): 880-892.
[8] Fukuoka S, Nakagawa N., Sumi T. and Zhang H., 2013. Advances in River Sediment Research; Taylor & Francis Group: London, UK.
[9] Alauddin M. and Tsujimoto T., 2012. Optimum configuration of groynes for stabilization of alluvial rivers with fine sediment. International Journal of Sediment Research (Elsevier publishing), Vol. 27, No. 2, pp. 158–167.
[10] Bahrami-Yarahmadi M, Pagliara S., Yabarehpour E. and Najafi N., 2020. Study of Scour and Flow Patterns around Triangular-Shaped Spur Dikes. KSCE J Civ Eng. 2020; 24(11), 3279–3288.
[11] Ettema R., Muste M., 2004. Scale effects in flume experiments on flow around a spur dike in flatbed channel. Journal of Hydraulic Engineering 130(7):635-646, DOI: 10.1061/(ASCE)0733-9429(2004)130:7(635)
[12] Duan J.G., 2009. Mean flow and turbulence around a laboratory spur dike. Journal of Hydraulic Engineering 135(10):803-811, DOI: 10.1061/(ASCE)HY.1943-7900.0000077
[13] Jeon J., Lee J.Y., Kang S., 2018. Experimental investigation of three dimensional flow structure and turbulent flow mechanisms around a nonsubmerged spur dike with a low length-to-depth ratio. Water Resources Research 54:3530-3556, DOI: 10.1029/2017WR021582
[14] Koutrouveli T.I., Dimas A.A., Fourniotis N.Th., Demetracopoulos A.C., 2019. Groyne spacing role on the effective control of wall shear stress in open-channel flow. Journal of Hydraulic Research 57(2):167- 182, DOI: 10.1080/00221686.2018.1478895
[15] Safie and Tominaga, 2020. Effects of pile arrangement on the flow around a pile-group groyne. JSCE. 8, 207-220.
[16] Alauddin M., Tashiro T. and Tsujimoto T., 2011. Experimental investigation of channel responses against different configurations of groynes, Advances in River Engineering, JSCE, vol.17, 335-340.
[17] Uddin M.N. and Rahman M.M., 2012. Flow and erosion at a bend in the braided Jamuna River. International Journal of Sediment Research. 27(4), 498–509.

CIVIL ENGINEERING JOURNAL

Article no. 17

THE CIVIL ENGINEERING JOURNAL 1-2022

SERVICE LIFE PREDICTION OF BASALT FIBER REINFORCED CONCRETE UNDER SALT FREEZE-THAW CYCLES

*Wenjie Xu and Zhirui LI**

*School of Water Conservancy, North China University of Water Resources and Electric Power, Zhengzhou 450046, China; 1542315987@qq.com, * 97410419@qq.com*

ABSTRACT

To address the reduced durability of concrete structures under salt freeze-thaw erosion in Northwest China, basalt fiber reinforced concrete and common concrete with different mixing amounts were selected to predict their service life in three freeze-thaw conditions. Results showed that the damage on concrete under fresh water freeze-thaw condition is lower than that caused by salt freeze-thaw erosion, the addition of basalt fiber can effectively slow down the degradation of mechanical properties of concrete under salt freeze-thaw erosion, and the lowest degradation rate is reached when the content of basalt fiber is 0.15%. Fiber hinders the expansion of cracks and reduces the pores, and in turn improves the frost resistance durability of concrete. The service life prediction results obtained with Gray Model and Weibull Model are roughly similar, among which, Gray Model needs less sample volume, while Weibull Model presents more accurate prediction results.

KEYWORDS

Basalt fiber reinforced concrete, Mechanical property, Weibull Model, Gray Model, Service life prediction

INTRODUCTION

Aging is a common phenomenon of concrete materials with passage of time, and freeze-thaw damage is one of its main reasons. Affected by environmental temperature change, free water in concrete materials produces expansion pressure and permeability pressure. The combination of the two causes denudation, internal and external crack expansion, and internal structural looseness of concrete materials, reducing their fracture performance and flexural toughness. In Northwest China, because of large amount of salt ions and acid group anions in the soil, most concrete structures' surface layers peel off or crack before expiry due to salt freeze-thaw erosion, impacting its normal functions. Therefore, it is of great practical significance to research the mechanical property attenuation rules and damage mechanisms of concrete materials in simulated environment.

Basalt fiber (BF) is a kind of natural green fiber with superior performance. Scholars at home and abroad have done a lot of research on its properties and applications recently. Li Weimin[1] et al. studied the impact compression properties of basalt fiber reinforced concrete (BFRC), and drew a conclusion that BF can improve the mechanical properties of concrete and the degree of improvement is concerned with the mixing amounts. Feng Zhongju [2] et al. predicted the service life of concrete with different mix proportions on the basis of local temperature and Gray Theory. Xie Liyun [3] et al. established a linear and polynomial damage degradation model based on relative dynamic elastic modulus and strength as damage variables, which can accurately predict the degree of freeze-thaw damage and degradation of fiber recycled concrete. Ahmet B.Kizilkanat [4] et al. compared the mechanics and fracture properties of BFRC with glass fiber reinforced concrete, and came to a conclusion that the extensibility, bending resistance and crack resistance of BFRC are superior to those of glass fiber reinforced concrete. Boxin Wang et al. [5] re-searched the

durability of concrete under the erosion and freeze-thaw action of carbonate and sulfate ions, and established new logical function models on concrete freeze-thaw damage. R. Ralegaonkar et al.[6] proposed the mix proportions of short-cut BF that strengthens the mortar performance and evaluated its advantages and disadvantages in application. Audrius Vaitkus [7] et al. densified the concrete mixture and found that its design performance can be significantly improved by adding silicon powder, steel or polypropylene crude fiber. At present, most research focus on the performance improvement of fiber concrete at early stage, but mechanical attenuation rules and damage mechanisms of BFRC in actual service have not been elaborated.

There is few research on the damage mechanisms of BFRC after salt freeze-thaw erosion so far, thus the present paper studies the mechanical properties of BFRC under the action of freeze-thaw cycles with basalt fiber mixing amount and freeze-thaw media as variables, and compares the analysis results with common concrete (PC). On this basis, Weibull Model and Gray Model are used to predict the frost resistance durability of BFRC with four mixing amounts under the environment of Gansu Province. The variation rules of parameters as the freeze-thaw cycles and fiber contents change are analyzed to lay the theoretical and experimental foundation for fracture mechanics research of concrete.

EXPERIMENT OVERVIEW

Materials and mix proportions

Tab. 1 - Basalt fiber performance index

Fiber length（mm）	*Diameter（μm）*	*Density（kg/m³）*	*Fracture ductility rate（%）*	*Elastic Modulus（GPa）*	*Tensile strength（MPa）*	*Moisture content（%）*
18	*7-20*	*2 650*	*3.2*	*90~110*	*3 000~3 500*	*≤0.1*

Tab. 2 - Concrete mix design

Species	*Cement kg/m3*	*Water kg/m3*	*Fine aggregate kg/m3*	*Coarse aggregate kg/m3*	*Fly ash kg/m3*	*Sand rate /%*	*Fly ash /%*
PC	*265*	*180*	*640*	*1 200*	*115*	*35*	*30*
BFRC	*265*	*180*	*640*	*1 200*	*115*	*35*	*30*

Po42.5 cement was adopted in the experiment. Fine aggregate was natural river sand, with fineness modulus of 2.9, water-binder ratio of 0.45 and mud content of 1.8%. Continuous grading coarse aggregate with particle size of 5mm-20mm was adopted, and no needle flake particles were allowed. The 19.45g/m3 JDU-1 high performance concrete air-entraining agent was used as additive, accounting for 0.005% of the specimen. This study applied fresh water and 18mm short-cut BF, whose main performance indexes were shown in Table 1. In addition, BFRC with fiber contents of 0%, 0.05%, 0.1%, 0.15% and 0.2% was selected, with mix proportions shown in Table 2.

Indoor rapid freeze-thaw experiment

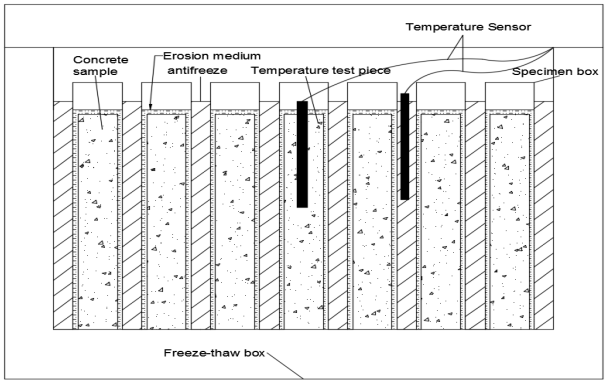

Fig. 1 - Concrete freeze-thaw test design

The specimens were made and maintained in accordance with the Standard for Testing Methods of Concrete Physical and Mechanical Properties [8]. The experiment selected three freeze-thaw solutions, respectively fresh water, 3% NaCl, and 5% Na_2SO_4, and four fiber mixing amounts, and took PC as a control group. In each freeze-thaw environment, 21 cubic specimens and 24 prism specimens were designed. Before specimen production, the inner wall of the test mold was coated with release agent, the dosage of experimental materials was accurate to ±0.5% and the dosage of aggregate was accurate to ±1%. In order to avoid caking effect caused by uneven distribution of fibers during mixing with water, coarse aggregate and fibers were dry mixed for 2min before concrete mixing to ensure the uniform distribution of fibers. Then the mixing and molding of concrete was completed within 15min. The molded specimens were covered with impermeable film and stored at 20±5℃ for 1-2 days and nights. Then the film was removed and the specimens were numbered. The specimens were maintained for 28d, and then the freeze-thaw test was carried out, with 25 freeze-thaw cycles as a period.

HDK-9 rapid freeze-thaw testing machine was used for indoor rapid freeze-thaw test, with test layout shown in Figure 1. The experimental process is as follows:

(1) The specimens were molded, numbered and maintained for 24d, then taken out and immersed in three different freeze-thaw erosion solutions for 4d, with liquid level 30mm higher than the specimens. The freeze-thaw test began after 28d.

(2) After 28d, take the specimens into test molds containing different freeze-thaw media with liquid level always 5mm higher than the specimens and number them. Put the specimens into the freeze-thaw machine and make sure that the freeze-thaw liquid level was higher than test molds' liquid level.

(3) Each freeze-thaw cycle was completed within 2-4h, with thawing time not less than 1/4 of the whole process.

(4) The center temperature of the specimens was -20℃-7℃, better from -18℃±2℃ to 5±2℃.. The cooling time from 16℃ to 3℃ and heating time from 3℃ to 16℃ were not less than 1/2 of each cycle.

(5) Specimens in the freeze-thaw machine were always kept at full load to ensure the same freeze-thaw effect.

RESULTS ANALYSIS

Mass loss analysis

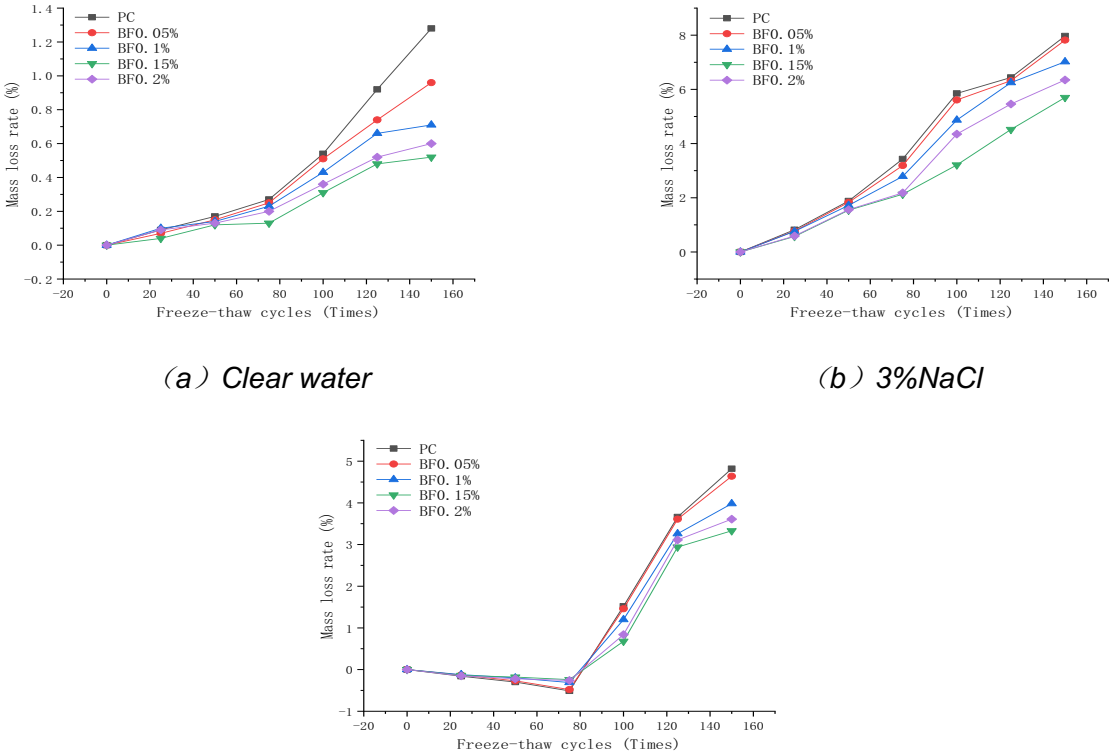

（a）Clear water

（b）3%NaCl

（c）5%Na_2SO_4

Fig. 2 Change curve of concrete mass loss rate

Figure 2 demonstrates the variation curves of mass loss rate of PC and BFRC in three types of freeze-thaw media. The mass loss varies due to different erosion mechanisms of different media. According to Figure 2, with the increase of loads on the specimens, small cracks appear inside the specimens due to freeze-thaw action. The mass loss of specimens tends to increase as the freeze-thaw cycles continue, and such mass loss gradually extends to the surface layer, causing the mortar and aggregate to fall off. As control group, PC shows many small vertical cracks on the surface, while fewer vertical cracks are found on the concrete specimens mixed with BF, indicating that BF prevents the formation of vertical cracks. Finally, PC is seriously damaged, with peeling on the edges, while concrete specimens mixed with BF shows better integrity and less peeling. The tensile strength generated inside the concrete effectively slows down its failure speed. Less BF shows no significant influence, but excessive BF causes more holes and tiny cracks, reducing the tensile strength. When the fiber content is 0.15%, the specimens show the best integrity, with less peeling.

In Figure 2 (a), in the fresh water freeze-thaw test, the mass loss of specimens increases slowly during the first 75 freeze-thaw cycles and begin to accelerate after 75 cycles. Under water pressure effect, only water can enter the surface layer through subtle channels, and no major erosion is generated, thus mass loss of the whole group is relatively small. In Figure 2 (b), in the 3% NaCl freeze-thaw test, the mass loss rates of fiber concrete and PC under the condition of 50 freeze-thaw cycles showed the same trend, and were both less than 2%. After 50 freeze-thaw cycles, the mass loss rate of concrete showed an increasing trend. The increasing trend of BF0.05% was close to that of PC. After 100 freeze-thaw cycles, the 0.05% mass loss of PC and BF has exceeded 5% and met the conditions for stopping the test, the mass loss of specimens increases

rapidly, as NaCl can absorb water, which increases the water retention time of specimens and exacerbates the damage. Furthermore, the existence of permeability pressure aggravates the peeling of aggregate and mud on the surface layer. In Figure 2 (c), in the 5% Na_2SO_4 solution. After 150 freeze-thaw cycles, the mass loss of PC is close to 5%, the curve of BF0.05% mass loss rate is same with that of PC, and the lowest mass loss rate of fiber concrete can reach 3.33%. The mass loss of concrete increases gradually for the first 75 cycles due to SO_4^{2-} crystals sticking to the specimens. With the in-crease of freeze-thaw cycles, cracks on the specimens expand and the parts of specimens begin to fall off, demonstrating a sharp increase of mass loss.

Flexural strength analysis

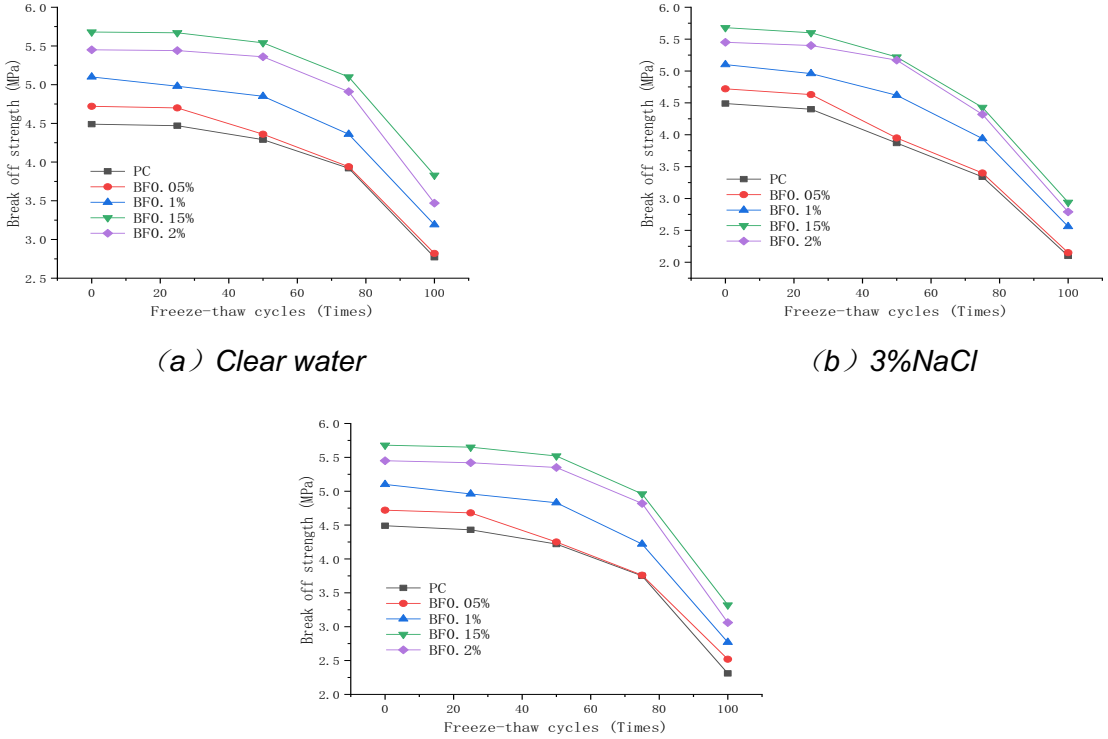

（a）Clear water　　（b）3%NaCl

（c）5%Na_2SO_4

Fig. 3 - Curve of concrete flexural strength change

Figure 3 shows the variation curves of flexural strength of PC and BFRC in three types of freeze-thaw media. The toughness of BF mainly relies on the bridging effect of fibers across the two edges of cracks. Such toughening effect effectively restrains the deformation of concrete matrix, hinders the formation of micro crack zone, and increases the cohesive force of fracture process zone, so as to prevent the expansion of macro cracks and improve the fracture toughness of concrete. The bridging effect of BF can also consume some energy for concrete matrix in the loading process, increasing the energy consuming capacity of concrete in the fracture process and improving its fracture energy. However, according to Figure 3, the flexural strength of BFRC specimens decreases with the increase of BF content when it exceeds 0.15%, as the addition of BF increases the weak transition layers, pores and defects between fiber and concrete matrix while increasing the energy consuming capacity in the fracture process. Too many fibers cause more internal defects of concrete, reducing its fracture toughness and fracture energy. In brief, the flexural strength of all BFRC specimens is higher than that of concrete without BF, so it can be concluded that BF can effectively improve the fracture properties of specimens.

Based on Figure 3(a), Under the action of freezing and thawing of clear water, the curve of BF0.15% and BF0.2% does not decrease significantly after 50 freeze-thaw cycles, and the flexural

strength of BF0.15% and BF0.2% decreases slightly after 75 freeze-thaw cycles. After thawing, the strength began to drop sharply, and the slope of the BF0.2% flexural strength decline curve was the largest, indicating that the BF0.2% concrete specimens were damaged more severely than BF0.15% after 100 freeze-thaw cycles. A certain amount of BF added into the concrete can not only increase the initial flexural strength of concrete, but also effectively slow down the decrease of its flexural strength in the fresh water freeze-thaw condition. Before complete breakage, the flexural strength of specimens mixed with BF is significantly higher than that of PC after the same numbers of freeze-thaw cycles. In Figure 3(b), After 50 freeze-thaw cycles, both the flexural strength of fiber concrete and PC show a downward trend, but the degrees and rates of decline are different. The flexural strength of fiber concrete decreases before 75 freeze-thaw cycles, but the highest flexural strength still meets the relevant requirements of C30 concrete, after 75 cycles, the flexural strength decreases significantly. For common concrete or concrete mixed with fewer fibers, the flexural strength decreases steadily after 25 freeze-thaw cycles, and the decrease rate gradually increases, indicating that BF enhances the frost resistance and salt erosion resistance of concrete to a certain extent. In Figure 3(c), The BF0.05% flexural strength curve of the concrete specimen is close to that of PC after 50 freeze-thaw cycles. The flexural strength of concrete mixed with fiber before 75 freeze-thaw cycles does not change significantly, and it fails after 100 freeze-thaw cycles. The concrete specimens are damaged after 100 freeze-thaw cycles. This is because micro cracks appear inside the concrete as the freeze-thaw cycles continues. The sulfate solution infiltrated into the concrete specimens undergoes physical and chemical reactions, producing physical crystals or chemically expansive products. The addition of fibers inhibits the expansion of micro cracks, but it restrains the crystallization of dilatant generated in hydration reaction, which expands the internal damage. The flexural strength of the specimens suddenly drops when re-straining ability of fiber network structure in the specimens reaches the peak. After 100 freeze-thaw cycles, the flexural strength of fiber concrete is still greater than that of PC, indicating that a certain amount of fiber can effectively inhibit the production of dilatant in the reaction of sulfate and hydration products in the concrete, so as to slow down cracking and peeling and improve the frost resistance of concrete.

Compressive strength analysis

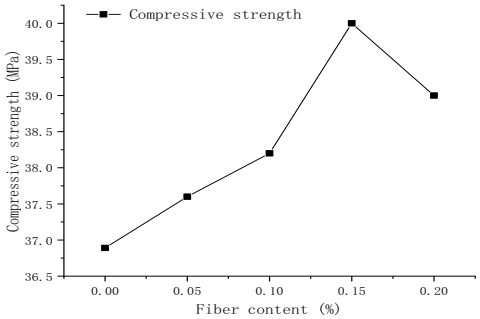

(a) Relationship between fiber content and compressive strength when not frozen and thawed

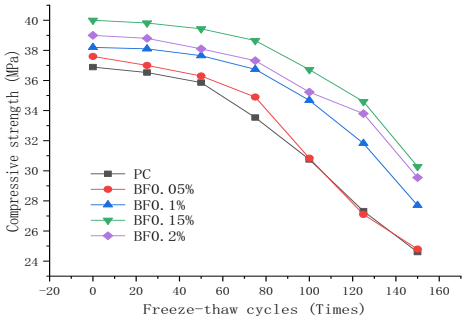

(b) Clear water

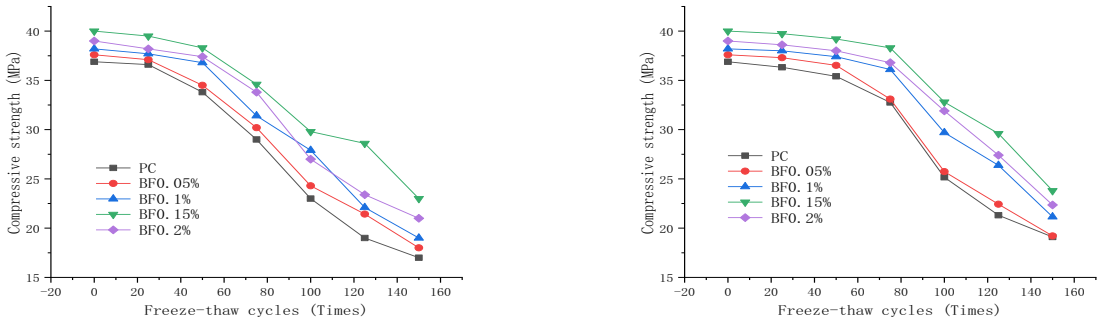

（c）3%NaCl　　（d）5%Na_2SO_4

Fig. 4 - Change curve of concrete compressive strength

Figure 4 shows the variation curves of compressive strength of PC and BFRC in three types of freeze-thaw media. Essentially, internal damage resulting from freeze-thaw cycles is responsible for the compressive strength decrease. All the four mixing amounts of BF enhance the compressive strength of concrete after 28d, and such enhancement effect first increases and then decreases with the increase of fiber content. BF forms a network structure inside the concrete, and most fibers are in an oblique and slightly lateral position. Single fiber bonded to the cement matrix enhances the bonding strength and inhibits the lateral expansion of concrete. The fiber network structure strengthens the integrity of concrete, facilitating the integration of aggregate and cement and effectively improving the compressive strength of specimens.

According to Figure 4, the descent speeds of compressive strength of BFRC in the three types of media are lower than those of PC. One reason is that, due to disorderly distribution of BF in the specimens reduces the stress concentration, which changes the trends and ex-tension paths of cracks, and increases the fracture energy. In addition, the three-dimensional frameworks formed by BF inside the matrix support the aggregate settlement and relieve the shrinkage and deformation of concrete, improving the compressive strength of concrete. With the increase of basalt fiber content, the fiber in concrete matrix tends to cake, resulting in other defects. As the freeze-thaw cycles continue, the relevant products increase and expand, after the service capacity of the fibers reaches the maxi-mum value, the compressive strength of concrete gradually decreases.

Based on Figure 4(a), the addition of BF before freeze-thaw test can increase the compressive strength of concrete, and it reaches the optimal value when the content of BF is 0.15%. In Figure 4(b), After 75 freeze-thaw cycles, the compressive strength has shown a significant downward trend and it decreased to 90% of the initial strength. After 100 freeze-thaw cycles, the compressive strength has dropped to 83.3% of the initial strength. However, the strength of BF0.1%, BF0.15%, and BF0.2% did not decrease significantly before 75 freeze-thaw cycles, and the strength decreased after 75 freeze-thaw cycles, but the decline was not significant. The compressive strength of BFRC drops significantly after 100 freeze-thaw cycles in fresh water, and the whole decline curve is relatively gentle. In Figure 4(c), After 25 freeze-thaw cycles, the strength of the specimen has decreased significantly, and with the increase in the number of freeze-thaw cycles, the rate of decline has continued to increase. After 100 freeze-thaw cycles, the strength has dropped to 23 MPa, which is only 62.3% of the initial strength. However, the strength of BF0.15% and BF0.2% began to decrease significantly after 75 freeze-thaw cycles, and the decline rate of BF0.2% became larger. After 100 freeze-thaw cycles, the strength of BF0.2% was less than BF0.1%. After 100 freeze-thaw cycles, the decline rate of BF0.2% slowed down, and the decline rate of BF0.1% increased. The decline rate of BF0.15% decreased significantly after 50 freeze-thaw cycles. After 75 freeze-thaw cycles, it increased, and the rate of decline rate slowed down after 100 freeze-thaw cycles. After 150 freeze-thaw cycles damage has occurred. In Fig. 4(d), Fiber concrete and ordinary concrete have little change in strength under the first 75 freeze-thaw cycles. PC and

BF0.05% will produce less strength loss after 75 freeze-thaw cycles. After 75 freeze-thaw cycles, the strength loss rate will increase and the strength will decrease. Fast-er, after 150 freeze-thaw cycles, the compressive strength has dropped to 19MPa, which is only 50% of the initial strength. However, the compressive strength of BF0.1%, BF0.15%, and BF0.2% did not change significantly after 75 freeze-thaw cycles, and the slope of the curve was small. More than 75 freeze-thaw cycles increased the slope of the curves of BF0.1%, BF0.15%, BF0.2% and decreased the compressive strength significantly. The strength decrease rate of BF0.1% and BF0.15% is greater than that of BF0.2%. After 100 freeze-thaw cycles, strength decline of BF0.1% and BF0.15% has slowed down, but the BF0.2% strength still declines at a relatively large rate. In salt solution, the internal gaps of specimens are filled with a series of products generated in physical and chemical reactions of salt ions penetrated into the specimens, so the compressive strength in the early and medium stage changes slightly. As the freeze-thaw cycles continue, cracks in the concrete expand and new cracks appear due to chlorine salt erosion and ice-crystal pressure effect, aggravating internal defects and reducing the compressive strength.

FREEZE-THAW CYCLE ACTION MODEL AND SERVICE LIFE PREDICTION

Based on analysis of mechanical properties of PC and BFRC after freeze-thaw action in the last chapter, it is concluded that a certain amount of fiber can enhance the frost resistance of concrete. Therefore, three comparatively optimal mixing amounts of BFRC, respectively 0.1%, 0.15% and 0.2%, were selected for service life prediction, and Weibull Model and Gray Model were used for analysis.

Service life prediction based on Weibull Model

At present, there are three common probability distribution models used for service life prediction of concrete, respectively Normal Model, Lognormal Model and Weibull Model. Normal Model and Lognormal Model show less applicability and flexibility in reliability analysis, thus failure states of concrete cannot be actually simulated [9]. The Weibull Model is relatively simple and flexible, applicable to various situations. It presents fewer requirements on sample size compared with the Normal Model and Lognormal Model. Capable to provide relatively accurate prediction results with a small amount of data, it is widely used in mechanical property analysis of concrete materials [10].

Tab. 3 - Weibull Distribution of Concrete with Different Fiber Contents in NaCl Solution

Experimental conditions	*Number of freeze-thaw cycles (n)*	*Survival rate R(n)*	*X=ln(n)*	*Y=ln(ln(1/Rn))*
BF0.1% NaCl	*25*	*0.991*	*3.2189*	*-4.7060*
	50	*0.9741*	*3.9120*	*-3.6404*
	75	*0.8843*	*4.3175*	*-2.0959*
	100	*0.7411*	*4.6052*	*-1.2052*
	125	*0.6547*	*4.8283*	*-0.8590*
	150	*0.4826*	*5.0106*	*-0.3167*
BF0.15% NaCl	*25*	*0.992*	*3.2189*	*-4.8243*
	50	*0.9752*	*3.9120*	*-3.6844*
	75	*0.9031*	*4.3175*	*-2.2835*
	100	*0.7928*	*4.6052*	*-1.4602*
	125	*0.721*	*4.8283*	*-1.1174*
	150	*0.5649*	*5.0106*	*-0.5602*
BF0.2% NaCl	*25*	*0.9918*	*3.2189*	*-4.7995*
	50	*0.975*	*3.9120*	*-3.6762*
	75	*0.892*	*4.3175*	*-2.1690*
	100	*0.7533*	*4.6052*	*-1.2613*
	125	*0.6872*	*4.8283*	*-0.9805*
	150	*0.5132*	*5.0106*	*-0.4048*

Tab. 4 - Weibull Distribution of Concrete with Different Fiber Contents in Na_2SO_4 Solution

Experimental conditions	*Number of freeze-thaw cycles (n)*	*Survival rate R(n)*	*X=ln(n)*	*Y=ln(ln(1/Rn))*
BF0.1% Na_2SO_4	*25*	*0.997*	*3.2189*	*-5.8076*
	50	*0.9894*	*3.9120*	*-4.5416*
	75	*0.9362*	*4.3175*	*-2.7192*
	100	*0.7988*	*4.6052*	*-1.4932*
	125	*0.7122*	*4.8283*	*-1.0806*
	150	*0.5636*	*5.0106*	*-0.5562*
BF0.15% Na_2SO_4	*25*	*0.9972*	*3.2189*	*-5.8767*
	50	*0.9926*	*3.9120*	*-4.9026*
	75	*0.9423*	*4.3175*	*-2.8229*
	100	*0.8276*	*4.6052*	*-1.6648*
	125	*0.7846*	*4.8283*	*-1.4164*
	150	*0.603*	*5.0106*	*-0.6815*
BF0.2% Na_2SO_4	*25*	*0.9971*	*3.2189*	*-5.8416*
	50	*0.9924*	*3.9120*	*-4.8758*
	75	*0.9317*	*4.3175*	*-2.6487*
	100	*0.8082*	*4.6052*	*-1.5467*
	125	*0.7312*	*4.8283*	*-1.1613*
	150	*0.571*	*5.0106*	*-0.5792*

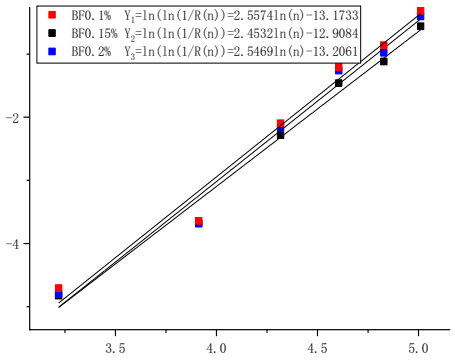

Fig. 5 - Linear regression diagram of durability life in NaCl

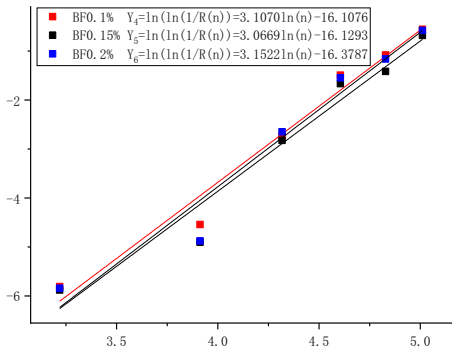

Figure 6 - Linear regression of durability life in Na_2SO_4

Tab. 5 - Weibull linear regression results of durability life in NaCl

Basalt content	*Durable life*	*b*	*c*	*R2*
0.1%	*N1*	*2.5574*	*-13.1733*	*0.9729*
0.15%	*N2*	*2.4532*	*-12.9084*	*0.9810*
0.2%	*N3*	*2.5469*	*-13.2061*	*0.9754*

Tab 6 - Weibull linear regression results of durability life in Na_2SO_4

Basalt content	*Durable life*	*b*	*C*	*R2*
0.1%	*N4*	*3.1070*	*-16.1076*	*0.9694*
0.15%	*N5*	*3.0669*	*-16.1293*	*0.9492*
0.2%	*N6*	*3.1522*	*-16.3787*	*0.9477*

Substituting the obtained parameters into function Y=bx + C, the Weibull distribution life prediction models of specimens with three mixing amounts under the freeze-thaw action of Na_2SO_4 and NaCl can be obtained respectively. Taking various parameters of Weibull distribution model into consideration, this paper uses two parameters to predict the durability of BFRC. Taking D(n) as the damage degree of concrete after n freeze-thaw cycles, the reliability function R(n) = 1 - D(n) is obtained based on the calculation formulas of concrete related variables, and linear regression analysis is performed by the least square method. The analysis results of BFRC in two kinds of freeze-thaw media are summarized as follows, where Tables 3 and 4 are Weibull distribution values, Tables 5 and 6 are linear regression results, and Figures 5 and 6 are regression curves:

According to relevant specifications, the specimens are considered expired when their relative elastic modulus reaches 60% of the initial value. Substituting R(n) = 0.6 into the above formula, conclusion is drawn as follows: N1 = 132 times, N2 = 146 times, N3 = 137 times, N4 = 143 times, N5 = 154 times, and N6 = 145 times. It can be concluded that the optimum durability is achieved when the content of basalt fiber reaches 0.15%, and damage caused by NaCl to concrete is higher than that of Na_2SO_4 under the action salt freezing.

Gray Model

Belonging to fuzzy prediction, Gray Model can be used to derive unknown elements in the system, and finally obtain the complete information with ambiguity [11]. Substitute the obtained data into formulas (1) and (2) for verification.

$$C = \frac{S_1}{S_2} \tag{1}$$

Where, S1 is the residual variance, S2 is the original data variance, and C is the posterior error ratio. When C is less than 0.35, the accuracy of prediction results is high, and when C is less than 0.50, the accuracy is qualified. The minimum error probability P is:

$$P = P(\left|\varepsilon^0(i) - \bar{\varepsilon}\right| < 0.6745 S_2) \quad (2)$$

Where, ε is the residual mean, and $\varepsilon^0(i)$ is the predicting residual at different times. When P is larger than 0.95, the accuracy of prediction results is high, and when P is larger than 0.80, the accuracy is qualified. The relative dynamic elastic modulus prediction models and accuracy test results of concrete under different working conditions are summarized in Table 7, among which, all the models meet the test requirements and show high accuracy.

Tab. 7 - Relative dynamic elastic modulus prediction model and accuracy test

Freeze-thaw solution	*Fiber content*	*Posterior difference ratio /C*	*probability error /P*	*Predictive model*
3%NaCl	*0.1*	*0.27*	*1.00*	*-8.9105e-0.1262t+9.9105*
	0.15	*0.27*	*1.00*	*-10.9392e-0.1004t+11.9392*
	0.2	*0.27*	*1.00*	*-9.60345e-0.1160t+10.6034*
5%Na_2SO_4	*0.1*	*0.3*	*1.00*	*-10.8542e-0.1029t+11.8542*
	0.15	*0.34*	*1.00*	*-12.7191e-0.0865t+13.7191*
	0.2	*0.31*	*1.00*	*-11.4173e-0.0973t+12.4173*

Tab. 8 - The relative dynamic elastic modulus of basalt fiber concrete based on gray. prediction

Number of freeze-thaw cycles	*BF0.1%*		*BF0.15%*		*BF0.2%*	
	3%NaCl	*5%Na_2SO_4*	*3%NaCl*	*5%Na_2SO_4*	*3%NaCl*	*5%Na_2SO_4*
0	*1.000*	*1.000*	*1.000*	*1.000*	*1.000*	*1.000*
25	*1.056*	*1.061*	*1.045*	*1.054*	*1.052*	*1.059*
50	*0.931*	*0.958*	*0.945*	*0.967*	*0.937*	*0.960*
75	*0.821*	*0.864*	*0.855*	*0.887*	*0.834*	*0.871*
100	*0.723*	*0.779*	*0.773*	*0.813*	*0.743*	*0.791*
125	*0.638*	*0.703*	*0.699*	*0.746*	*0.661*	*0.717*
150	*0.562*	*0.634*	*0.633*	*0.684*	*0.589*	*0.651*
175		*0.572*	*0.572*	*0.627*		*0.590*
200				*0.575*		

Where, t stands for the number of freeze-thaw cycles. At the 25th freeze-thaw cycle, t = 1; at the 50th freeze-thaw cycle, t = 2; and so on. The calculation results refer to cumulative value of dynamic elastic modulus, which is 1 when t = 0; the dynamic elastic modulus at t = 1 is the value at t = 1 minus the value at t = 0; the dynamic elastic modulus at t = 2 is the value at t = 2 minus the value at t = 1, and so on. The prediction results of relative dynamic elastic modulus are shown in Table 8.

According to the specification, the specimens are considered expired when their relative elastic modulus reaches 60% of the initial value, conclusion is drawn as follows: N1 = 125 times, N2 = 150 times, N3 = 150 times, N4 = 175 times, N5 = 125 times, and N6 = 150 times. It can be concluded that the optimum durability is achieved when the content of basalt fiber reaches 0.15%, and damage caused by NaCl to concrete is higher than that of Na_2SO_4 under the action salt freezing.

Service life prediction and analysis of BF

Li Jinyu [12] et al. concluded that the average number of freeze-thaw cycles in different regions around China is as follows: 120 times in Northeast China, 84 times in North China, and 118

times in Northwest China. He also pointed out that one outdoor freeze-thaw cycle is equivalent to 12 indoor freeze-thaw cycles.

Tab. 9 - Life prediction of basalt concrete

WEIBULL	3%NaCl			5%Na_2SO_4		
	BF0.1%	BF0.15%	BF0.2%	BF0.1%	BF0.15%	BF0.2%
Northwest	13.4	14.8	13.9	14.5	15.6	14.7
North China	18.8	20.8	19.5	20.4	22	20.7
Northeast	13.2	14.6	13.7	14.3	15.4	14.5

Tab. 10 - Life prediction of basalt concrete

GRAY MODEL	3%NaCl			5%Na_2SO_4		
	BF0.1%	BF0.15%	BF0.2%	BF0.1%	BF0.15%	BF0.2%
Northwest	12.7	15.2	12.7	15.2	17.7	15.2
North China	17.8	21.4	17.8	21.4	25	21.4
Northeast	12.5	15	12.5	15	17.5	15

Based on the environment in Gansu Province, this study takes the annual freeze-thaw cycles in Northeast China, North China, and Northwest China to calculate the frost-resistant durability of BFRC in Gansu Province with two prediction models, as summarized in Tables 9 and 10.

Comparing Weibull Model with Gray Model, it is concluded that the salt-freezing resistance of concrete is optimal when the fiber content is 0.15%, and the damage of 5% Na_2SO_4 on concrete structures is slightly less than 3% NaCl. In service life prediction, the Weibull Model can use relative dynamic elastic modulus damage as a variable to derive more accurate number of freeze-thaw cycles. The Gray Model can only be used for fuzzy inference based on the present data, and final data refers to data obtained before the relative dynamic modulus of elasticity reaches 60%, thus such results obtained are relatively general.

CONCLUSIONS

(1) This study uses Weibull Model and Gray Model to conduct service life prediction of BFRC under the environment of Gansu Province with three mixing amounts. The prediction results obtained with these two models are similar. With different emphases, the results obtained by Weibull Model are more accurate than Gray Model, and optimum durability is achieved when the content of BFRC is 0.15%. In salt invasion, the damage caused by SO_4^{2-} is less than that caused by Cl^-.

(2) With the increasing number of freeze-thaw cycles, the compressive strength and flexural strength of BFRC in three kinds of media reduce to varying degrees, and the mass loss rate-increases. The influence degree of these three kinds of freeze-thaw media on the mechanical properties of BFRC is: 3% NaCl > 5% Na_2SO_4 > water.

(3) In the same freeze-thaw environment, the frost resistance capability of concrete first in-creases and then decreases with the increase of BF content. The reason is that BF slows down the expansion of micro cracks in the specimens in the stress process, showing a toughing and anti-cracking effect and slowing down the decline of frost resistance. However, excessive BF causes weaker transition layer between itself and concrete matrix, causing more internal defects and weakening the frost resistance of concrete. As a consequence, optimal frost resistance is obtained when the fiber content is 0.15%.

REFERENCES

[1] Li Weimin, Xu Jinyu. Impact behavior and constitutive model of basalt fiber reinforced concrete[J]. Engineering Mechanics, 2009(1).

[2] Feng Zhongju, Chen Sixiao, Xu Hao, et al. Durability evaluation of concrete in alpine salt marshes based on grey system theory[J]. Journal of Traffic and Transportation Engineering, 2018,18(06):18-26.
[3] Xie Guoliang, Shen Xiangdong, Liu Jinyun, Zhang Bin. Freezing resistance and damage degradation model of bas-alt fiber recycled concrete[J].Composite Materials Science and Engineering,2021(04):55-60.
[4] Kizilkanat A B , Kabay N , Veysel Akyüncü, et al. Mechanical properties and fracture behavior of basalt and glass fiber reinforced concrete: An experimental study[J]. Construction and Building Materials, 2015, 100:218-224.
[5] Boxin Wang, Jingjing Pan, Ruichang Fang, Qing Wang. Damage model of concrete subjected to coupling chemical attacks and freeze-thaw cycles in saline soil area[J]. Construction and Building Materials.2020,242:118205.
[6] Ralegaonkar R , Gavali H , Aswath P , et al. Application of chopped basalt fibers in reinforced mortar: A review[J]. Construction and Building Materials, 2018, 164(MAR.10):589-602.
[7] Audrius Vaitkus, Judita Gražulytė ， OrcID, et al. Concrete Modular Pavement Structures with Optimized Thickness Based on Characteristics of High Performance Concrete Mixtures with Fibers and Silica Fume[J]. Materi-als.2021,14(12),3423.
[8] The 2019 edition of "Standards for Test Methods of Physical and Mechanical Properties of Concrete" is released[J]. Commercial Concrete,2019(11):9.
[9] Ministry of Housing and Urban-Rural Development of the People's Republic of China. Test method for long-term performance and durability of ordinary concrete: GB/T50082-2009［S］. Beijing: China Construction Industry Press, 2009:10-14.
[10] Zhang Yana, Liu Xingwang, Du Yao, Liu Yan. Durability evaluation of concrete structures based on fuzzy exten-sion analytic hierarchy process[J].Journal of Hebei Agricultural University,2014,37(01):102-105.
[11] Zhang Yizhe. Research on fatigue damage of high-speed EMU frame based on working condition recognition[D]. Beijing Jiaotong University, 2019.
[12] Huang Weiqing. Software reliability evaluation based on cloud theory and grey model[D]. Xi'an University of Posts and Telecommunications, 2016.
[13] Li Jinyu, Peng Xiaoping, Deng Zhenggang, Cao Jianguo, Guan Yushi, Lin Li, Tian Juntao, Li Fang, Wang Aiqin, Wang Zhigang, Peng Tao, Cai Meizhu, Zhang Xiumei. Quantitative design of concrete frost resistance[J]. Concrete, 2000 (12) : 61-65.